Search for vector-like partners of the top and bottom quarks with the ATLAS experiment

BERGISCHE
UNIVERSITÄT
WUPPERTAL

Fakultät für Mathematik
und Naturwissenschaften

Dissertation

Jens Roggel

August 2022

Erstgutachter: Priv.-Doz. Dr. Frank Ellinghaus
Zweitgutachter: Prof. Dr. Wolfgang Wagner
Drittgutachter: Prof. Dr. Johannes Erdmann

Abgabedatum: 11.08.2022
Prüfungsdatum: 27.01.2023

Abstract

In this dissertation, a search for pair-produced vector-like partners T and B of the top and bottom quarks in events with an isolated lepton, at least four jets, and high missing transverse momentum is presented. Data from proton–proton collisions at a centre-of-mass energy of $\sqrt{s} = 13\,\text{TeV}$ at the Large Hadron Collider, recorded by the ATLAS experiment from 2015 to 2018 and corresponding to an integrated luminosity of $139\,\text{fb}^{-1}$, are analysed. The vector-like quarks are assumed to decay into a W, Z, or Higgs boson and a third-generation quark. Signal and background events are separated by neural networks, trained for various signal hypotheses. As no significant deviations from the Standard Model expectation are observed, upper limits on the production cross-section of T and B quarks as a function of their masses are derived for various decay scenarios. The strongest limits on the masses are 1.59 TeV for a weak-isospin (T, B) doublet assuming mass degenerate vector-like quarks and 1.47 TeV (1.46 TeV) for exclusive $T \to Zt$ ($B \to Wt$) decays. Lower limits on the mass of the T and B quarks are derived for all combinations of branching ratios. Furthermore, improvements of the ATLAS Monte Carlo validation system are discussed, and the results of a dedicated study of the interference effect between top-quark pair production and single top-quark production in association with a W boson are presented in this dissertation.

Contents

Introduction

All known elementary particles and their interactions, except for gravity, are described by the Standard Model (SM) of particle physics. Its theoretical predictions have been successfully probed in numerous experiments. Despite its great success, there are still some open questions that cannot be answered by the SM. These are fundamental physics phenomena, e.g. gravity, as well as theoretical shortcomings, like the required fine-tuning due to radiative corrections to the Higgs boson mass. The open questions indicate the need for beyond the SM (BSM) theories, which introduce new particles and theoretical concepts in order to solve the limitations of the SM. Several BSM theories include vector-like quarks (VLQs), which are the simplest extension of the SM quark sector that has not been already excluded.

In this dissertation, a search for pair-produced VLQs with the ATLAS experiment at the Large Hadron Collider (LHC) is presented. The analysed data set corresponds to an integrated luminosity of $139\,\text{fb}^{-1}$, collected in proton–proton (pp) collisions at a centre-of-mass energy of $\sqrt{s} = 13\,\text{TeV}$ during the LHC Run 2 from 2015 to 2018. The search focuses on vector-like partners of the top and bottom quarks, whose left- and right-handed components transform identically under weak interactions. VLQs can contribute to the radiative corrections to the Higgs boson mass and, therefore, solve the related fine-tuning problem. They decay into a boson and a quark via flavour-changing neutral and charged currents. Vector-like top quarks (VLTs) carry an electric charge of $+2/3\,e$, while vector-like bottom quarks (VLBs) have an electric charge of $-1/3\,e$. VLQs are assumed to decay into a W, Z, or Higgs boson and a third-generation quark.

The presented search focuses on events in final states containing an isolated electron or muon, jets, and large values of the missing transverse momentum ($E_{\text{T}}^{\text{miss}}$). The analysis is most sensitive to the $Z(\rightarrow \nu\bar{\nu})t + X$ decay mode in the case of VLTs, and to the $Wt + X$ scenario for VLBs, where X denotes one of the other possible VLQ decays. In order to account for the different signal scenarios, the analysis strategy is based on the application of neural networks (NNs), trained for various signal hypotheses.

Apart from the search for VLQs, developments concerning the Monte Carlo (MC) event generation are discussed in this dissertation. The extension and improvement of the ATLAS MC validation system are explained, allowing for a careful validation of the MC generator versions and infrastructure that is used for the production of MC samples in ATLAS. In addition, a set of validation results illustrates changes in the MC generators and infrastructure affecting the MC predictions. Furthermore, a dedicated study of the handling of the interference effect between top-quark pair production ($t\bar{t}$) and single top-quark production in association

with a W boson and a bottom quark (tWb) is presented. So far, the overlap between the final states has been resolved by applying diagram removal (DR) and diagram subtraction (DS) techniques in the generation of the tW sample. As the related uncertainty is one of the leading systematic uncertainties in several searches, like the search for VLQs presented in this dissertation, different implementations of the DR and DS techniques are studied. The predictions for $t\bar{t} + tW$ are compared to a prediction from a new generator being able to simulate the $pp \to b\bar{b}\ell^+\nu\ell^-\bar{\nu}$ final state taking quantum interference effects between Feynman diagrams with the same final state into account.

The structure of this dissertation is as follows: The first part focuses on the theoretical concepts, including an overview of the SM in Chapter 1, the introduction of VLQs in Chapter 2, and the concepts of MC event simulation in Chapter 3. The ATLAS MC validation system and procedure are explained and discussed in Chapter 4. Afterwards, the LHC and the ATLAS detector with its subsystems are described in Chapter 5. Before describing the search for VLQs, the reconstruction of physics objects in ATLAS is explained in Chapter 6. The presentation of the search for VLQs in Chapter 7 starts with an overview about the data set used and the simulated MC events. Afterwards, properties of signal and background processes are described before the event selection is discussed. Then, the statistical techniques are explained and the final results are presented. Finally, the results are compared to other VLQ searches and an outlook is given.

The results of a dedicated study for the treatment of the interference effect between top-quark pair production and single top-quark production in association with a W boson and a bottom quark are discussed in Chapter 8. Finally, the results of this dissertation are summarised and concluded.

1 The Standard Model of Particle Physics

The SM [1, 2] is the theoretical framework that so far provides the most precise description of the fundamental particles and their interactions. Since its development in the 1960s and 1970s, it has been thoroughly tested and the various predictions have been confirmed by numerous experimental results. The latest major confirmation of the SM was the discovery of the Higgs boson by the ATLAS and CMS collaborations at the LHC in 2012 [3, 4].

This chapter introduces the building blocks of the SM, i.e. the elementary particles, their interactions, and its mathematical formulation. Afterwards, a selection of experimental results validating the theoretical predictions and their consistency is shown. At the end of this chapter, the limitations of the theory are discussed and the need for theories beyond the SM is motivated.

As common in the field of particle physics, the natural unit system will be used throughout this dissertation, setting the speed of light in vacuum c and the reduced Planck constant $\hbar$ to unity. Electric charges are expressed in units of the elementary charge e.

1.1 Particles and interactions in the Standard Model

The constituents of the SM, the elementary particles, are classified according to their spin as fermions or bosons. Fermions are spin-½ particles, whereas bosons have integer spin. Fermions are further split into quarks and leptons based on their charges. Leptons carry electric charge, while quarks carry additionally one of three possible colour charges denoted as red, blue, and green. As shown in Table 1.1, both, quarks and leptons, are ordered in three pairs of particles each, which are called generations. Each generation contains an up-type quark with electric charge $Q = +2/3$ and a down-type quark with $Q = -1/3$. The up-type quarks are denoted as up, charm, and top, and the down-type quarks as down, strange, and bottom.

The lepton pairs consist of a charged lepton with $Q = -1$ and an associated electrically neutral lepton neutrino. The charged leptons are called electron, muon, and tau. Neutrinos are considered to be massless in the SM, while all other fermions are massive. Except for a higher mass, fermions of higher generations are identical copies of the first generation. Only the particles of the first generation are stable and thus are the building blocks of all ordinary matter. Particles of higher generations are unstable and, with the exception of neutrinos, decay into lighter particles. An antiparticle is assigned to each fermion, doubling the number

Table 1.1: Overview of the leptons and quarks in the SM, with their electric charges and masses according to the Particle Data Group [5]. Neutrinos are considered to be massless in the SM.

	Leptons			Quarks		
Generation	Name	Charge	Mass	Name	Charge	Mass
I	electron (e)	-1	511 keV	up (u)	$+2/3$	2.2 MeV
	e neutrino (ν_e)	0	0 eV	down (d)	$-1/3$	4.7 MeV
II	muon (μ)	-1	106 MeV	charm (c)	$+2/3$	1.27 GeV
	μ neutrino (ν_μ)	0	0 eV	strange (s)	$-1/3$	93 MeV
III	tau (τ)	-1	1.78 GeV	top (t)	$+2/3$	172.8 GeV
	τ neutrino (ν_τ)	0	0 eV	bottom (b)	$-1/3$	4.18 GeV

of fermions in the SM. Antiparticles have the same mass as their associated particle but opposite quantum numbers.

In the SM, the interactions between the fundamental particles are mediated through the spin-1 gauge bosons listed in Table 1.2. The electromagnetic force is mediated by the massless photon. It couples to the electric charge and hence the electromagnetic force acts on all fermions except for neutrinos. As the photon is itself electrically neutral, it does not exhibit self-coupling. The weak interaction is mediated by charged W bosons and the neutral Z boson, which couple to the weak isospin of a particle. The up-type quarks and neutrinos carry a weak isospin of $+1/2$, while its value for the down-type quarks and charged leptons is $-1/2$. Due to the non-zero weak isospin for all fermions, the weak interaction is the only force in the SM acting on all leptons and quarks. As the observed weak gauge bosons are massive, the spatial range of the weak interaction is limited. Gluons are the mediators of the strong force and act on the colour charge of particles. Like the photon, gluons are massless and electrically neutral, but each gluon is in one of eight colour states. Thus, gluons exhibit self-couplings and the strong interaction only affects quarks and gluons.

The particle content of the SM is completed by the Higgs boson, which is electrically neutral, has a mass of 125.3 GeV [5], and is the only known scalar particle in the SM. It plays an important role in giving masses to all other SM particles.

Table 1.2: List of the gauge bosons in the SM. For each boson, its mass and electric charge, as well as the interaction it mediates is listed [5].

Particle	Charge	Mass	Interaction
photon (γ)	0	0 GeV	electromagnetic
W boson	± 1	80.4 GeV	weak
Z boson	0	91.2 GeV	weak
gluon (g)	0	0 GeV	strong

Mathematically, the SM is a renormalisable quantum field theory that is based on the invariance under the gauge group

$$\mathrm{SU}(3)_C \otimes \mathrm{SU}(2)_L \otimes \mathrm{U}(1)_Y, \tag{1.1}$$

where $\mathrm{SU}(3)_C$ is the symmetry group of the strong interaction and $\mathrm{SU}(2)_L \otimes \mathrm{U}(1)_Y$ the symmetry group of the electroweak interaction. Particles are described as field functions of space-time coordinates and their dynamics are encoded in a Lagrangian density $\mathcal{L}$, which will be referred to as Lagrangian in the following.

In general, the dynamics of free fermions are described by the Dirac equation with the following Lagrangian:

$$\mathcal{L} = \bar{\psi}\left(i\gamma^\mu \partial_\mu - m\right)\psi. \tag{1.2}$$

Here, ψ is the fermion field, γ^μ are the Dirac matrices, ∂_μ is the partial derivative, and m the mass of the fermion. Requiring the invariance of the Lagrangian under local gauge transformations of a given symmetry group implies the existence of massless gauge fields, whose number is equal to the number of generators of the respective symmetry group.

The full SM Lagrangian comprising the dynamics and interactions of all elementary particles contains contributions from the unified electroweak interaction, quantum chromodynamics (QCD), the electroweak symmetry breaking with the Higgs potential, as well as the Yukawa couplings of the fermions to the Higgs field. In the following, these contributions are discussed with their underlying theory.

1.2 Electroweak theory

The electroweak theory [6, 7] describes electromagnetic and weak interactions and unifies them in the symmetry group $\mathrm{SU}(2)_L \otimes U(1)_Y$. It includes flavour-conserving, neutral interactions mediated by the Z boson and the photon, as well as flavour-changing, charged currents mediated by the $W^\pm$ bosons. The latter are maximally parity violating. This is a direct consequence of the vector minus axial vector (V − A) structure of the weak interaction, resulting in the charged W bosons coupling solely to left-handed fermions. A new quantum number, T, called weak isospin is introduced by the symmetry group $\mathrm{SU}(2)_L$, where the subscript denotes coupling to left-handed particles only. The generators of this group are the weak isospin operators which can be expressed as $T_i = \frac{\sigma_i}{2}(i = 1, 2, 3)$, where the σ_i are the three Pauli matrices. The left- and right-handed components of the fermion fields, denoted as ψ_L and ψ_R, can be expressed as

$$\psi_{\mathrm{L,R}} = \frac{1}{2}\left(1 \mp \gamma^5\right)\psi, \tag{1.3}$$

where $\gamma^5 = i\gamma^0\gamma^1\gamma^2\gamma^3$ is the product of Dirac matrices. They transform differently under the operators of the weak symmetry group. While left-handed fermions transform as $\mathrm{SU}(2)_L$ doublets, right-handed fermions transform as singlets. The fermions are accordingly arranged in the following weak-isospin doublets and singlets:

$$\begin{pmatrix} \nu^i \\ \ell^i \end{pmatrix}_L, \begin{pmatrix} u^i \\ d'^{,i} \end{pmatrix}_L, \ell^i_R, u^i_R, d^i_R, \tag{1.4}$$

where ℓ denotes the charged lepton, ν the associated neutrino, u the up-type quark, and d the down-type quark in three fermion generations $i = 1, 2, 3$. As neutrinos only participate in the weak interaction, which acts solely on left-handed fermions, right-handed neutrinos are not included in the SM.

The weak eigenstates of the down-type quarks, denoted as d' above, do not correspond directly to their mass eigenstates, but are linear combinations instead. The mixing is described by the the Cabibbo–Kobayashi–Maskawa (CKM) matrix [8, 9]:

$$\begin{pmatrix} d' \\ s' \\ b' \end{pmatrix} = \underbrace{\begin{pmatrix} V_{ud} & V_{us} & V_{ub} \\ V_{cd} & V_{cs} & V_{cb} \\ V_{td} & V_{ts} & V_{tb} \end{pmatrix}}_{V_{\mathrm{CKM}}} \begin{pmatrix} d \\ s \\ b \end{pmatrix}. \tag{1.5}$$

A common representation of the unitary CKM matrix is

$$V_{\mathrm{CKM}} = \begin{pmatrix} c_{12}c_{13} & s_{12}c_{13} & s_{13}e^{-i\delta} \\ -s_{12}c_{23} - c_{12}s_{23}s_{13}e^{i\delta} & c_{12}c_{23} - s_{12}s_{23}s_{13}e^{i\delta} & s_{23}c_{13} \\ s_{12}s_{23} - c_{12}c_{23}s_{13}e^{i\delta} & -c_{12}s_{23} - s_{12}c_{23}s_{13}e^{i\delta} & c_{23}c_{13} \end{pmatrix}, \tag{1.6}$$

with $s_{ij} = \sin\theta_{ij}$, $c_{ij} = \cos\theta_{ij}$, three mixing angles θ_{12}, θ_{13}, θ_{23}, and a phase δ which violates the charge conjugation.

The second part of the symmetry group, $\mathrm{U}(1)_Y$, introduces a new conserved quantity, the hypercharge Y, which can be related to the electric charge and the third component of the weak isospin, T_3, using the Gell-Mann Nishijima formula [10, 11]

$$Q = T_3 + \frac{Y}{2}. \tag{1.7}$$

In order to respect the local gauge invariance of the Lagrangian under both symmetry groups, the partial derivative in the Dirac Lagrangian is replaced by the covariant derivative

$$D_\mu = \partial_\mu - ig\frac{\sigma_i}{2}W^i_\mu - ig'\frac{Y}{2}B_\mu, \tag{1.8}$$

where W^i_μ $(i = 1, 2, 3)$ and B_μ are the gauge fields associated with $\mathrm{SU}(2)_L$ and $\mathrm{U}(1)_Y$, respectively. The corresponding coupling constants are g and g'. For the introduced gauge

fields, an additional kinetic term has to be added to the Lagrangian

$$\mathcal{L}_{\text{gauge}} = -\frac{1}{4} W^i_{\mu\nu} W^{i\,\mu\nu} - \frac{1}{4} B_{\mu\nu} B^{\mu\nu}. \tag{1.9}$$

Here, $W^i_{\mu\nu}$ and $B_{\mu\nu}$ represent the field tensors of the respective gauge group defined as

$$\begin{aligned} W^i_{\mu\nu} &= \partial_\mu W^i_\nu - \partial_\nu W^i_\mu + g\epsilon^{ijk} W^j_\mu W^k_\nu, \\ B_{\mu\nu} &= \partial_\mu B_\nu - \partial_\nu B_\mu. \end{aligned} \tag{1.10}$$

The totally antisymmetric Levi-Civita tensor ϵ^{ijk} is the structure constant of the $\mathrm{SU}(2)_L$ group and is related to the generators of the group via the commutator relation $[T^i, T^j] = i\epsilon^{ijk} T^k$. The corresponding term in the field tensor represents the non-abelian structure of the weak interaction allowing self-couplings of the W_μ fields. The neutral field W^3_μ mixes with the gauge field of the $\mathrm{U}(1)_Y$ symmetry group to give the physical photon and Z boson fields.

$$\begin{pmatrix} Z_\mu \\ A_\mu \end{pmatrix} = \begin{pmatrix} \cos\theta_W & -\sin\theta_W \\ \sin\theta_W & \cos\theta_W \end{pmatrix} \begin{pmatrix} W^3_\mu \\ B_\mu \end{pmatrix} \tag{1.11}$$

Here, A_μ denotes the photon field, Z_μ the field of the Z boson, and θ_W is the weak mixing angle. If the Z boson would correspond directly to the W^3 of $\mathrm{SU}(2)_L$ instead, it would couple only to left-handed particles and right-handed anti-particles. This is in contradiction to experimental results showing that the Z boson couples to both chiral states even if not equally. The coupling constant of the photon is $e = g\sin\theta_W = g'\cos\theta_W$, while the weak coupling of the flavour-conserving interaction mediated by the Z boson is $e/(\sin\theta_W \cos\theta_W)$. The off-diagonal elements of the $\frac{\sigma_i}{2} W^i_\mu$ matrix can be expressed as

$$W^\pm = \left(W^1 \mp iW^2\right)/\sqrt{2}, \tag{1.12}$$

which are the definitions of the physical $W^\pm$ bosons. As these couplings connect the up- and down-type elements of the left-handed fermions, these interactions are flavour-changing. The final electroweak Lagrangian can be written as

$$\mathcal{L}_{\text{EW}} = \sum_f \bar{\psi}_f i\gamma^\mu D_\mu \psi_f + \mathcal{L}_{\text{gauge}}, \tag{1.13}$$

where the sum runs over all fermions f. No mass terms for fermions or the gauge fields are included in this Lagrangian. While experimental observations show that the fermions, as well as W and Z bosons are massive, the introduction of any explicit mass term in this Lagrangian would break the invariance under local gauge transformation. The charged fermions and bosons obtain non-zero masses through the Higgs mechanism, which retains the gauge invariance.

1.3 The Higgs mechanism

The Higgs mechanism [12, 13] relies on the concept of spontaneous symmetry breaking, which breaks the $\mathrm{SU}(2)_L \otimes \mathrm{U}(1)_Y$ symmetry of the unified electroweak theory into the observed $\mathrm{U}(1)_{\mathrm{EM}}$ symmetry. For this, a new complex SU(2) doublet of scalar fields ϕ, known as Higgs field, is introduced

$$\Phi = \begin{pmatrix} \phi^+ \\ \phi^0 \end{pmatrix} = \frac{1}{\sqrt{2}} \begin{pmatrix} \phi_1 + i\phi_2 \\ \phi_3 + i\phi_4 \end{pmatrix}, \tag{1.14}$$

where the superscripts denote the electric charge of the corresponding field. The Lagrangian of this new field can be written as

$$\mathcal{L}_{\mathrm{Higgs}} = (D_\mu \Phi)^\dagger (D^\mu \Phi) - V(\Phi). \tag{1.15}$$

Here, the first term describes the kinematic of the Higgs field and the interactions with gauge bosons, while the latter term is the Higgs potential $V(\Phi)$, which is defined as

$$V(\Phi) = \mu^2 \Phi^\dagger \Phi + \lambda \left(\Phi^\dagger \Phi\right)^2. \tag{1.16}$$

The potential V depends on the two parameters μ^2 and λ. The parameter λ is considered to be positive, since the case $\lambda < 0$ is unphysical because it results in non-stable minima. For μ^2 larger than zero, a single minimum of the potential exists at $\Phi = 0$, as shown in Figure 1.1a. On the other hand, the potential in the case $\mu^2 < 0$, illustrated in Figure 1.1b, has an infinite collection of degenerate minima satisfying the relation

$$\Phi^\dagger \Phi = -\frac{\mu^2}{2\lambda} = \frac{v^2}{2}. \tag{1.17}$$

The choice of a minimum, which corresponds to the physical vacuum state, spontaneously breaks the symmetry of the Lagrangian. According to the Goldstone theorem [14], a spontaneously broken continuos symmetry results in massless scalar particles, referred to as Goldstone bosons. In order to ensure charge conservation, the minimum of the potential is chosen such that the vacuum expectation value is non-zero only for the neutral component:

$$\langle 0|\Phi|0\rangle = \frac{1}{\sqrt{2}} \begin{pmatrix} 0 \\ v \end{pmatrix}. \tag{1.18}$$

Expanding the field about the vacuum expectation value, the Higgs doublet can be written in the unitary gauge as

$$\Phi(x) = \frac{1}{\sqrt{2}} \begin{pmatrix} 0 \\ v + H(x) \end{pmatrix}, \tag{1.19}$$

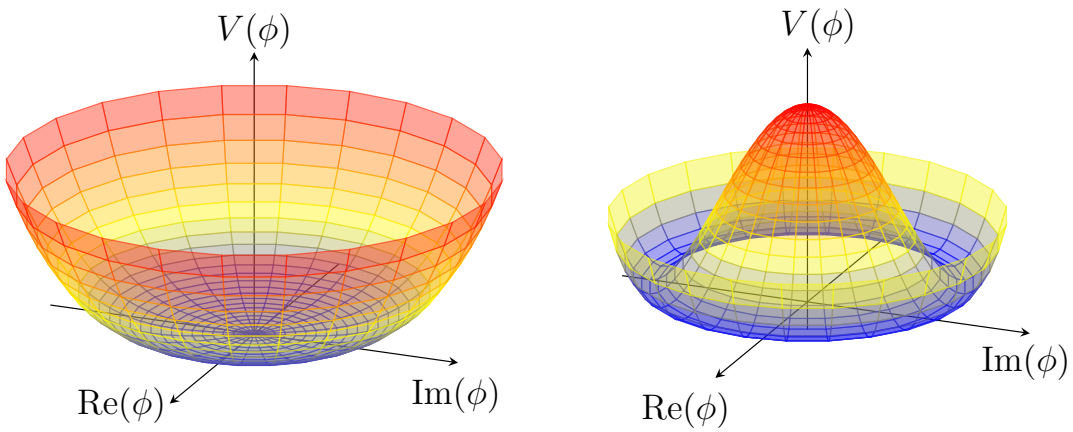

(a) **(b)**

Figure 1.1: Higgs potential $V(\phi)$ for $\lambda > 0$ and (a) $\mu^2 > 0$ or (b) $\mu^2 < 0$.

where the field $H(x)$ describes fluctuations around the minimum and represents a massive scalar boson, referred to as Higgs boson. In this specific gauge, the Goldstone bosons are absorbed by the gauge bosons, adding longitudinal polarisation components. Inserting the new expression for the Higgs field into the formula for the Higgs potential yields

$$V(\Phi) = \frac{1}{2}m_H^2 H^2 + \frac{1}{2v}m_H^2 H^3 + \frac{1}{8v^2}m_H^2 H^4 + \text{const.}, \tag{1.20}$$

with the Higgs boson mass defined as $m_H = \sqrt{2\lambda}\nu$. The second and third term represent three- and four-point Higgs boson self-interactions, respectively. Evaluating the first term in Equation 1.15 at the vacuum expectation value, the mass terms for the gauge bosons can be obtained:

$$\Delta\mathcal{L} = \frac{v^2}{8}\left[g^2\left(W_\mu^1\right)^2 + g^2\left(W_\mu^2\right)^2 + \frac{v^2}{8}\left(g'B_\mu - gW_\mu^3\right)\right]. \tag{1.21}$$

Using the expressions for $W^\pm$ from Equation 1.12 and the relations between the neutral fields from Equation 1.11, the gauge boson masses follow to

$$m_W = \frac{vg}{2}, \quad m_Z = \frac{v}{2}\sqrt{g^2 + g'^2} \quad \text{and} \quad m_A = 0. \tag{1.22}$$

Interactions between the Higgs boson and the gauge bosons follow when including the expansion of the Higgs doublet from Equation 1.19 in the above calculation.
Finally, the fermions obtain their mass through Yukawa interactions with the Higgs doublet, which are described by the following Lagrangian:

$$\mathcal{L}_{\text{Yukawa}} = \sum_{f=\ell,q} y_f\left[\bar{\psi}_{f,L}\Phi\psi_{f,R} + \bar{\psi}_{f,R}\Phi^\dagger\psi_{f,L}\right], \tag{1.23}$$

with the Yukawa coupling y_f to the fermion f. The terms in the Yukawa Lagrangian are $\mathrm{SU}(2)_L$ singlets and therefore do not break the gauge invariance. Inserting the selected vacuum expectation value in the Lagrangian, the tree level predictions for the fermion mass m_f follows to $m_f = y_f \frac{v}{\sqrt{2}}$. This shows that more massive particles have a stronger coupling to the Higgs boson.

1.4 Quantum chromodynamics

The strong interactions of quarks and gluons are described by the theory of QCD using $\mathrm{SU}(3)_C$ as the underlying symmetry, where the subscript C indicates the quantum number colour. The symmetry group $\mathrm{SU}(3)_C$ has eight generators T_a, with $a = 1, \ldots, 8$, which are related to the Gell-Mann matrices λ_a by $T_a = \frac{1}{2}\lambda_a$. Accordingly, the same number of gauge fields G^a_μ is introduced, corresponding to the eight gluons. As for the electroweak theory, a covariant derivative is introduced in order to ensure local gauge invariance:

$$D_\mu = \partial_\mu - i g_s T_a G^a_\mu, \tag{1.24}$$

where g_s is the strong coupling constant, commonly given as $\alpha_\mathrm{s} = g_s^2/4\pi$. Adding a kinematic term for the gluon fields, the QCD Lagrangian can be written as

$$\mathcal{L}_\mathrm{QCD} = \sum_q \bar{\psi}_q \left(i\gamma^\mu D_\mu\right) \psi_q - \frac{1}{4} G^a_{\mu\nu} G^{a\mu\nu}, \tag{1.25}$$

where ψ_q represents the quark fields for all quark flavours q and $G^a_{\mu\nu}$ is the gluon field tensor given by

$$G^a_{\mu\nu} = \partial_\mu G^a_\nu - \partial_\nu G^a_\mu + g_s f^{abc} G^b_\mu G^c_\nu. \tag{1.26}$$

In this relation, the f^{abc} are the structure constants of the $\mathrm{SU}(3)_C$ group, defined by the commutator relation $[\lambda_i, \lambda_j] = 2i f_{ijk} \lambda_k$. As the generators of this group do not commute, the structure constants do not vanish, resulting in the non-abelian structure of QCD. The corresponding term in Equation 1.26 gives rise to gluon self-interactions. These self-interactions lead to a strong dependence of the coupling α_s on the energy scale Q, which can be expressed at leading order as

$$\alpha_\mathrm{s}\left(Q^2\right) = \frac{\alpha_\mathrm{s}\left(\mu^2\right)}{1 + \beta\, \alpha_\mathrm{s}\left(\mu^2\right) \ln\left(Q^2/\mu^2\right)}. \tag{1.27}$$

Here, $\alpha_\mathrm{s}(\mu^2)$ is the value of the strong coupling at a reference scale μ^2, and the parameter β is defined as

$$\beta = \frac{33 - 2n_f}{12\pi}, \tag{1.28}$$

where n_f is the number of active quark flavours with $m_q < Q$. As $n_f \leq 6$ in the SM, two key features of QCD can be derived from the expression for α_s. At high energies, α_s becomes sufficiently small that perturbation theory is valid and can be used for predictions. As the coupling vanishes in the high energy limit $Q \to \infty$, quarks act as quasi-free particles, an effect known as asymptotic freedom [15, 16]. On the other hand, the value of α_s increases with decreasing energy up to an order of magnitude where perturbation theory is not predictive. This strong coupling prevents quarks and gluons from existing as free particles and makes them subject to confinement [17] forming colour-neutral states referred to as hadrons. These can be either combinations of three quarks with each possible colour once, called baryons, or quark-antiquark pairs, labelled as mesons.

1.5 Probing the Standard Model

Since its formulation in the 1960s and 1970s, the SM has been able to describe most observed phenomena in particle physics and all predicted elementary particles were discovered in various experiments. For example, the electroweak gauge bosons were discovered at CERN in 1983 [18, 19] and the heaviest particle, the top quark, more than 10 years later at the Tevatron [20, 21]. The last missing piece of the SM, the Higgs boson, was discovered by ATLAS and CMS at CERN in 2012 [3, 4]. As the experiments and related techniques are continually developed, the precision of cross-section measurements and other measurable variables, like particle mass or width, has been subsequently improved. Additionally, higher collision energies and larger data sets enable the possibility to explore a larger variety of processes, even those with smaller cross-sections.
As described in the previous sections for some examples, the SM does not fix all parameters but contains a set of free parameters:

- Nine parameters for the Yukawa couplings to the Higgs field that determine the masses of quarks and charged leptons.
- Three coupling constants describing the strength of the gauge interactions, g, g', and g_S.
- Two parameters that define the Higgs sector, m_H and v.
- Four parameters defining the CKM matrix, three mixing angles θ and a CP violating phase δ.
- One CP violating phase θ_{CP} in the QCD sector, which is experimentally found to be effectively zero [22, 23].

These 19 free parameters cannot be calculated from first principles but need to be determined in experiments. So far, experimental results have confirmed the consistency of the SM successfully. In the following, a selection of various types of important measurements is presented.

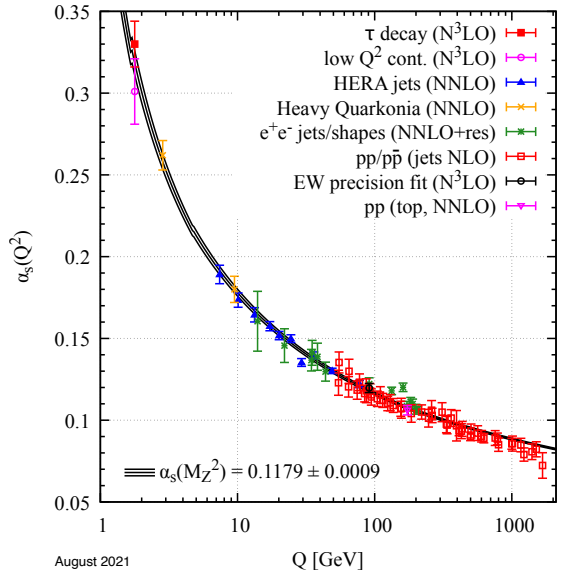

Figure 1.2: Measurements of the strong coupling α_s as a function of the energy scale Q [5]. The mass of the Z boson is chosen as the reference scale for α_s.

An example is the measurement of the strong coupling parameter α_s. This parameter has been measured by various experiments at a broad range of energies, and the results, illustrated in Figure 1.2, confirm the aforementioned dependence of α_s on the energy scale Q.
The latest discovery of the SM was the one of the Higgs boson in 2012. Since then, its mass has been measured for different production and decay modes. Individual results from the measurements in the $H \to ZZ^\star \to 4\ell$ and $H \to \gamma\gamma$ decay channels for Run 1 and Run 2 data, as well as combined results are shown in Figure 1.3a. A good compatibility between all independent measurements is visible. The precision of the measured mass has been improved by the combination of single analyses.
Due to radiative corrections, particle masses can influence predictions of process properties like the cross-section or decay rate, even if they are not directly involved in the process. This relation allows, for example, to determine the mass of the top quark indirectly. Figure 1.3b shows the indirect determination of W boson and top-quark mass from global fits to electroweak precision data when including and excluding the Higgs boson mass in the fit, respectively. In addition, the results are compared to direct measurements for both particles. The fact that direct and indirect measurements agree, confirms the underlying theory describing the relations between the various parameters.
The global electroweak fit performed by the Gfitter group [25] allows to validate the consistency between the measurements for various fundamental SM parameters. Figure 1.3c shows the deviations of the fit results from the individual measurements for each parameter, where none of the deviations exceeds 2.5σ for all considered quantities. This confirms that all the measurements can be explained simultaneously by the SM predictions.
Lastly, Figure 1.4 shows a summary of cross-section measurements for various processes

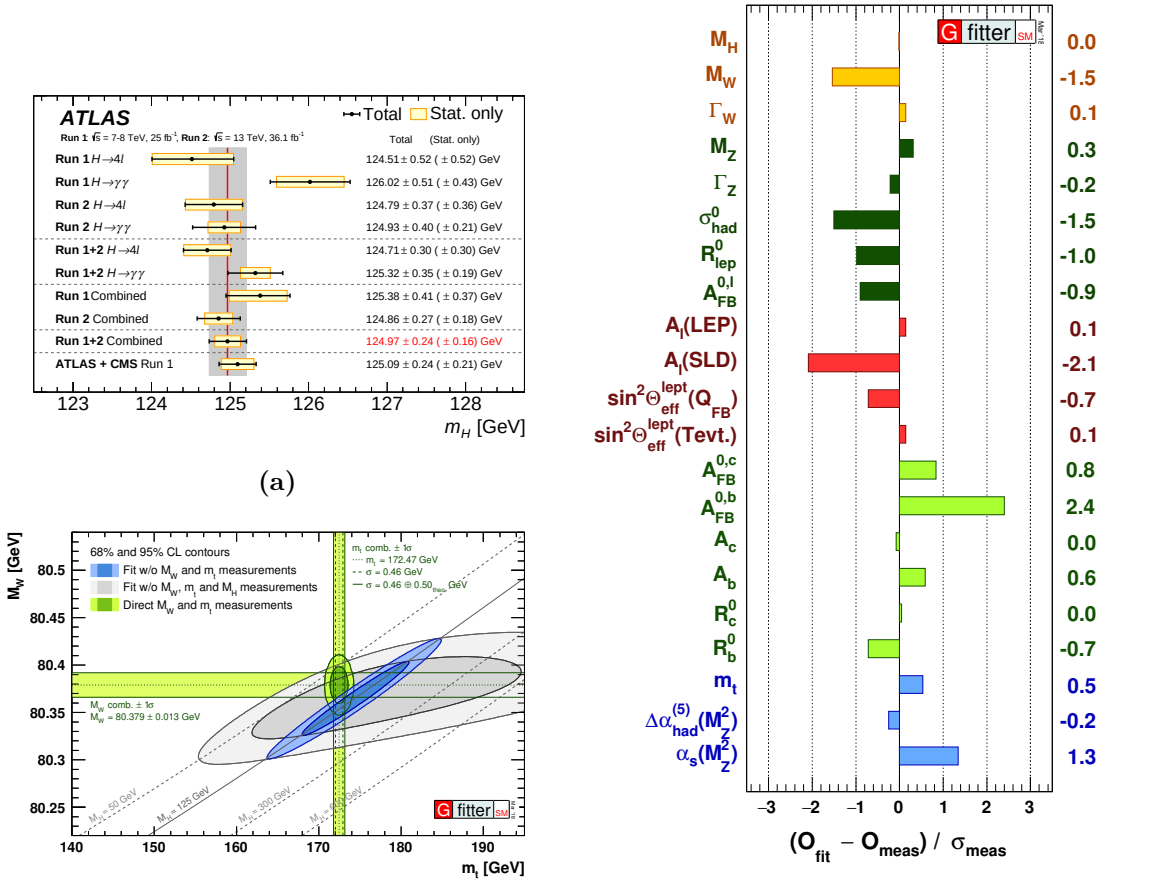

Figure 1.3: (a) Summary of Higgs boson mass measurements from individual and combined analyses with their statistical-only and total uncertainties [24]. The red vertical line and the corresponding grey shaded uncertainty band indicate the central value and total uncertainty of the combined ATLAS Run $1+2$ measurement. (b) The 68 % and 95 % confidence level contours obtained from scans for the W boson mass versus the top-quark mass for the global fit including (blue) and excluding (grey) the measurements of the Higgs boson mass [25]. The direct measurements of the top-quark and W boson masses are excluded from the fits but included in the figure as green bands and ellipses. (c) Comparisons of the fit results from the global electroweak fit with direct measurements, where differences are given in units of the experimental uncertainties [25].

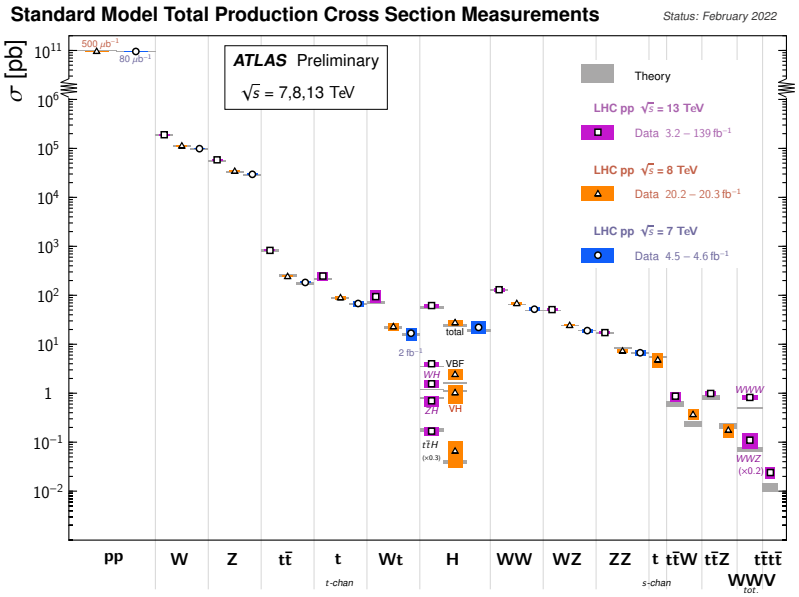

Figure 1.4: Summary of several SM cross-section measurements performed by ATLAS, corrected for branching fractions, compared to the corresponding theoretical expectations. The theoretical expectations are calculated at NLO or higher order and their uncertainties are quoted from the original measurements [26].

performed by ATLAS using *pp* collision data from the LHC at different centre-of-mass energies. The experimental results are compared to theoretical predictions and, overall, the measured cross-sections agree with the SM predictions over a range of more than 10 orders of magnitude in the cross-sections.

1.6 Limitations of the Standard Model

The SM of particle physics is a successful theory describing the majority of the known processes of particle physics with high precision. Nonetheless, there are some fundamental physical phenomena that cannot be explained by the SM. Therefore, a more general theory is needed in order to solve the limitations of the SM.

Three of the four fundamental forces are described by the SM, only gravitational effects are not included. Gravity is described by the classical theory of general relativity instead. The gravitational force is many orders of magnitudes weaker than the other interactions at the electroweak scale $\Lambda_{\mathrm{EW}} \sim \mathcal{O}(10^2\,\mathrm{GeV})$. However, it becomes relevant at energies around the Planck scale $\Lambda_{\mathrm{P}} \sim \mathcal{O}(10^{19}\,\mathrm{GeV})$. Thus, gravity would have to be included in a general unified theory.

Another experimental observation that cannot be explained by the SM are neutrino oscillations [27], for which the neutrinos are required to have a non-zero mass. However, the SM contains neither neutrino mass terms nor right-handed neutrinos. The current experimental

lower bound at the 95 % confidence level (CL) on the sum of the three neutrino masses is $\sum_\nu m_\nu > 0.06\,\text{eV}$ [28], and the corresponding upper limit $\sum_\nu m_\nu < 0.12\,\text{eV}$ [29].
An asymmetry between baryonic matter and antimatter has been observed in cosmological measurements [30], which can be partially explained by CP violation in the SM. However, the CP violation source in the weak sector in form of a phase in the CKM matrix [8] is not nearly strong enough to explain the full effect.
Cosmological observations such as the rotation curves of galaxies [31] do not match the predictions from baryonic matter but require the existence of a non-luminous component in the universe, called dark matter. Measurements of the cosmic microwave background [29] show that there is about five times more dark matter than ordinary matter in the universe. The SM does not provide candidates that might explain the origin of dark matter. Thus, theories containing particles to explain the existence of dark matter are necessary.
In addition to these unexplained observations, there are also theoretical considerations motivating additions to the SM. The SM contains the aforementioned 19 free parameters, which have to be determined in experiments. This large number of free parameters raises the question if there is a more fundamental theory with less parameters. Another example is the existence of exactly three generations of quarks and leptons, for which the SM does not provide an explanation. Similarly, the size of the mass difference between the lightest particle, the electron with a mass of 511 keV, and the heaviest particle, the top quark with a mass of approximately 173 GeV, is seen to be unnatural, and its reason is unknown.
Another relevant problem is the so-called hierarchy problem which is based on the large energy difference between the electroweak scale and the Planck scale. The Higgs boson mass is composed of a bare mass term $m_{H,\text{bare}}$ and an additional term Δm_H which arises from quantum loop corrections. The Higgs boson mass term can be written as

$$m_H^2 = m_{H,\text{bare}}^2 + \Delta m_H^2. \tag{1.29}$$

In contrast to fermions and gauge bosons, there is no symmetry protecting the Higgs boson as a scalar particle against such radiative corrections [32].
The correction term for e.g. a fermion loop as illustrated in Figure 1.5 is given by

$$\Delta m_H^2 = -\frac{y_f^2}{16\pi^2}\left[2\Lambda^2 + \mathcal{O}\left(m_f^2 \ln\left(\frac{\Lambda}{m_f}\right)\right)\right], \tag{1.30}$$

including a quadratic divergence Λ^2. Here, Λ is the cut-off scale, which is the energy scale where new physics becomes relevant and the SM ceases to be valid. The parameter y_f is the fermion Yukawa coupling, and m_f the fermion mass. As the loop corrections are proportional to the Yukawa coupling squared, the largest contribution originates from the heaviest particle in the SM, the top quark. If the SM would be valid up to energies of the Planck scale, the correction term would be in the same order squared. In order to get the observed Higgs boson mass of 125 GeV, the bare mass term has to be of the same order as the correction term.

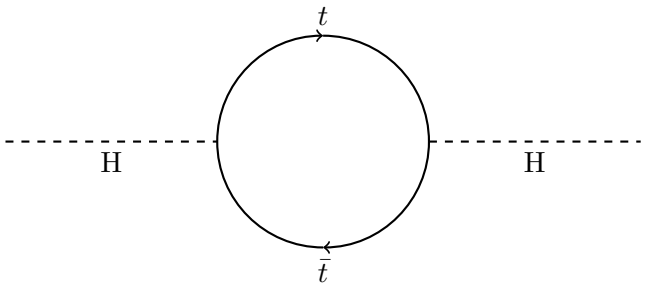

Figure 1.5: Example for loop-corrections to the Higgs boson mass with top quarks.

Thus, the squared bare mass needs to be fine-tuned with an extreme precision. An alternative to this unnatural solution are theories providing new particles cancelling these divergences.

2 Vector-like quarks

As the top quark is the heaviest particle in the SM, it plays an important role in the radiative corrections to the Higgs boson mass. Many theories beyond the SM try to solve the related fine-tuning problem by explaining the Higgs boson mass naturally. They therefore include a heavy partner of the top quark, i.e. a particle with similar quantum numbers, which contributes to the radiative corrections to the Higgs boson mass, thereby cancelling out the top-quark contributions. Heavier, chiral copies of the top quark, such as in a chiral fourth generation of quarks, are already excluded by measurements of the Higgs boson cross-section and branching ratios [33]. An alternative extension of the SM quark sector are VLQs. VLQs are hypothetical, coloured spin-1/2 fermions whose right- and left-handed chiral components have the same transformation properties under the symmetry group $\mathrm{SU}(2)_L$ [34]. For these particles, a mass term such as

$$\mathcal{L}_{\mathrm{VLQ}} = m_{\mathrm{VLQ}}\bar{\psi}\psi \tag{2.1}$$

does not break the gauge symmetry of the Lagrangian and is independent of the Higgs mechanism. VLQs enter the loop diagrams of Higgs boson production and decay such as $H \to gg$ or $H \to \gamma\gamma$. However, these contributions are suppressed by the mass of the VLQ such that an extension of the SM quark sector with VLQs is compatible with the present Higgs boson precision measurements. Due to the mixing with the top quark, vector-like top quarks contribute to the radiative corrections to the Higgs mass, as shown in Figure 2.1. These contributions can resolve the quadratic divergences and the fine-tuning problem.
VLQs appear in several models extending the SM. In "Little Higgs" models [35, 36], the Higgs boson is a pseudo-Goldstone boson arising from a spontaneously broken global symmetry. Analogously, "Composite Higgs" [37, 38] models introduce a new strongly interacting sector with the Higgs as a composite pseudo-Goldstone boson. The VLQs are required to induce the electroweak symmetry breaking and explain the lightness of the Higgs boson [34]. In these

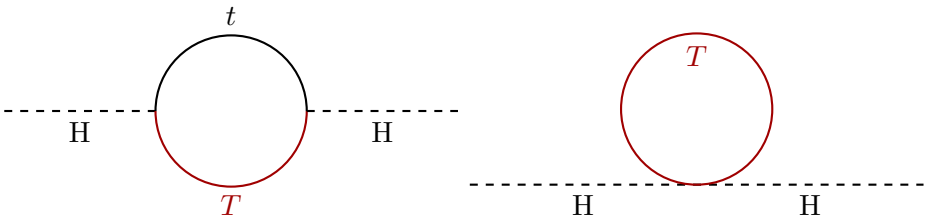

Figure 2.1: Example Feynman diagrams for loop-corrections to the Higgs boson mass including vector-like top quarks.

Table 2.1: $SU(2)_L$ multiplets of VLQs with their electric charges and hypercharges [34].

Multiplet	Hypercharge $U(1)_Y$	Charge
Singlets		
T	$+2/3$	$+2/3$
B	$-1/3$	$-1/3$
Doublets		
(X,T)	$+7/6$	$+5/3,\ +2/3$
(T,B)	$+1/6$	$+2/3,\ -1/3$
(B,Y)	$-5/6$	$-1/3,\ -4/3$
Triplets		
(X,T,B)	$+2/3$	$+5/3,\ +2/3,\ -1/3$
(T,B,Y)	$-1/3$	$+2/3,\ -1/3,\ -4/3$

theories they are predicted to be around the $\mathcal{O}(1\,\text{TeV})$ scale. Furthermore, some non-minimal supersymmetric extensions include VLQs to increase the corrections to the Higgs mass [39]. VLQs also appear in grand unified theories based on the group E_6 [40] and as Kaluza-Klein states of the quarks in models of extra dimensions [41, 42].

In the minimal scenarios in which the VLQs are present beside the SM particles, the VLQs interact with the SM quarks via Yukawa couplings [43]. Classifying the VLQs according to their quantum numbers, gauge invariant interaction terms can only be written for seven $SU(2)_L$ multiplets: two singlets, three doublets, and two triplets. Table 2.1 shows the $SU(2)_L$ multiplet realisations of VLQs with relevant quantum numbers. Vector-like partners of the bottom and top quark, B and T, have electrical charges $-1/3$ and $+2/3$, respectively, and can be arranged in singlets, doublets, and triplets. Some of the presented multiplets include VLQs with exotic charges. The vector-like X quark has the electric charge $+5/3$ and the vector-like Y quark $-4/3$.

2.1 Phenomenology

At the LHC, VLQs can be produced singly via electroweak interactions, or in pairs mainly via the strong interaction. Representative Feynman diagrams for $T\bar{T}$ and $B\bar{B}$ production and decay are shown in Figure 2.2. At the LHC, pair production is dominant for VLQ masses below approximately 1 TeV, and the corresponding cross-section depends only on the mass of the new quark. The predicted cross-section for VLQ pair production is shown as a function of the VLQ mass in Figure 2.3. It ranges from 195 fb to 0.132 fb for quark masses from 800 GeV to 2000 GeV [44]. Single production of VLQs via electroweak interactions has an additional dependency on the couplings between the new quarks and the weak gauge bosons. Its cross-section can surpass the pair production cross-section for masses above ~ 1 TeV.

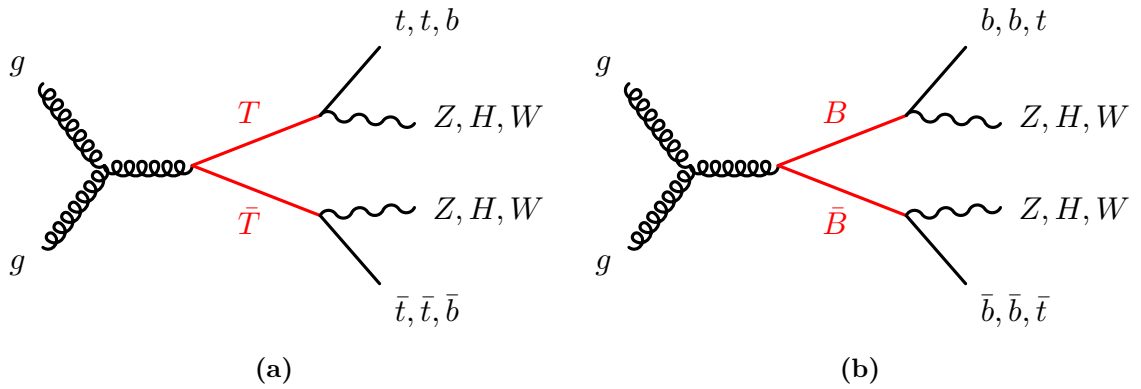

Figure 2.2: Representative Feynman diagrams for pair production and decay of vector-like (a) top and (a) bottom partners.

Vector-like quarks can mix with their SM counterparts, i.e. T quarks can mix with all up-type quarks, and B quarks can mix with down-type quarks, and modify their couplings to the W, Z and Higgs bosons. However, due to experimental constraints and the large mass difference between the quarks from the different generations, a common assumption is that VLQs couple mainly to third-generation quarks [34]. The mixing between VLQs and SM quarks depends on the multiplet and is parametrised in terms of the mixing angles $\theta^q_{L,R}$, where L, R denotes the left- and right-handed components, and $q = u, d$ the up- and down-type sector, respectively. The mixing angles for the left- and right-handed sectors are not independent but related via

$$\begin{aligned} \tan\theta^q_R &= \frac{m_q}{M_Q}\tan\theta^q_L \quad \text{(singlets, triplets)}, \\ \tan\theta^q_L &= \frac{m_q}{M_Q}\tan\theta^q_R \quad \text{(doublets)}. \end{aligned} \tag{2.2}$$

For each multiplet, one mixing angle is dominating, while the other is suppressed by a factor $m_\mathrm{q}/M_\mathrm{Q}$, where m_q is the mass of the SM particle and M_Q the mass of the VLQ.
Extending the SM quark sector with VLQs, which mix with the SM quarks, is a simple way to break the Glashow-Iliopoulos-Maiani mechanism [45], allowing VLQ decays via flavour-changing neutral currents in addition to flavour-changing charged currents. Under the assumption of VLQ mixing only with third-generation quarks, the following decays are possible [46]:

$$\begin{aligned} T &\to Wb, Zt, Ht, \\ B &\to Wt, Zb, Hb, \\ X &\to Wt, \\ Y &\to Wb. \end{aligned}$$

The branching ratio for each possible decay mode depends on the VLQ mass and the $\mathrm{SU}(2)_L$ multiplet realisation. For the $\mathrm{SU}(2)_L$ singlets all three decay modes are possible. For doublets

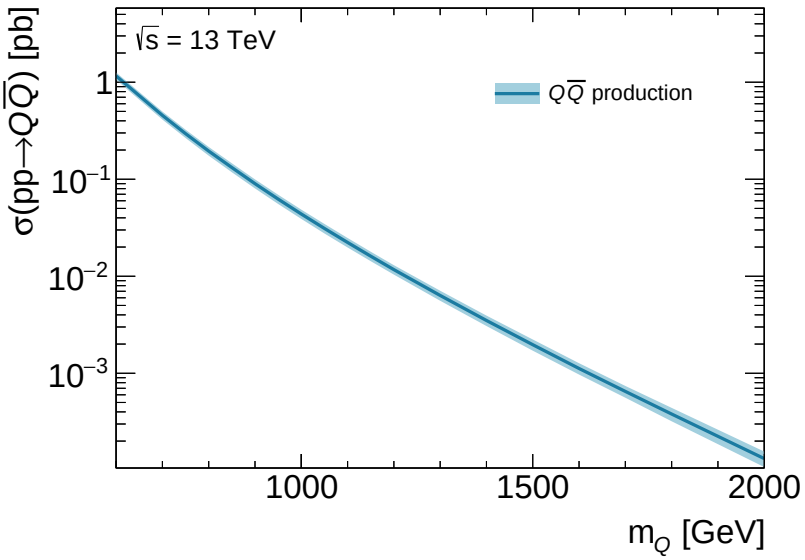

Figure 2.3: Cross-section for pair production of vector-like quarks in pp collisions at $\sqrt{s} = 13\,\text{TeV}$ as a function of their mass calculated with Top++ 2.0 [44] at next-to-next-to-leading order (NNLO) in QCD including the resummation of next-to-next-to-leading logarithmic (NNLL) soft-gluon terms. The width of the curve represents the uncertainty from variations in the parton distribution functions (PDFs) and scale.

and triplets, splitting of the masses within a multiplet occurs due to the mixing with lighter partners. However, the mass differences are found to be of $\mathcal{O}(1\,\text{GeV})$ such that decays between the members of a multiplet, e.g. $T \to WB$, are suppressed [34].
For the (T, B) doublet, the possible decay modes depend on the generalised CKM matrix elements V_{Tb} and V_{tB} [46]. For $V_{Tb} \sim V_{tB}$, the same decays as for the singlets are possible. However, for the doublet scenario the couplings have a dominant right-handed component in contrast to the singlet case. Therefore, the polarisation of the decay products differs between the two scenarios. As the top quark is much heavier than the bottom quark, the most natural assumption is $V_{Tb} \ll V_{tB}$, i.e. the top quark mixes much more with its partners than the bottom quark. Thus, this scenario, where the decays $T \to Wb$ and $B \to Zb, Hb$ are suppressed, is considered when referring to the (T, B) doublet. On the other hand, the mixing $V_{Tb} \gg V_{tB}$ would only allow the decays that are suppressed in the aforementioned case. However, this scenario is not natural in terms of mass hierarchy and is disfavoured by constraints on b quark mixing [46]. For the (X, T) doublet, the X quark decays only via a flavour-changing interaction into a W boson and a top quark, whereas the T quark decays via $T \to Zt, Ht$ which are the decay modes as for the (T, B) doublet. For the (B, Y) doublet, the Y quark decays via $Y \to Wb$, and for the B quark only neutral couplings to the SM quarks are allowed and hence the possible decay modes are $B \to Zb, Hb$.
Figure 2.4 shows the possible decays and the branching ratios as a function of the mass for the singlet and doublet realisations for T and B quarks. While for the T quark the

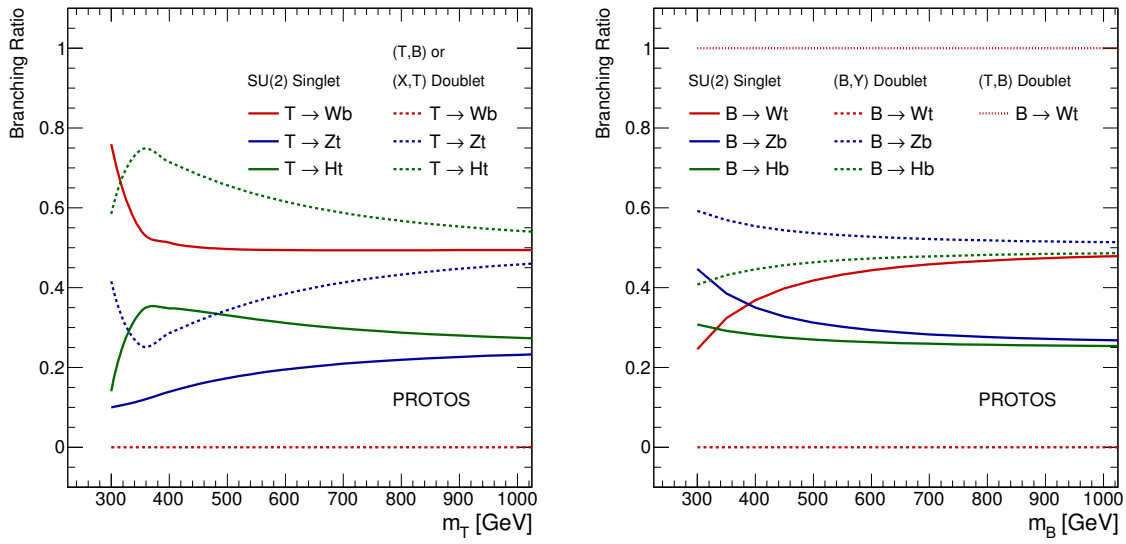

Figure 2.4: Branching ratios of the vector-like (a) top and (b) bottom partners as a function of the heavy quark mass m_T and m_B, respectively. In both cases the branching ratios are given for a SU(2) singlet and two SU(2) doublet scenarios [47].

branching ratios are the same in both doublet realisations, the branching ratios of the B quark differ between the two doublets (B, Y) and (T, B). In the limit of large VLQ masses, the branching ratios converge against a fixed value for each scenario, which is typically marked when presenting lower limits on the quark mass in the branching ratio plane. For high T masses they converge to $\mathcal{B}(T \to Zt) \simeq \mathcal{B}(T \to Ht) \simeq 0.25$ and $\mathcal{B}(T \to Wb) \simeq 0.5$ for the T singlet, and to $\mathcal{B}(T \to Zt) \simeq \mathcal{B}(T \to Ht) \simeq 0.5$ for the doublets. In case of the B, they converge to $\mathcal{B}(B \to Wt) \simeq 0.5$ and $\mathcal{B}(B \to Zb) \simeq \mathcal{B}(B \to Hb) \simeq 0.25$ for the singlet B, and to $\mathcal{B}(B \to Zb) \simeq \mathcal{B}(B \to Hb) \simeq 0.5$ for the (B, Y) doublet.

2.2 Searches for vector-like quarks

Searches for pair-produced VLQs targeting different final states have been performed both by ATLAS [48–55] and CMS [56–59] at the LHC at $\sqrt{s} = 13\,\text{TeV}$. As shown in Figure 2.5 for vector-like partners of the top quark, the ATLAS searches cover different areas in the branching ratio plane. A statistical combination of all ATLAS VLQ searches using the $36\,\text{fb}^{-1}$ data set has been performed and results in improved mass limits at the 95 % CL compared to the individual searches [60]. The T quark is excluded for masses below 1.31 TeV in the singlet representation, and below 1.37 TeV assuming a weak-isospin doublet (T, B). While a singlet B is excluded for masses below 1.22 TeV, a B in the (T, B) and (B, Y) doublet realisation is excluded for masses below 1.37 TeV and 1.14 TeV, respectively. Figure 2.6 shows the lower limits on the VLQ mass and corresponding exclusion contours as a function of the VLQ branching ratios.

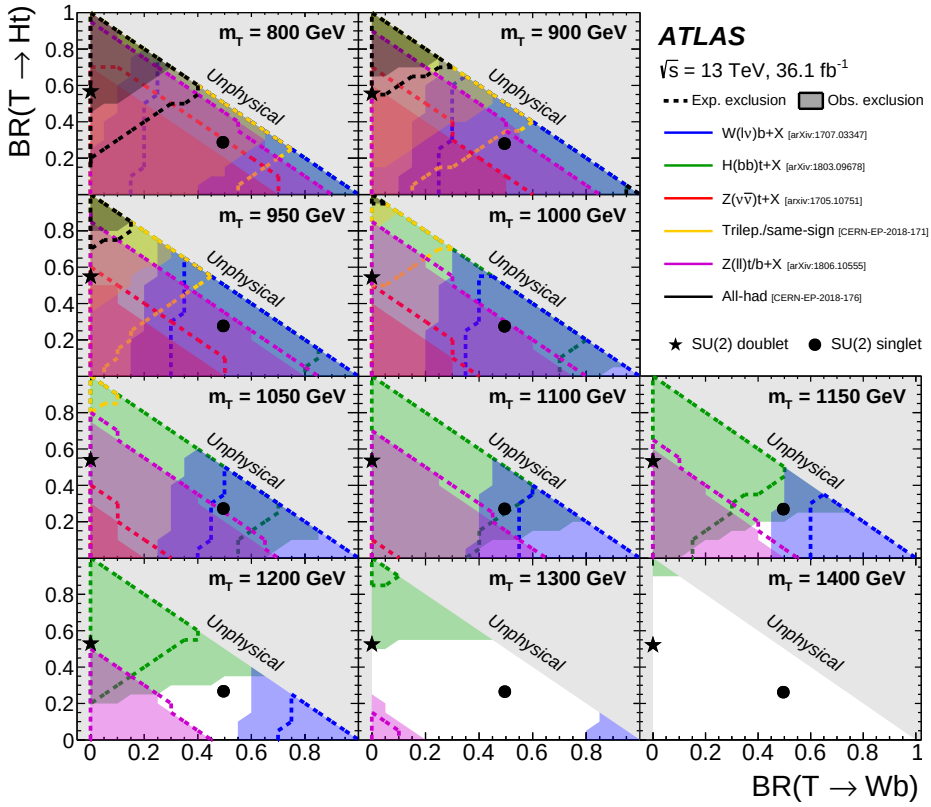

Figure 2.5: Expected and observed exclusion in the $\mathcal{B}(T \to Ht)$ versus $\mathcal{B}(T \to Wb)$ plane for different T quark masses. The coloured areas indicate the exclusion range of the various analyses contributing to the final combination [60].

Model-independent lower limits on the VLQ mass were calculated for all combinations of branching ratios under the assumptions $\mathcal{B}(T \to Zt) + \mathcal{B}(T \to Ht) + \mathcal{B}(T \to Wb) = 1$ and $\mathcal{B}(B \to Zb) + \mathcal{B}(B \to Hb) + \mathcal{B}(B \to Wt) = 1$. For any combination of decays into SM particles, $T(B)$ quark masses are excluded below 1.31 GeV (1.03 GeV).

First VLQ searches have been published for the full Run 2 data set by both collaborations. A search for VLQs with at least one leptonically decaying Z boson and a third-generation quark has been performed by ATLAS using the 139 fb^{-1} data set. This analysis sets improved lower limits on the mass of a T quark in the (B,T) doublet of 1.46 TeV and of 1.60 TeV for the scenario where the T quarks decay only in a Z boson and a top quark [55]. CMS has published a VLQ search in the fully hadronic state [56] setting the most stringent mass limits for a B quark in the (B,Y) doublet of 1.45 TeV and the case where the B quark decays into a Higgs boson and a bottom quark with a lower limit on the B mass of 1.57 TeV.

Single production of VLQs is also searched for by both ATLAS and CMS [51, 52, 61–65]. Exclusion limits on the signal mass are set for various decay scenarios and different values of the coupling parameters to the electroweak bosons.

A complementary ansatz to the direct searches presented above has been carried out in Ref. [66], where current differential cross-section measurements are used to constrain VLQ

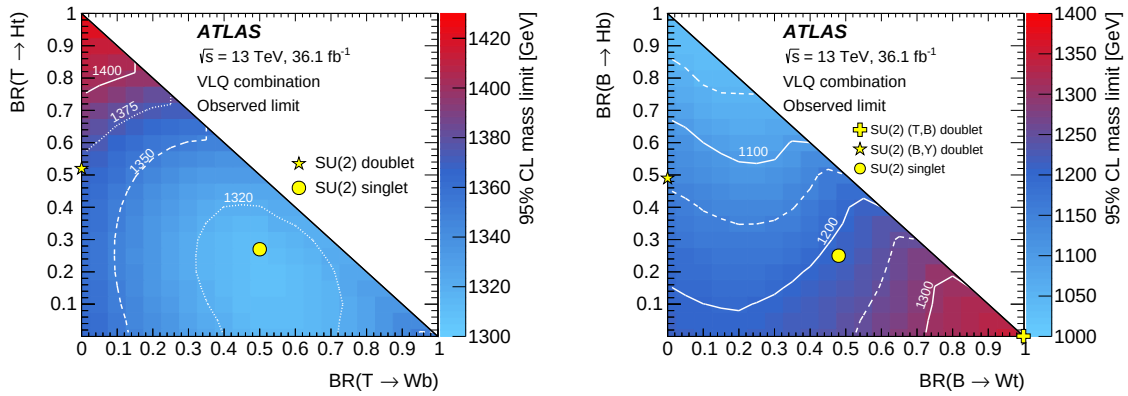

(a) **(b)**

Figure 2.6: Observed limits at 95 % CL on the mass of the vector-like partner of (a) the top quark and (b) the bottom quark as a function of the branching ratios under the assumption that the three single branching ratios sum up to unity [60].

model parameters. The results show that these measurements can have complementary sensitivity to the ATLAS pair-production combination.

The focus in this thesis is laid on the search for pair-produced VLQs with one isolated lepton, jets, and high missing transverse momentum in the final state. A search for this final state has been performed by ATLAS using the 36 fb^{-1} data set and considering only vector-like partners of the top quark. This search set lower limits on the T mass at 870 GeV (1.05 TeV) for the weak-isospin singlet (doublet) model and at 1.16 TeV for the $T \to Zt$ decay mode [50]. In this dissertation, this final state is exploited using the full Run 2 data set. As it is a single lepton analysis, it is complementary to the aforementioned search looking at a leptonically decaying Z boson and consequently requiring at least two leptons in the analysis selection. The orthogonality of phase spaces considered in the various VLQ analyses is important for a later statistical combination.

3 Event simulation

With the help of high energy physics experiments, predictions from the SM are verified, its parameters are precisely measured, and searches for physics beyond the SM are performed. For this purpose, the experimental data are compared to theoretical predictions that rely on the simulation of physics processes from SM and BSM theories, and the simulation of particle interactions with the detectors. The complex task of simulating defined physics processes is solved by MC event generators. These programs generate MC events based on quantum field theory predictions using pseudo-random numbers to solve numerical evaluations.
In the simulation of *pp* collisions, different processes need to be well described. Starting from the distribution of the partons in the protons, followed by the hard interactions of two partons, the radiation and hadronisation of coloured partons, and the decay of unstable hadrons. Multiple interactions between spectator partons within a *pp* collision are included as well in the simulation. The described processes happen on different energy and length scales and can therefore be treated independently due to the factorisation theorem [67].
The individual steps of the event simulation are illustrated in Figure 3.1 and described in the following sections. A more detailed review can be found in Ref. [68]. In addition, the MC event generators being relevant for this dissertation and the ATLAS detector simulation are briefly introduced.

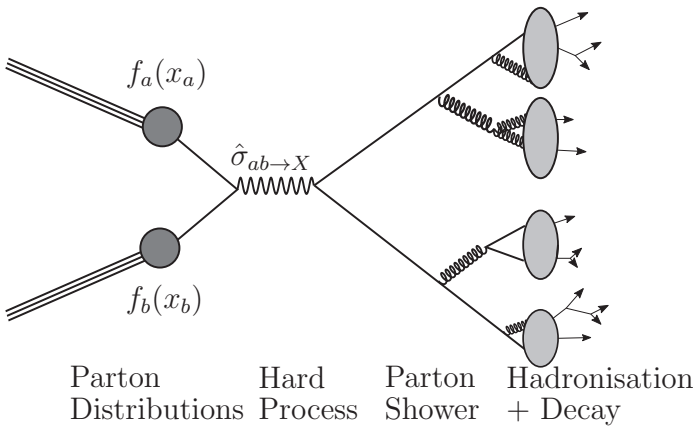

Figure 3.1: Sketch of a *pp* collision illustrating the different steps of the event simulation. Sketch is adapted from Ref. [69].

3.1 Factorisation theorem

Due to the high energy of the colliding protons, their constituents, called partons, behave nearly as free particles in the hard scattering due to the effect of asymptotic freedom. Therefore, a pp collision can be formulated as the interaction of two partons. According to the factorisation theorem, the pp cross-section for producing a final state X is given by

$$\sigma_{pp\to X} = \sum_{a,b} \int_0^1 dx_a dx_b f_a(x_a, \mu_F^2) f_b(x_b, \mu_F^2) \hat{\sigma}_{ab\to X}(x_a x_b s, \mu_F^2, \mu_R^2), \tag{3.1}$$

where s is the centre-of-mass energy squared, and the sum runs over the partons a and b that initiate the process. The partonic cross-section $\hat{\sigma}_{ab\to X}$ can be calculated at fixed order in perturbation theory introducing a renormalisation scale μ_R. The PDFs $f_i(x_i, \mu_F^2)$ give the probability for a parton of type i carrying the momentum fraction x of the proton at a given energy scale $Q^2 = \mu_F^2$. The factorisation scale, μ_F, separates short- from long-distance processes, i.e. the hard process from the PDFs.
The PDFs are universal, i.e. independent of the specific process, and are determined in fits of parametrised functions to data from deep inelastic scattering processes, hadron colliders, and fixed target experiments. PDF sets are provided by various groups, e.g. CTEQ [70] or NNPDF [71], using different parametrisations of the PDFs and measurements in the fits. The energy dependence of the PDFs is formulated by the DGLAP evolution equations [72–74]. PDFs for different types of quarks and the gluon of the NNPDF3.0 PDF set are shown in Figure 3.2 for two different energy scales.

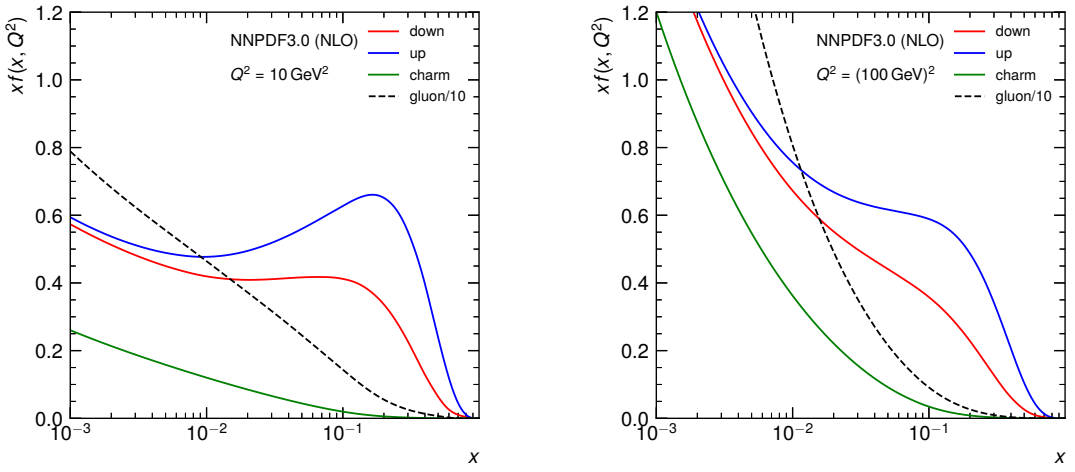

Figure 3.2: The NNPDF3.0NLO parton distribution function of the proton for up, down, and charm quarks and the gluon at scales (a) $Q^2 = 10\,\mathrm{GeV}^2$ and (b) $Q^2 = 10^4\,\mathrm{GeV}^2$ [71, 75].

3.2 Hard scattering cross-section

The all-order partonic cross-section $\hat{\sigma}_{ab\to X}$ [76] for the inclusive X production, where X is an arbitrary final state, can be written as

$$\hat{\sigma}_{ab\to X} = \frac{1}{2\hat{s}} \sum_{k=0}^{\infty} \int d\Phi_{X+k} |\sum_{l=0}^{\infty} \mathcal{M}^{(l)}_{X+k}(\Phi_{X+k}, \mu_F, \mu_R)|^2. \tag{3.2}$$

While the sum over k corresponds to real emissions ("legs"), the sum over l is related to virtual corrections ("loops"). The matrix element (ME) $\mathcal{M}^{(l)}_{X+k}$ for producing X in association with k additional final-state partons and l loops is calculated based on the relevant Feynman diagrams, representing the possible transitions of the initial to the final state. The integration is performed over the final-state phase space Φ_{X+k}. Lastly, the parton flux is given by the factor $1/(2\hat{s}) = 1/(2x_a x_b s)$.
In practice, the cross-section calculation is performed at a fixed order in the strong coupling constant α_s. Therefore, the nested sums are limited to certain values for $k + l$. The simplest case with $k = l = 0$ relates to the leading order (LO) for inclusive X production. The accuracy of the prediction can be improved by increasing the number of summands. The calculation of the X production cross-section at $\mathrm{N}^n\mathrm{LO}$ order uses $k + l \leq n$. Figure 3.3 shows a selection of Feynman diagrams for the $t\bar{t}$ production at LO ($k = 0$, $l = 0$) and next-to-leading order (NLO) ($k + l \leq 1$).

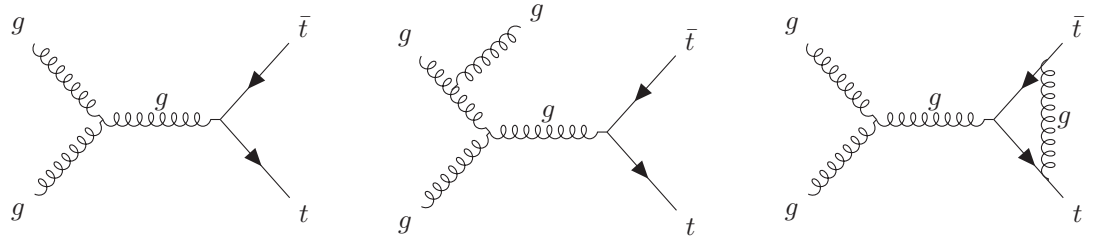

Figure 3.3: Example of Feynman diagrams for $t\bar{t}$ production at (a) leading order and at next-to-leading order with (b) a real emission and with (c) a virtual correction, respectively.

Different types of singularities can appear in this calculation that have to be treated properly in order to get a finite cross-section. In the determination of the cross-section for the $X + k$ process, with $k \geq 1$, the integration over the Φ_{X+k} phase space includes configurations where some of the k partons are collinear or soft. This leads to singularities that can be regulated by introducing cuts on the parton properties, like their transverse momenta, in order to remove the problematic parts of the phase space. Ultraviolet divergences appearing in virtual corrections are treated by renormalisation. Infrared divergences show up in both virtual

contributions and real emissions, which cancel each other out, order by order in perturbation theory, according to the known KLN theorem [77, 78].

3.3 Parton shower

The fixed-order calculations of the ME in the hard process describe the momenta of the outgoing partons to a given precision, but is not suitable to describe additional soft or collinear emissions. Basically, it is possible to generate and evaluate the ME for the hard process with accompanying resolved partons. However, this becomes computationally expensive and is therefore often not practicable especially for the case of multiple additional partons. Parton showers (PS) provide approximate higher-order real emissions corrections to the hard scattering by simulating the $1 \to 2$ splitting of partons to create a multi-parton final state [79]. These simulations include both the successive emissions of quarks and gluons from final and initial state partons. PS algorithms are formulated as an evolution in an ordering variable, for example the transverse momentum, starting from the high scale of the hard process down to a lower scale of $\mathcal{O}(1\,\mathrm{GeV})$, associated with the hadronisation of the partons.
In the collinear limit, the cross-sections of different parton multiplicities factorise. The approximated cross-section for a final state with $n+1$ partons, i.e. after a parton splitting, can be related to the n-parton cross-section via

$$d\sigma_{n+1} \simeq d\sigma_n \frac{dq^2}{q^2} \frac{\alpha_\mathrm{s}}{2\pi} dz P_{ji}(z). \tag{3.3}$$

Here, $P_{ji}(z)$ are the Altarelli-Parisi splitting functions [72], a set of universal, but flavour-dependent functions, giving the probability for an initial particle i to split into two partons where parton j carries a momentum fraction z of the initial parton. The four splitting functions P_{qq}, P_{gq}, P_{gg}, and P_{qg} correspond to the branchings $q \to qg$, $q \to gq$, $g \to gg$, and $g \to q\bar{q}$ respectively. The evolution variable of the PS, q^2, can differ between PS generators. Apart from the transverse momentum, typical choices are the opening angle or the virtuality. The soft ($z \to 0$, $z \to 1$) and collinear ($q \to 0$) divergences appearing in the above expression are removed by introducing a cut-off Q_0, e.g. on the relative transverse momentum between two partons, that decides if the partons are resolvable. Emissions below this cut-off are not resolvable and are considered as no emissions. The probability of not-resolvable emissions from a parton i during the evolution from an initial scale Q^2 to a lower scale q^2 is given by the Sudakov form factor. The form factor is defined by the following expression

$$\Delta_i(Q^2, q^2) = \exp\left[-\sum_j \int_{q^2}^{Q^2} \frac{dk^2}{k^2} \frac{\alpha_\mathrm{s}}{2\pi} \int_{Q_0^2/k^2}^{1-Q_0^2/k^2} P_{ji}(z) dz \right], \tag{3.4}$$

where the sum goes over all possible emissions. Final-state radiation (FSR) is simulated in a PS via an iterative algorithm. For a parton i, $\Delta_i(Q^2, q^2) = \rho$ is solved for q^2, where ρ is

a random number between 0 and 1. If the solution is above Q_0, a resolvable branching is produced at scale q^2, otherwise the evolution is terminated. This is repeated for all partons, starting with the lower scale q^2, until q^2 is below the cut-off and no more resolvable emissions are possible. In the case of initial-state radiation (ISR), the incoming particles are radiating before they enter the hard process. ISR showers are based on a backward-evolution algorithm that starts with the scale of the hard scattering and develops the shower backwards while taking PDF effects into account.
In addition to QCD radiation, electromagnetic radiation can be included in the PS as well, but is suppressed with $\alpha_{em}/\alpha_{\mathrm{s}}$ compared to the former.

3.4 Matching and merging

As explained in the previous section, the PS generates additional emissions on top of the basic process from the hard scattering. These additional emissions are approximated in the soft and collinear limits. Thus, soft and collinear parton emissions are well described even for higher parton multiplicities, while hard, large-angle emissions are not well modelled. On the other hand, fixed-order matrix element calculations are good for the simulation of hard, well-separated partons, but have problems to describe soft and collinear partons.
Thus, a combination of both approaches is desirable to get a good description of the full multi-parton final state. However, a PS cannot simply be combined with the ME calculation due to potential double counting of some phase-space regions. For example, there is an overlap between the first real emission at NLO with the hardest emission from the PS. Similar overlaps exist at LO when the basic process is described with additional resolved partons by the ME. In order to remove the overlaps, two ideas, called merging and matching, exist for a correct combination of the PS with fixed-order ME calculations.

The term matching refers to the combination of an NLO ME calculation with a PS where in the latter the hardest emission is simulated with tree-level accuracy. Two widely-used methods (Powheg [80] and MC@NLO [81]) exist for the subtraction of the overlap from the ME calculation.

Merging is related to the combination of tree-level calculations containing multiple well-separated partons with the PS. The most known methods for multi-jet merging at LO are CKKW [82], CKKW-L [83], and MLM [84]. In these approaches, a merging scale is introduced to separate the phase space described by the ME and the PS.

In some cases it is required that besides an NLO ME calculation also additional jets achieve NLO accuracy. Different methods for the NLO matching and merging exist, e.g. FxFx [85], MiNLO [86], and MEPS@NLO [87].

3.5 Hadronisation

The parton shower evolution stops at the hadronisation scale of $Q_0 \simeq 1\,\text{GeV}$. At this scale, the strong coupling α_s becomes large and non-perturbative QCD effects are dominant. The effect of confinement leads to the formation of colour-singlet primary hadrons, which may decay further. Event generators rely on phenomenological models to describe this transition. Two common models that are used in MC generators are the cluster model [88] and the Lund string model [89, 90].
The cluster hadronisation model is based on the concept of QCD preconfinement [91]. After splitting all gluons at the end of the PS into quark-antiquark pairs, the partons are grouped to form colour-singlet clusters. Clusters with an invariant mass below $3 - 4\,\text{GeV}$ decay into pairs of hadrons. Heavier clusters undergo first cluster breakups and decay into lighter clusters or a lighter cluster and a hadron. This splitting is repeated until all cluster are transformed into hadrons.
In the Lund string model, the effects of confinement are represented as a colour string between a quark and an antiquark with a linearly rising potential depending on the distance between the quarks. Gluons are considered as kinks on the strings in this model. When the quark-antiquark pair moves apart, the string is stretched and the potential energy stored in the string increases. If energetically favourable, the string breaks by the production of a new quark-antiquark pair, so that the system is split into two colour-singlet systems. If the invariant mass of one of the systems is large enough, further string breaks may occur. This process is repeated until all energy is converted into quark-antiquark pairs connected via short strings that form the hadrons.

3.6 Underlying event and pile-up

Apart from the hard scattering and its associated radiation, additional interactions can occur during the pp collision that need to be simulated. These interactions are labelled as underlying event (UE). Additional activity is expected from colour connections between partons and the beam remnants, and from multiple parton interactions in the same pp collision. As the UE is dominated by soft processes, which cannot be reliably calculated with perturbative QCD methods, phenomenological inspired models are needed for the modelling of these processes. As these models contain parameters that are not known from first principles and cannot be calculated at present, their values need to be tuned to experimental data [92].

Additional pp collisions in the same or neighbouring bunch crossing, called pile-up, are simulated via inelastic pp collisions, referred to as minimum bias events.

3.7 Monte Carlo event generators

The aforementioned physical processes and concepts are implemented in different forms in the various existing Monte Carlo event generators providing detailed simulations of high-energy proton-proton collisions. These generators are often classified as either multi-purpose or ME generators. Multi-purpose event generators are able to simulate the full chain from the hard interaction to the formation of hadrons and their decay. ME generators perform fixed-order ME calculations, but do not simulate PS or UE contributions. Therefore, they have to be interfaced with an additional PS. For an improved treatment of specific particle decays, dedicated MC programs can be used.
In the following, the MC generators that are relevant for the studies in this thesis are briefly introduced concentrating on their main features.

Multi-purpose Monte Carlo generators

- Pythia [93, 94] is a multi-purpose MC event generator using LO calculations for $2 \to n$ processes, where $n \leq 3$, and a PS with emissions ordered in the transverse momentum. The hadronisation is modelled based on the Lund String model and the simulation of the UE is included.

- Herwig [95, 96] is a multi-purpose event generator with LO and NLO accurate ME and a PS with angular ordered emissions. This generator uses the cluster hadronisation model and includes the simulation of the UE.

- Sherpa [97] is a muti-purpose MC event generator with LO and NLO accurate ME. The default PS is based on Cantani-Seymour dipole factorisation [98] and the hadronisation is simulated using the cluster hadronisation model. The NLO matrix elements are matched to the PS using a variant of the MC@NLO algorithm [99] and the merging for different jet multiplicities follows the MEPS@NLO [87, 99, 100] prescription.

Matrix-element generators

- Powheg-Box [101–103] is a tool-box providing ME calculations at NLO accuracy in QCD. The Powheg method is used to match the ME calculation with a PS.

- MadGraph5_aMC@NLO (MG5_aMC@NLO) [104] is a ME generator providing automated LO and NLO ME calculations. The matching of the NLO ME calculation with the PS is done via the MC@NLO method.

- Protos [105] is a LO ME generator specialised for the simulation of new physics processes including top quarks. The vector-like quark signal samples, used in this thesis, were generated with Protos.

Specialized generators for particle decays

During the hadronisation process, unstable particles like heavy-flavour hadrons and τ-leptons are decayed. These decays can be handled by the multi-purpose MC generators, but often these decays are simulated using decay tables from dedicated programs like EvtGen [106] and Tauola [107], respectively. For an improved treatment of quantum-electrodynamic (QED) radiative corrections in the decays, a specialised generator called Photos [108, 109] exists. The decays of heavy resonances are often handled by MadSpin [110, 111] when they are generated at NLO by MG5_aMC@NLO. This tool preserves spin correlations amongst the decay products and accounts for off-shell effects properly. In contrast to the previously mentioned decay programs being afterburners, i.e. run at the end of process generation, MadSpin is executed between the ME calculation and the PS step.

3.8 ATLAS detector simulation

So far, the event simulation depends only on the beam type (pp) and the beam energy (13 TeV) but is independent of any experiment. The output of the MC generators is a list of four-vectors of all stable particles produced in the event. A typical definition of a stable particle with lifetime τ in hadron collisions is $\tau > 30\,\text{ps}$. This information is used to perform *particle level* studies.
In order to compare the result of the MC simulation with the data measured by the experiment, the MC events have to be analysed after the reconstruction in the detector, i.e. at *reconstruction level*. The standard simulation for the ATLAS detector [112] contains a detailed description of the detector geometry and interaction of the particles with the detector material using the Geant4 [113] software. A faster variant of the ATLAS detector simulation, known as AFII, is also available using a parametrized response of the calorimeters [114]. The detector responses are digitised into the same format as data, before both data and simulated events are used in the object reconstruction.

4 ATLAS Monte Carlo generator validation

In the ATLAS physics programme, the simulation of collision events with MC event generators plays an important role in order to successfully probe the SM and search for physics beyond. A smooth operation of the event simulation, executed within the ATLAS software framework Athena [112], is therefore crucial.
A large set of MC event generators, mainly written and maintained by authors external to the ATLAS collaboration, are available in the particle physics community. At CERN, the generator installations are centrally provided by the Generator Services project [115]. In order to use the MC event generators in the Athena framework, interface packages exist, allowing flexible configurations of the generator settings for the various physics processes to be simulated. As the MC generators, the Athena framework, and ATLAS interface packages are each continually updated, a reliable validation of new versions is important to ensure that no unexpected changes are introduced that might degrade the physics modelling or the performance of the event generation.
The validation of new generator versions is performed within the ATLAS Physics Modelling Group (PMG). Various MC generators are tested using a set of selected physics processes in order to spot possible issues and unwanted features far before the updated software is used in the official MC production. For this purpose, a partially automated validation procedure has been established in ATLAS.
In the following, the ATLAS MC event generation procedure is briefly introduced focusing on aspects relevant for the validation. Afterwards, the MC validation strategy is explained, and the validation system developed as a part of this thesis is described in more detail. Finally, various use cases ranging from minor updates of generator versions up to the validation of the updated ATLAS simulation infrastructure for the LHC Run 3 are illustrated.

4.1 Monte Carlo production

Due to the broad range of the ATLAS physics programme, various SM processes and BSM signals are simulated in the Athena framework. The basis for the generation of a MC sample is a python file, called job option, that specifies the process definition, generator parameter settings, and Athena parameters. The default generation workflow [116] for multi-purpose MC event generators can be divided into several subsequent steps. First, the job option is passed to the interface, which configures the generator based on the specified settings. The generator produces the requested number of events and returns them back to the interface,

which stores them in the standard HepMC [117] format. In a final step, the events are converted to a Root-style format [118] and are stored together with metadata in an output file, called Evnt file. Programs like EvtGen or Photos running after the PS, so-called afterburners, modify the event record of existing HepMC files before the conversion into the final output format. In the case of ME generators, which require an additional multi-purpose MC generator for showering and fragmentation, events are stored in the Les Houches Event (Lhe) file format [119]. These files are later processed by a PS, such as Pythia or Herwig, producing again the standard output files.
For an efficient MC production, the generation of an MC sample is split into several sub-jobs with sequential random number seeds, which are executed on the world-wide LHC Computing Grid [120]. Each data set is uniquely identified by two parameters. The data set identifier (DSID) allows to connect the sample to the used job option, and the event generation tag (e-tag) decodes the generator version via the Athena release used in the production of the sample. Each Athena release contains always one version of each generator. Thus, samples generated for the same process with various generator versions have the same DSID but different e-tags. Both Lhe and Evnt files are used in the MC generator validation. Furthermore, Evnt files are used to perform general particle-level studies and as input for the detector simulation.

4.2 Monte Carlo validation procedure

Updates of the simulation infrastructure or the MC generators include bug fixes or new features, improving for example the performance of the event generation or the modelling of physics processes. To ensure that these changes do not cause any unexpected behaviour in the MC event generation, a validation procedure is in place. The validation of MC event generators for the LHC Run 2 has been documented in Ref. [121]. During the following long-shutdown, the validation system has been updated and used to validate the simulation infrastructure and MC generator versions that will be used for the production of Run 3 MC samples.
In general, the MC validation includes some basic technical sanity checks and particle-level comparisons. For the latter, histograms for new samples, referred to as monitored samples, are compared to histograms from a reference sample. As outlined in the following, the ATLAS MC validation procedure can be divided into three steps:

Technical validation

A technical validation is performed based on the nightly builds of the ATLAS simulation software using the ATLAS release tester [122]. Each generation job includes basic checks, e.g. on the number of produced events and the job completion. Thus, short tests are performed on local machines, producing just $\mathcal{O}(10 - 100)$ events, which indicate if the setup works

technically. Additionally, longer tests run on the GRID, generating $\mathcal{O}(10000)$ events that are used for simple comparisons of basic physical observables. Histograms are created from EVNT files using RIVET [123] or via simple plotting scripts running over LHE files. They are then compared to defined reference histograms and the compatibility is evaluated using statistical tests. These tests allow solving possible issues before a new ATHENA release is built.

Physics validation

A careful physics validation at particle level is usually performed when a new generator version is available. Once a new generator version is installed and included in an ATHENA release, the production of multiple physics samples is launched. Typically, standard validation samples include one million events in order to find also minor differences and distinguish them from statistical fluctuations. Different possible combinations of ME generators, parton showers, and afterburners are tested, including also the merging of ME and parton shower for example via the CKKW-L approach. The physics processes used in the validation are chosen such that they cover the broad spectrum of the ATLAS physics programme. They include several SM processes (inelastic pp collisions, dijet, vector boson, diboson processes, top-quark pair production), processes with distinct signatures like photons, taus, or b-jets, and some exotic processes (e.g. supersymmetric models).
Once the validation samples are generated, RIVET jobs are launched producing histograms from a set of pre-defined routines. The list of considered RIVET routines contains a set of general MC analyses studying basic event properties and kinematic distributions of final state objects (e.g. `MC_ELECTRONS`, `MC_MUONS`), process specific analyses (e.g. `MC_TTBAR`, `MC_WJETS`), and real data measurements (e.g. `ATLAS_2018_I1656578`). The latter analyses are provided by experiments and contain observables used in physics analyses. In addition, they often include unfolded reference data that help to evaluate if changes in the MC distributions improve or degrade the modelling of a specific process. The output of a sample to be validated is then compared to a set of defined reference histograms produced with a previous version of the generator that has been successfully validated in the past. This is done using a validation tool called PAVER (PMG Architecture for validating Evgen with RIVET). The agreement between distributions is quantified with several statistical tests. In addition, comparisons of the metadata, the cross-sections, and the systematic variation weights are performed. Usually, the majority of distributions does not show any statistically significant difference between the monitored and reference files. In these cases, the generator version is called validated and can be used in the central MC production. However, if deviations are observed, the ATLAS generator experts are consulted in order to understand the reason for the discrepancies. These can be for example related to intended changes in the generators documented in the corresponding release notes. If the deviations are, however, unexpected and not related to the ATLAS software, they are reported to the generator authors, who provide patches to fix the issue if needed. At the same time, the ATHENA release is blacklisted in the case of a major

issue in order to prevent any usage in the MC event generation. For minor features related to a single process, the release can still be used for the generation of other process types.

Specific process validation

Validations of particular processes are performed before launching large-scale productions of samples relevant for many physics analyses in ATLAS. Here, parameter settings of the specific processes are revisited and optimised. A documented example is the production of SHERPA 2.2.11 W/Z+jets samples in Ref. [124].
In contrast to samples for the main SM processes, which are centrally provided by the PMG group, dedicated BSM signal MC samples are studied and validated by individual analysis teams.

4.3 Validation system PAVER

During the second long-shutdown of the LHC, the validation tool to perform the particle-level validation has been revisited and improved. Previously, the so-called Job Execution Monitor (JEM) was based on the HEPMCANALYSIS [125] validation tools for the particle-level analysis. The agreement between two histograms was evaluated with several statistical tests, and the validation results were monitored on a website. Apart from the flexible website, a useful feature of JEM has been the storage of histograms in a cache for further usage. Thus, the histograms can serve as reference in case the corresponding sample has been successfully validated previously. However, this system also had a few shortcomings with respect to a more advanced particle-level validation. It was restricted to the comparison of exactly two files, and the comparison to reference data was not possible. In addition, the validation of systematic weight variations was not included. These alternative weights, representing mainly PDF or scale variations, are stored in the MC samples and are used in the analyses to create alternative histograms in which the nominal weight is replaced by the alternative weight. Issues related to these weights would thus directly affect the systematic uncertainties of ATLAS physics analyses.
In order to overcome these shortcomings, PAVER has been developed as part of this dissertation using the existing JEM tool as basis. Instead of using the HEPMCANALYSIS tool, PAVER utilizes RIVET and the associated YODA file format. Advantages of RIVET are an active support and development, a large number of available analyses covering different processes and final states, and the fact that many experiments preserve their measurements in the form of RIVET analyses. These can then be incorporated in the MC validation. PAVER includes reference data per default in the validation if available for the respective RIVET analysis. Apart from the official RIVET routines, custom routines can be included as well.
While the old system restricted the validation to a comparison of two MC samples, comparisons of several monitored files to a reference file are possible in PAVER at the same time. Another

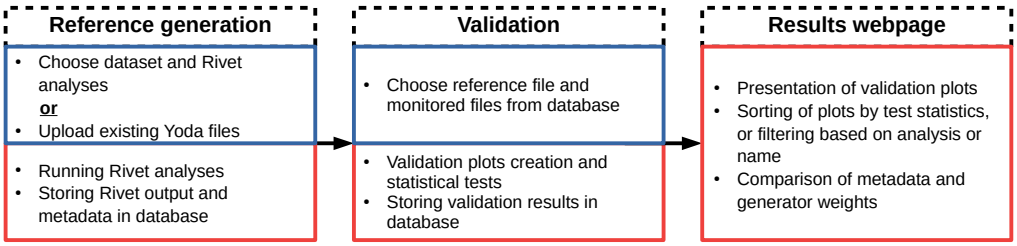

Figure 4.1: Validation workflow in PAVER including the reference generation, validation, and presentation of the results on the website. Steps that need input from the user are marked in blue.

feature that has been considered in the development of PAVER is the validation of systematic weight variations. The new Rivet 3 series [126] includes an improved handling of these additional weights, which allows an efficient creation of histograms for all weight variations. At present, validation plots for the alternative weights are only produced for weight distributions. As the number of validation plots would increase directly by a factor corresponding to the number of alternative weights, presenting validation plots for all observables and variations is impracticable.

The validation workflow in PAVER can be divided into three steps as illustrated in Figure 4.1. In a first step, reference histograms for a validation sample, specified by DSID and e-tag, are created by Rivet for a number of given routines and stored in the Yoda format. The user can select between two options: Yoda files can be either produced on the local machines hosting the service or Yoda files, which have been already produced on the grid, can be uploaded into the PAVER system. In both cases, the Yoda files are stored in a database together with additional metadata of the respective validation sample. The metadata are retrieved from the Evnt file in the case of systematic variations names, and from the ATLAS metadata interface [127] for further sample information like the cross-section. As the analyses could in principle change between Rivet releases, the Rivet and Yoda versions are stored in the database as well in order to have the possibility to check the versions used for the production of a specific Yoda file.

In the next step, the user can select a reference file and a number of monitored files from the database for the validation. The system automatically creates a validation plot, comparing the monitored samples to the reference sample, for all observables included in the selected Rivet analyses. In addition, it performs two kinds of statistical tests, namely χ^2 and Kolmogorov-Smirnov tests. The validation results are finally presented on a user-friendly, flexible website. For each sample in the validation, its name and relevant metadata are displayed in a way such that differences can be easily detected. As the number of weight variations can be of the order of $\mathcal{O}(100)$, an automatic comparison is in place indicating if the weight names and their order are the same and highlighting possible differences. The validation plots can be sorted according to the results of the statistical tests like the χ^2 per number of degrees of

freedom (ndf) or their p-values. Plots are highlighted by coloured frames if the agreement between a monitored sample and a reference sample evaluated by the statistical tests falls below pre-defined thresholds. The user can also simply filter the presented routines, e.g. to concentrate on the histograms of a specific analysis. An example of the validation results webpage is illustrated in Appendix A.

4.4 Validation use cases and results

In the chain of MC event generation, changes in various places could have an impact on the generated events. Thus, careful validation is essential when modifications are introduced in order to ensure that no unexpected features enter in the MC event generation. Typical use cases for which a physics validation is performed are

- software infrastructure upgrades, e.g. changes of the compiler version,
- minor MC generator revisions including mainly bug fixes,
- major new MC generator releases introducing new features,
- modifications of the generator interfaces,
- changes in the file formats,
- and updates of tools like LHAPDF.

In the case of major software upgrades or file format changes, all types of MC generators are considered in the validation. If changes are related to single components of a specific generator, checks are only performed for the physics processes generated by the corresponding generator. A list of all generator versions that have been validated so far using the new system can be found in Table 4.1. Apart from the generator release validations, one major validation campaign has been performed for the new Athena release. The next generation of MC samples mainly used for the analysis of LHC Run 3 data will be generated with the new Athena release. The most relevant changes for the MC event generation are the upgrade to Python 3 and HepMC 3 [128].

In the following, illustrative results representing diverse differences between generator versions that have been found during the validation of particular MC samples are discussed. The detailed update history for each generator lists the bug fixes and modifications introduced by the authors. It can serve as a reference if changes observed in the validation are related to a specific modification and are thus intended.
During the validation of Sherpa 2.2.11, which was carried out with respect to the previous release 2.2.10, differences were observed in the jet multiplicity looking at samples generating the hard process with multiple additional jets. An example for Z+jets production is shown in Figure 4.2a. These differences between the generator versions were found to be related to improvements in the merging procedure combining ME and PS.

Table 4.1: List of MC event generator versions that have been considered in the ATLAS MC validation since the new validation system, PAVER, is in place. The reference version relates to the MC generator releases that were used for the first set of validations. Later validations are always performed with respect to the most recent successfully validated generator version.

Generator	Reference version	Monitored version
POWHEG-BOX	v1, v2	-
SHERPA	2.2.10	2.2.11, 2.2.12, 3.0.0alpha
MG5_aMC@NLO	2.7.3	2.8.1, 2.9.2, 2.9.3, 2.9.5, 2.9.9, 3.3.1
PYTHIA	8.244	8.245, 8.303, 8.305, 8.306, 8.307
HERWIG	7.21	7.22
EVTGEN	1.7.0	2.0.0, 2.1.1
EPOS [129]	1.5.6	1.6.0, 1.8.0, 2.0.1
TAUOLA	1.1.6	1.1.8
PHOTOS	3.61	3.64

Another difference that could be traced back directly to changes in the generator settings was observed during the validation of PYTHIA 8.245. The distribution of the transverse momentum of the W boson in POWHEG+PYTHIA 8 $W(\rightarrow e\nu)$+jets events, shown in Figure 4.2b, exhibits deviations between the PYTHIA versions at small transverse momenta. The reason for these differences is a change in the settings of the primordial k_T representing the transverse momentum of the initial-state partons.
However, sometimes unexpected changes occur. The MG5_aMC@NLO 2.9 series introduces new strategies in order to speed up the computation of LO processes [130]. Whether this optimised strategy is applied for a process, is automatically decided by the generator on a process-specific basis. A first validation was carried out for MG5_aMC@NLO 2.9.2, but some compilation errors were detected for NLO processes such that this version was discarded. Instead, validation was continued with the bug-fixed version 2.9.3. In some distributions of a Z+jets LO validation sample, differences were observed with respect to the reference version 2.8.1. Two examples, the pseudorapidity of the leading-p_{T} muon and the jet multiplicity distribution, are shown in Figures 4.2c and 4.2d, respectively. Investigations of the differences revealed that the new strategy was applied per default for this process and the old behaviour can be restored by setting the strategy parameter in the generator settings back to the old strategy.

Apart from changes in the external generators, also changes or bugs in the generator interfaces can affect the generated events. During the validation of PYTHIA 8.245, it was recognized that specific weights related to the CKKW-L merging were not properly retrieved by the PYTHIA interface impacting physics distributions sensitive to the merging. After the interface was fixed, the distributions were compared again and clear differences were visible between the wrong and correct setup as illustrated in Figure 4.3.
A major validation effort was related to the new ATHENA software version. Detailed checks

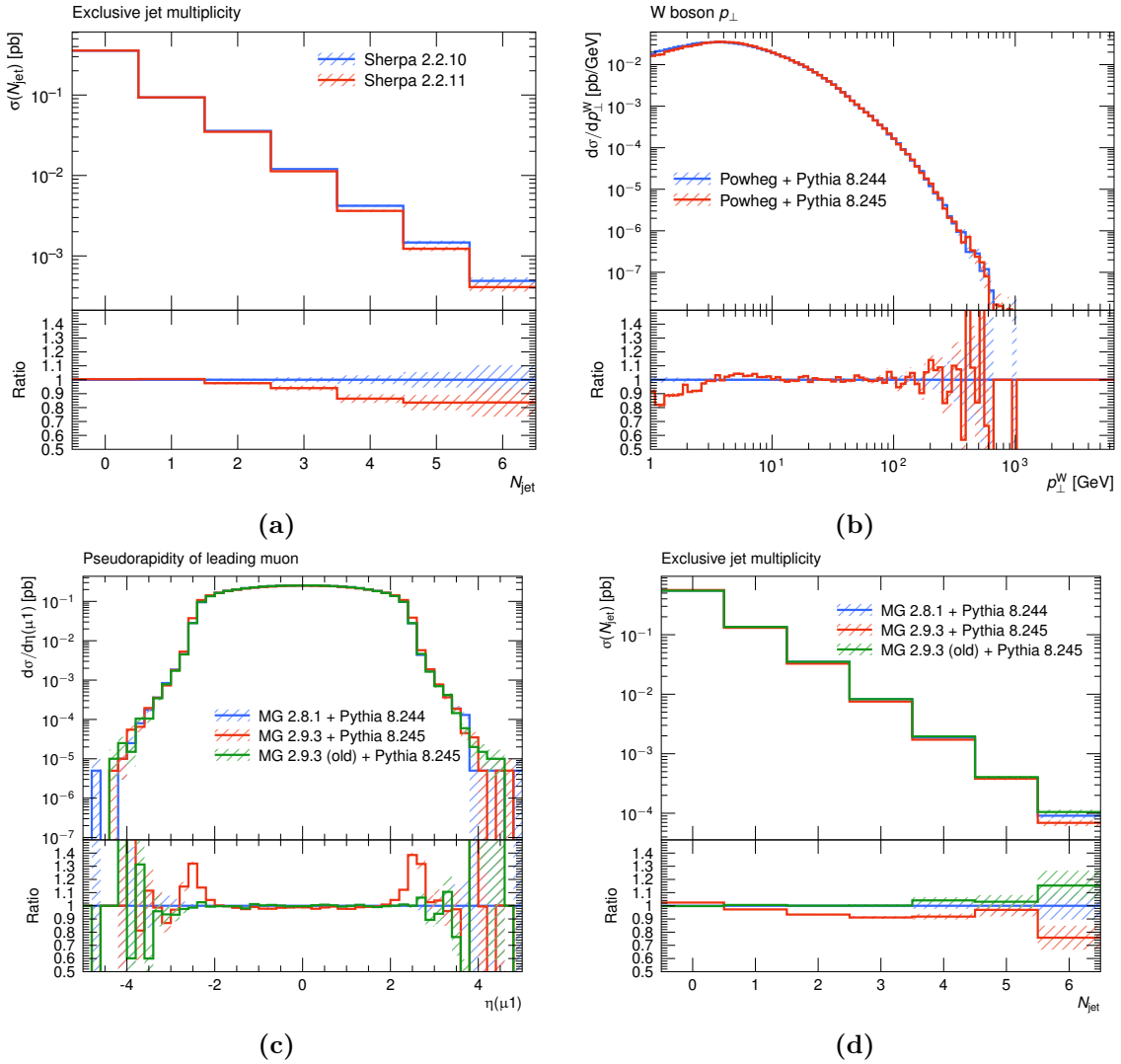

Figure 4.2: Examples of results obtained during the validation of various generator versions. (a) Jet multiplicity distribution of the SHERPA $Z(\to ee) + 0, 1, 2j$@NLO $+ 3, 4j$@LO sample comparing SHERPA 2.2.10 and SHERPA 2.2.11. (b) Distribution of the transverse momentum of the W boson in POWHEG+PYTHIA 8 $W(\to e\nu)$+jets events comparing PYTHIA versions 8.244 and 8.245. Examples of validation results obtained from MG5_aMC@NLO 2.9.3 validation against MG5_aMC@NLO 2.8.1 using MG5_aMC@NLO+PYTHIA 8 $Z(\to \mu\mu)$+jets events at LO: (c) Pseudorapidity distribution of the leading-p_{T} muon and (d) jet multiplicity distribution. For the green line, the speed strategy setting was set to the old behaviour. All samples are normalised to the same arbitrary cross-section of 1 pb.

for all generators were performed and some issues could be identified and fixed. An example is the validation of PYTHIAB, which is an ATLAS modification of PYTHIA aimed at an efficient generation of events related to B-physics and, thus, has its own generator interface. Several differences, an example is shown in Figure 4.4a, were observed. After some investigation, the origin of the differences was found to be related to a UserHook not being properly initialised in the interface in the new ATHENA release. After fixing the issue, the various observables

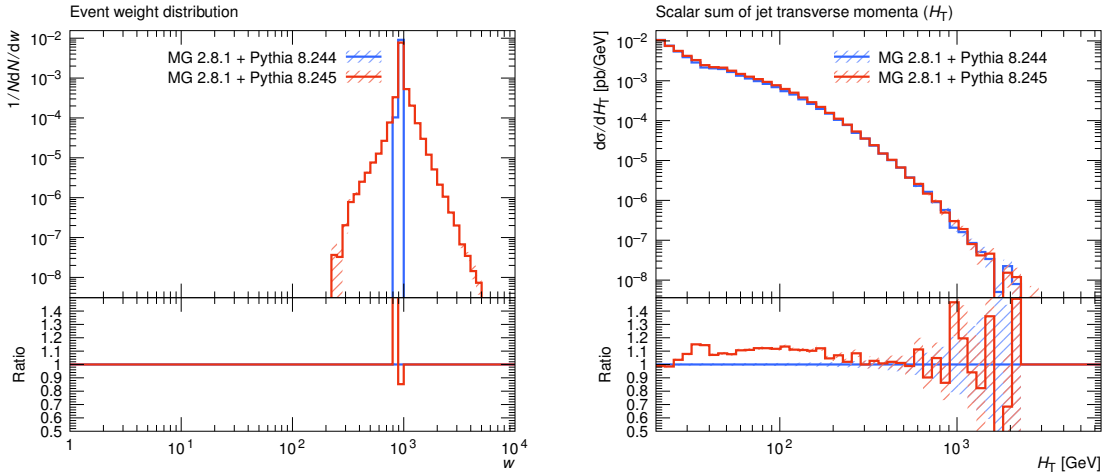

(a) **(b)**

Figure 4.3: Distributions of (a) event weights and (b) H_T, defined as the scalar sum of jet transverse momenta, for MG5_aMC@NLO+Pythia 8 $Z(\to \mu\mu) + 0, 1, 2j$@LO production using CKKW-L merging. The reference sample in blue corresponds to the interface version including the weight bug, while the monitored sample (red) includes the bug-fixed version. All samples are normalised to the same arbitrary cross-section of 1 pb.

were checked again and found to agree well between the software releases.

Several changes to the generator interfaces were necessary when introducing the new version of the HepMC format. An example is the validation for Sherpa using the same generator version but different HepMC series. Large differences between the validation samples produced with the old HepMC 2.6.11 version and new version HepMC 3.2.4 were detected. An example is shown in Figure 4.4b for dileptonic $t\bar{t}$ events. The comparison to reference data clearly indicates that the reference sample agrees well with data, while the new sample deviates. It turned out that the new HepMC format introduces changes that were incompatible with the existing generator interface resulting in unexpected changes in various observables. Good agreement between the samples was restored by adapting parts of the Sherpa generator interface for the needs of HepMC 3. This example illustrates that changes in the generators or file formats can require subsequent changes in the corresponding generator interfaces in order to produce consistent results.

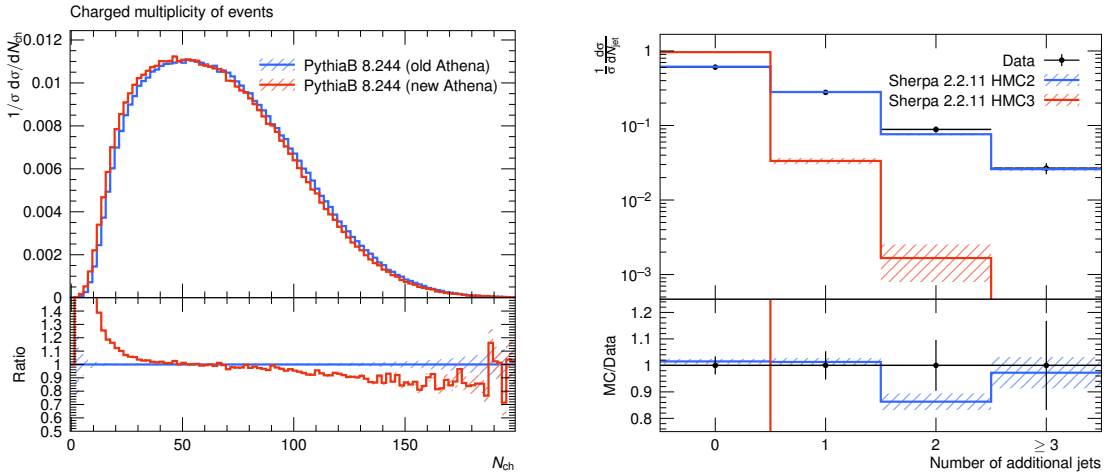

(a) **(b)**

Figure 4.4: Examples of validation results obtained during the validation of MC generators for the new major ATHENA release. In (a), the multiplicity of charged particles in an event is compared for PYTHIAB $Z(\to \mu\mu) + J/\Psi(\to \mu\mu)$ events between the old ATHENA release (blue line) and the new one (red line). In (b), the impact of the HEPMC version change without the necessary modification of the generator interface is illustrated by the additional number of jets distribution for dileptonic $t\bar{t}$ events generated with SHERPA. The reference data from Ref. [131] are provided by RIVET.

4.5 Conclusion and outlook

A new validation system, called PAVER, has been established and successfully used in a series of MC event generator validations. It is based on RIVET that provides a long list of analyses including a broad set of observables that can be exploited in the validation process. This is important, as changes might impact only single observables. Several expected changes could be identified and traced back to intended modifications by the generator authors. On the other hand, the validation system helped to detect several unintended features mainly in the early phase of the new major ATHENA release before being used in the official MC production. New features in the validation system, like the possibility to validate more than two versions of a sample at the same time and the comparisons to reference data, are found to be a useful improvement of the validation system.

In the process of validating new generator versions, a few aspects have been noted that might be improved in the future. In the validation procedure, samples produced with new generator versions are compared to reference samples. In case the reference contains undetected issues already, these will also be not easily recognized in the validations of updated generator revisions as long as the specific issue does not change. Including reference data in the validation is a start to mitigate these shortcomings. A further improvement could be the comparison of MC sample properties to SM expectations. For example, the branching ratios of generated top quarks, W and Z bosons could be calculated from the generated MC validation samples and

compared to the expected values. If these would be visualised, differences could be easily spotted in the validation system.
Further improvements could be related to a higher level of standardisation and automation of the validation chain. An example is the automatic production of YODA files during the generation of the validation samples in the MC production system using a set of pre-defined RIVET analyses. This would further reduce the timescale of validations and the amount of related work.

5 The ATLAS experiment at the Large Hadron Collider

In order to probe the SM and search for physics beyond, a number of experiments exists. Since several decades, experiments at particle accelerators play a leading role in this research area. In the following, the Large Hadron Collider and one of the experiments investigating the particle collisions, the ATLAS experiment, are described.

5.1 The Large Hadron Collider

The LHC [132] is a circular particle accelerator and storage ring at the European Organization for nuclear research (CERN), near Geneva. It is installed in a 27 km long tunnel that was constructed for the Large Electron-Positron Collider (LEP) and lies approximately 100 m below the surface. It is designed to collide protons at a centre-of-mass energy of $\sqrt{s} = 14\,\text{TeV}$ and is the most powerful accelerator in the world. At the beginning, the LHC delivered proton-proton (pp) collisions at $\sqrt{s} = 7\,\text{TeV}$ in 2010 and 2011, and at $\sqrt{s} = 8\,\text{TeV}$ in 2012. After a first long shut down in 2013 and 2014, the centre-of-mass energy was increased to $\sqrt{s} = 13\,\text{TeV}$ for the pp collisions during Run 2 (2015-2018). The collision energy has been further increased to $\sqrt{s} = 13.6\,\text{TeV}$ for the data-taking period which started in 2022 (Run 3). The accelerated particles collide at four interaction points, where the major experiments (ALICE [133], ATLAS [134], CMS [135] and LHCb [136]) are located to detect and analyse the products of the collisions. ATLAS and CMS are multi-purpose detectors. Both experiments cover a broad programme of SM measurements and searches for new physics. The LHCb experiment is designed for studies of b-hadron physics. Apart from pp collisions, the LHC can accelerate and collide heavy ions, producing lead–lead or proton–lead collisions. The ALICE experiment is specialised to study collisions with heavy ions.
In order to achieve the final energies for collisions, the protons are accelerated in several pre-accelerators before the injection in the LHC. A scheme of the CERN accelerator complex is shown in Figure 5.1. At the beginning of the chain, protons are extracted from hydrogen gas using an electric field. These protons are accelerated in a first step in the linear accelerator LINAC2 to an energy of 50 MeV. The beam is then transferred to the Proton Synchrotron Booster (PSB), which accelerates the protons to 1.4 GeV, followed by the Proton Synchrotron (PS) increasing the beam energy up to 25 GeV. Before the beam is injected in the LHC, the last pre-accelerator, the Super Proton Synchrotron (SPS), accelerates the protons to 450 GeV.

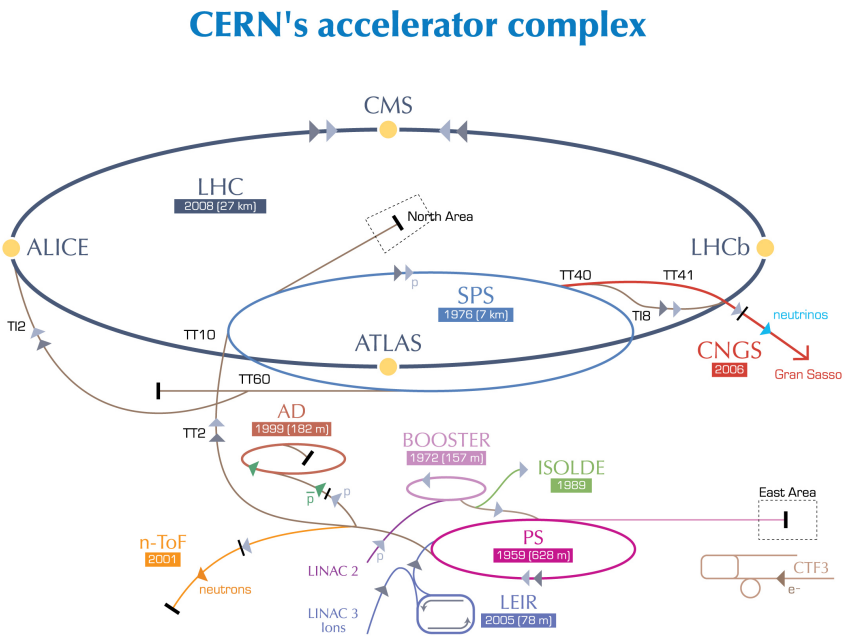

Figure 5.1: Schematic view of the CERN accelerator complex [137].

In the LHC, the proton beams are accelerated in opposite directions to an energy of 6.5 TeV per beam for an operation at $\sqrt{s} = 13\,\text{TeV}$. In order to keep the protons on a circular path, superconducting dipole magnets are installed along the ring providing magnetic fields of 8 T. This high magnet field strength is achieved by cooling the magnets below 2 K using superfluid helium.

Due to the filling schemes and the acceleration, the beams are not continuous but consist of proton bunches containing about $1.15 \cdot 10^{11}$ protons each. In each beam exist 3564 bunch places at a bunch spacing of 25 ns which corresponds to a maximum collision frequency of 40 MHz. Technically, a maximum of 2556 proton bunches can be filled in each beam to accommodate the rise time of kicker and dumping magnets.

A characteristic parameter of accelerators is the instantaneous luminosity which is given in the case of Gaussian beam profiles and head-on collisions by

$$\mathcal{L} = \frac{N_\text{b}^2 n_\text{b} f_\text{r}}{4\pi\sigma_\text{x}\sigma_\text{y}}, \tag{5.1}$$

where N_b is the number of protons per bunch, n_b the number of bunches per beam, f_r the revolution frequency, and the widths of the beam profile σ_x and σ_y. In practice, this equation has to be modified due to effects like non-Gaussian beam profiles or collisions of the beams at some crossing angle. The beam size can be also expressed as a function of the parameter β^*, which is the value of the beta function at the collision point. Table 5.1 compares some of the aforementioned LHC machines parameters for each year of Run 2 to their design values.

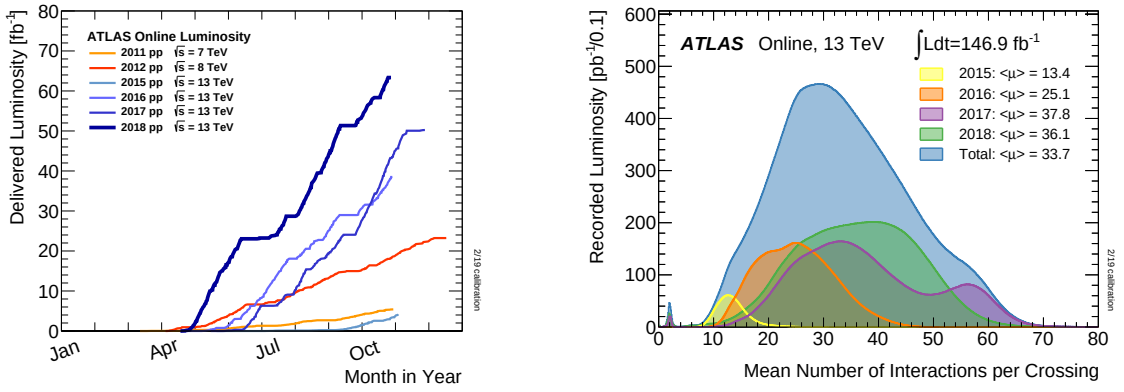

(a) **(b)**

Figure 5.2: (a) Delivered luminosity for high energy pp collisions during stable beams for the years of LHC data taking [138]. (b) Luminosity-weighted distribution of the mean number of interactions per crossing for the period 2015-2018 [139].

The event rate in LHC collisions is given by

$$\frac{dN}{dt} = \mathcal{L} \cdot \sigma, \tag{5.2}$$

where σ is the cross-section of a particular scattering process and $\mathcal{L}$ the instantaneous luminosity. Often the integrated luminosity, which is the integral of the instantaneous luminosity over the active accelerator time, is used. With this information, the total number of produced events can be calculated by

$$N = \sigma \cdot \int \mathcal{L} dt. \tag{5.3}$$

The experiments at the LHC have dedicated subdetectors for the measurement of the delivered luminosity. For the ATLAS experiment, the delivered luminosity is shown separated by year on the left-hand side of Figure 5.2. In this dissertation, only data collected at a centre-of-mass energy of $\sqrt{s} = 13\,\text{TeV}$ from 2015 to 2018 are used. The high bunch density and collision frequency can cause several simultaneous pp interactions. These events are called pile-up and are related to additional pp collisions in the same (in-time pile-up) or neighbouring bunch crossings (out-of-time pile-up). A measure of the pile-up activity is the mean number of interactions per bunch crossing μ. The distributions of μ for each year of Run 2 are shown in Figure 5.2b.

The ATLAS experiment recorded data corresponding to an integrated luminosity of $147\,\text{fb}^{-1}$ and an average μ value of $\langle\mu\rangle = 33.7$ during Run 2. Of the recorded data set only data fulfilling additional data quality requirements are used for physics analyses, resulting in a data set corresponding to an integrated luminosity of $139\,\text{fb}^{-1}$.

Table 5.1: LHC machine parameters for Run 2 compared to the design parameters [140].

Parameter	Design	2015	2016	2017	2018
Beam energy [TeV]	7.0	6.5	6.5	6.5	6.5
Bunch spacing [ns]	25	25	25	25	25
Beam focus β^* [cm]	55	80	40	40/30	30/27/25
Number of bunches per beam	2808	2244	2200	2556-1868	2556
Bunch population $N_b[10^{11}p]$	1.15	1.2	1.25	1.25	1.1
Peak luminosity $[10^{34}\text{cm}^{-1}\text{s}^{-1}]$	1.0	< 0.6	1.5	2.0	2.1

5.2 The ATLAS experiment

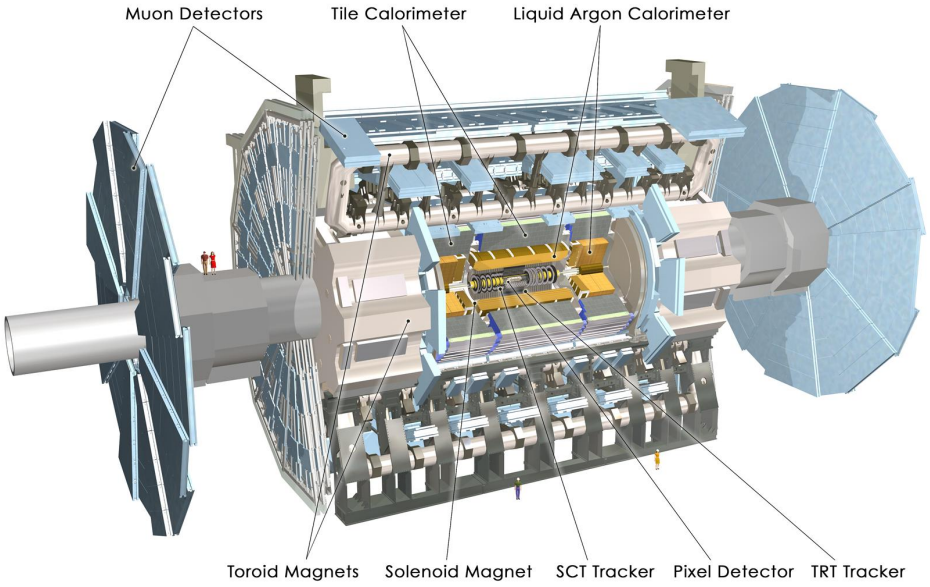

Figure 5.3: Overview of the ATLAS detector with the various subsystems and the magnet system [141].

The ATLAS detector [134] is a multi-purpose detector installed at the LHC. Figure 5.3 shows the 44 m long, 25 m high, and about 7000 t heavy detector. In the central part of the detector, the barrel region, the different subdetector systems are arranged cylindrically around the beam pipe. At both ends, the detector systems are installed in disk shaped layers perpendicular to the beam pipe. These parts are called end-cap regions and forward region for the part close to the beam pipe. Due to this forward-backward cylindrical symmetry, the ATLAS detector covers a solid angle of nearly 4π around the interaction point.

The inner-detector system (ID) is the part closest to the beam pipe and corresponds to the tracking system of the experiment. It is immersed in a solenoidal magnetic field of 2 T in order to bend the trajectories of charged particles allowing the measurement of their transverse momenta. The calorimeter system surrounding the ID absorbs most of the particles, except

Table 5.2: General performance goals of the ATLAS detector [134]. The energy E and the transverse momentum p_{T} are given in units of GeV. The symbol $\oplus$ denotes that the terms are added in quadrature.

Subdetector	Resolution	Coverage
Inner detector	$\sigma_{p_{\mathrm{T}}}/p_{\mathrm{T}} = 0.05\,\% \cdot p_{\mathrm{T}} \oplus 1\,\%$	$\lvert\eta\rvert < 2.5$
EM calorimeter	$\sigma_E/E = 10\,\%/\sqrt{E} \oplus 0.7\,\%$	$\lvert\eta\rvert < 3.2$
Hadronic calorimeter	$\sigma_E/E = 50\,\%/\sqrt{E} \oplus 3\,\%$	$\lvert\eta\rvert < 3.5$
Had. forward calorimeter	$\sigma_E/E = 100\,\%/\sqrt{E} \oplus 10\,\%$	$3.1 < \lvert\eta\rvert < 4.9$
Muon spectrometer	$\sigma_{p_{\mathrm{T}}}/p_{\mathrm{T}} = 10\,\%$ at $p_{\mathrm{T}} = 1\,\mathrm{TeV}$	$\lvert\eta\rvert < 2.7$

for muons and neutrinos, and measures their energies. The muon spectrometer (MS) with superconducting toroid magnets is the outermost subsystem that detects the muon trajectories and measures their momenta.

Particles produced in the pp collisions go through the different subdetectors and create characteristic signatures in the detector. This is the basis for the reconstruction of measured particles that are used in the ATLAS measurements and searches. The design of the subdetectors is based on the performance goals listed in Table 5.2.

5.2.1 Coordinate system

ATLAS uses a right-handed coordinate system with its origin at the nominal interaction point in the centre of the detector. The x-axis is defined from the interaction point to the centre of the LHC ring, the y-axis goes upward, and the z-axis points along the axis of the beam pipe. Due to the shape of the detector, cylindrical coordinates (r,ϕ) are used in the transverse plane, with ϕ being the azimuthal angle around the beam pipe. The polar angle θ is measured with respect to the z-axis. Often the rapidity

$$y = \frac{1}{2} \ln \left[\frac{E + p_z}{E - p_z} \right] \tag{5.4}$$

with the energy E of the particle and the z-component of its momentum p_z is used instead of the angle θ. For particles with a small mass compared to their energy ($m \ll E$) the rapidity is equal to the pseudorapidity defined as

$$\eta = -\ln \left(\tan \frac{\theta}{2} \right). \tag{5.5}$$

Transverse variables like the missing transverse momentum $E_{\mathrm{T}}^{\mathrm{miss}}$ or the transverse momentum $p_{\mathrm{T}} = p \sin\theta$ are defined in the x-y-plane. The angular distance ΔR between two particles is defined in the pseudorapidity-azimuthal angle space as

$$\Delta R = \sqrt{(\Delta\eta)^2 + (\Delta\phi)^2}. \tag{5.6}$$

5.2.2 Inner detector

The ID [142, 143] is the innermost subdetector of the ATLAS experiment providing tracking information of charged particles within $|\eta| < 2.5$. It is designed for the reconstruction of primary and secondary vertices, the measurement of charged-particle momenta, and the identification of electrons. The ID is immersed in a 2 T magnetic field parallel to the beam axis, generated by a superconducting solenoid magnet. Thus, electrically charged particles are deflected in ϕ-direction by the magnetic field with a radius proportional to their momenta, allowing for the measurement of the charge and the momentum of these particles.
Figure 5.4 shows a schematic view of the ID in the barrel region. The ID is composed of three types of independent subdetectors, sorted by increasing radius from the interaction point: Pixel detector, semi-conductor tacker (SCT), and transition radiation tracker (TRT).

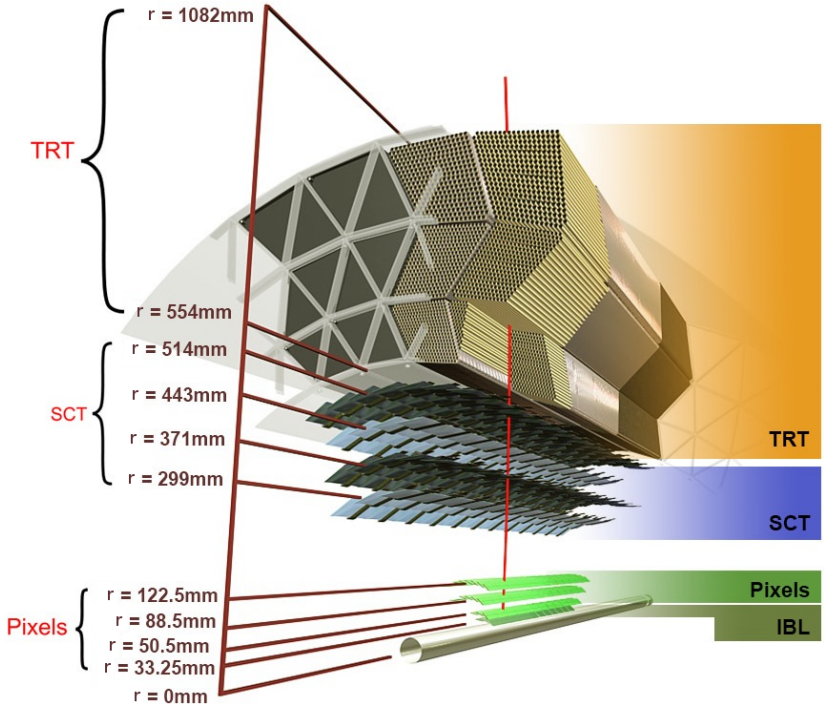

Figure 5.4: Schematic view of the barrel part of the ID with its different subdetectors [144].

Pixel detector

The pixel detector is the part of the ID located closest to the beam pipe and consists of semi-conductor pixel sensors. It covers the region $|\eta| < 2.5$ and is composed of four cylindrical layers in the barrel region, and of three concentric disks in both end-cap regions. The pixels in the three outer layers and the disks have a size of 50 µm × 400 µm. The precision of the location measurement is 10 µm in the $r - \phi$ plane, and 115 µm in z- and r-direction in the barrel and end-cap region, respectively.

During the first long shutdown, the innermost layer, called insertable B-layer (IBL) [145], was installed in order to improve the performance of the tracking system. It is located at a radius of 33 mm and consists of pixels with a size of 50 µm × 250 µm. Due to its closer location to the interaction point and the smaller pixel sizes, the IBL allows for an improved spatial resolution of 60 µm in the z-coordinate. This improved accuracy is needed for a precise vertex reconstruction, the identification of jets originating from b-hadrons, and the identification of pile-up vertices and their separation from the main interaction vertex of the hard interaction..

Semi-conductor tracker

The SCT is a silicon microstrip detector surrounding the pixel detector. The strips have a size of 80 µm × 6.4 cm and are arranged in four layers in the barrel region and in nine layers of disks in both end-caps, covering a pseudorapidity range of $|\eta| < 2.5$. Each layer contains two sets of sensors glued back-to-back at a stereo angle of 40 mrad, where one set of the strips is oriented parallel to the beam line in the barrel region and perpendicular in the end-cap regions. This allows for a measurement of the hit position along the strip direction. The SCT provides a resolution of 17 µm in the $r - \phi$ plane and 580 µm in $z(R)$-direction in the barrel (end-cap) region.

Transition radiation tracker

The outermost part of the ID is the TRT, extending the tracking capability of the ID up to a radius of one meter in a region of $|\eta| < 2.0$. The TRT is built out of 4 mm-diameter straw tubes filled with two different gas mixtures (xenon-based and argon-based). Charged particles traversing the TRT straw ionise the gas mixture and the resulting electrons drift to the anode wire inside the tube. The drift-time is used for the location measurement of the hit with a local resolution of 130 µm. Typically, 36 hits per track are measured by the TRT. Apart from providing tracking information, an important feature of the TRT is the capability of particle identification. The tubes are interleaved with polypropylene fibres and foils acting as transition-radiation material. Produced transition-radiation photons are absorbed by the gas mixture and the measured signal is again the resulting ionisation. As the transition radiation depends on the Lorentz γ-factor and therefore on the particle mass, electrons can be separated from charged pions.

5.2.3 Calorimeters

The calorimeter system [146] surrounds the ID and covers the region $|\eta| < 4.9$. It is designed to absorb the energy of most particles, except for muons and neutrinos, and is used to identify electrons, photons, and jets. ATLAS uses sampling calorimeters consisting of alternating layers of absorbing and active material. Due to interactions between the particles and the absorber material, particle showers are produced which are detected by the active material.

In the case of electromagnetic interactions, the particles lose their energy via bremsstrahlung and pair production, while hadronic particles are stopped by inelastic hadronic interactions. Different techniques depending mainly on the physics requirements are used for different parts of the calorimeter system, as illustrated in Figure 5.5. The electromagnetic calorimeter is suited for precise measurements of electrons and photons. Hadronic and forward calorimeters have a coarser granularity, being sufficient for jet reconstruction and $E_{\mathrm{T}}^{\mathrm{miss}}$ measurements.

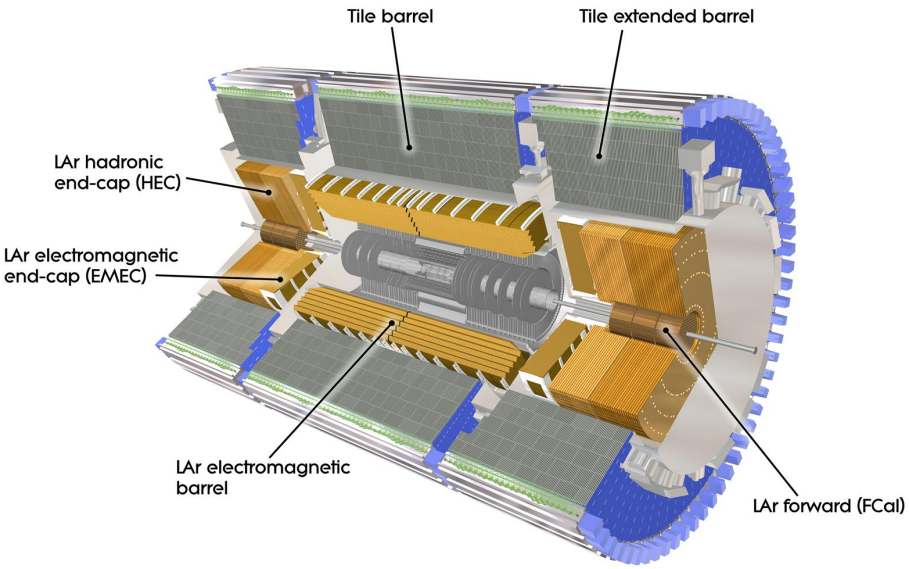

Figure 5.5: Cut-away view of the ATLAS calorimeter system [147].

Electromagnetic calorimeter

The electromagnetic calorimeter (ECAL) uses liquid argon (LAr) as active material and lead plates as absorbers that are structured in accordion geometry, providing a complete coverage in ϕ without any cracks. The ECAL is divided into a barrel part covering the range $|\eta| < 1.475$, and two end-cap components comprising the region between $1.375 < |\eta| < 3.2$. Additional material before the first active layer in the transition region between the barrel and end-caps at $1.37 < |\eta| < 1.52$ degrades the energy resolution in this particular pseudorapidity range. The ECAL is segmented in depth into three longitudinal layers for $|\eta| < 2.5$, differing by their thickness and the cell structure in the $\eta - \phi$ plane. The first layer is finely segmented in η with a cell-size of typically 0.003×0.1 in $\Delta\eta \times \Delta\phi$. This allows for a precise measurement of the electron and photon position. The middle layer collecting most of the energy of the showers has a thickness of 16 radiation lengths (X_0)[1] and a granularity in $\Delta\eta \times \Delta\phi$ of 0.025×0.025. The third layer has a granularity twice as coarse in η, collects the tails of the EM showers, and

[1]The radiation length X_0 is defined as the mean distance over which an electron looses all but $1/e$ of its energy.

is used for triggering. In the central region $|\eta| < 1.8$, a LAr presampler is installed to correct for energy losses of electrons and photons in front of the calorimeter. The total thickness of the ECAL is $> 22X_0$ in the barrel part, and $> 24X_0$ in the end-caps.

Hadronic calorimeter

The main purpose of the hadronic calorimeter is the containment of hadronically interacting particles and the energy measurement of jets. It is composed of various independent calorimeter types covering different pseudorapidity ranges. The tile calorimeter covers the central region $|\eta| < 1.7$ and is split into barrel ($|\eta| < 1.0$) and extended barrel ($0.8 < |\eta| < 1.7$) parts. It consists of steel as the absorber and scintillating tiles as the active material. The tile calorimeter is segmented in three longitudinal layers and cells of 0.1×0.1 in $\Delta\eta \times \Delta\phi$. The total thickness of the calorimeter is 9.7λ at $\eta = 0$ [2]. The hadronic end-cap calorimeter covers the range $1.5 < |\eta| < 3.2$ and consists of two independent wheels per end-cap, where the inner one has a finer granularity. Copper absorbers are used with LAr as the active material.

Forward calorimeter

The LAr-based forward calorimeter covers the very forward region of $3.1 < |\eta| < 4.9$ and is divided into three layers. Copper is used as absorber material in the first layer, which is optimised for electromagnetic measurements, while the other two layers are made of tungsten and are optimised for the energy measurement of hadronic interactions. Covering the region up to $|\eta| = 4.9$ is important for the measurement of $E_{\mathrm{T}}^{\mathrm{miss}}$.

5.2.4 Muon spectrometer

The MS [148] is the outermost subdetector of the ATLAS experiment. It is designed for the detection of charged particles exiting the calorimeters and the measurement of their momenta in $|\eta| < 2.7$. The MS chambers are placed within and around the superconducting air-core toroid magnets. In the central region, a magnetic field of up to 2.5 T is provided by a large barrel toroid, while two smaller magnets generate the magnetic field of up to 3.5 T in the end-caps. Each toroid consists of eight superconducting coils being equally distributed around the beam pipe providing magnetic fields that bend the muon tracks in η direction. As shown in Figure 5.6, four types of muon chambers are installed in the detector. Thin gap chambers (TGCs) and resistive plate chambers (RPCs) are mainly used for triggering, while the monitored drift tubes (MDTs) and cathode strip chambers (CSCs) make precise measurements of the tracks. The chambers are arranged in three cylindrical layers in the barrel region, and consist of three wheels perpendicular to the beam in the end-caps.

[2] The hadronic interaction length λ is the mean distance over which the energy of a hadron is reduced to $1/e$ of its initial energy.

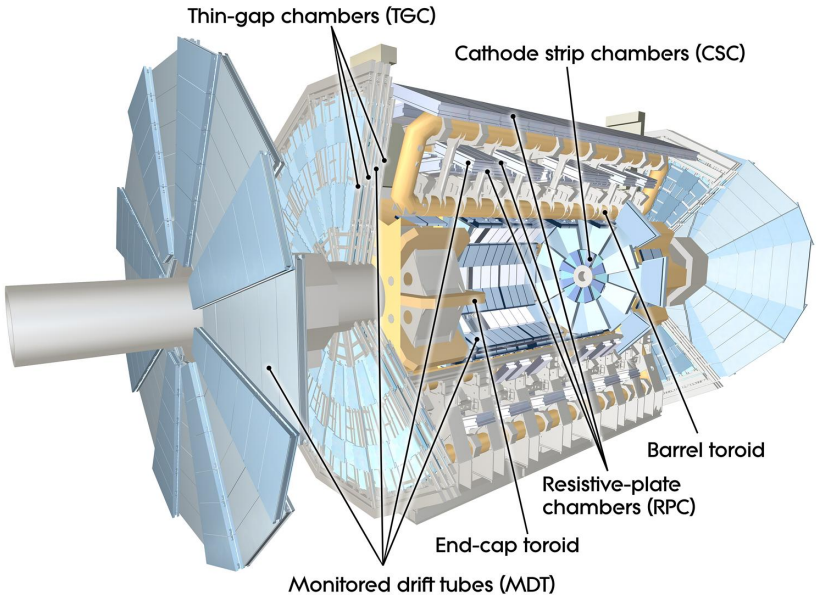

Figure 5.6: Cut-away view of the ATLAS muon system [149].

Precision tracking chambers

MDT chambers are proportional drift tubes used for the precise tracking of muons in $|\eta| < 2.7$. The innermost of the three MDT layers is replaced with CSCs for $|\eta| > 2.0$ due to their higher rate capability. The MDT chambers provide measurements of the hit coordinates in the bending plane with a resolution of 35 µm per chamber. The CSCs are multi-wire proportional chambers providing simultaneous measurements of η and ϕ. Their spatial resolution in the bending plane is similar to the one of the MDTs, while their resolution in ϕ is 5 mm.

Trigger Chambers

The maximum drift time in the MDTs of about 700 ns exceeds the time resolution requirements for triggering purposes of a few nanoseconds. Thus, faster trigger chambers are used for triggering within $|\eta| < 2.4$. RPC chambers are installed in the barrel region ($|\eta| < 1.05$) and consist of two resistive parallel plates filled with a gas mixtures in between which are read out by two sets of orthogonal pick-up strips. The TGCs, which are multi-wire proportional chambers with a small wire-to-cathode distance for fast readout, cover the end-cap region ($1.05 < |\eta| < 2.7$). Apart from triggering, TGCs and RPCs provide tracking information that is complementary to the precision tracking chambers. In particular, they measure the track coordinate in the non-bending direction. The typical spatial resolution of the position measurements is about $5 - 10$ mm for both coordinates.

5.2.5 Trigger system

In Run 2, bunch crossings occurred with a frequency of up to 40 MHz due to the bunch spacing of 25 ns. This high collision rate exceeds the technical capabilities for processing and storage of the events such that the ATLAS experiment cannot record every event. Event signatures being interesting for physics analyses have much lower cross-sections than soft processes dominating the pp cross-section. In order to select and store these interesting events, a two stage trigger system [150, 151] is in place reducing the recording rate down to 1 kHz on average.

The first-level, hardware-based trigger (L1) searches for high-p_T objects and large missing transverse momentum using information from the calorimeters and the muon spectrometer. The L1 trigger reduces the rate of accepted events from the initial rate down to a maximum of 100 kHz, providing the decision to keep the data from an event within 2.5 µs after the related bunch-crossing occurred. Regions-of-Interest (ROIs) in η and ϕ within the detector are identified and passed to the second trigger stage for further processing.

The second stage of the trigger system is the software-based high-level trigger (HLT), reducing the event rate to about 1 kHz. The HLT algorithms start the refined object reconstruction from the ROIs. However, this simplification of using only particular regions is not appropriate in some cases such as in the $E_{\mathrm{T}}^{\mathrm{miss}}$ reconstruction, where the full solid angle of the calorimeter coverage is considered instead. The HLT makes a decision within an average time of 500 ms depending on the trigger menu and the number of pile-up interactions. Accepted events are finally stored on disk. The list of individual triggers used in an LHC run is defined in the ATLAS trigger menu [150]. It contains the corresponding trigger thresholds and prescale factors, which can be adapted for each run if needed. Consecutive runs with constant run conditions and trigger thresholds are grouped into periods.

Missing transverse momentum triggers

Particles that interact neither via the electromagnetic nor the strong force leave no visible signature in the detector. The search for vector-like quarks, presented in this thesis, aims at final states with large missing transverse momentum coming from neutrinos or a charged lepton that is not reconstructed in the detector. In order to select this type of events, missing transverse momentum triggers [152] are used.

The $E_{\mathrm{T}}^{\mathrm{miss}}$ triggers are based on the transverse momentum imbalance of the calorimeters only, where muons are approximately invisible and thus treated like neutrinos. The L1 decision is based on the $E_{\mathrm{T}}^{\mathrm{miss}}$ calculation from projective towers of calorimeter cells. Several HLT algorithms were developed in order to reconstruct $E_{\mathrm{T}}^{\mathrm{miss}}$. The cell $E_{\mathrm{T}}^{\mathrm{miss}}$ is calculated considering all calorimeter cells above a certain noise threshold. Another approach is based on topological clusters built from calorimeter cells. This offers the possibility to identify the origin of the clusters as electromagnetic or hadronic, and therefore to apply an appropriate calibration to the topological clusters. In the mht algorithm, $E_{\mathrm{T}}^{\mathrm{miss}}$ is calculated as the negative

Table 5.3: List of $E_{\mathrm{T}}^{\mathrm{miss}}$ triggers used in the vector-like quark search to select data from LHC Run 2 from 2015 to 2018. For each year the table shows the trigger names, the used HLT logarithm, and the L1 and HLT thresholds applied. For trigger names where two HLT thresholds are given, the first is related to the pufit algorithm and the second to the cell algorithm. In 2017, the cell $E_{\mathrm{T}}^{\mathrm{miss}}$ was used in conjunction with the pufit algorithm even through this is not given explicitly in the trigger names.

Year	Period	Trigger name	HLT algorithm	L1/HLT threshold [GeV]
2015		HLT_xe70_mht	mht	50/70
2016	A-D3	HLT_xe90_mht_L1XE50	mht	50/90
2016	D4-F1	HLT_xe100_mht_L1XE50	mht	50/100
2016	F2-	HLT_xe110_mht_L1XE50	mht	50/110
2017	B1-D5	HLT_xe110_pufit_L1XE55	pufit, cell	55/110, 50
2017	D6-	HLT_xe110_pufit_L1XE50	pufit, cell	50/110, 50
2018	B-C5	HLT_xe110_pufit_xe70_L1XE50	pufit, cell	50/110, 70
2018	C6-	HLT_xe110_pufit_xe65_L1XE50	pufit, cell	50/110, 65

vectorial transverse momentum sum of calibrated anti-k_t jets with a radius parameter of $R = 0.4$, which are reconstructed from topological clusters. The pufit algorithm corrects the high energy deposits in the calorimeter for pile-up effects that are associated with low energy signals. Topological clusters are combined into patches and categorised based on their energy. The contributions from pile-up to $E_{\mathrm{T}}^{\mathrm{miss}}$ are estimated via a fit to the lower energy deposits. The $E_{\mathrm{T}}^{\mathrm{miss}}$ is calculated from the high energy patches after subtracting the estimated pile-up contributions. Combinations of the cell and pufit algorithms were used in the second half of Run 2 in order to improve the performance of the HLT. The list of $E_{\mathrm{T}}^{\mathrm{miss}}$ triggers used in the search for vector-like quarks can be found in Table 5.3.

5.2.6 Luminosity measurement

A good determination of the integrated luminosity is especially important to reach a high precision in the measurements of SM parameters and processes, especially in cross-section measurements. In order to determine accurately the luminosity recorded by the ATLAS experiment, the visible interaction rate per bunch crossing μ_{vis} is measured with several independent detectors following the methods in Refs. [153, 154]. The instantaneous per-bunch luminosity can be expressed as

$$\mathcal{L}_b = \frac{\mu_{\mathrm{vis}} f_r}{\sigma_{\mathrm{vis}}}, \tag{5.7}$$

where σ_{vis} the visible cross-section that is defined as the total inelastic cross-section times acceptance and efficiency of the detector. The absolute luminosity calibration of the detector, i.e. determination of σ_{vis}, is done in so-called van der Meer scans [155] that are performed in special low-luminosity runs.

The two primary subdetectors used for the bunch-by-bunch luminosity measurement are a Cherenkov detector called LUCID (LUminosity measurements using Cherenkov Integrated Detector) and the beam conditions monitor (BCM). LUCID is placed at $z = \pm 17\,\mathrm{m}$ from the interaction point and the diamond detector BCM at $z = \pm 1.84\,\mathrm{m}$, respectively. Considering data quality requirements, the integrated luminosity of the ATLAS Run 2 data set was measured to be $139\,\mathrm{fb}^{-1}$ with a total uncertainty of $1.7\,\%$ [154].

6 Event Reconstruction

The basis for each search and measurement in ATLAS is the proper reconstruction of the physics objects from the measured detector signals using specialised reconstruction algorithms. In a first step, charged particle tracks are identified from the measured hits in the ID and MS, and the primary hard-scatter interaction vertex is determined. The final physics objects are then reconstructed considering the information about energy deposits in the detector. Electrons, muons, missing transverse momentum, jets, as well as b-jets are used in this thesis. The reconstruction and identification algorithms for these objects and the object selection requirements applied in the search for VLQs are described in this chapter. Two sets of quality requirements are defined for the selection of electrons and muons. Baseline leptons are used in the procedure to remove the overlap between physics objects and to veto against additional leptons. Signal leptons have to fulfil tighter requirements and are used both in the reconstruction of kinematic variables and the event selection.

6.1 Tracks and primary vertices

Charged particles traversing the magnetic field inside the ID are deflected onto a helical trajectory with a curvature inversely proportional to their momenta. In order to identify these particles and determine their momenta, tracks are reconstructed based on fitting a trajectory model to measurements in the ID [144].

Track reconstruction employs an iterative track finding algorithm with an "inside-out" strategy. First, track seeds are formed from three measurements in the silicon detectors. A combinatorial Kalman filter [156] is then used to build track candidates by adding further silicon hits to the seeds that are compatible with the primary trajectory. Incorrectly assigned hits and such shared between track candidates are resolved by an ambiguity solver. Good quality tracks are then extrapolated into the TRT and combined with its measurements. In a final step, the reconstructed tracks are refitted with a global χ^2 method for a precise estimate of the track parameters.

Tracks are specified by a set of five parameters in ATLAS: (d_0, z_0, ϕ, θ, q/p). Here, ϕ and θ, are the azimuthal and polar angles of the track, and q/p is the charge of the track divided by its momentum. The transverse impact parameter d_0 is defined as the distance from the beamline to the point of closest approach of the track in the transverse plain. The longitudinal impact parameter z_0 is defined as the longitudinal difference along the beam line from the point where d_0 is measured to a reference point, which can be the primary vertex of the event

or the centre of the detector. In the later object reconstruction, z_0 is given with respect to the primary vertex.

Primary vertices, defined as the interaction points of pp collisions, are reconstructed by an iterative vertex finding algorithm [157]. A seed vertex is combined with tracks, using a χ^2 minimisation to find the best vertex position. In each iteration, less compatible tracks are down-weighted and the vertex position is recomputed. Tracks that are incompatible with the determined vertex are removed and considered as input for further vertex finding.

All vertices with at least two associated tracks with $p_{\mathrm{T}} > 500\,\mathrm{MeV}$ are retained as primary vertex candidates. The hard-scatter vertex is then defined as the primary vertex with the highest sum of squared transverse momenta of associated tracks, while the remaining vertices are considered as pile-up interactions.

6.2 Electrons

Electrons are reconstructed from energy deposits in the calorimeters and associated tracks. The electron reconstruction is based on a dynamic clustering approach building variable-size clusters, called superclusters [158]. These allow recovering energy from bremsstrahlung photons in contrast to fixed-size clusters.

First, topologically connected energy deposits in the calorimeter cells above a set of noise thresholds are grouped into so-called topo-clusters [159]. Only clusters with an associated energy deposited largely in the ECAL are further considered. After refitting the ID tracks allowing for additional energy loss from bremsstrahlung, they are matched to the EM topo-clusters, that are then input for the supercluster building. Those associated with a well-reconstructed track are used as supercluster seeds. Clusters near these seed candidates are identified as satellite clusters if they fall within a certain window around the seed cluster centre. Cluster seeds with their associated satellite clusters form the superclusters, which are matched to tracks in order to build the final electron candidates. The basic concept of the supercluster algorithm is illustrated in Figure 6.1.

The electron four-momentum is built using the energy of the supercluster and the η- and ϕ-direction from the best-matched track. Due to energy losses in material upstream of the

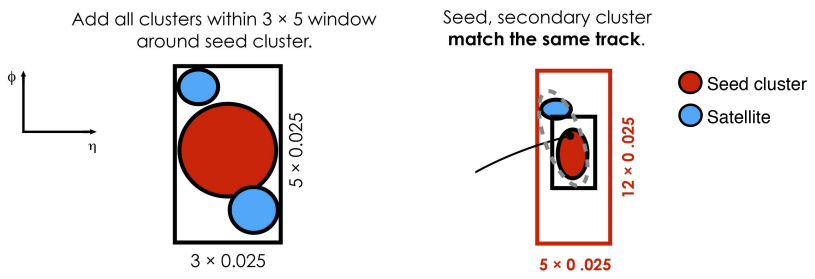

Figure 6.1: Illustration of the supercluster algorithm for electrons [158].

calorimeter, the measured cluster energy does not correspond to the original electron energy and must be calibrated. Multivariate regression techniques are used to estimate the energy of electrons based on shower development properties. The final electron energy and resolution correction factors [160] are derived by comparing simulated $Z \to ee$ events to data.
To avoid misidentification of hadronic activity as electrons and to distinguish between good electrons and those originating from heavy-hadron decays, several identification criteria are defined. They rely on a multivariate, likelihood-based method combining information of the primary electron track, the electromagnetic shower development, and the quality of the track-to-cluster matching into a single variable. The electron identification imposes a cut on this likelihood discriminant and some additional requirements as on the number of hits in the ID. Three main operation points are discussed in Ref. [161], differing in their selection efficiencies and background rejection rates: *Loose*, *Medium*, *Tight*. In this analysis, another operation point called *LooseAndBLayer* is used, which requires an extra hit in the IBL compared to the *Loose* working point.
Electrons from semi-leptonic decays of heavy hadrons are characterized by additional activity near the electron in the ID and calorimeter, and are rejected by calorimeter- and track-based isolation requirements. The calorimeter isolation variable ($E_{\mathrm{T}}^{\mathrm{cone20}}$) is built by summing up the transverse energy of topo-clusters falling in a cone of $\Delta R = 0.2$ around the electron excluding the energy of the electron cluster and subtracting additional leakage and pile-up corrections. Analogously, the track-based isolation variable ($p_{\mathrm{T}}^{\mathrm{varcone20}}$) is defined as the scalar sum over the transverse momenta of selected tracks within a variable-sized cone with $\Delta R = \min(10\,\mathrm{GeV}/p_{\mathrm{T}}, 0.2)$ while excluding tracks matched to the electron.
The efficiency of the electron reconstruction, identification, and isolation is measured in $Z \to ee$ and $J/\Psi \to ee$ events using the tag-and-probe method. The tag electron in the decay has to fulfil stringent requirements, and the second one, called probe electron, is only selected by a requirement on the invariant mass of the electron pair. This allows for an unbiased measurement of the efficiencies by applying the selection criteria to the probe electrons. The efficiencies are measured separately for data and simulated events in bins of η and E_{T} such that differences can be corrected for in form of scale factors applied to the simulation.
The baseline selection requirements for electrons in this analysis are $p_{\mathrm{T}} > 10\,\mathrm{GeV}$, $|\eta| < 2.47$, excluding the calorimeter transition region $1.37 < |\eta| < 1.52$, and *LooseAndBLayer* identification. A good association between the matched track and the hard-scatter primary vertex is ensured by requirements on the transverse impact parameter significance, defined as the ratio of d_0 to its uncertainty, $|d_0|/\sigma_{d_0} < 5$, and the longitudinal impact parameter, $|z_0 \sin\theta| < 0.5\,\mathrm{mm}$. Furthermore, baseline electrons are required to be isolated, restricting the surrounding activity by $E_{\mathrm{T}}^{\mathrm{cone20}}/E_{\mathrm{T}}^{e} < 0.2$ and $p_{\mathrm{T}}^{\mathrm{varcone20}}/p_{\mathrm{T}}^{e} < 0.15$. Signal electrons must fulfil in addition to the baseline criteria $p_{\mathrm{T}} > 28\,\mathrm{GeV}$ and satisfy the *Tight* identification working point.

6.3 Muons

Muon candidates [162, 163] are primarily reconstructed from hits in the ID and the MS taking also information from the calorimeters into account. The reconstruction of MS tracks starts with the combination of local hit patterns into short track segments in the individual MS layers. The segments in different MS layers are connected into tracks using a global χ^2 fit. Hits can be removed or added to the track based on their compatibility with the trajectory, in which case the track is refitted. Four different muon reconstruction strategies are used, corresponding to the following muon types:

- Combined (CB) muons are identified by matching independently reconstructed tracks in the ID and MS and combined tracks are built with a global track fit based on ID and MS hits, taking energy loss in the calorimeters into account. Most of the muons are reconstructed by an "outside-in" algorithm, which extrapolates the MS tracks into the ID. A complementary "inside-out" strategy extrapolates ID tracks to the MS and searches for compatible MS hits.

- Extrapolated (ME) muons are reconstructed by MS tracks that cannot be matched to ID tracks. They are used in the region $2.5 < |\eta| < 2.7$ that is not covered by the ID.

- Segment-tagged (ST) muons are identified by ID tracks extrapolated to the MS that match to at least one reconstructed MS segment. ST muons are used when muons cross only one layer of the MS due to their low p_{T} or the reduced acceptance of the MS in some regions.

- Calorimeter-tagged (CT) muons are identified by matching an ID track to an energy deposit in the calorimeter consistent with a minimum-ionising particle. This muon type recovers acceptance in the region $|\eta| < 0.1$ where the MS is only partially instrumented.

The different muon types can overlap. In case two muon types share the same ID track, preference is given to CB muons, then ST and CT muons. Overlap with ME muons in the MS is resolved by using the better reconstructed track. The muon parameters are then taken either directly from the ID track fit or a combined ID and MS track fit depending on the muon type.
After the reconstruction, good muon candidates are identified using requirements on the track fit quality, the number of ID and MS hits, and the compatibility of the individual measurements in both subdetectors. Different identification working points are defined in Ref. [163], of which two are used in this analysis: *Loose* and *Medium*. The *Medium* identification working point gives a good efficiency while keeping the systematic uncertainties small. Its selection accepts only CB muons within the ID acceptance $|\eta| < 2.5$. The *Loose* identification working point provides the highest efficiency and adds CT and ST muons in the range $|\eta| < 0.1$ to all muons passing the *Medium* selection.

While muons from light-hadron decays and misidentified hadrons can be effectively suppressed by identification and vertex association requirements, muons originating from heavy-hadron decays are rejected using isolation criteria. The isolation variables are calculated similarly as for electrons except that in the case of the track-based isolation variable the radius of the cone is $\Delta R = \min(10\,\text{GeV}/p_{\text{T}}, 0.3)$.
Similar to electrons, the muon momentum needs to be calibrated in order to bring data and simulation in agreement. Correction factors for the muon momentum and resolution are obtained by a binned likelihood fit comparing the dimuon invariant mass distributions of $Z \to \mu\mu$ and $J/\Psi \to \mu\mu$ events in data and simulation [162]. The efficiencies of muon reconstruction, identification, isolation, and vertex association are measured by the tag-and-probe method using the same type of events as for the calibration. Corrections for the simulation are derived in form of p_T and η dependent scale factors.
In the analysis, the baseline muon requirements are a *Loose* identification, $p_{\text{T}} > 10\,\text{GeV}$, and $|\eta| < 2.5$. Furthermore, muon candidates have to fulfil a selection on the track impact parameters $|d_0|/\sigma_{d_0} < 3$ and $|z_0 \sin\theta| < 0.5\,\text{mm}$. Signal muons are required to pass all baseline requirements and in addition satisfy the *Medium* identification working point criteria and $p_{\text{T}} > 28\,\text{GeV}$. The isolation of signal muons is ensured by a cut on the track-based isolation variable, $p_{\text{T}}^{\text{varcone30}}/p_{\text{T}}^{\mu} < 0.06$, corresponding to the *TightTrackOnly* isolation working point.

6.4 Jets

Due to the colour confinement of QCD, quarks and gluons produced in high-energy collisions do not exist as free, isolated particles and therefore cannot be directly observed by the detector. Instead, they evolve into collimated sprays of hadrons, known as jets. These jets can be reconstructed from the detector signals and contain characteristic properties of the initial partons.

The jet reconstruction starts with the clustering of calorimeter cells into three-dimensional topo-clusters using a nearest-neighbour algorithm as in the reconstruction of electrons. An origin correction is applied to each topo-cluster based on the expectation that jets produced in the hard-scatter process originate from the primary vertex of the event. The particle-flow algorithm [164] then combines measurements from the tracker and calorimeters. First, the algorithm attempts to match selected tracks to topo-clusters in the calorimeter. Topo-clusters that are not matched to any track are assumed to contain energy deposited from neutral particles. The expected energy deposit in the calorimeter from the particle that produced the track is estimated based on the track momentum and topo-cluster position. In order to avoid overlap between momentum measurements and energy measurements for charged particles in the ID and calorimeter, respectively, the estimated energy of the track is subtracted cell-by-cell from the associated calorimeter energy. No subtraction is performed in cases where the advantages of the tracker become smaller, such as for high-p_{T} jets, where the resolution of the tracker degrades and the calorimeter performance is excellent, and thus track information

is ignored. The particle-flow algorithm therefore becomes equivalent to a reconstruction purely based on calorimeter information at high energies, but exhibits an improved jet energy and mass resolution, as well as pile-up stability at low energies.

The collection of particle-flow objects made out of tracks, and both modified and unmodified topo-clusters, is then input to a jet-finding algorithm that decides which constituents form the individual jets. The anti-k_t clustering algorithm [165] implemented in the FastJet [166] software package is the primary jet definition used in ATLAS. This algorithm is infrared and collinear safe, meaning that an additional collinear splitting or soft emissions do not alter the jets found in an event. The anti-k_t algorithm relies on the two distance metrics

$$d_{ij} = \min\left(\frac{1}{k_{\mathrm{T}i}^2}, \frac{1}{k_{\mathrm{T}j}^2}\right) \cdot \frac{\Delta R_{ij}^2}{R^2} \tag{6.1}$$

$$d_{i\mathrm{B}} = \frac{1}{k_{\mathrm{T}i}^2} \tag{6.2}$$

where ΔR_{ij} is the distance between inputs i and j in the η-ϕ plane, and $k_{\mathrm{T},x}$ the transverse momentum of input x. The parameter R regulates the final jet size. The distance between the inputs i and j is given by d_{ij}, while $d_{i\mathrm{B}}$ denotes the distance between input i and the beam. First, the algorithm identifies the smallest of the distances and if it is a d_{ij}, the two inputs are combined to a pseudo-jet that replaces its two constitutes in the list of inputs. If the smallest distance is a $d_{i\mathrm{B}}$ instead, input i is declared as a jet and removed from the input list. Then, the distances are recalculated and the procedure is repeated until all inputs are combined into jets.
The anti-k_t algorithm assigns small distances to high momentum particles, that are close by. Thus, preference in the clustering is given to these particles in the clustering and softer particles are sequentially added resulting in jets with an approximately circular shape. In the following, jets are clustered with a radius parameter $R = 0.4$, referred to as small-R jets.

After the reconstruction of jets from the detector signals, the jet energy scale (JES) is calibrated to correct for detector effects and imperfect simulation [167]. The calibration is mainly based on MC simulation, and the jet momenta are corrected to that of truth jets built from the stable final-state particles in the simulation. The calibration is performed in multiple, consecutive stages that are illustrated in Figure 6.2 and explained below. The derived corrections are applied to both data and simulation, except for the last stage where a correction is only applied to data in order to correct for remaining differences between data and simulation.
Excess energy from pile-up activity affects the measured jet energy and therefore two corrections are applied to minimise its impact. The per-event pile-up contribution to the jet p_{T} is subtracted based on the jet area A, which is calculated using ghost association [168], and the event pile-up p_{T} density $\langle p_{\mathrm{T}}/A \rangle$. In order to remove any remaining pile-up dependency,

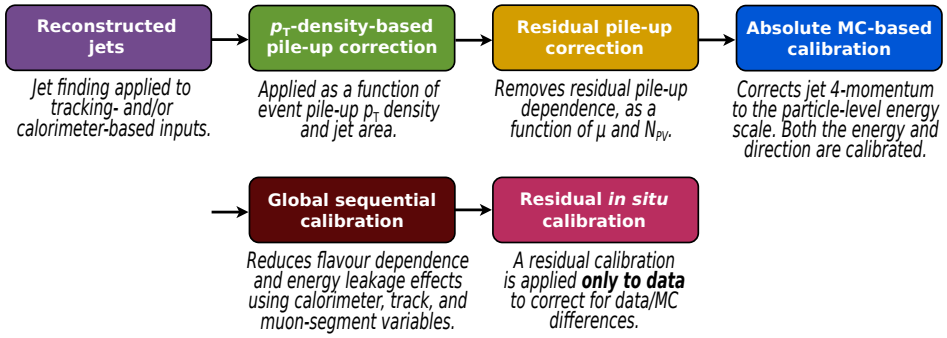

Figure 6.2: Calibration stages of the jet energy scale. Corrections are applied to the four-momenta of the jets [167].

a residual correction is derived as a function of the mean number of interactions per bunch crossing, μ, and of the number of primary vertices in an event, N_{PV}.

In the following step, the absolute jet energy and pseudorapidity calibrations correct the four-momenta of reconstructed jets to agree in energy and direction with matched truth jets from dijet MC, compensating for energy losses in passive material and mis-measurements. The correction is derived from the jet energy response defined as the energy ratio of reconstructed and truth jets. Different energy responses related to transitions in the calorimeter geometry and technology cause a bias in the jet η reconstruction, which is reduced by an additional correction.

After the energy calibration, residual dependencies of the jet energy on the shower shape and constituent particles of the jet remain, and are corrected for by the global sequential calibration (GSC). The GSC consists of several independent correction steps, each reducing the dependency on an observable, which stems from a set of tracking and calorimeter information. The GSC also accounts for the punch-through effect, describing jets not fully contained in the calorimeter causing activity in the muon chamber behind the jet.

In the final step of the JES calibration, an in-situ jet calibration is applied to data to correct for the remaining differences between data and simulation caused by imperfect modelling of the involved physics processes and the detector. The calibration relies on the transverse momentum balance between a jet and a well-measured reference object, and is subdivided into three consecutive stages. First, the η intercalibration corrects the energy scale of forward jets within $|\eta| > 0.8$ to that of well-calibrated jets in the central $|\eta| < 0.8$ region using dijets events. Afterwards, jets with p_{T} up to 1.2 TeV are calibrated with $Z \to \ell\ell/\gamma$+jet events. Jets with larger transverse momentum are calibrated using the multi-jet balance method, which measures the recoil of a single high-p_{T} jet against a system of softer jets calibrated in the previous step. In order to use well-defined jet masses in the analysis, a jet mass scale (JMS) calibration is applied analogously to the absolute JES calibration but makes use of the jet mass response instead of energy.

In order to separate jets originating from the hard-scatter interaction from pile-up jets, a technique called jet vertex tagging (JVT) [169] is employed. The JVT procedure builds a multivariate discriminant combining track information and their association to the primary vertex and contribution to the calibrated jet p_{T}. The JVT score ranges from zero for pile-up like jets up to one for hard-scatter like jets, and can be used to suppress pile-up jets. Efficiencies of JVT are measured in $Z(\rightarrow \mu\mu)$+jets events with the tag-and-probe method. Differences of the efficiencies between data and MC are compensated by scale factors.
Jets in the analysis are required to have $p_{\mathrm{T}} > 25\,\mathrm{GeV}$ and fall within the region $|\eta| < 2.5$. Furthermore, JVT > 0.5 is required for jets within $|\eta| < 2.4$ and $p_{\mathrm{T}} < 60\,\mathrm{GeV}$ to suppress pile-up jets. In the analysis, these small-R jets are used as input for a technique called jet reclustering in order to reconstruct massive particles decaying into several collimated jets. Large-R jets are constructed from the selected small-R jets using the anti-k_t algorithm with $R = 1.0$. The impact of soft radiation is reduced by removing constituent small-R jets with p_{T} less than 5 % of the large-R jet p_{T}. The reclustered large-R jets are required to a have a mass larger than 50 GeV and $p_{\mathrm{T}} > 150\,\mathrm{GeV}$.

6.5 Flavour tagging

Hadrons containing b-quarks produced in high energy pp collisions have a relatively long lifetime of the order of $\tau \sim 1.5\,\mathrm{ps}$. Therefore, they can traverse several millimetres from the interaction point before they decay in the detector, resulting in a secondary vertex. This is illustrated in Figure 6.3. The identification of b-hadrons is performed by various b-tagging algorithms [170, 171] in a two-stage approach. First, low-level algorithms reconstruct the characteristic properties of b-jets on the basis of tracks from charged particles matched to a jet, and reconstructed displaced vertices. Afterwards, their results are combined by multivariate classifiers into a single discriminant for an improved b-tagging performance.

One class of low-level algorithms are IP2D and IP3D that rely on the impact parameter significances of tracks matched to jets. Likelihood-ratio based discriminants are used in these algorithms to distinguish between b-, c-, and light-flavour jets. Both algorithms assume that the properties of each track in a jet are independent of all other tracks. However, in b-hadron decays several charged particles can be produced, resulting in multiple tracks. In order to account for correlations between tracks, the RNNIP tagger is employed using a recurrent neural network (RNN) trained on track impact parameters as well as kinematic and angular information.
Another class of low-level taggers attempts to reconstruct secondary vertices. The secondary vertex finding algorithm, SV1, reconstructs a single displaced secondary vertex in a jet, starting from the set of all two-track vertices which are iteratively removed until a single vertex remains. Apart from the existence of a secondary vertex within a jet, the algorithm provides additional discriminating information like the number of tracks associated with the

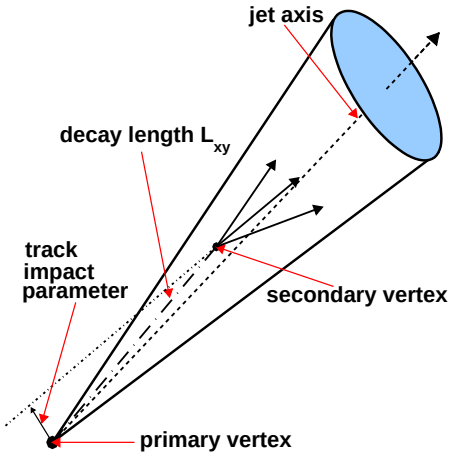

Figure 6.3: Schematic view of a b-hadron decay inside a jet. The most relevant variables for the b-tagging are indicated [172].

secondary vertex, their invariant mass, and the decay length corresponding to the distance between primary and secondary vertex.
JetFitter is a multi-vertex algorithm that tries to reconstruct the full b-hadron decay chain by exploiting the decay structure of weak b- and c-hadron decays. It is based on the assumption that the decay vertices lie on single line determined by the flight direction of the b-hadron, which allows for the reconstruction of vertices with a single associated track. Apart from discriminating variables for b-tagging, the algorithm provides a set of dedicated charm tagging variables.
High-level taggers combine the inputs obtained from the low-level algorithms using multivariate classifiers. For the DL1r tagger, a deep feed-forward neural network (DNN) is trained on simulated $t\bar{t}$ and Z' events to discriminate b-jets from c-jets and light-flavour jets. It includes information from all explained low-level algorithms and also considers the jet p_{T} and η to take advantage of the correlations to other inputs. The DNN has a multidimensional output corresponding to the probabilities for a jet to be a b-jet (p_b), c-jet (p_c) or light-flavour jet (p_{light}). These are combined into the final DL1r discriminant defined as

$$D_{\mathrm{DL1r}} = \ln\left(\frac{p_b}{f_c p_c + (1 - f_c) p_{\mathrm{light}}}\right), \tag{6.3}$$

where $f_c = 0.018$ is the effective c-jet fraction in the background training sample.
The performance of the b-tagging algorithm is given by the efficiency to correctly identify a jet originating from a b-hadron and corresponding c-jet, τ-jet, and light-flavour jet rejection rates. In this analysis, the 77 % b-tagging efficiency working point of the DL1r algorithm is used, being equivalent to a requirement on the final discriminant of $D_{\mathrm{DL1r}} > 2.195$. The

efficiencies of the working point are measured separately for simulation and data. In order to correct for differences coming from mis-modelling of the input variables, scale factors are derived in various jet p_{T} bins.

6.6 Missing transverse momentum

Momentum conservation in the transverse plane to the beam axis implies that the momenta of all final state particles in an event should ideally sum up to zero given that the colliding bunches have approximately zero transverse momentum. Neutral, weakly-interacting particles, like neutrinos in the SM or various particles predicted in BSM models, cannot be directly measured with the ATLAS detector. This causes a momentum imbalance in the transverse plane, referred to as missing transverse momentum [173, 174] with its magnitude

$$E_{\mathrm{T}}^{\mathrm{miss}} = \sqrt{(E_x^{\mathrm{miss}})^2 + \left(E_y^{\mathrm{miss}}\right)^2}. \tag{6.4}$$

The missing transverse momentum vector $\vec{E}_{\mathrm{T}}^{\mathrm{miss}}$ is given by

$$E_{\mathrm{T},x(y)}^{\mathrm{miss}} = E_{x(y)}^{\mathrm{miss},e} + E_{x(y)}^{\mathrm{miss,jets}} + E_{x(y)}^{\mathrm{miss},\mu} + E_{x(y)}^{\mathrm{miss,soft}}, \tag{6.5}$$

where each term is calculated as the negative sum of transverse momenta of the respective calibrated objects introduced in previous sections. The track-based soft term is computed from the tracks associated with the primary hard-scatter vertex but not to any calibrated object. Compared to a soft term built from energy deposits in the calorimeter, the track-based soft term does not include the signal from neutral particles, but is still superior due to its robustness against pile-up effects.

Electrons and muons fulfilling the respective baseline object selection requirements introduced above are input for the $E_{\mathrm{T}}^{\mathrm{miss}}$ calculation. The jet selection is specified by the $E_{\mathrm{T}}^{\mathrm{miss}}$ working point. In this analysis, the *Tight* $E_{\mathrm{T}}^{\mathrm{miss}}$ working point selects all jets with $p_{\mathrm{T}} > 20\,\mathrm{GeV}$ that have to pass JVT > 0.5 if the jet has $|\eta| < 2.4$ and $p_{\mathrm{T}} < 60\,\mathrm{GeV}$, without including forward jets with $|\eta| > 2.4$ and $20\,\mathrm{GeV} < p_{\mathrm{T}} < 30\,\mathrm{GeV}$. A special overlap removal procedure is carried out in the $E_{\mathrm{T}}^{\mathrm{miss}}$ calculation to resolve for ambiguities in detector signals, which is explained in detail in Ref. [174]. A perfectly reconstructed $E_{\mathrm{T}}^{\mathrm{miss}}$ would correspond to the magnitude of the vector sum of transverse momenta of the invisible particles in an event. However, as $E_{\mathrm{T}}^{\mathrm{miss}}$ is based on many different objects reconstructed in all parts of the detector, and thus mismeasurements, miscalibrations, and particles going trough uncovered parts of the detector have a direct impact on its calculation. In addition, contributions from pile-up interactions entering the $E_{\mathrm{T}}^{\mathrm{miss}}$ reconstruction affect the true $E_{\mathrm{T}}^{\mathrm{miss}}$ from the interaction of interest.

6.7 Overlap removal

Many objects are reconstructed from energy deposits in the calorimeters or tracks in the ID. Therefore, overlap between object candidates is possible. In order to resolve this overlap, an algorithm is used to define how the objects are treated. The jets and baseline leptons are input for the overlap removal. Only objects passing this step are used in the further analysis. The overlap between objects is defined by their angular distance measured in units of $\Delta R_y = \sqrt{(\Delta y)^2 + (\Delta\phi)^2}$ with the rapidity y instead of the pseudorapidity η.
The procedure is as follows:

- Muon/Electron: If an electron and a muon share an ID track, the muon is discarded if it is a CT muon, otherwise the electron is rejected.
- Jet/Electron: If a jet overlaps with an electron within $\Delta R_y = 0.2$, the jet is removed and the object interpreted as an electron. Then, electrons are rejected if they are within $\Delta R_y = 0.4$ of a remaining jet.
- Jet/Muon: Any jet with less than three associated tracks is removed if a muon is within $\Delta R_y = 0.2$ of the jet or if a muon track can be matched to a track associated with the jet. Then, any muon found within $\Delta R_y = \min(0.4, 0.04 + 10\,\text{GeV}/p_{\text{T}}^{\mu})$ to a remaining jet is removed.

7 Search for vector-like top and bottom partners

In Section 2, VLQs have been introduced as the simplest extension of the SM quark sector that is not already excluded by the discovery of the Higgs boson and the measurements of its properties. Various types of VLQs, differing for example in their electric charges and the allowed decay modes, are predicted in BSM theories.

In this search, the focus is laid on pair-produced vector-like partners of the top and bottom quarks, assuming only decays into a boson and a quark of the third generation as motivated in Section 2.1. Even after this restriction, a large number of final states is possible for pair-produced VLQs. In the ATLAS VLQ search programme, various final states are covered by different analyses. The presented search selects events with one isolated lepton, jets, and high missing transverse momentum in the final state. This final state is chosen to target the case $T\bar{T} \to Zt + X$, with a leptonic decay of the top quark and an invisible decay of the Z boson into two neutrinos. Here, the X denotes one of three possible decay modes of the vector-like top quark. One b-tagged jet is expected from the top-quark decay. Further jets originate from hadronic decays of the second boson and quark. The same final state is also sensitive to $B\bar{B} \to Wt + X$, and especially the case where X corresponds to Wt.

The basis for this search are the data recorded by the ATLAS experiment during the LHC Run 2 and simulated MC events, introduced in Section 7.1. Based on the aforementioned general characteristics of the events of interest, a first event selection is defined in Section 7.2. Characteristic properties of the signal are exploited, and variables allowing to distinguish between the VLQ signal and the SM background processes are introduced. In addition, data and MC are compared after this preselection. Afterwards, in Section 7.3, a dedicated kinematic reweighting for the $t\bar{t}$ and single top-quark processes is derived in order to compensate for modelling issues at high transverse momenta of the top quarks.

NNs are found in Ref. [175] to be a powerful tool to distinguish between signal and background events in the investigated channel. Thus, after correcting the $t\bar{t}$ and single top-quark background processes with the help of the reweighting, artificial NNs are trained for various signal hypotheses in a dedicated training region that is designed to contain a large fraction of the signal. The NN architecture and the training procedure are explained in Section 7.4. The NN output distribution is split into a signal-enriched part, called signal region (SR), and a background-enriched control region (CR), where the $t\bar{t}$ process has the highest contributions. Two additional CRs for the W+jets and single top-quark background processes are defined in

Section 7.5. These CRs are used to constrain the background normalisation in the statistical evaluation and to validate the NNs. Apart from the nominal distributions and their related statistical uncertainties, systematic uncertainties reflecting the modelling of the background processes and the uncertainties in the object reconstruction and calibration are considered in the analysis. The different sources of systematic uncertainties are explained in Section 7.6. The SRs and CRs are used in the statistical evaluation of the analysis, which is discussed in Section 7.7. The profile likelihood fit and the limit setting procedure are explained before the results obtained from the profile likelihood fit and the exclusion limits on the signal cross-section and masses are presented in Section 7.8. Finally, the obtained results are compared to existing VLQ searches, and an outlook for further improvements is given.

7.1 Data and simulated samples

This search uses LHC pp collision data recorded with the ATLAS detector from 2015 to 2018 at a centre-of-mass energy of $\sqrt{s} = 13\,\text{TeV}$. The data set, collected during stable beam conditions and with all detector subsystems operational [176], corresponds to an integrated luminosity of $139\,\text{fb}^{-1}$. Events were selected online during data-taking by the $E_{\text{T}}^{\text{miss}}$ triggers listed in Section 5.2.5.
MC simulated events are used for the modelling of the background processes and the VLQ signals. As discussed in Section 3.7, various MC generators exist for the simulation of the ME, the PS, and the decays. In the following, the generator setups for the physics processes considered in this analysis are described. An overview about the simulated samples, including the ME generator and the PDF set, the PS and hadronisation model with the set of tuned parameters (tune), can be found in Table 7.1.

Table 7.1: List of ME generator, PDF set, PS, and tune for the background processes and VLQ signal.

Process	ME generator	PDF set	PS and hadronisation	Tune
$t\bar{t}$/single top	Powheg-Box v2	NNPDF3.0nlo	Pythia 8.230/8.235	A14
V+jets	Sherpa 2.2.1	NNPDF3.0nnlo	Sherpa	internal
Diboson	Sherpa 2.2.1-2.2.2	NNPDF3.0nnlo	Sherpa	internal
$t\bar{t}V$	MG5_aMC@NLO 2.3.3	NNPDF3.0nlo	Pythia 8.210	A14
$tWZ(\to \nu\nu)$	MG5_aMC@NLO 2.6.7	NNPDF3.0nlo	Pythia 8.244	A14
$t\bar{t}H$	Powheg-Box v2	NNPDF3.0nlo	Pythia 8.230	A14
VLQ signal	Protos v2.2	NNPDF2.3lo	Pythia 8.186	A14

The production of $t\bar{t}$ events was modelled using the Powheg-Box v2 generator at NLO with the NNPDF3.0nlo set of PDFs and the h_{damp} parameter, which controls the matching of the Powheg ME to the PS and effectively regulates the high-p_{T} radiation, set to $1.5\,m_{\text{top}}$ [177], with $m_{\text{top}} = 172.5\,\text{GeV}$. The renormalisation and factorisation scales were set dynamically on an event-by-event basis to $\sqrt{m_{\text{top}}^2 + p_{\text{T}}^2(t)}$, with $p_{\text{T}}(t)$ being the transverse momentum of

the top quark. The events were interfaced to Pythia 8.230 to model the PS, hadronisation, and UE. The cross-section was corrected to the theory prediction at NNLO+NNLL in QCD calculated using Top++ 2.0.

Samples for single top-quark production were produced with the Powheg-Box v2 generator at NLO in QCD using the NNPDF3.0nlo set of PDFs with the five-flavour scheme for tW production and s-channel single top-quark production, and the four-flavour scheme for t-channel single top-quark events. The DR scheme [178] is applied on the tW sample to remove interference and overlap with $t\bar{t}$ production, and the renormalisation and factorisation scales were set to m_{top}. The events were interfaced with either Pythia 8.230/8.235. The samples were normalised to their NLO QCD cross-sections [179, 180] for the t-channel and s-channel, with additional NNLL soft-gluon terms for the tW-channel [181, 182].

The production of $t\bar{t}V$ events was modelled using the MG5_aMC@NLO 2.3.3 generator, interfaced to Pythia 8.210. Similarly, the production of tWZ events was modelled using MG5_aMC@NLO 2.6.8 at NLO, interfaced to Pythia 8.244. The DR scheme was employed to handle the interference between tWZ and $t\bar{t}Z$, and was applied to the tWZ sample. The production of a top-quark pair in association with a Higgs boson ($t\bar{t}H$) was modelled by the Powheg-Box v2 generator, interfaced to Pythia 8.230. These processes containing top quarks and vector bosons or a Higgs boson were generated at NLO in QCD using the NNPDF3.0nlo PDF set and normalised to their NLO cross-section predictions.

The production of V+jets was simulated with the Sherpa 2.2.1 generator using NLO-accurate matrix elements for up to two partons, and LO-accurate matrix elements for up to four partons calculated with the Comix [183] and OpenLoops [184–186] libraries. Similarly, diboson (VV) events were generated, depending on the process, with Sherpa 2.2.1 or 2.2.2, using matrix elements at NLO accuracy in QCD for up to one additional parton and at LO accuracy for up to three additional partons. For V+jets and diboson samples, the NNPDF3.0nnlo set of PDFs was used and the generated hard-scattering events were matched with the Sherpa PS using the MEPS@NLO prescription and the set of tuned parameters developed by the Sherpa authors. While V+jets samples were normalised to an NNLO prediction [187], the diboson samples were normalised to the total cross-section provided by Sherpa at NLO in QCD.

Signal samples for pair production of T and B quarks were generated at LO with Protos v2.2, interfaced with Pythia 8.186 for the parton shower and hadronisation. The samples were produced for masses from 800 GeV up to 2 TeV, with a mass spacing of 100 GeV from 1 TeV to 1.8 TeV, assuming couplings of the VLQs according to the weak-isospin singlet model, but with equal branching ratios into the three decay modes (Zt, Ht, Wb). In order to obtain the desired branching ratios, an event-by-event reweighting based on generator information is performed. For each VLQ event the additional event weight is calculated by

$$w(a,b) = \frac{\mathcal{B}(Q \to a) \cdot \mathcal{B}(\bar{Q} \to b)}{1/3 \cdot 1/3}, \tag{7.1}$$

where $\mathcal{B}(Q \to a)$ and $\mathcal{B}(\bar{Q} \to b)$ are the desired branching ratios for a VLQ decay into a and b, with a and b symbolising one of the three VLQ decay modes and Q is either a T or B quark. For example, when reweighting for the $\mathcal{B}(T \to Zt) = 100\,\%$ scenario, events where both T quarks decay via the desired decay mode are multiplied by a weight factor of nine and all other events by a factor zero.
Additional samples, assuming couplings according to the weak-isospin doublet model are produced at 1.2 TeV in order to evaluate the dependence of the analysis on the weak-isospin of the VLQ. The signal cross-sections were calculated with Top++ 2.0 at NNLO+NNLL in QCD.

For all nominal samples showered with Pythia 8, using the A14 set of tuned parameters [188] and the NNPDF2.3lo [189] set, the EvtGen program was used to model the decays of heavy-flavour hadrons.
All nominal samples were processed with the full simulation of the ATLAS detector, while some samples used to estimate systematic uncertainties were processed with the faster detector simulation. In order to incorporate pile-up effects, minimum-bias interactions were generated with Pythia 8.186 using the A3 [190] set of tuned parameters and overlaid onto the simulated hard-scatter events. The resulting events were weighted to match the pile-up profile of the recorded data. Finally, the simulated events were reconstructed using the same software as the collision data. Corrections were applied to the simulated events in order to match the object identification efficiencies, energy scales and resolution to those determined from data in auxiliary measurements.

7.2 Basic event selection

Based on the targeted event topology, a first event selection is defined for checks of the data–MC modelling, the identification of relevant SM background processes, and the investigation of signal and background properties. Furthermore, this selection serves as a basis for all subsequent steps for which additional requirements on event properties are imposed. The requirements of the preselection are summarised in Table 7.2.
First, all events have to pass the $E_{\mathrm{T}}^{\mathrm{miss}}$ triggers listed in Section 5.2.5. Furthermore, a set of data quality requirements is imposed. Only events in which all subdetectors were fully operational are further considered. Events are removed when noise bursts in the calorimeters occurred. In each event, at least one primary vertex is required, and events are rejected if it contains a poorly measured muon or a jet that does not pass the loose jet cleaning criteria.
Events are required to have exactly one signal electron or muon satisfying the object requirements in Section 6. In order to suppress contributions from dileptonic background processes, events with an additional baseline lepton are vetoed. In addition, at least four small-R jets, of which at least one is b-tagged, are required. Furthermore, the azimuthal angle between the direction of the missing transverse momentum and the leading (j_1) and

Table 7.2: General event preselection.

Preselection
$E_{\mathrm{T}}^{\mathrm{miss}}$ triggers
Event cleaning
$= 1$ signal lepton (e or μ)
no additional baseline lepton
≥ 4 jets
≥ 1 b-jet
$E_{\mathrm{T}}^{\mathrm{miss}} > 250\,\mathrm{GeV}$
$m_{\mathrm{T}}^{W} > 30\,\mathrm{GeV}$
$\lvert\Delta\phi(j_{1,2}, \vec{E}_{\mathrm{T}}^{\mathrm{miss}})\rvert > 0.4$

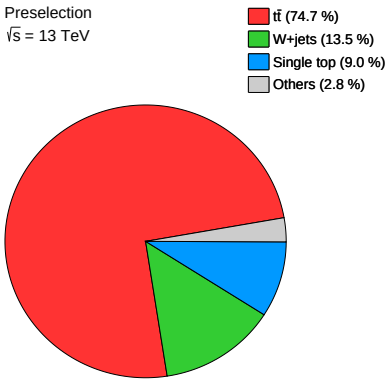

Figure 7.1: Relative contributions of the individual SM processes after the preselection.

subleading (j_2) small-R jet, ordered in p_{T}, has to fulfil the condition $|\Delta\phi(j_{1,2}, \vec{E}_{\mathrm{T}}^{\mathrm{miss}})| > 0.4$. This requirement rejects events with $E_{\mathrm{T}}^{\mathrm{miss}}$ from mismeasured jets. In order to further reduce the QCD multijet background, the transverse mass, m_{T}^{W}, that is introduced in the next section, has to fulfil the requirement $m_{\mathrm{T}}^{W} > 30\,\mathrm{GeV}$. Due to the expectation of large $E_{\mathrm{T}}^{\mathrm{miss}}$ in signal events, $E_{\mathrm{T}}^{\mathrm{miss}} > 250\,\mathrm{GeV}$ is required, at which level the $E_{\mathrm{T}}^{\mathrm{miss}}$ triggers are fully efficient. A dedicated study has been performed to check the impact of the $E_{\mathrm{T}}^{\mathrm{miss}}$ trigger choice compared to single-lepton triggers. The $E_{\mathrm{T}}^{\mathrm{miss}}$ triggers cover inefficiencies of the single muon trigger. The benefit of using both $E_{\mathrm{T}}^{\mathrm{miss}}$ and single-lepton triggers is negligible.

As shown in Figure 7.1, the largest background contribution after applying the preselection criteria originates from the $t\bar{t}$ process with about 74.7 %. For the $t\bar{t}$ background, 77 % of the events are classified as lepton+jets events based on generator information and the remaining 23 % as dilepton events. In order to pass the preselection, additional jets from QCD radiation are required for dileptonic $t\bar{t}$ events. In case of a hadronically decaying τ lepton, which is reconstructed as a jet, one additional jet from radiation is required, while for other dileptonic $t\bar{t}$ events at least two additional jets must occur. Further important background processes are W+jets and single top-quark production with contributions of 13.5 % and 9 %, respectively. For the single top-quark background, the single top-quark production in association with a W boson (tW-channel) is dominating with a fraction of about 86 %. Smaller contributions to the SM background after the preselection originate from diboson (1.3 %) and $t\bar{t}V$ (1.1 %) events. The fraction of the minor background processes $t\bar{t}H$, tWZ, and Z+jets is about 0.4 %. They are summarised in the category "Others". Contributions from other rare top-quark background processes such as the production of three or four top-quarks are found to be negligible. Contributions from all-hadronic $t\bar{t}$ events are studied in order to evaluate the impact of fake backgrounds and are found to be negligible.

7.2.1 Properties of signal and background

In this section, the properties of VLQ signal events are studied after the preselection in order to find discriminating variables between the signal and the SM background processes. For simplicity, the background distributions of two major backgrounds, $t\bar{t}$ and W+jets, are compared only to one VLT signal scenario ($m_T = 1.2\,\text{TeV}$, $\mathcal{B}(T \to Zt) = 100\,\%$). Afterwards, the distributions of vector-like top and bottom quarks are compared for various decay scenarios. In addition, the effect of the assumed VLQ couplings on the kinematic distribution is studied by comparing samples produced according to the singlet and the doublet models.

Discriminating variables

The preselection requires a large missing transverse momentum of at least 250 GeV because the signal events are expected to have additional sources of $E_{\text{T}}^{\text{miss}}$ compared to a $t\bar{t}$ event. Figure 7.2a shows the $E_{\text{T}}^{\text{miss}}$ distribution after the preselection for the $t\bar{t}$ and W+jets background processes, and a VLT signal with a mass of 1.2 TeV and exclusive $T \to Zt$ decays. While the two background processes peak at the minimum required $E_{\text{T}}^{\text{miss}}$, the signal process exhibits a flat distribution and tends to have a higher fraction of events at large values of $E_{\text{T}}^{\text{miss}}$ compared to the background. The flat distribution can be explained by the required decay of the VLTs into top quarks and Z bosons, as a Z boson decays invisibly, i.e. $Z \to \nu\bar{\nu}$, with a branching ratio of 20 % resulting in large values of $E_{\text{T}}^{\text{miss}}$.
As mentioned before, the major fraction of $t\bar{t}$ events after the preselection is classified as lepton+jets events, as the lepton and jet requirements of the preselection exactly match the characteristics of a semi-leptonic $t\bar{t}$ decay. A kinematic variable that targets the leptonic decay of the W boson is the transverse mass, m_{T}^{W}, which is calculated based on lepton and $E_{\text{T}}^{\text{miss}}$ information as

$$m_{\text{T}}^{W} = \sqrt{2p_{\text{T}}^{\ell} E_{\text{T}}^{\text{miss}} (1 - \cos\Delta\phi(\ell, \vec{E}_{\text{T}}^{\text{miss}}))}. \tag{7.2}$$

Here, p_{T}^{ℓ} is the transverse momentum of the lepton and $\Delta\phi(\ell, \vec{E}_{\text{T}}^{\text{miss}})$ the angle between the lepton momentum and $E_{\text{T}}^{\text{miss}}$ in the transverse plane. Apart from resolution effects, m_{T}^{W} is bound from above by the W boson mass in events where the lepton and the $E_{\text{T}}^{\text{miss}}$ only originate from a leptonic W boson decay. Processes with additional sources of $E_{\text{T}}^{\text{miss}}$, like the VLQ signal, can exceed this boundary. The m_{T}^{W} distribution after the preselection is shown in Figure 7.2b. As expected, a high fraction of the signal events exceed this W boson mass threshold, while for a large fraction of $t\bar{t}$ and W+jets events m_{T}^{W} is below the W boson mass.
A generalisation of the transverse mass is the m_{T2} variable [191, 192], targeting decay topologies from pair production with two branches, referred to here as a and b, both with measured particles and invisible particles. Invisible particles are not solely weakly interacting particles traversing the detector without depositing energy but can also be particles that are not identified by the detector. The transverse mass m_{T} of the particles in branch i, $i \in \{a, b\}$, is

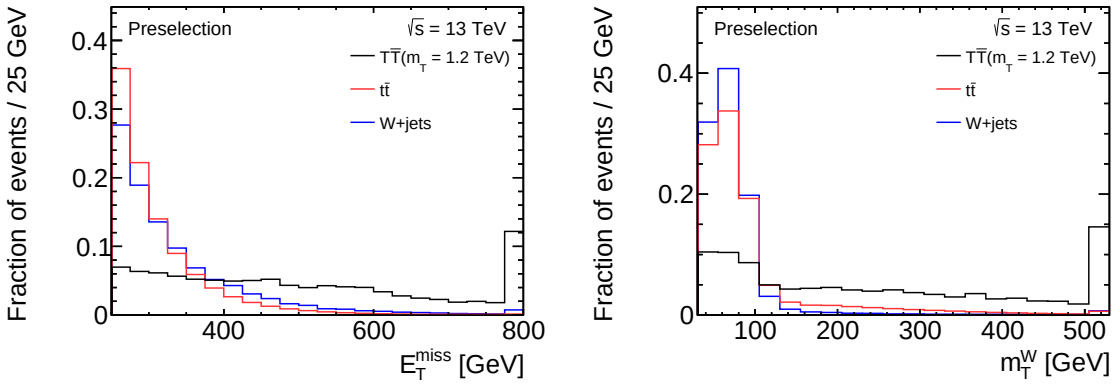

Figure 7.2: Comparison of (a) $E_{\mathrm{T}}^{\mathrm{miss}}$ and (b) m_{T}^{W} distributions after the preselection for the dominant background processes $t\bar{t}$ and W+jets, and a VLT signal ($m_T = 1.2\,\mathrm{TeV}$, $\mathcal{B}(T \to Zt) = 100\,\%$). The last bin in each distribution contains the overflow.

given by

$$m_{\mathrm{T},i}^2 = \left(\sqrt{p_{\mathrm{T},i}^2 + m_{p_i}^2} + \sqrt{q_{\mathrm{T},i}^2 + m_{q_i}^2}\right)^2 - (\vec{p}_{\mathrm{T},i} + \vec{q}_{\mathrm{T},i})^2\,, \tag{7.3}$$

where p denotes the sum of visible particle momenta and q the sum of unmeasured momenta in each branch.

The m_{T2} variable is defined by the minimisation over all combinations of missing transverse momenta $\vec{q}_{\mathrm{T},a}$ and $\vec{q}_{\mathrm{T},b}$, with $\vec{q}_{\mathrm{T},a} + \vec{q}_{\mathrm{T},b} = \vec{E}_{\mathrm{T}}^{\mathrm{miss}}$, of the maximum of the corresponding transverse masses $m_{\mathrm{T},a}$ and $m_{\mathrm{T},b}$:

$$m_{\mathrm{T2}} = \min_{\vec{q}_{\mathrm{T},a}+\vec{q}_{\mathrm{T},b}=\vec{E}_{\mathrm{T}}^{\mathrm{miss}}} \left[\max(m_{\mathrm{T},a}, m_{\mathrm{T},b})\right]. \tag{7.4}$$

The unmeasured particles and their assumed masses m_{q_a} and m_{q_b} define the specific variants of the m_{T2} variable.

In this analysis, the asymmetric transverse mass, am_{T2} [194, 195], is used in which the undetected particles are a W boson and a neutrino. This variable is designed to suppress dileptonic $t\bar{t}$ background with one undetected charged lepton. The situation is illustrated in Figure 7.3. One branch contains the detected charged lepton, a b-jet, and a neutrino, and the other a second b-jet and the undetected W boson. Therefore, the assumed masses for the undetected particles are $m_{q_a} = 80\,\mathrm{GeV}$ and $m_{q_b} = 0\,\mathrm{GeV}$. As only at least one b-tagged jet is required in the preselection, the two jets with the highest b-tagging score are considered in the am_{T2} calculation. Since the assignment of the b-jets to the lepton is ambiguous, both combinations are calculated, and the minimum is taken as the final variable. For dileptonic $t\bar{t}$ events, fulfilling the assumptions in the am_{T2} reconstruction, am_{T2} is bound from above by the top-quark mass as shown in Figure 7.3b. Other processes like W+jets or the considered

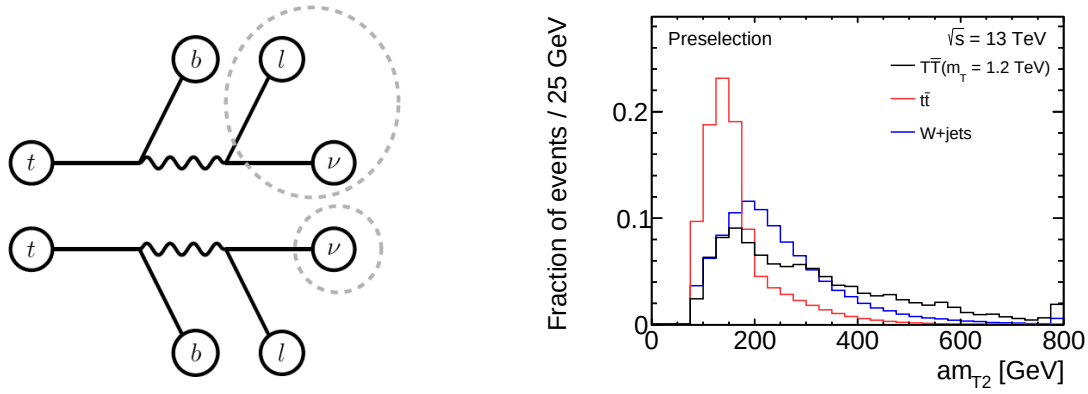

(a) **(b)**

Figure 7.3: (a) Illustration of the construction of the am_{T2} variable, which is used to discriminate against dileptonic $t\bar{t}$ background with an undetected lepton. The dashed lines symbolise that the corresponding particles are assumed to be undetected for the construction of the variable [193]. (b) Shape distributions of am_{T2} after the preselection for the $t\bar{t}$ and W+jets background processes, and a VLT signal ($m_T = 1.2\,\mathrm{TeV}$, $\mathcal{B}(T \to Zt) = 100\,\%$).

signal do not exhibit such a clear structure as a large fraction of their events exceed the top-quark mass boundary.

So far, variables mainly related to the lepton and missing transverse momentum have been discussed. However, jets can contain characteristic information of the underlying process as well. Distributions of the jet and b-jet multiplicities are shown in Figure 7.4. In general, signal events tend to have higher jet multiplicities, as the bosons originating from a VLQ decay can subsequently decay into jets. In the given example, two additional jets, compared to $t\bar{t}$ events, originate from the decay of a Z boson. For the b-jet multiplicity, two b-jets are expected for the $t\bar{t}$ process. However, the probability of identifying both b-jets is restricted by the efficiency of the b-tagging working point, which is chosen to be 77 % in this analysis. Most of the $t\bar{t}$ and signal events contain one or two b-tagged jets, while for the signal about 20 % of the events contain three or four b-jets. In these cases, the additional b-jets originate from a decay of a Z boson for which the branching ratio into two b-quarks is about 15 %. The W+jets background is already strongly reduced after the preselection requiring at least one b-jet. This requirement removes about 80 % of the W+jets events compared to a selection without any restriction on the b-jet multiplicity.

Another discriminating variable is the effective mass, m_{eff}, defined as the scalar sum of the transverse momenta of all calibrated objects in an event and $E_{\mathrm{T}}^{\mathrm{miss}}$. In this analysis m_{eff} is therefore defined by

$$m_{\mathrm{eff}} = p_{\mathrm{T}}(\ell) + \sum_{i}^{n_j} p_{\mathrm{T}}(j_i) + E_{\mathrm{T}}^{\mathrm{miss}}, \tag{7.5}$$

where the sum runs over the number of jets, n_j. The m_{eff} distribution is shown in Figure 7.5a

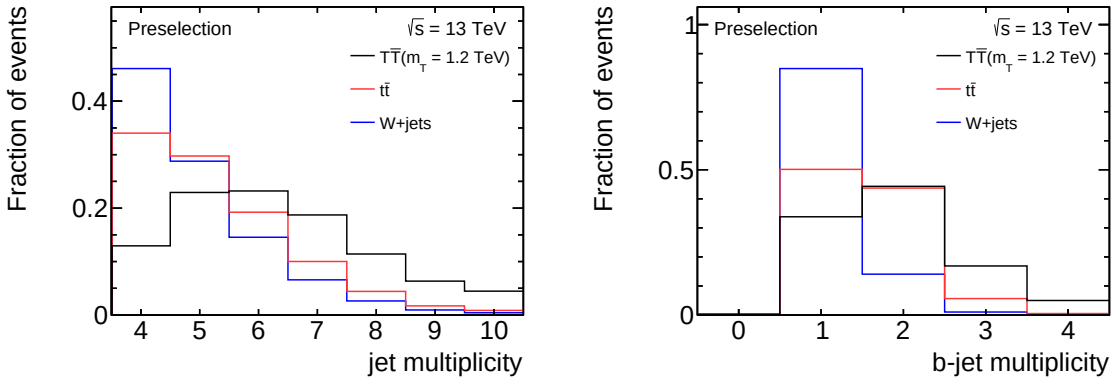

(a) (b)

Figure 7.4: Shape distributions of (a) the jet multiplicity and (b) the b-jet multiplicity after the preselection for $t\bar{t}$, W+jets, and a VLT signal ($m_T = 1.2\,\text{TeV}$, $\mathcal{B}(T \to Zt) = 100\,\%$).

and peaks slightly below $2 \cdot m_{\text{VLQ}}$ for the VLQ signal, while for the two selected background processes a peak at around 900 GeV is visible. Thus, m_{eff} is a powerful variable with increasing separation power for higher signal masses.

Due to the high mass of the VLQs ($\mathcal{O}(1\,\text{TeV})$), the decay products receive a large transverse momentum. As a consequence, jets from subsequent hadronic decays can be close to each other in the detector. In order to make use of this signal characteristic, jets with a large radius parameter of $R = 1.0$ are reconstructed from small-R jets following the procedure described in Section 6.4. The distribution of the large-R jet multiplicity is shown in Figure 7.5b and illustrates that the signal tends to have a higher large-R jet multiplicity than the background processes. For the given $T\bar{T} \to Zt Z\bar{t}$ signal, the hadronic decay of a Z boson can explain the additional large-R jets compared to the $t\bar{t}$ background.

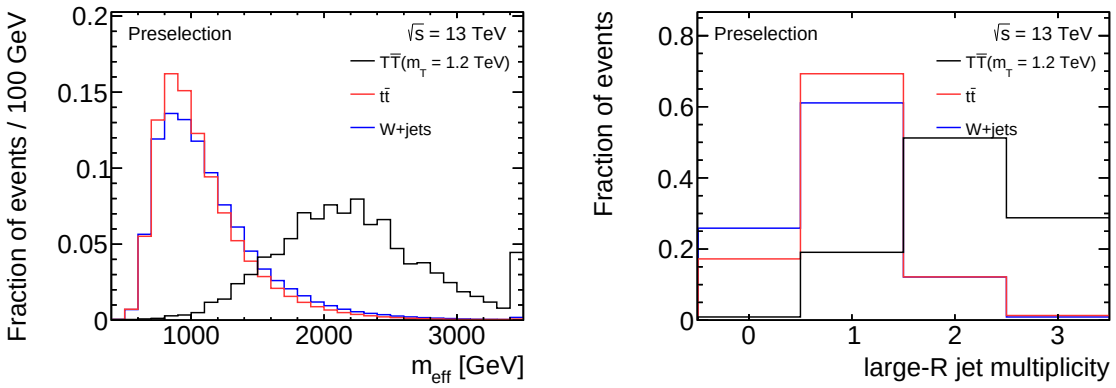

(a) (b)

Figure 7.5: Shape distributions of (a) the effective mass m_{eff} and (b) the number of reclustered large-R jets after the preselection for $t\bar{t}$, W+jets, and a VLT signal ($m_T = 1.2\,\text{TeV}$, $\mathcal{B}(T \to Zt) = 100\,\%$).

As the reclustered large-R jets can capture the decay products of hadronically decaying resonances like the Z bosons of the signal or W bosons from top-quark decays, their properties can represent characteristics of the resonance. The mass distributions of the leading and subleading large-R jet, sorted in p_{T}, are shown in Figures 7.6a and 7.6b, respectively. No peak structure is visible for the W+jets process, as the large-R jets do not capture any hadronic resonance. The mass distribution of the leading-p_{T} large-R jet for the $t\bar{t}$ process shows peaks around the W boson and top-quark masses. In very boosted events, the large-R jet can capture all decay products of the top quark, while in less boosted events, the large-R jet contains only the jets from the W boson decay. For the signal, peaks around the top quark and W/Z boson masses are visible in the mass distribution of the leading large-R jet. In the mass distribution of the subleading large-R jet no clear structure for the two background processes is visible, while the peaks in the signal distribution are characteristic for the existence of a second hadronic resonance.
Apart from the mass, the substructure of large-R jets might contain interesting information. The number of small-R jets that are used in the reclustering of the leading large-R jet is shown in Figure 7.6c. For the signal, the leading large-R jet consists of one small-R jet in about 40 % of the events, while for the background processes, on average, more small-R jets are captured by the large-R jet. This can be explained by the high mass of the VLQs, which leads to boosted decay products. Often this boost is strong enough that the resulting jets from subsequent hadronic decays overlap in the detector and cannot be separately resolved. In these cases, the large-R jet consists of a single small-R jet.

Signal scenarios

Only one specific signal scenario, the pair production of vector-like top quarks exclusively decaying into Z bosons and top quarks, has been discussed so far. In the following, the properties of the VLT signal with branching ratios according to the SU(2) singlet and doublet scenarios are studied as well as properties of the VLB signal. For the latter case, the SU(2) singlet scenario and the exclusive $B \to Wt$ decay, corresponding to the (T, B) doublet scenario, are discussed. For all cases, couplings according to the SU(2) singlet model are considered.
The aforementioned VLT signal scenarios are compared in the lepton p_{T}, $E_{\mathrm{T}}^{\mathrm{miss}}$, the jet and b-jet multiplicity distributions in Figure 7.7. While the lepton p_{T} distributions of the $\mathcal{B}(T \to Zt) = 100\,\%$ and SU(2) doublet scenarios have a similar shape, the leptons in the SU(2) singlet case exhibit a harder p_{T} spectrum. In the case of the SU(2) singlet, about 50 % of the T quarks decay into a W boson and a bottom quark, while this decay mode is absent for the two other considered scenarios. A lepton that originates from a W boson of the VLT decay is expected to have a harder p_{T} spectrum than a lepton from a top-quark decay. The assumption that the $Z \to \nu\bar{\nu}$ decay becomes an additional source of $E_{\mathrm{T}}^{\mathrm{miss}}$ is supported by the $E_{\mathrm{T}}^{\mathrm{miss}}$ distribution in Figure 7.7b. The distribution for the $\mathcal{B}(T \to Zt) = 100\,\%$ scenario shows a harder $E_{\mathrm{T}}^{\mathrm{miss}}$ spectrum than the other two decay scenarios. However, compared to the

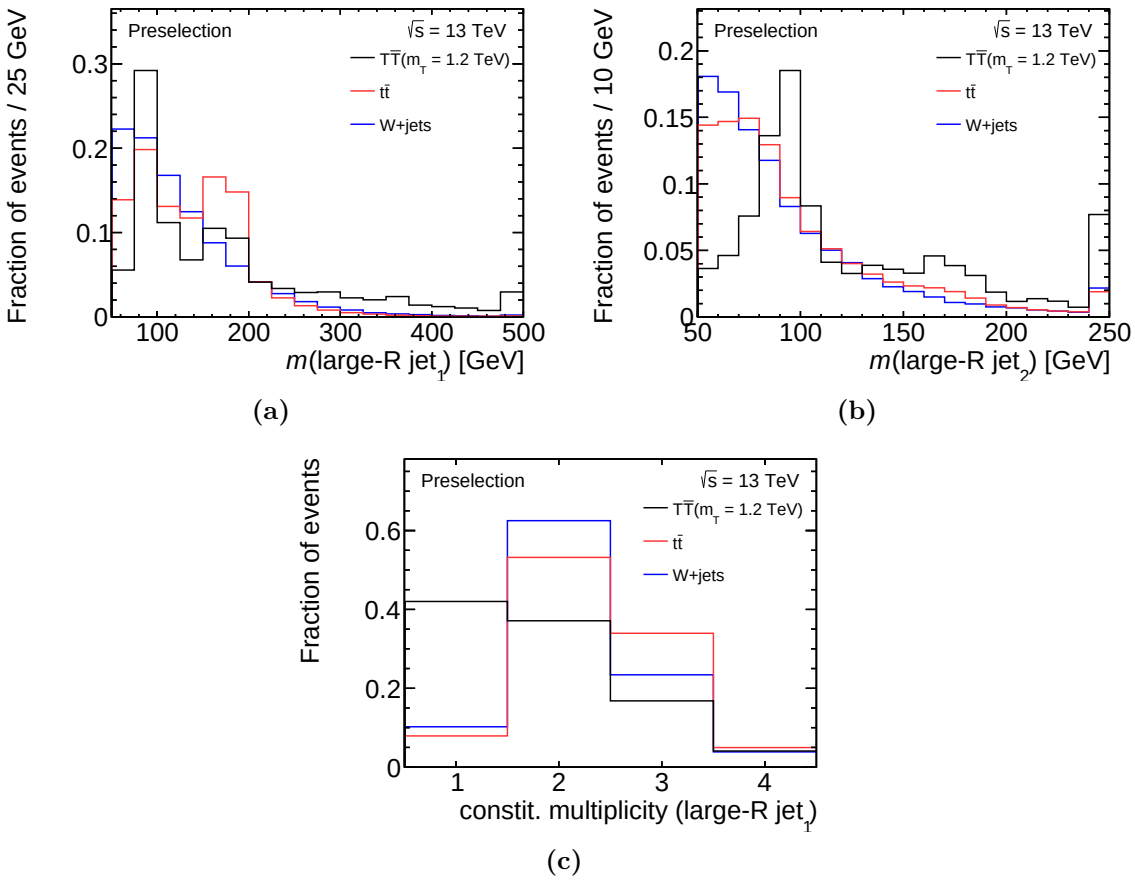

Figure 7.6: Distributions of (a) the leading and (b) the subleading large-R jet mass, ordered in p_{T}, after the preselection for the two main background processes, $t\bar{t}$ and W+jets, and a VLT signal with a mass of 1.2 TeV and exclusive $T \to Zt$ decays. In (c), the distribution of the number of small-R jets within the leading large-R jet is shown for the same processes.

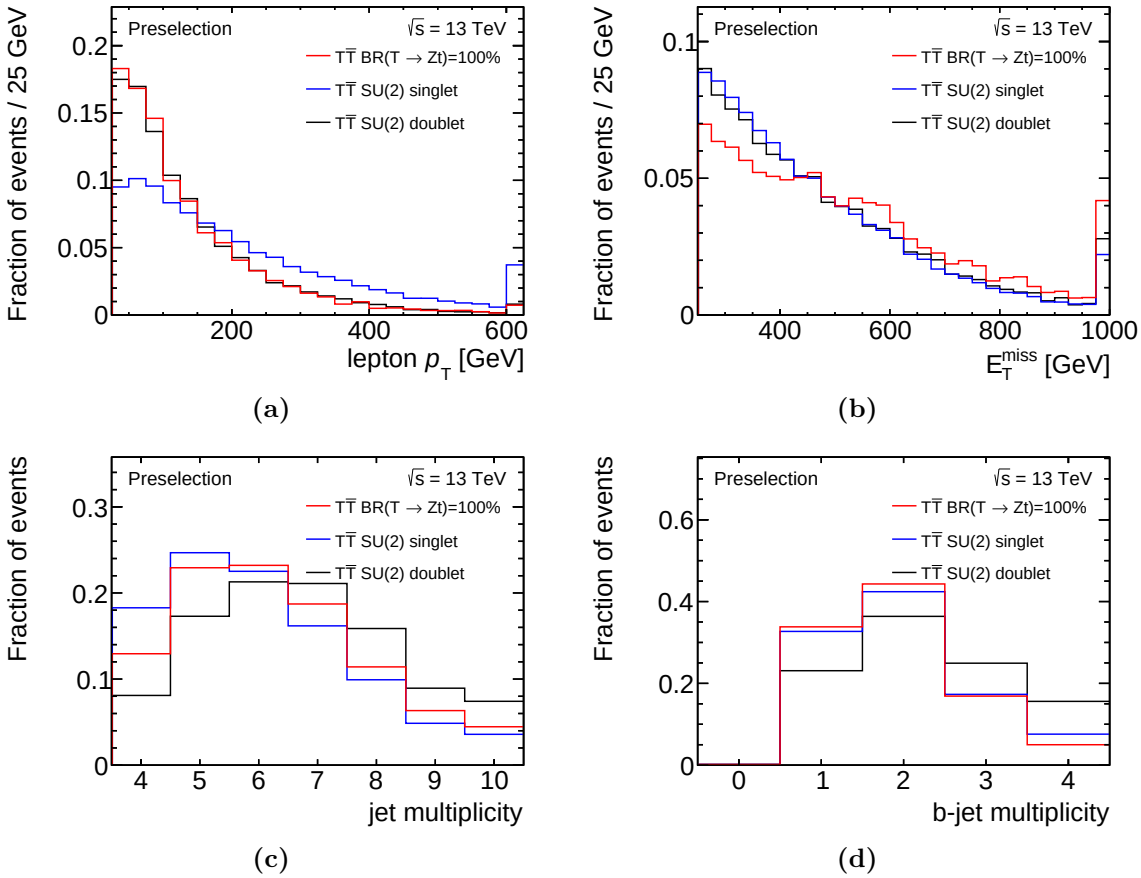

Figure 7.7: Comparison of various decay scenarios of the T quark in (a) the lepton p_{T}, (b) $E_{\mathrm{T}}^{\mathrm{miss}}$, (c) jet multiplicity, and (d) b-jet multiplicity distributions after the preselection for a signal mass of $m = 1.2\,\mathrm{TeV}$. The cases with exclusive $T \to Zt$ decays and decays according to the weak-isospin singlet and doublet models are compared.

discussed background distributions, the signals always tend to higher values of $E_{\mathrm{T}}^{\mathrm{miss}}$. Finally, the jet and b-jet distributions show that for a higher fraction of VLT decays via $T \to Ht$ in the doublet case, the events tend to exhibit a higher jet multiplicity, which can be explained by the high branching ratio of the Higgs boson into bottom quarks of about 58 %. The SU(2) singlet scenario tends to have a smaller jet multiplicity than the $\mathcal{B}(T \to Zt) = 100\,\%$ case, as less jets are expected from the Wb decay mode than from the Zt decay mode.

In a next step, the properties of vector-like bottom quarks are studied, focusing on a high fraction of $B \to Wt$ decays. Figure 7.8a compares the VLT signal with exclusive $T \to Zt$ decays to the VLB signal with decays according to the SU(2) singlet and (T, B) doublet models. The lepton p_{T} distribution exhibits a harder p_{T} spectrum for the VLB cases than for the considered VLT signal as a W boson cannot originate directly from a VLT decay in contrast to a VLB decay. On the other hand, the $E_{\mathrm{T}}^{\mathrm{miss}}$ spectrum of the two VLB signals, shown in Figure 7.8b, is softer than the VLT spectrum due to the invisibly decaying Z bosons. Comparing the $E_{\mathrm{T}}^{\mathrm{miss}}$ distributions of the two VLB scenarios to the VLT SU(2) singlet and

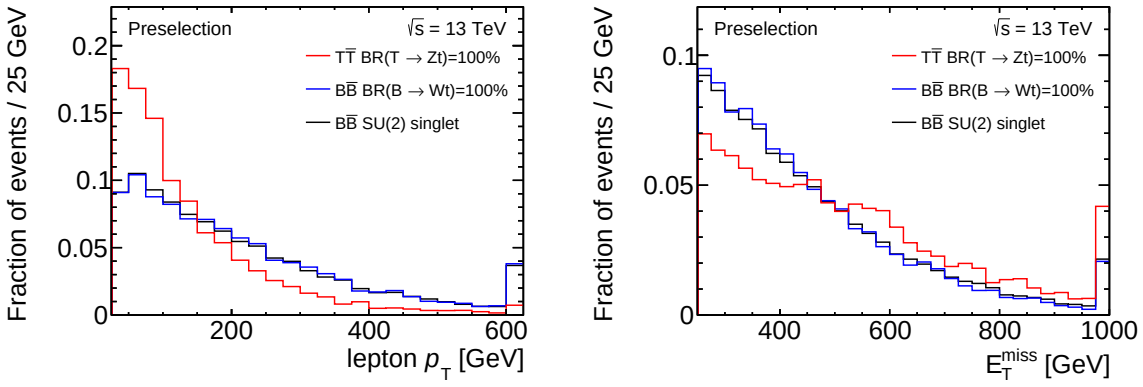

(a) (b)

Figure 7.8: Comparison of the distributions of (a) lepton p_{T} and (b) $E_{\mathrm{T}}^{\mathrm{miss}}$ after the preselection for VLQs with a mass of 1.2 TeV. The scenario of exclusive $T \to Zt$ decays is compared to two VLB signals with $B \to Wt$ decays and branching ratios according to the SU(2) singlet.

doublet scenarios, the $E_{\mathrm{T}}^{\mathrm{miss}}$ shapes look similar. Further distributions, including also a comparison of the VLB signal with background processes, can be found in Appendix B.1.

Singlet versus doublet couplings

The VLQ signal events are generated assuming couplings according to the SU(2) singlet model. In order to be able to evaluate the impact of this choice, possible kinematic differences arising from the different chirality of the singlet and doublet couplings are studied. For this purpose, signal samples with the different couplings are compared for a signal mass of 1.2 TeV and a fixed branching fraction according to the (T, B) doublet.

The kinematic differences are illustrated for the lepton p_{T} distribution in Figure 7.9. The coupling affects the polarisation of the top quark in the $T \to Zt$, $T \to Ht$, and $B \to Wt$ decays, where the lepton p_{T} spectrum is tighter in the case of doublet couplings. This effect is more pronounced in the case of the VLT signal, Figure 7.9a, than for the VLB signal shown in Figure 7.9b. This can be explained by the origin of the lepton. While for the VLT signal the lepton comes most likely from a top-quark decay, it can either originate from a W boson or a top-quark decay in the $B \to Wt$ case. The observed difference propagates to variables related to the lepton p_{T} like m_{T}^{W}.

7.2.2 Comparison of data and MC

The general modelling of the SM prediction is validated after the basic event selection by comparing the SM prediction to data for some sensitive variables. First, the transverse momentum distribution of the lepton is compared separately for electrons and muons in Figures 7.10a and 7.10b, respectively. Comparing the agreement between data and simulation, similar trends are visible in both channels allowing to not distinguish between the lepton flavour

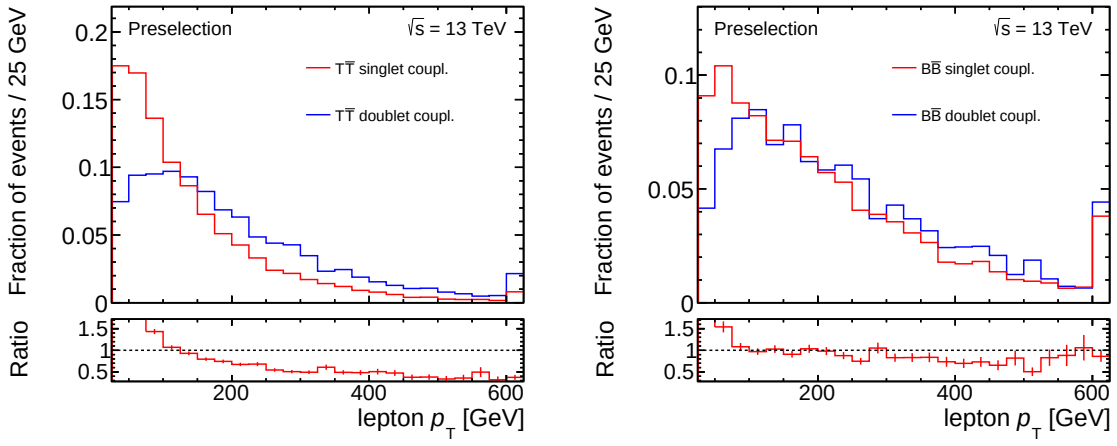

(a) **(b)**

Figure 7.9: Comparison of the lepton p_{T} distribution after the preselection for (a) a VLT and (b) a VLB signal with a mass of $m = 1.2\,\mathrm{TeV}$ and branching ratios according to the SU(2) (T, B) doublet for couplings according to the singlet and doublet models.

in the following. The SM prediction overestimates the data in all bins of the distributions. The difference in the lepton p_{T} distribution is about 15 % up to 200 GeV but increases towards higher values. The same trend of a worse agreement between data and simulation is visible in the m_{eff} distribution, shown in Figure 7.10c. In this variable, defined as the sum of transverse momenta of all objects in an event and $E_{\mathrm{T}}^{\mathrm{miss}}$, the poor modelling in the tail of the distribution is even more pronounced with deviations of the data from the SM prediction of up to 50 %. This slope in the m_{eff} distribution is a known issue that is observed in several other analyses. One reason are missing higher-order QCD corrections in the modelling of the top-quark backgrounds. Figure 7.10d shows the jet multiplicity distribution and a roughly constant deviation of about 10 % is visible in all bins of the distribution indicating that the mismodelling is already related to the basic process and not a specific effect of additional jet radiation.

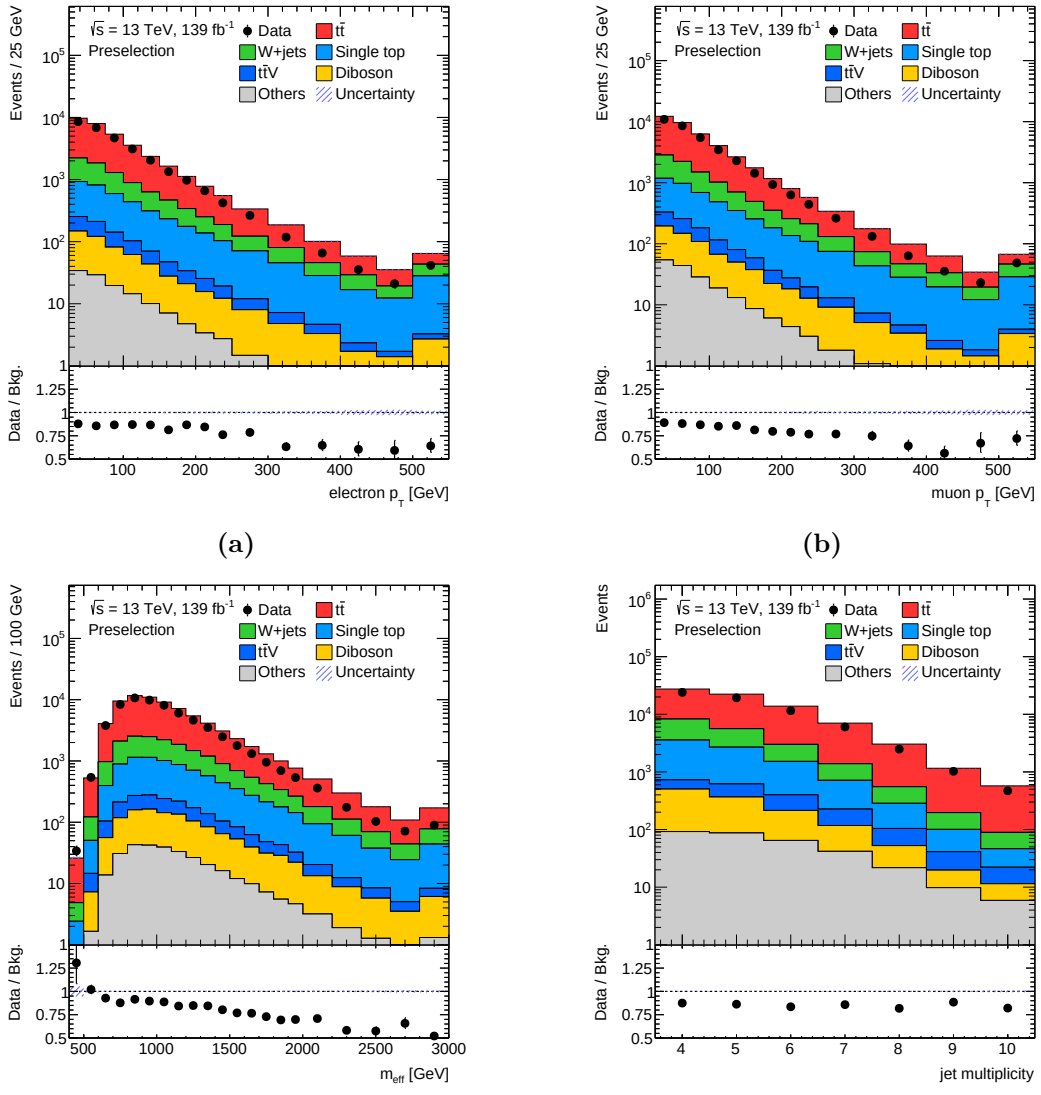

Figure 7.10: Comparison of data and simulation in (a) the electron p_{T} (b) the muon p_{T}, (c) m_{eff}, and (d) jet multiplicity distributions after the preselection. Contributions from $t\bar{t}H$, tWZ, and Z+jets are summarised as "Others". The lower panels show the ratio of the data to the SM prediction. The uncertainty bands include the MC statistical uncertainties only. The last bin contains overflow events.

7.3 Kinematic top reweighting

As outlined in the section before, differences between data and simulation after the preselection are caused by a poor modelling of the top quark at high transverse momenta [196, 197]. In order to compensate for this effect and improve the modelling, a data-driven reweighting procedure depending on kinematic properties of the affected events is employed. The corrections are derived for the $t\bar{t}$ and single top-quark processes, where the latter is dominated by the tW channel. The similarity between the $t\bar{t}$ and tW processes, and the fact that both are based on the same generator settings is the reason for the assumption that both processes should be corrected simultaneously. Reweighting factors, which are applied in the form of event weights for the $t\bar{t}$ and single top-quark processes, are derived as a function of m_{eff} in various bins of the jet multiplicity.

A dedicated top reweighting region, mainly enriched in $t\bar{t}$ events, is defined in order to derive these reweighting factors. The fraction of single top-quark events is kept small in this region to avoid a strong dependency of the reweighting on the interference handling between $t\bar{t}$ and tW. The region is defined to be kinematically close to the training region by requiring a transverse mass of the lepton and $E_{\text{T}}^{\text{miss}}$ of $m_{\text{T}}^{W} > 120\,\text{GeV}$ and at least one reclustered large-R jet. To ensure orthogonality to other regions defined in this analysis, a requirement on the asymmetric transverse mass of $am_{\text{T2}} < 180\,\text{GeV}$ is imposed. This cut is not a simple inversion, but the requirement is strengthened to reduce the signal contamination in the tails of the m_{eff} distribution in the top-reweighting region. As shown in Figure 7.11a, these criteria select a part of the phase space relatively pure in $t\bar{t}$ events, which makes a fraction of 90 % of the selected events. Single top-quark events contribute with about 4 %, and the fraction of all other SM processes in the top-reweighting region is therefore about 6 %. The m_{eff} distribution in the top-reweighting region before applying any reweighting factors is shown in Figure 7.11b. The same trends as after the preselection are visible.

The reweighting factors are separately derived for four bins of the jet multiplicity, containing four, five, six, or at least seven jets. For a jet multiplicity bin i, they scale the $t\bar{t}$ and single top-quark event yields, n_{top}^{i} to the difference of the observed data, n_{data}^{i} in a bin of the m_{eff} distribution. The reweighting factors are calculated as

$$f_i(m_{\text{eff}}) = \frac{n_{\text{data}}^{i}(m_{\text{eff}}) - n_{\text{other}}^{i}(m_{\text{eff}})}{n_{\text{top}}^{i}(m_{\text{eff}})}, \tag{7.6}$$

where the event yields and correspondingly the reweighting factors can vary between the bins of the m_{eff} variable. The calculated reweighting factors are shown in Figure 7.12. In all considered jet bins, the obtained reweighting factors decrease towards larger values of m_{eff}, corresponding to larger corrections. In order to avoid relying too much on the binning and statistical fluctuations, the correction factors are fitted by a linear function up to effective masses of 2500 GeV, assuming a flat behaviour from this points upwards. This threshold is a protection against artificially large correction factors that would become even negative at some point.

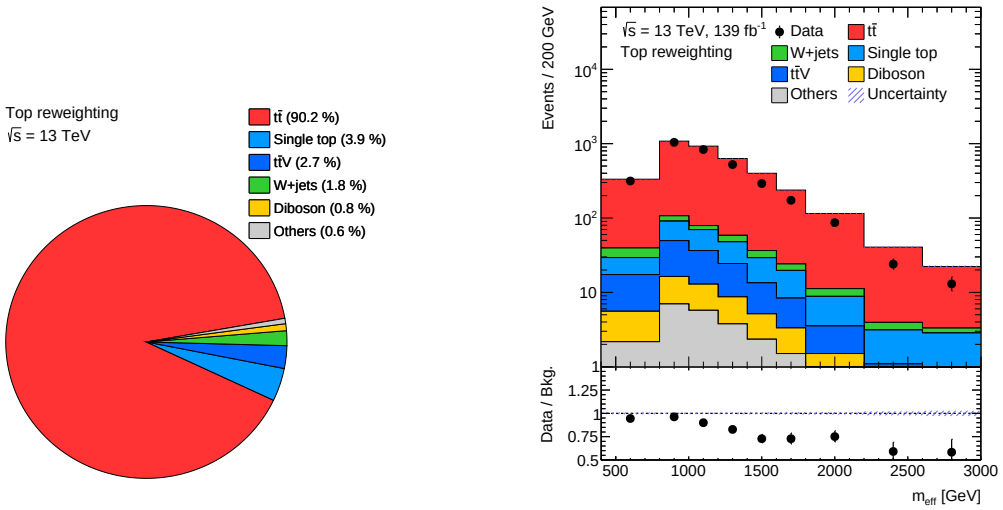

(a) **(b)**

Figure 7.11: (a) Contributions from the SM processes to the top-reweighting region. (b) Distribution of the effective mass m_{eff} after applying the selection criteria of the top reweighting region. Contributions from $t\bar{t}H$, tWZ, and Z+jets are summarised as "Others". The lower panels show the ratio of the data to the SM prediction. The hatched band includes the MC statistical uncertainties. The last bin contains overflow events.

The uncertainty on the reweighting function, σ_i is evaluated from the uncertainties of the fit parameters taking their correlation into account. With a linear function $f(m_{\text{eff}}) = a \cdot m_{\text{eff}} + b$, the uncertainty becomes

$$\sigma_i^2 = m_{\text{eff}}^2 \sigma_a^2 + \sigma_b^2 + 2 m_{\text{eff}} \rho_{ab} \sigma_a \sigma_b \tag{7.7}$$

with uncertainties on the slope, σ_a and the offset, σ_b, and the correlation coefficient ρ_{ab}. The 68 % CL is chosen as the reweighting uncertainty and is indicated by dashed lines in Figure 7.12.

Different studies on the reweighting are performed in order to justify the functional form of the reweighting function, the choice of the cut-off threshold, and the assigned systematic uncertainty. In Figure 7.13a, linear reweighting functions with different choices of the cut-off threshold are compared for the five jets bin. The selected cut-off at 2.5 TeV fits best with the binned reweighting factors and the assigned uncertainty covers the various choices of the threshold. Instead of a linear reweighting function, other types of functional forms are studied and compared in Figure 7.13b. Again, the simplest approach of a first-order polynomial works well and the assigned systematic uncertainty covers most of the differences to alternative functional forms.

The derived reweighting factors are applied on all $t\bar{t}$ and single top-quark events. The data–MC agreement after applying the kinematic top reweighting is illustrated in Figure 7.14 with the

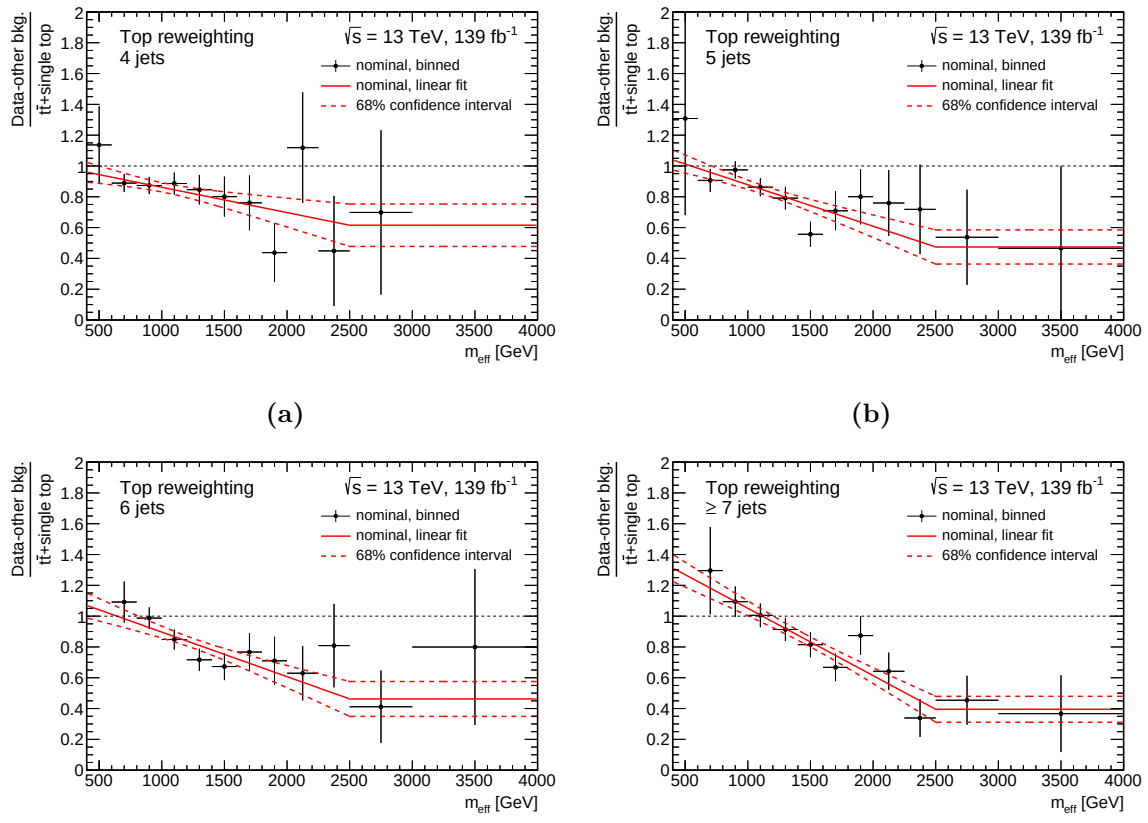

Figure 7.12: Derived correction factors of the kinematic top reweighting as a function of m_{eff}, given for four bins of the jet multiplicity: (a) four jets, (b) five jets, (c) six jets, (d) at least seven jets. The error bars indicate the statistical uncertainty. The results of the linear fits up to $m_{\text{eff}} = 2500\,\text{GeV}$ are shown as a solid red line and a constant behaviour is assumed above this threshold. The dashed red lines represent the 68 % CL interval of the fit parameters that is used as the systematic uncertainty for the reweighting.

example of the m_{eff} and lepton p_{T} distributions in the top reweighting region. Compared to the situation before the reweighting, indicated by a dashed black line in the upper panel, the agreement is significantly improved. In order to verify that the reweighting factors can be applied in other regions of the analysis as well, and improve the modelling as expected, kinematic distributions are compared after the preselection. Two examples, the m_{eff} and jet multiplicity distributions are shown in Figure 7.15. In both distributions, the agreement between data and SM prediction is improved. In the following, the top-reweighting factors are applied in all distributions in the following sections unless stated otherwise.

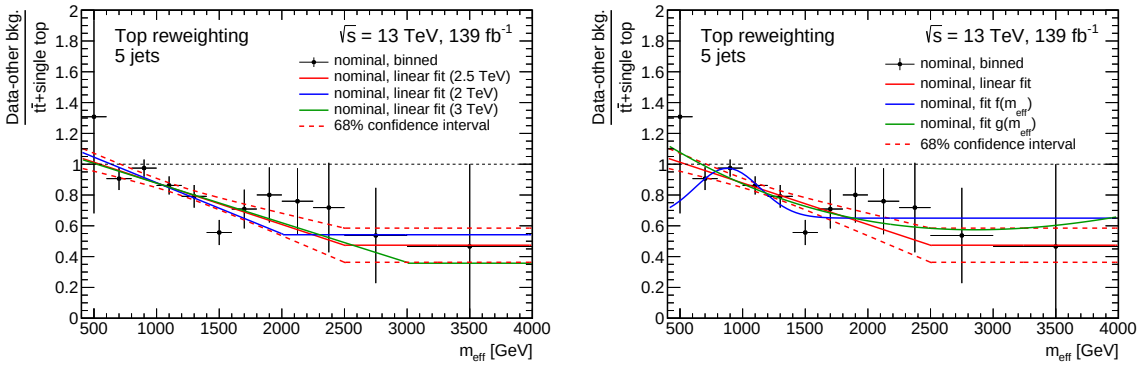

(a) **(b)**

Figure 7.13: Study of different reweighting functions illustrated for the case of the five jets bin. (a) Linear reweighting function for various values of the cut-off threshold. (b) Comparison of various functional forms of the reweighting function. Fit function $f(m_{\text{eff}})$ is a Gaussian function with an additional offset and $g(m_{\text{eff}})$ is a third-order polynomial.

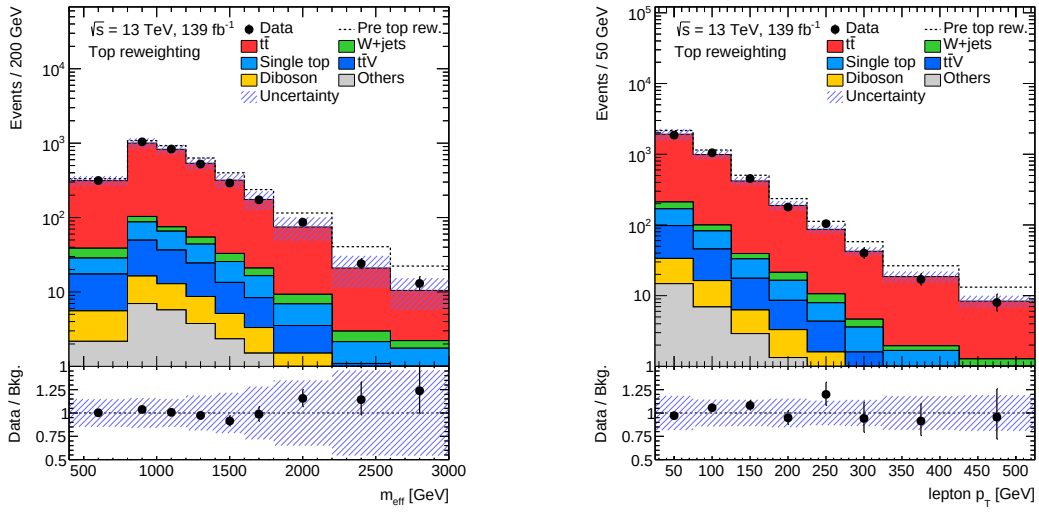

(a) **(b)**

Figure 7.14: Distributions of (a) m_{eff} and (b) lepton p_{T} in the top-reweighting region after applying the reweighting factors to the $t\bar{t}$ and single top-quark processes. The dashed lines indicate the total background before the reweighting. The hatched bands include statistical and systematic uncertainties. Minor background contributions from $t\bar{t}H$, tWZ, and Z+jets are combined into "Others". The ratios of the data and the expected background events are shown in the bottom panels of the plots. The last bin in each distribution contains the overflow.

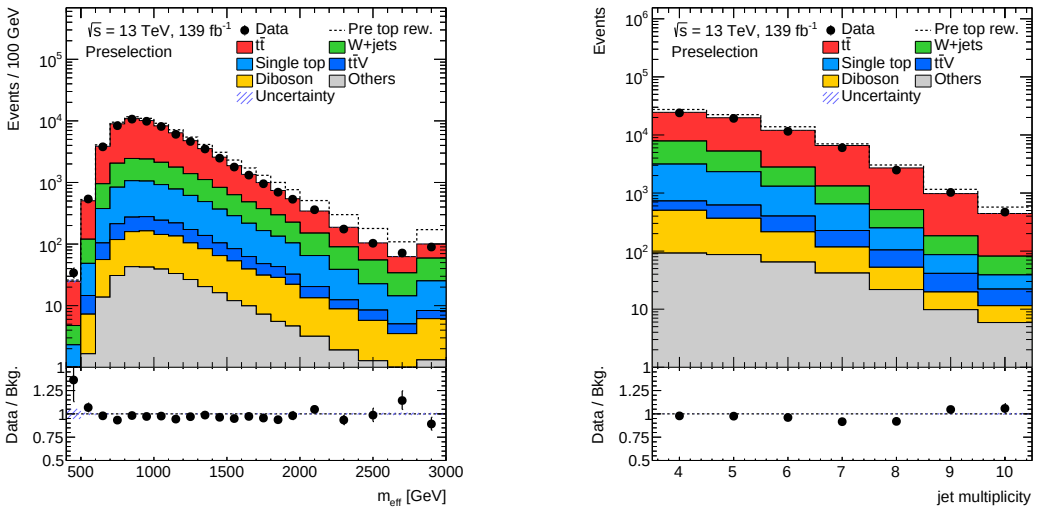

(a) **(b)**

Figure 7.15: Distributions of (a) m_{eff} and (b) the jet multiplicity after applying the preselection requirements and the kinematic top reweighting. The dashed lines indicate the total background before the reweighting. The hatched bands include MC statistical uncertainties only. Minor background contributions from $t\bar{t}H$, tWZ, and Z+jets are combined into "Others". The ratios of the data and the expected background events are shown in the bottom panels of the plots. The last bin in each distribution contains the overflow.

7.4 Signal and background separation

After studying the signal and background properties, and ensuring that the background processes are modelled well after the preselection, further requirements are imposed on the events in order to reduce the contribution from background processes before the training of the NNs. However, these requirements are kept relatively loose in order to ensure a good acceptance for various signal hypotheses. The final separation between signal and background processes is subject to the NN training later.

In addition to the preselection, defined in Section 7.2, events have to pass $m_{\mathrm{T}}^{W} > 120\,\mathrm{GeV}$ and $am_{\mathrm{T2}} > 200\,\mathrm{GeV}$. Furthermore, at least one reclustered large-R jet is required, as a hadronic resonance is always expected for the VLQ signal. These additional requirements define the training region selection.

The background composition after the selection of the training region is shown in Figure 7.16a. The largest contribution stems from the $t\bar{t}$ process with about 47.9 % of the selected events. Further important background processes are single top-quark production (18.5 %), W+jets (16.1 %), and $t\bar{t}V$ (10.2 %). All other considered background processes have an event fraction of 7.1 %.

As the $t\bar{t}$ background is the most relevant one in the training region, its decay modes are further studied, and visualised in Figure 7.16b. About 21 % of the $t\bar{t}$ events are classified as 2ℓ events or ℓ+jets event each, where a lepton, ℓ, is either a muon or an electron. In the former case, one of the two leptons must not be reconstructed in order to fulfil the lepton requirement of the analysis resulting in an additional source for $E_{\mathrm{T}}^{\mathrm{miss}}$. The largest fraction of $t\bar{t}$ events is classified as ℓ+τ-lepton event (38 % $\ell + \tau_{\mathrm{had}}$, 17 % $\ell + \tau_{\mathrm{lep}}$). In the case of a leptonic tau decay, the tau decays into an electron or a muon and neutrinos, while jets and neutrinos are the results of a hadronic tau decay. The additional neutrinos might explain why more ℓ+τ-lepton events than 2ℓ events pass the tight $E_{\mathrm{T}}^{\mathrm{miss}}$ selection in this analysis.

After focusing on the background reduction and composition, the signal composition is studied in order to get an impression of the analysis sensitivity for the various signal decay modes. The composition of the signal events in the training region is illustrated in Figure 7.17a for a VLT signal and in Figure 7.17b for a VLB signal, assuming a VLQ mass of 1.2 TeV and equal branching ratios in the three decay modes each. For VLQ pair production, this assumption results in twice the fraction of events where the VLQs decay via different decay modes than events in which both VLQs decay via the same mode. In the case of VLT pair production, the analysis has the highest sensitivity, as expected, for $Zt + X$ events, where X denotes either Zt, Ht, or Wb. However, the analysis selects also a reasonable fraction of signal events with VLTs decaying into either Wb or Ht, which should allow to cover a large part of the VLQ branching ratio plane.

For the VLB signal, the situation is different. In almost 90 % of the selected events, at least one B quark decays into Wt, while for the remaining events the VLBs decay via either Zb or Hb. The relatively small selection efficiency for the two latter decay modes can be understood

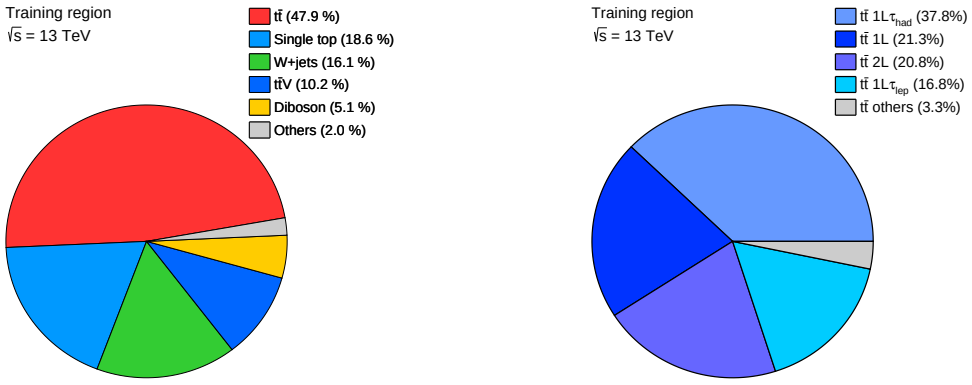

(a) **(b)**

Figure 7.16: (a) Pie chart visualising the contributions of different background processes in the training region. Minor contributions from $t\bar{t}H$, tWZ, and Z+jets are summarised as "Others". The fraction of various decay modes for the $t\bar{t}$ process is shown in (b), where "$t\bar{t}$ others" refers to the decay modes that are not explicitly listed in the legend.

from the one charged lepton requirement. In both cases, the lepton would have to originate from a Z or Higgs boson decay into two leptons where the second lepton must not be identified, or from a heavy-flavour quark decay.

Another hint on the analysis sensitivity for the various signal hypotheses is given by the product of the signal acceptance and efficiency in the training region, which is shown in Figure 7.17c for five signal hypotheses. In all cases, the selection efficiency increases as a function of the VLQ mass. As an example, the selection efficiency is about 2.4 % at 800 GeV and about 4.8 % at 1800 GeV for the exclusive decay of the VLTs into Z bosons and top quarks. The highest selection efficiency is achieved for the $\mathcal{B}(B \to Wt) = 100\,\%$ scenario with about 6 % efficiency for a VLB mass of 2 TeV. Comparing the efficiencies of the $\mathcal{B}(B \to Wt) = 100\,\%$ and $\mathcal{B}(T \to Zt) = 100\,\%$ scenarios, the analysis has the highest selection efficiency for the latter case for VLQ masses below 1.2 TeV, while for larger masses the former case is more efficiently selected. The shape of the $\mathcal{B}(T \to Zt) = 100\,\%$ distribution becomes almost flat at masses above 1.6 TeV in contrast to the other considered scenarios.

Kinematic differences in the lepton p_{T} distribution between the singlet and doublet couplings of the VLQ have been discussed in Section 7.2.1, see Figure 7.9. For the T quark, these differences result in an increased acceptance in the training region in the doublet case resulting in conservative limits, while for the B quark the acceptance is similar between singlet and doublet couplings.

7.4.1 Neural networks

In order to improve the separation between signal and background processes with respect to a classical cut-and-count approach, NNs are employed. This allows for the combination of

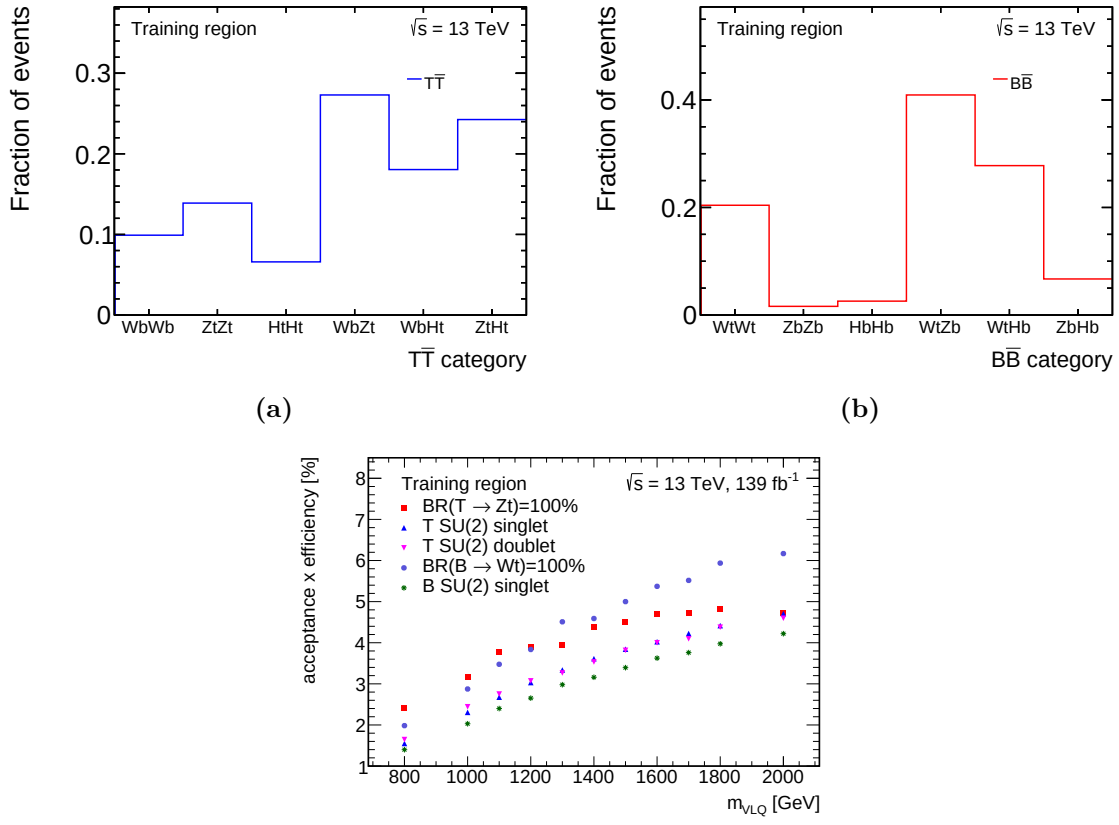

Figure 7.17: Fraction of signal events in the various signal decay modes after the training-region selection for (a) $T\bar{T}$ and (b) $B\bar{B}$ production assuming a signal mass of 1.2 TeV and equal branching rations for the three possible decay modes. (c) Product of signal acceptance and efficiency for five benchmark signal decay scenarios as a function of the VLQ mass.

various discriminating variables into one final discriminant, the NN output, taking correlations between the variables into account. Training NNs for different signal hypotheses allows to cover a broad range of the phase space of interest. In this thesis, the NN implementation of the NeuroBayes [198, 199] package is used. In the following, the NN architecture, the preprocessing of the input variables, and the NN training are explained before the usage of NNs in the search for VLQs is discussed.

Neural network architecture

The NeuroBayes NN is a three-layer feed-forward network, whose general structure is illustrated in Figure 7.18. The first layer is called input layer and contains a set of $n + 1$ nodes, with one node for each of the n input variables and one additional bias node. The second layer is referred to as hidden layer and consists of a user-specific number of nodes, m, while the third layer, called output layer, consists of solely a single node. Each node is connected with every

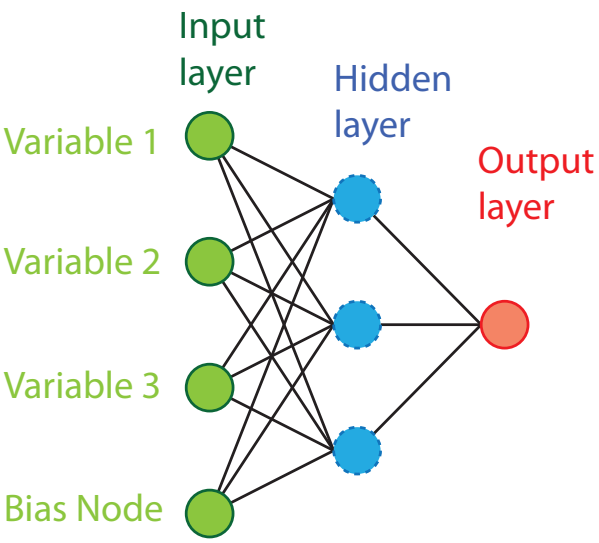

Figure 7.18: Schematic diagram of a three-layer feed-forward network. In this example, three input variables and a bias node are used in the input layer, three nodes in the hidden layer, and one node in the output layer, returning the final output discriminant, NN_{out}.

node of the next layer, where the connections represent weights which are determined in the NN training procedure.
The input of each hidden node h_l is given by

$$h_l\left(x_1, x_2, ..., x_n\right) = \sum_k w_{kl} x_k, \tag{7.8}$$

where x_k are the input values, the index k runs over all nodes of the input variables and the bias node, and w_{ij} are the weights between the i-th input node and the j-th node of the hidden layer. The output of the three-layer NN is calculated via

$$o_{\text{NN}} = S\left(\sum_l w_l \cdot S\left(\sum_k w_{kl} \cdot x_k\right)\right), \tag{7.9}$$

where the index l runs over the hidden-layer nodes and w_l is the weight between the output node and node l of the hidden layer. As non-linear activation function the symmetric sigmoid function is used, which is defined as

$$S(x) = \frac{2}{1 + e^{-x}} - 1. \tag{7.10}$$

The sigmoid function maps all values to the interval [-1,1] and has a linear response in the region around zero. The final discriminant, NN_{out}, is obtained by mapping o_{NN} to the interval $[0, 1]$ via a linear transformation.

Preprocessing

Before the training of the NN, the input variables are transformed in a preprocessing step to facilitate an optimal training and to prevent extreme outliers in the input variables from impacting the training. In a first step, the input variables are transformed to flat distributions and discretised in 100 bins of variable size such that each bin contains the same number of events. Then, the distribution of the signal events is divided for each bin by the sum of signal and background events, yielding a purity distribution for each variable. The purity distributions are fitted with a regularised spline function to obtain a continuous transformation of the original input distributions to the purities, thereby reducing statistical fluctuations in the input variables significantly. The continuous purity functions are applied to the input variables and thereby yield a set of corresponding purity values. The resulting purity distributions are further transformed into distributions with a mean of zero and a width of one, which are used as input for the NN.
The described procedure is applied to all continuous input variables. For discrete inputs or variables that do not exist in each event, an individual preprocessing is applied. For example, the spline function that is fitted to a variable that is not calculated in each event contains an additional delta distribution. As the last step of the preprocessing procedure, the relative importance of each input variable is determined according to the loss of correlation to target when removing the respective variable in an iterative procedure. For that, the correlation matrix of all transformed input variables is calculated, diagonalised, and the correlation to the target function is determined. The latter assumes a value of one for signal events and of zero for background events. Then, the loss in total correlation to target when removing a variable from the input is computed. The variable with the smallest loss is discarded and the procedure is repeated until only the most powerful variable is left. At the end of this iterative procedure, a ranked list of input variables ordered in their importance is obtained. In order to simplify the NN training, only variables above a certain threshold are further considered.

Training

In order to use an NN to discriminate between signal and background processes, the weights between the nodes have to be determined based on true categories of the events. In this case, simulated MC samples for signal and background processes are used in the training, in which the event weights of the signal and background categories are modified such that the total sum of weights for signal and background are equal. Thus, the fraction of the sum of weights for signal and background is 50 % each. The weights of the connections between the different nodes are calculated via an iterative backpropagation algorithm by minimisation of the entropy loss function. Here, the entropy loss function is defined as

$$E = \sum_k \log\left(\frac{1 + t_k \cdot o_k + \epsilon}{2}\right), \tag{7.11}$$

where t_k is the corresponding target value of a simulated event k with $t_k = 1$ for signal events and $t_k = -1$ for background events. The NN output for a given event is denoted by o_k and a regularisation constant ϵ is included in order to avoid instabilities for events with a completely wrong classification such as $o_k \approx -t_k$.
To check the quality of the training only 80 % of the MC samples are used for the training. The remaining 20 % of the input samples are processed to verify that no overtraining happened during the training.

7.4.2 Neural networks in the search for VLQs

As mentioned above, neural networks are employed for the separation of signal and background events. The training set consists of MC simulated signal and background events, where only the four major background processes, namely $t\bar{t}$, W+jets, single top-quark production, and $t\bar{t}V$ are considered. The individual processes are weighted according to their number of expected events, and signal and background are finally scaled such that they have equal contributions. Instead of training a separate NN for each possible signal mass point, signal masses from 1 TeV to 1.5 TeV are combined in the training sample. The combination of several signal mass points for the NN training simplifies the analysis and keeps a good separation performance for all signal masses used in the training. Events at different signal masses enter with the same cross-section when composing the training sample in order to avoid that the lower masses with higher cross-sections dominate. Acceptance effects of the various signal masses in the training region are kept such that higher masses are slightly preferred. As discussed in Section 7.2.1, kinematic differences exist between the various possible signal decay modes. In order to have a good coverage for a large area in the signal branching ratio plane, NNs are trained for various signal branching ratio hypotheses. For $T\bar{T}$ production, four NNs are trained for different branching ratios $\mathcal{B}(Zt, Ht, Wb)$ covering the branching ratio plane where this analysis is sensitive: $(0.8, 0.1, 0.1)$, $(0.2, 0.4, 0.4)$, $(0.4, 0.1, 0.5)$, $(0.4, 0.5, 0.1)$. Similarly, three NNs are trained for $B\bar{B}$ production considering the branching ratios $\mathcal{B}(Zb, Hb, Wt) =$ $(0.1, 0.1, 0.8)$, $(0.4, 0.1, 0.5)$, and $(0.1, 0.4, 0.5)$. The choice of the branching ratios for the NN training is illustrated in Figure 7.19.
For each of these seven NNs, the preprocessing and training procedure is carried out separately. The final set of input variables considered in the preprocessing consists of 13 observables, listed in Table 7.3. All of these variables are used in at least one NN training. The list of input variables contains kinematic variables reflecting event properties, like m_{eff} or the b-jet multiplicity, or object properties, like the transverse momenta of the lepton or the large-R jets.
The modelling of the input variables is validated in all analysis regions. The distributions of the effective mass, the transverse mass, the missing transverse momentum, and the asymmetric transverse mass in the training region are shown in Figure 7.20. In these plots, the SM prediction is compared to data, showing a reasonable agreement within the statistical and

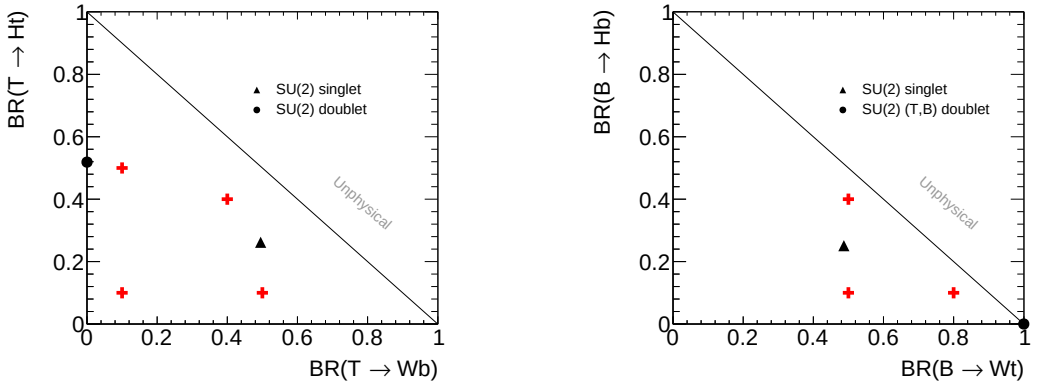

(a) **(b)**

Figure 7.19: Signal branching ratios for which dedicated NNs are trained. The red crosses represent the branching ratios that are considered for the training of neural networks. Four NNs are trained for (a) $T\bar{T}$ production, while three NNs are trained for (b) $B\bar{B}$ production. The black markers indicate the branching ratios for SU(2) singlet and doublet.

Table 7.3: Input variables to the NN training, approximately sorted in descending discriminating power between signal and background.

Variable	Description
m_{eff}	scalar sum of the transverse momenta of leptons, jets, and $E_{\text{T}}^{\text{miss}}$
$N_{b\text{-jets}}$	b-jet multiplicity
m_{T}^{W}	transverse mass of lepton and $E_{\text{T}}^{\text{miss}}$
am_{T2}	asymmetric transverse mass
$p_{\text{T}}(\text{large-R jet}_2)$	transverse momentum of subleading-p_{T} large-R jet
$\lvert\Delta\phi(\text{jet}_1, E_{\text{T}}^{\text{miss}})\rvert$	azimuthal angle separation between $E_{\text{T}}^{\text{miss}}$ and leading-p_{T} jet
$E_{\text{T}}^{\text{miss}}$	missing transverse momentum
$\eta(\text{jet}_1)$	pseudorapidity of leading-p_{T} jet
$m(\text{large-R jet}_1)$	mass of leading-p_{T} large-R jet
$N_{\text{const}}(\text{large-R jet}_1)$	number of small-R jets reclustered to the leading-p_{T} large-R jet
$p_{\text{T}}(\ell)$	transverse momentum of lepton
$p_{\text{T}}(\text{jet}_3)$	transverse momentum of third-leading jet, sorted in p_{T}
$p_{\text{T}}(\text{jet}_2)$	transverse momentum of subleading-p_{T} jet

systematic uncertainties. In addition, the expected signal distributions for a VLT and VLB signal of mass 1.2 TeV and exclusive $T \to Zt$ and $B \to Wt$ decays are overlaid in order to give an impression of the separation power of the input variables. The distributions for the other input variables can be found in Appendix B.2.

The entropy loss function is minimised in the training of the NN. Once an increase above a certain threshold is detected, the NN training is stopped and the final training results are taken from the previous iteration. Even though NeuroBayes is not known to be prone to overtraining, checks for potential overtraining are done using 20 % of the input sample. An automatic check is the comparison of the entropy loss function between the training and

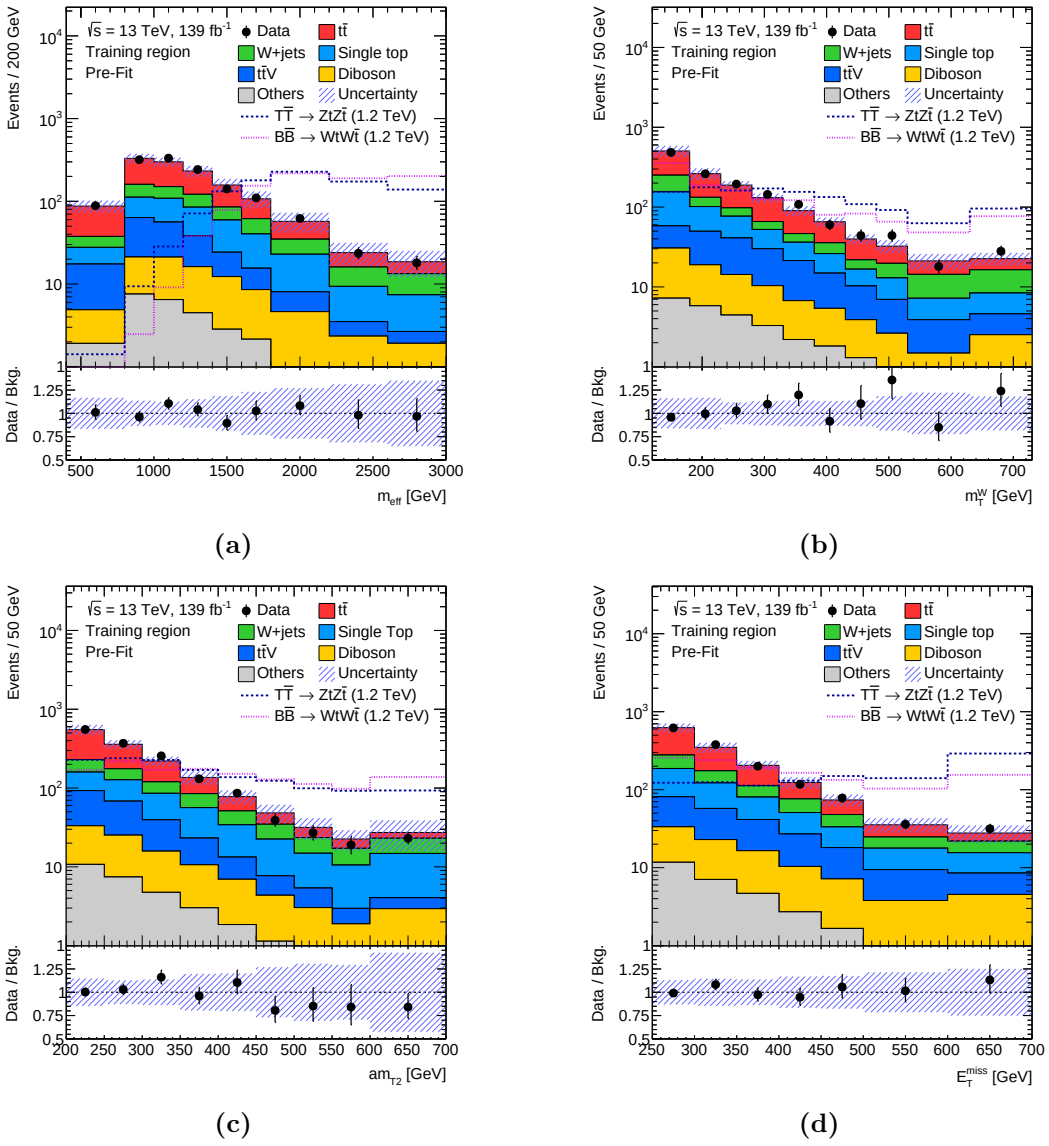

Figure 7.20: Distributions of NN input variables in the training region for (a) m_{eff}, (b) m_{T}^{W}, (c) am_{T2}, and (d) $E_{\text{T}}^{\text{miss}}$. Minor contributions from $t\bar{t}H$, tWZ, and Z+jets are summarised as "Others". The hatched bands include statistical and systematic uncertainties. The ratios of the data and the expected background events are shown in the bottom panels. The last bin in each distribution contains the overflow. The benchmark signal processes, normalised to the total background expectation, are overlaid as dashed lines.

test samples. The entropy loss function as a function of the number of iterations is shown in Figure 7.21 for one NN training. The errors of the training and test samples are always decreasing with respect to the previous iteration, indicating that no overtraining happened.

The NN output distribution of the same NN as used for the illustration of the training is shown in Figure 7.22. The shape comparison of the major background processes and an exemplary signal, Figure 7.22a, shows the expected good separation between signal and background. The

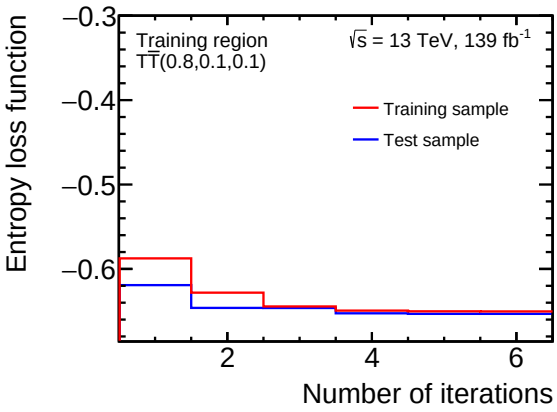

Figure 7.21: Entropy loss in the training (red line) and the test (blue line) samples as a function of the number of iterations for the NN trained for the VLT signal with $\mathcal{B}(Zt, Ht, Wb) = (0.8, 0.1, 0.1)$.

shapes of the W+jets, single top-quark, and $t\bar{t}V$ processes look quite similar, while the shape of the $t\bar{t}$ process differs, indicating a slightly better separation from signal. Figure 7.22b shows the same distribution but with the background processes scaled to their number of expected events. Again, a signal distribution is overlaid indicating a large signal-to-background fraction for high values of the NN_{out} distribution. In order to investigate the composition of the SM processes in the background- and signal-enriched parts of the distribution, it is split into a low-NN_{out} CR and a SR at $NN_{\text{out}} = 0.5$. Corresponding pie charts of the background composition are shown in Figures 7.23a and 7.23b for the low-NN_{out} CR and SR, respectively. In the low-NN_{out} CR, $t\bar{t}$ production is the dominant process with an event fraction of about 50 %. Further relevant processes are single top (18 %), W+jets (16 %), and $t\bar{t}V$ (10 %). In the SR, $t\bar{t}$ is still the most relevant process with an event fraction of about 32 %. However, compared to the low-NN_{out} CR the background composition slightly changes as contributions from $t\bar{t}V$ (14 %), W+jets (19 %), and especially single top-quark production (26 %) become more relevant.

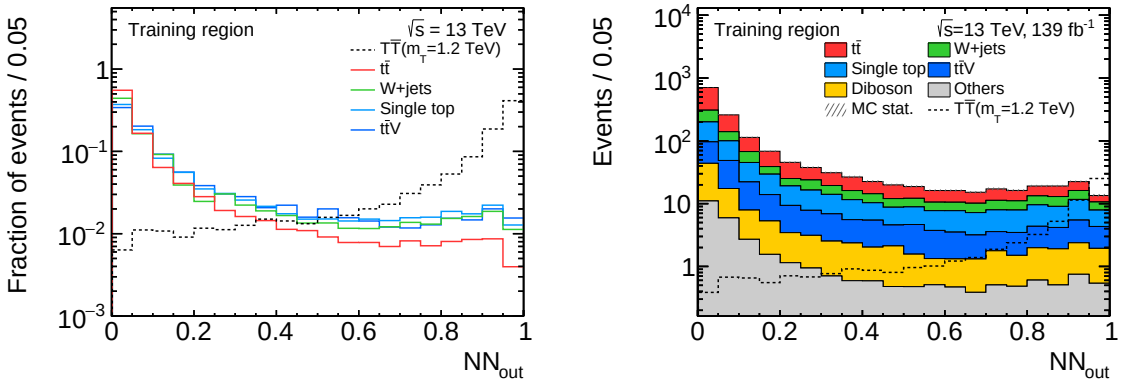

(a) (b)

Figure 7.22: Neural network output distributions of a NN trained for the VLT signal with a branching ratio of $\mathcal{B}(Zt, Ht, Wb) = (0.8, 0.1, 0.1)$. (a) Shape distributions of the major background processes are compared with a VLT signal with a mass of 1.2 TeV and the same branching ratios as used in the training of the NN. All distributions are normalised to unit area. (b) Stacked distribution of the network output distribution in the training region. The signal expectation, normalised to cross-section, of the same VLT signal as in (a) is overlaid.

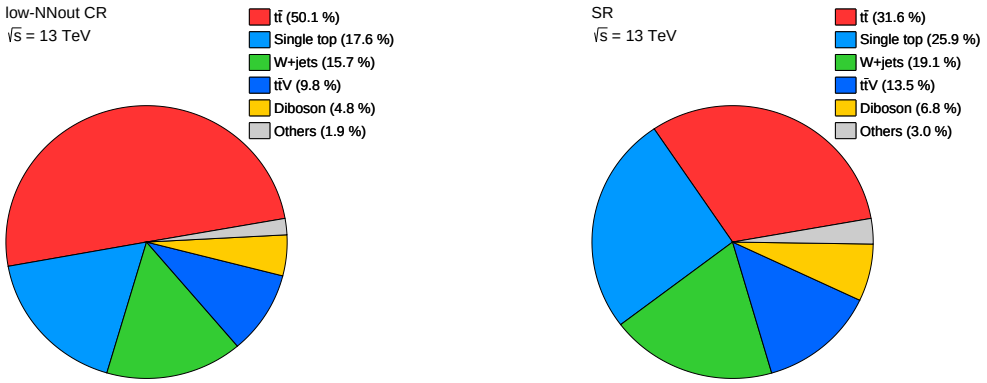

(a) (b)

Figure 7.23: Pie charts visualising the background composition in (a) the low-NN_{out} CR and (b) the SR. Contributions from $t\bar{t}H$, tWZ, and Z+jets are summarised as "Others".

7.5 Background estimation

As shown in the previous section, $t\bar{t}$ production is the dominating background process in the background-enriched part of the NN output distribution. Thus, it can be used to constrain its normalisation and is therefore called low-NN_{out} CR. Two other major background processes in the SR are W+jets and single top-quark production. Dedicated CRs, which are enriched in the respective background and have a small signal contamination, are defined for these two processes. Both CRs are defined kinematically close to the training region but kept orthogonal.

The definitions of all analysis regions are summarised in Table 7.4. The various requirements for the W+jets and single top-quark CRs are discussed in the following.

Table 7.4: Overview of the event selections for the training region, top-reweighting region, and the control regions for W+jets and single top-quark production. The training region is split into the low-NN_{out} CR and the SR based on a cut on the NN output distribution.

Preselection				
$E_{\text{T}}^{\text{miss}}$ triggers = 1 signal lepton no additional baseline lepton ≥ 4 jets ≥ 1 b-jet $E_{\text{T}}^{\text{miss}} > 250\,\text{GeV}$ $m_{\text{T}}^{W} > 30\,\text{GeV}$ $\lvert\Delta\phi(j_{1,2}, \vec{E}_{\text{T}}^{\text{miss}})\rvert > 0.4$				
	Training region low-NN_{out} CR/ SR	**Top-reweighting region**	**W+jets CR**	**Single-top CR**
m_{T}^{W} [GeV]	> 120	> 120	$\in [30, 120]$	$\in [30, 120]$
am_{T2} [GeV]	> 200	< 180	> 200	> 200
b-jet multiplicity	≥ 1	≥ 1	$= 1$	≥ 2
large-R jet multiplicity	≥ 1	≥ 1	≤ 1	≤ 1
m(large-R jet) [GeV]	-	-	< 150	< 150
lepton charge	-	-	$+1$	-
$\Delta R(b_1, b_2)$	-	-	-	> 1.4
NN_{out}	$< 0.5/ \geq 0.5$	-	-	-

The W+jets CR is defined by inverting the m_{T}^{W} requirement of the training region to a window around the W boson mass peak of $m_{\text{T}}^{W} \in [30, 120]\,\text{GeV}$. This ensures orthogonality to the training and top-reweighting regions. The cut on the asymmetric transverse mass is kept the same as for the training region, i.e. $am_{\text{T2}} > 200\,\text{GeV}$. Furthermore, exactly one b-tagged jet is required. Including events without b-jets to the W+jets CR would allow to increase the purity of the W+jets process in the CR. However, the additional events would be W+light-flavour jets, leading to a larger difference in the flavour composition between the W+jets CR and the SR. In order to reduce the contribution from semi-leptonic $t\bar{t}$ events, a hadronic top-quark veto is imposed by requiring maximally one reclustered large-R jet, additionally limiting its mass to a maximum of 150 GeV.

The higher parton density of up quarks in protons compared to down quarks results in a larger production cross-section of W^++jets than W^-+jets events in pp collisions at the LHC. The effect of the charge asymmetry is strengthened even further by the fact that W bosons produced in pp collisions are mainly left-handed [200] and the requirement of large missing transverse momentum in the analysis. Due to the V–A coupling of the W bosons to fermions, a lepton from a W boson decay is boosted in the flight direction of the W boson, while the anti-lepton is boosted in the opposite direction. Thus, $W^+ \to \ell^+\nu$ events, where the neutrino is boosted in the flight direction of the W boson, are favoured compared to $W^- \to \ell^-\bar{\nu}$ events by the high missing transverse momentum requirement. The effect of the lepton charge

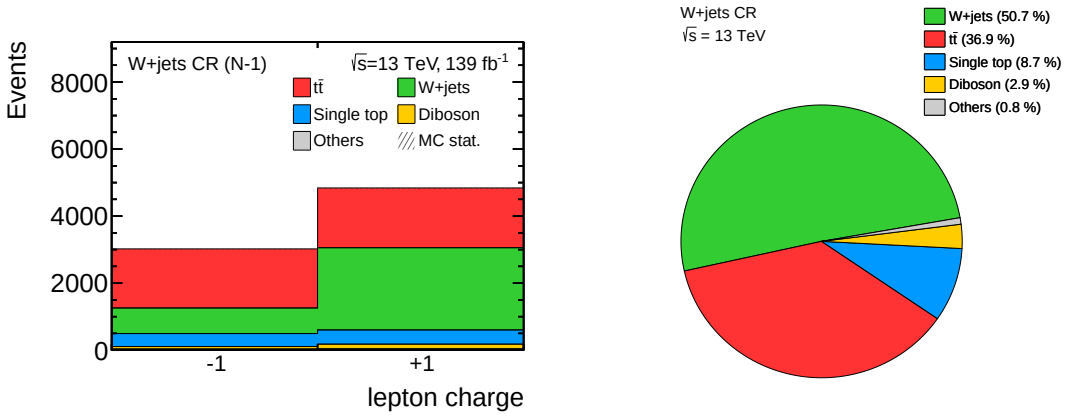

(a) **(b)**

Figure 7.24: (a) N-1 plot for the lepton charge in the W+jets CR, i.e. all requirements for the W+jets CR selection are applied except for the cut on the lepton charge. (b) Pie chart visualising the composition of the SM processes in the W+jets CR. In both plots contributions from $t\bar{t}H$, tWZ, and Z+jets are summarised as "Others".

asymmetry is visualised in Figure 7.24a, showing the expected number of events per lepton charge in the W+jets CR without any requirement on the lepton charge itself. While the number of events for the $t\bar{t}$ process is similar for both lepton charges, a significant difference is visible for the W+jets events. In order to reduce the contributions of charge-symmetric processes in the W+jets CR, a positively charged lepton is required.

After applying the aforementioned selection requirements, W+jets events contribute with a fraction of about 51 % to the expected total event yield in the W+jets CR as illustrated in Figure 7.24b. Further major contributions originate from the $t\bar{t}$ and single top-quark processes with contributions of 37 % and 9 %, respectively. The signal contamination for a VLT signal with exclusive $T \to Zt$ decays and a mass of 1 TeV is well below 1 % and thus negligible.

The requirement on the b-jet multiplicity is motivated by keeping the flavour composition between the CR and SR similar. Thus, the flavour composition in the W+jets CR and training region is compared and shown in Figures 7.25a and 7.25b, respectively. While the fraction of W+charm-jets events is similar in both regions, the fraction of W+bottom-jets and W+light-jets events slightly differs, as at least one b-tagged jet is required in the training region compared to the requirement of exactly one b-tagged jet for the W+jets CR.

The modelling in the W+jets CR is validated in various observables, and three distributions are given as an example in Figure 7.26. A good agreement between data and the SM expectation is visible within the statistical and systematic uncertainties. It has to be noted that due to the handling of the normalisation component of systematic uncertainties of a process with a free floating normalisation factor, that will be explained in the following section, the displayed uncertainty might be smaller than the original one. In addition, the total background expectation before applying the reweighting factors on the $t\bar{t}$ and single top-quark processes

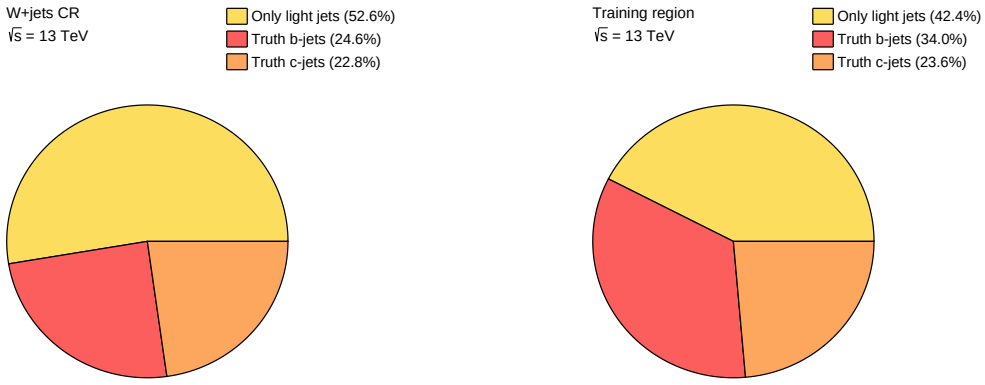

(a) **(b)**

Figure 7.25: Flavour composition of the W+jets process in the (a) W+jets CR and (b) training region.

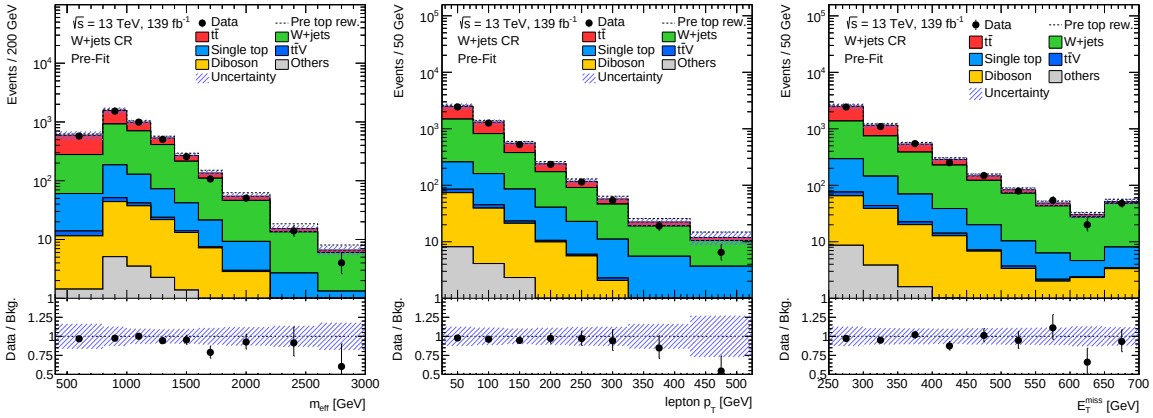

(a) **(b)** **(c)**

Figure 7.26: Distributions of (a) m_{eff}, (b) lepton p_{T}, and (c) $E_{\text{T}}^{\text{miss}}$ in the W+jets CR after applying the top reweighting factors and before applying the fit to the CRs and SR ("Pre-Fit"). Contributions from $t\bar{t}H$, tWZ, and Z+jets are summarised as "Others". The hatched bands indicate the total uncertainty. The total background prediction before applying the top reweighting is shown as a dashed line. The lower panels show the ratio of the data to the SM prediction. The last bin contains the overflow.

is overlaid as a dashed line. An improvement of the modelling in the m_{eff} variable is clearly visible as indicated by the data–MC ratio. Distributions of further variables can be found in Appendix B.3.

As mentioned before, another CR is defined for the single top-quark process. Similarly as for the W+jets CR, the single-top CR is kept orthogonal to the training and top reweighting-regions by requiring $m_{\text{T}}^{W} \in [30, 120]\,\text{GeV}$. Orthogonality to the W+jets CR is ensured by requiring at least 2 b-jets. A cut on the angular distance between the two leading b-jets, sorted

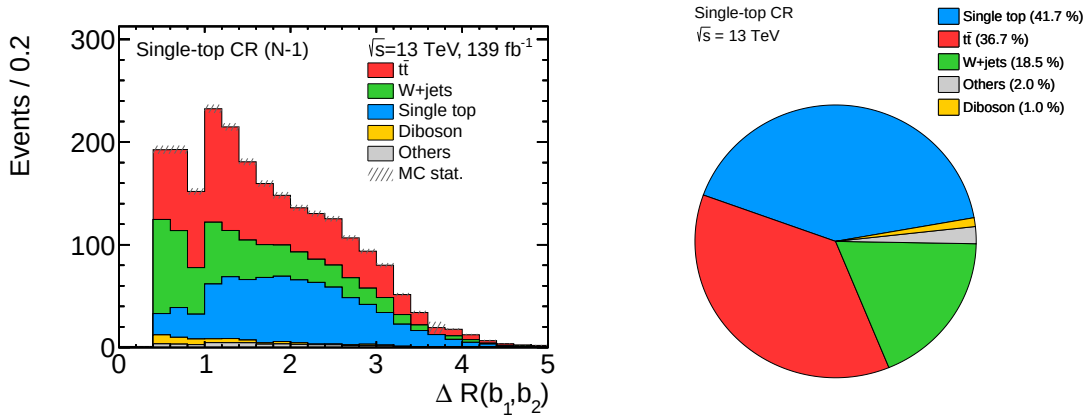

(a) **(b)**

Figure 7.27: (a) N-1 plot for the $\Delta R(b_1, b_2)$ variable in the single-top CR, i.e. all requirements for the single-top CR selection are applied except for the cut on $\Delta R(b_1, b_2)$. (b) Composition of the SM processes in the single-top CR. Contributions from $t\bar{t}V$, $t\bar{t}H$, tWZ, and Z+jets are summarised as "Others".

in p_{T}, of $\Delta R(b_1, b_2) > 1.4$ is imposed to reduce the contribution of $t\bar{t}$ and W+jets events as illustrated in Figure 7.27a. The fraction of $t\bar{t}$ events is reduced even further by requiring the same hadronic top-quark veto as for the W+jets CR, imposing selection requirements on the reclustered large-R jets. The cut on the asymmetric transverse mass of $am_{\mathrm{T2}} > 200\,\mathrm{GeV}$ is the same as for the training region.

After applying all selection criteria, the single-top CR consists of about 42 % single top-quark events as illustrated in Figure 7.27b. Looking closer at the production channel of the single top-quark, about 97 % of the single top-quark events are produced in association with a W boson (tW-channel), while the contribution from s- and t-channel production is small. The contribution from the $t\bar{t}$ process is of a similar order with an event fraction of 37 %, indicating the difficulty to separate between these two processes in a region of phase space where the interference effect between these two processes is dominant. The third major background is W+jets production with about 19 %, while the contribution from all other background processes amounts a few percent only. The signal contamination from a VLT signal with exclusive $T \to Zt$ decays and a mass of 1 TeV is about 0.2 %.

Again, the modelling in the single-top CR is validated in various observables. The distributions of m_{eff}, the lepton p_{T}, and $E_{\mathrm{T}}^{\mathrm{miss}}$ are shown in Figure 7.28 as an example. Compared to the situation before applying the top reweighting, indicated by the dashed lines, the agreement between data and the SM prediction is improved. However, differences are still evident, with a tendency of overestimating the observed data. These deviations are covered by large uncertainties mainly related to the modelling and the treatment of the interference between the $t\bar{t}$ and tW process. Further distributions can be found in Appendix B.3.

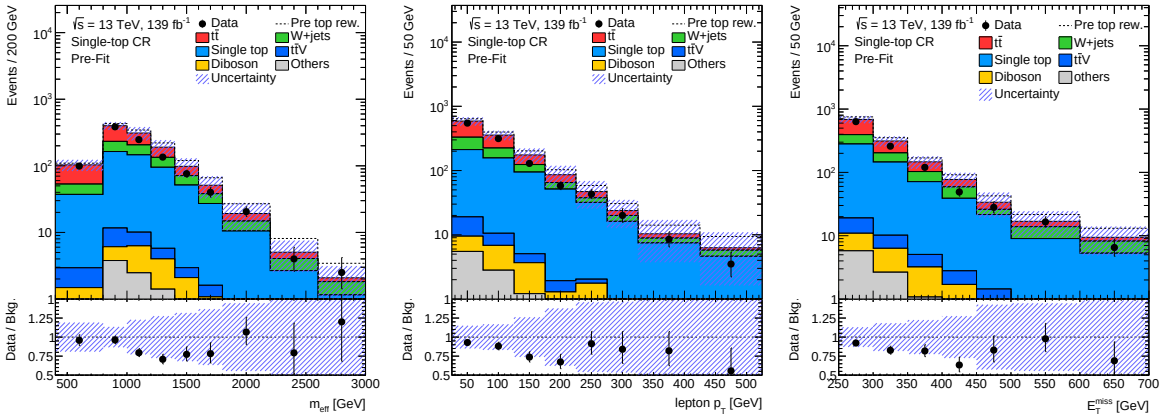

(a) **(b)** **(c)**

Figure 7.28: Distributions of (a) m_{eff}, (b) lepton p_{T}, and (c) $E_{\text{T}}^{\text{miss}}$ in the single-top CR after applying the top reweighting factors and before applying the fit to the CRs and SR ("Pre-Fit"). The contributions from $t\bar{t}H$, tWZ, and Z+jets are summarised as "Others". The hatched bands indicate the total uncertainty. The total background prediction before applying the top reweighting is shown as a dashed line. The lower panels show the ratio of the data to the SM prediction. The last bin contains the overflow.

7.6 Systematic uncertainties

Apart from uncertainties related to the statistical nature of the experiment, systematic uncertainties have to be considered when analysing experimental data. Sources for systematic uncertainties can be either experimental or theoretical. Experimental uncertainties are mainly related to the reconstruction of the final-state physics objects. They stem from detector limitations as well as from assumptions that are made during the reconstruction. Theoretical systematic uncertainties are associated with the modelling of the underlying processes. For example, some parameters are not determined a priori, and thus an assumption on their values has to be made. The impact of a chosen value is then covered by the corresponding systematic uncertainty. Both experimental and theoretical systematic uncertainties can affect the normalisation of signal and background processes as well as the shape of the distributions, i.e. bin-by-bin effects. In order to reduce statistical fluctuations and ensure a good fit stability, the systematic uncertainties are subject to a preprocessing procedure which is described in the following. Afterwards, first the theoretical systematic uncertainties considered in this analysis are explained and then the sources of experimental uncertainties are introduced.

7.6.1 Handling of systematic uncertainties

In order to avoid double counting of the normalisation components for the modelling systematic uncertainties of the background processes which are normalised in the fit, they are rescaled such that the sum of event yields in the CRs and SR is the same as the nominal prediction

for the considered process. Thus, only shape effects in binned distributions and acceptance effects between different analysis regions are considered.
Systematic uncertainties can be subject to statistical fluctuations. For example, the alternative MC sample to evaluate a systematic uncertainty can be statistically limited. These statistical fluctuations can cause unphysical under- and overestimates of the systematic uncertainty in single bins of a distributions. To overcome this effect, a smoothing procedure is applied averaging bin contents.
A systematic uncertainty can be either evaluated from one systematic variation, called one-sided systematics, or two systematic variations referred to as two-sided systematic uncertainty. In order to increase the fit stability, all systematic uncertainty templates are symmetrised. For a one-sided systematic, the given variation is mirrored about the nominal prediction, while for a two-sided systematic the two variations are shifted such that the nominal prediction is in the centre of the two variations.
Including all sources of systematic uncertainties, the statistical model becomes very complex. However, not all uncertainties have an impact on the final result. In order to simplify the statistical model and to improve the fit stability, a pruning procedure is applied separately for each CR and SR. The nuisance parameter for a systematic uncertainty is only considered if its effect on the event yield is larger than 1 % for a process in any bin. In this procedure, the normalisation and shape components for a source of systematic uncertainty are treated separately.

7.6.2 Theoretical systematic uncertainties

The largest source of systematic uncertainties considered in the analysis is related to modelling of the major background processes. For $t\bar{t}$ and single top-quark production a number of systematic uncertainties related to the modelling of the processes is applied.
The uncertainty on the matching procedure between ME generator and PS, denoted as "hard-scatter" uncertainty in the following, is assessed by comparing the nominal Powheg+Pythia samples to alternative samples produced with MG5_aMC@NLO+Pythia 8. Accordingly, the nominal samples are compared to Powheg+Herwig 7 samples to estimate the uncertainties in the modelling of the UE, PS, and hadronisation. Uncertainties related to the choice of the renormalisation and factorisation scales of the ME calculation are considered by independently varying the scales by factors 0.5 and 2. The impact of ISR is estimated by varying α_s in the A14 tune [188]. Similarly, the uncertainty related to FSR is assessed by varying the renormalisation scale for final-state parton-shower emissions by a factor of two. The uncertainty related to the choice of a scale for matching the ME-calculation of the $t\bar{t}$ process to the PS is evaluated by comparing the nominal sample to an alternative sample produced with the h_{damp} parameter set to $h_{\text{damp}} = 3.0\, m_{\text{top}}$.
Uncertainties due to PDFs are obtained using the PDF4LHC15 combined PDF set [201] with 30 symmetric eigenvectors. The nominal samples are reweighted to the central value and

the eigenvectors of the combined PDF set. The uncertainties are evaluated by taking the difference between the samples reweighted to the eigenvectors to the ones reweighted to the central value. The relative uncertainty is applied to the nominal samples.
A dominant systematic uncertainty in the modelling of the single top-quark process stems from the handling of the interference between $t\bar{t}$ and tW at NLO. The uncertainty is estimated by comparing the nominal sample for tW production generated with the DR scheme to an alternative sample using the DS scheme [178, 202]. An additional 30 % uncertainty is assigned to events with $t\bar{t}$ production in association with heavy-flavour jets [203].

Uncertainties on the top reweighting procedure arise from the functional form and statistical uncertainties in the top-reweighting region. These are accounted for by varying the parametrised function by $\pm 1\,\sigma$ from its nominal value, using the uncertainties of the fit parameters and taking their correlation into account. Each of the four jet bins for which the reweighting is determined is treated as an independent source of uncertainty.

For all other considered processes, namely V+jets, diboson, $t\bar{t}V$, $t\bar{t}H$, and tWZ production, the renormalisation and factorisation scales are independently varied by factors 0.5 and 2. In order to cover possible differences in the flavour composition of the W+jets background in the control and signal regions, a 30 % uncertainty is assigned to the heavy-flavour component of the W+jets process [204].

Backgrounds without a free floating normalisation parameter in the profile likelihood fit are assigned a theoretical uncertainty on the cross-section. For the $t\bar{t}H$ process an 11 % [205] uncertainty is considered, and for $t\bar{t}V$ and tWZ it amounts to 15 % and 12 % [205], respectively. The cross-section uncertainty is taken to be 6 % for diboson production [206] and to be 5 % for the Z+jets process [207].

7.6.3 Experimental systematic uncertainties

Apart from the theoretical systematic uncertainties, experimental uncertainties are considered in the analysis. Their sources are mainly the finite precision in the calibration and efficiency measurements for the reconstructed objects explained in Section 6. The most relevant experimental systematic uncertainties are those related to the jet calibration.

Lepton calibration

Uncertainties associated with leptons arise from the identification, isolation, and reconstruction efficiency determination for electrons and muons, as well as their energy scale and resolution measurements [158, 163]. They cover various sources of uncertainties which are relevant in the efficiency, scale, and resolution measurements. For muons, each efficiency uncertainty is split into a statistical and systematic component.

Jet calibration

The dominant uncertainties associated with jets stem from the uncertainties related to the small-R jet energy resolution (JER) and JES calibration [167]. Additional jet-related uncertainties are due to the JMS and the jet mass resolution (JMR), and the efficiency of the JVT requirements imposed to reject jets originating from pile-up.
The JES is calibrated in collision data, test-beam data, and simulation. Its uncertainty is decomposed into a set of 30 uncorrelated components, with contributions from the jet flavour composition, pile-up modelling, the single particle response, and jets not fully contained in the calorimeter. The JER uncertainties are split into 8 uncorrelated jet-p_{T} and η-dependent components. They are obtained from propagating the JES uncertainties and also taking into account uncertainty sources like the non-closure of the dijet balance or alternative MC generators. The Rtrk method [208] is used to derive the JMS uncertainties, which are composed of 8 independent components. The uncertainty on the JMR is estimated by comparing the nominal events to the same events in which the mass for each jet is smeared by a Gaussian function such that the measured jet mass resolution is worsened by 20 %. As the large-R jets are reclustered from small-R jets, no extra uncertainties are applied for the large-R jets.

Flavour tagging uncertainties

The flavour tagging efficiencies for b-, c-, and light-jets in simulation are corrected to match those measured in data, and uncertainties for these efficiency measurements are provided [170]. The flavour tagging uncertainties comprise 9 independent components for the b-jet identification, as well as 4 independent sources for c- and light-jets each. As the number of high-p_{T} b-jets is limited in data, an extrapolation uncertainty is included for jets with $p_{\mathrm{T}} > 400\,\mathrm{GeV}$. Furthermore, an uncertainty for the application of c-jet scale factors to τ-jets is applied. An extra 20 % uncertainty is applied on events containing only one b-tagged jet, where the jet with the second-highest b-tagging score does not originate from a truth bottom quark, to account for the selection of the two jets in the am_{T2} calculation.

Missing transverse momentum

The measurement of the missing transverse momentum is mainly affected by the calibrated objects in an event. The related uncertainties on these objects are propagated through the $E_{\mathrm{T}}^{\mathrm{miss}}$ calculation. Additional uncertainties are related to the scale and resolution of the track soft term [174].

Other experimental uncertainties

Additional contributions to the total systematic uncertainty come from the uncertainty in the integrated luminosity and the correction of the pile-up profile in simulation to match the one of data. The former was measured to be 1.7 % for the Run 2 data set recorded by ATLAS.

7.7 Statistical techniques

The statistical analysis is essential to evaluate the compatibility between the SM prediction and the observed data in a search for new physics. It is based on binned profile likelihood fits taking the predicted and observed events, as well as statistical and systematic uncertainties into account. Based on the concept of the likelihood function, hypothesis tests allow to evaluate the statistical relevance of a data excess compared to the SM prediction or to exclude a model of new physics. The concepts of likelihood fits and hypothesis tests are introduced in the following. A detailed explanation can be found in Ref. [209].

7.7.1 Profile likelihood fit

The statistical analysis is based on binned profile likelihood fits involving the expected and observed number of events in the bins of the CRs and the SR. The expected number of events in a bin i is defined as

$$E_i = \mu \cdot s_i + b_i. \tag{7.12}$$

Here, s_i is the number of expected events for the considered signal process with a free parameter μ for its normalisation, where the case $\mu = 1$ corresponds to the nominal signal prediction of the BSM model. The number of predicted background events, b_i, is defined as the sum of the predictions for the various background processes, $\sum_j \mu_j b_{ji}$, where μ_j is a multiplicative factor for background j. The factor μ_j is a free parameter for certain background processes whose normalisation is constrained by dedicated CRs, and fixed to one for other backgrounds.
Systematic uncertainties are included in the likelihood fit as nuisance parameters (NPs) with Gaussian constraint terms. Its probability density function (pdf) is

$$\rho(\theta) = \frac{1}{\sqrt{2\pi}\sigma} \exp\left(-\frac{(\theta-\theta_0)^2}{2\sigma^2}\right), \tag{7.13}$$

with mean θ_0 and standard deviation σ. It is common to define the NPs such that the mean of the pdf is zero and its standard deviation is one. Apart from the systematic uncertainties described in Section 7.6, the MC statistical uncertainties, γ, are considered for each bin in the fit using Poisson constraint terms. Assuming a Poisson distribution for data in each bin, the likelihood function, L, is therefore given by

$$L\left(\mu, \vec{\theta}\right) = \prod_{i=1}^{N} \frac{(\mu \cdot s_i + b_i)^{n_i}}{n_i!} e^{-(\mu \cdot s_i + b_i)} \prod_{j=1}^{M} \rho(\theta_j), \tag{7.14}$$

where n_i is the number of observed events in each bin and θ_j one of the M NPs with its constraint term $\rho(\theta_j)$. Both the signal and background expectation, s_i and b_i, depend implicitly on the NPs.

In the likelihood fits, the likelihood function is maximised within the constraints of the NPs. The signal strength is set to zero, i.e. $\mu = 0$, in so-called background-only fits, while the signal strength is a free parameter in signal-plus-background fits. Deviations of NPs from mean zero obtained in the maximisation of the likelihood function are called pulls, while the reduction of their variance is termed constraint. Pulls can happen when the prediction according to the systematic variation is found to agree better with data than the nominal prediction. The understanding of both pulls and constraints is important to verify the validity of the underlying statistical model.

7.7.2 Hypothesis tests

Hypothesis tests are performed to either determine the potential of a discovery or to set exclusion ranges for signal models. For the purpose of discovering a new signal process, the null hypothesis, H_0, which corresponds to the SM prediction, i.e. $\mu = 0$, is tested against an alternative hypothesis, H_1, including the background plus signal prediction. In the case of setting limits on signal model parameters, the roles of hypotheses are changed as the signal-plus-background prediction is considered as null hypothesis that is tested against the background-only hypothesis.

According to the Neyman-Pearson lemma [210], the likelihood ratio is the most powerful test statistic to distinguish between two hypotheses at a given significance level α. The so-called profile-likelihood ratio is defined as

$$\lambda(\mu) = \frac{L(\mu, \hat{\hat{\vec{\theta}}})}{L(\hat{\mu}, \hat{\hat{\vec{\theta}}})}. \tag{7.15}$$

Here, $\hat{\mu}$ and $\hat{\vec{\theta}}$ are the values of the signal strength and the set of NPs that maximise the likelihood function, and $\hat{\hat{\vec{\theta}}}$ maximises the likelihood function for a given signal normalisation μ. The likelihood ratio takes values in the range $0 \leq \lambda \leq 1$, where λ close to one implies good agreement between the data and the prediction for the considered value of μ.

Often the modified version

$$q_\mu = -2 \cdot \ln \lambda(\mu) \tag{7.16}$$

is used as the test statistic instead. In order to quantify the level of compatibility between the observed data and a considered value of μ, the p-value can be computed. It is defined as

$$p_\mu = \int_{q_{\mu,obs}}^{\infty} f(q_\mu|\mu)\, dq_\mu, \tag{7.17}$$

where $f(q_\mu|\mu)$ denotes the pdf of the statistic q_μ under the assumption of the signal strength μ, and $q_{\mu,obs}$ is the value of the test statistic observed from data. In particle physics, it is

common to convert the p-value into a significance Z, which is defined as

$$Z = \Phi^{-1}(1-p), \tag{7.18}$$

where Φ^{-1} is the quantile, i.e. the inverse of the cumulative distribution, of the standard Gaussian. To regard a hypothesis as excluded, the p-value has to be observed below a specified threshold. Exclusion limits on a signal model are conventionally set at the 95 % CL at which the p-value is below 5 %, corresponding to a Gaussian significance of $Z = 1.64$. When claiming the rejection of the background-only hypothesis, much stricter requirements are in place. A new discovery is claimed at the 5σ threshold, corresponding to $p_0 < 2.87 \cdot 10^{-7}$.

Assuming that the presence of a new signal only increases the event yield with respect to the SM prediction, the signal strength is bound from below by zero, i.e. $\mu \geq 0$. An extended version of the likelihood ratio, $\tilde{\lambda}$, is defined as

$$\tilde{\lambda} = \begin{cases} \dfrac{L\left(\mu, \hat{\hat{\vec{\theta}}}(\mu)\right)}{L\left(\hat{\mu}, \hat{\vec{\theta}}\right)} & \text{if } \hat{\mu} \geq 0, \\ \dfrac{L\left(\mu, \hat{\hat{\vec{\theta}}}(\mu)\right)}{L\left(0, \hat{\hat{\vec{\theta}}}(0)\right)} & \text{if } \hat{\mu} < 0. \end{cases} \tag{7.19}$$

In the case of $\hat{\mu} < 0$, $\hat{\mu}$ is replaced with zero, corresponding to the background-only prediction, as the best agreement between data and a non-negative value of μ occurs for $\mu = 0$.

When setting upper limits on the signal strength parameter μ, the case $\hat{\mu} > \mu$ is not considered as representing less compatibility with μ and therefore is not included further in the test by setting $q_\mu = 0$.

Using this consideration and the likelihood ratio $\tilde{\lambda}$, an extended test statistic is defined as

$$\tilde{q}_\mu = \begin{cases} -2\ln \dfrac{L\left(\mu, \hat{\hat{\vec{\theta}}}(\mu)\right)}{L\left(0, \hat{\hat{\vec{\theta}}}(0)\right)} & \text{if } \hat{\mu} < 0, \\ -2\ln \dfrac{L\left(\mu, \hat{\hat{\vec{\theta}}}(\mu)\right)}{L\left(\hat{\mu}, \hat{\vec{\theta}}\right)} & \text{if } 0 \leq \hat{\mu} \leq \mu, \\ 0 & \text{if } \hat{\mu} > \mu. \end{cases} \tag{7.20}$$

In order to set upper limits on the signal strength μ, the p_μ-value is calculated with the $\tilde{q}_\mu$ test statistic for a range of μ-values. The pdf of the test statistic can be obtained from pseudo-experiments following the respective hypothesis. As this sampling becomes computational expensive when scanning many possible signal hypotheses, e.g. all combinations of signal masses and branching ratios for VLQs, an approximation for the likelihood ratio can be used instead for which the pdf can be calculated analytically. The approximated test statistic is

given by

$$\tilde{q}_\mu = \begin{cases} \frac{\mu^2}{\sigma^2} - \frac{2\mu\hat{\mu}}{\sigma^2} & \text{if } \hat{\mu} < 0, \\ \frac{(\mu-\hat{\mu})^2}{\sigma^2} & \text{if } 0 \leq \hat{\mu} \leq \mu, \\ 0 & \text{if } \hat{\mu} > \mu. \end{cases} \tag{7.21}$$

Here, $\hat{\mu}$ follows a Gaussian distribution with mean μ' and the standard deviation σ. Instead of the p-value, the CL_s method [211] can be used in order to avoid exclusions due to statistical fluctuations. The CL_s is defined as

$$\mathrm{CL}_s = \frac{p_\mu}{1 - p_0}, \tag{7.22}$$

where p_0 is defined as the p-value for $\mu = 0$. Signal hypotheses are excluded at the 95 % CL when $\mathrm{CL}_s < 0.05$ for a given signal strength μ. The signal cross-section is multiplied with the upper limit on the signal strength in order to get the cross-section limit.

7.8 Results

The final step of the analysis is the statistical evaluation using the techniques described in Section 7.7. Simultaneous profile likelihood fits to the CRs and the SR are performed, using the overall number of events in the CRs and five bins in the signal-enriched part of the NN_{out} distribution. The binning of the SR is chosen as $[0.5, 0.7, 0.8, 0.9, 0.95, 1.0]$, where the fine binning at high NN_{out} values is motivated by the good separation power of the NN resulting in a large fraction of the signal events above $NN_{\mathrm{out}} > 0.9$. In principle, an even finer binning could be chosen to increase the sensitivity of the analysis. However, low statistics in observed data and simulated MC events could potentially lead to fit instabilities and a large impact of the MC statistics on the final result.

7.8.1 Background-only fit results

In order to evaluate the compatibility of the observed data with the SM expectation, likelihood fits are performed for each of the seven NNs under the background-only hypothesis. The obtained normalisation factors for the $t\bar{t}$, W+jets, and single top-quark processes vary between the fits for the different NNs, between 1.00 ± 0.28 and 1.14 ± 0.27 for $t\bar{t}$, between 0.91 ± 0.19 and 1.08 ± 0.17 for W+jets, and between 0.53 ± 0.30 and 0.60 ± 0.23 for single top-quark production. As the reweighting for the $t\bar{t}$ and single top-quark processes has been applied before, changing both the shape and normalisation of the two processes, the obtained normalisation factors cannot be interpreted as a simple scaling of the original cross-section. The reduction of the single top-quark contribution is sizeable but is still within the large difference between the nominal and alternative scheme to model the interference between the $t\bar{t}$ and tW processes.

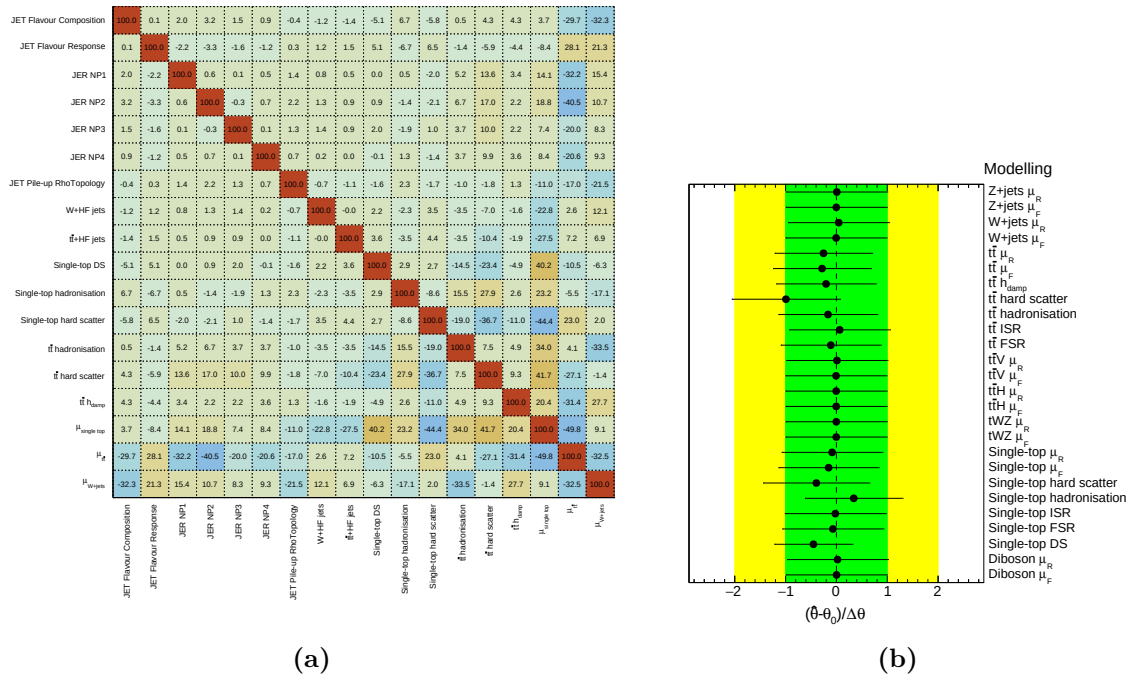

(a) **(b)**

Figure 7.29: (a) Correlations between NPs and normalisation factors in a background-only fit in CRs and SR. Only parameters having a correlation of at least 20 % with at least one other parameter are displayed in the matrix. (b) Pulls and constraints of NPs related to the modelling of the background processes. In both cases, the low-NN_{out} CR and SR corresponding to the NN trained for a VLT signal with $\mathcal{B}(Zt, Ht, Wb) = (0.8, 0.1, 0.1)$ are used in the fit.

One reason for the differences in the normalisation factors between the seven fits are the correlations between the normalisation factors and the systematic uncertainties, which are illustrated in Figure 7.29a for the NN trained for the VLT signal with $\mathcal{B}(Zt, Ht, Wb) = (0.8, 0.1, 0.1)$, serving as a benchmark signal in the following. The pre- and post-fit distributions of the CRs and the SR for this benchmark signal can be found in Appendix B.4. Large anti-correlations between the normalisation factors for $t\bar{t}$ and single top ($-49.8\,\%$) and the ones for $t\bar{t}$ and W+jets ($-32.5\,\%$) are visible. These anti-correlations can explain some of the differences between the normalisation factors between the different fits, as the fit resulting in the smallest normalisation factor for $t\bar{t}$ has the largest normalisation factor for W+jets. On the other hand, also pulls of the NPs can have an impact on the values of the normalisation factors. The strongest pulls are visible for the uncertainties related to the modelling of $t\bar{t}$ and single top, illustrated for the exemplary fit in Figure 7.29b. The NP pulls of all considered systematic uncertainties in this fit can be found in Appendix B.4. The largest pull in all fits is a -1σ pull for the $t\bar{t}$ hard scatter uncertainty in the discussed fit. All other pulls are smaller than 0.5σ. The largest constraint of about 25 % is visible for the single-top DS uncertainty. The systematic templates for this uncertainty are shown for the single-top CR and a SR in Figure 7.30. The same top reweighting is applied for both tW DR and tW DS. In order to be

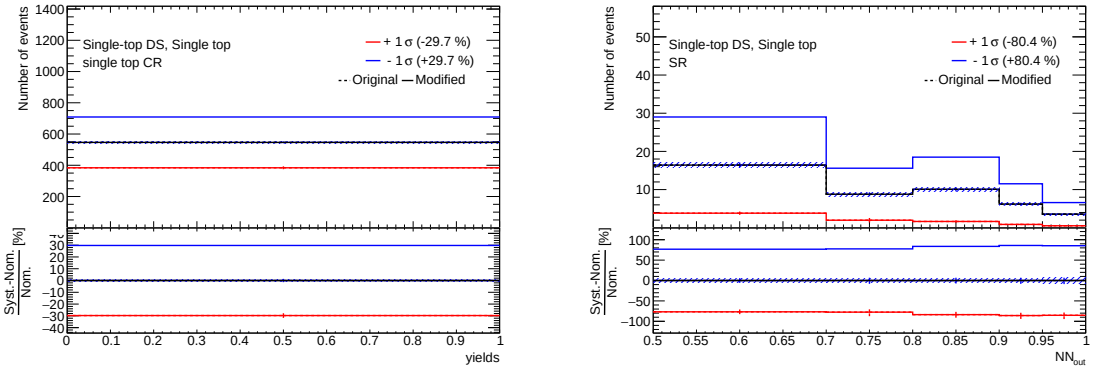

(a) **(b)**

Figure 7.30: Systematic variations corresponding to the single-top DS NP in (a) the single-top CR and (b) the SR. The lower panels show the relative difference between the predictions for the variations and the nominal.

on the conservative side, considering also potential effects of the reweighting, the uncertainty is symmetrised. Due to the size of this systematic uncertainty, the observed constraint is therefore expected.

After discussing the proper handling of the systematic uncertainties in the fit, the post-fit distributions are analysed in the following. First, the overall number of events for the different background processes in the CRs and the SR resulting from the fit, using the NN trained for $\mathcal{B}(Zt, Ht, Wb) = (0.8, 0.1, 0.1)$, are given in Table 7.5. In addition, the expected signal yields for a VLT signal are listed. The numbers for the NN trained for the VLB signal with $\mathcal{B}(Zb, Hb, Wt) = (0.1, 0.1, 0.8)$ are given in Appendix B.4. The large (anti-)correlations between the different processes lead to a strong reduction of the uncertainty on the total background prediction. A comparison of the observed data to the SM prediction indicates a good agreement within the uncertainties. As the SRs are divided into five bins, it is important to check the post-fit distributions as well. These are shown for three representative NNs in Figure 7.31. Overall a good agreement between the data and the background prediction is visible. In Figure 7.31a, a small upward fluctuation is visible in the fourth bin of the SR. Similarly, small fluctuations are visible in the three last bins of Figure 7.31b. The expected signal contributions are added on top of the background prediction, indicating that the most sensitive bins are the ones for $NN_{\text{out}} > 0.9$. The NN_{out} distributions of the other SRs can be found in Appendix B.5.

Table 7.5: Observed and expected event yields including their total uncertainty (stat.+syst.) in the control and signal regions considering an NN training for a VLT signal with a branching ratio of $\mathcal{B}(Zt, Ht, Wb) = (0.8, 0.1, 0.1)$ after the background-only fit. For comparison, the expected event yields for a VLT signal with a mass of 1.2 TeV and a branching ratio of $\mathcal{B}(Zt, Ht, Wb) = (0.8, 0.1, 0.1)$ are given.

	W+jets CR	Single-top CR	low-NN_{out} CR	SR
$t\bar{t}$	1720 ± 400	520 ± 130	730 ± 140	79 ± 31
W+jets	2610 ± 370	256 ± 47	231 ± 54	37.7 ± 9.1
Single top	170 ± 150	320 ± 140	143 ± 85	40 ± 30
$t\bar{t}V$	20.4 ± 3.2	15.9 ± 2.6	132 ± 21	23.9 ± 4.0
Diboson	140 ± 17	14.2 ± 2.4	65.4 ± 8.9	12.1 ± 1.8
Z+jets	14.0 ± 3.8	3.85 ± 0.75	4.80 ± 0.73	1.14 ± 0.13
$t\bar{t}H$	2.55 ± 0.33	5.59 ± 0.69	10.9 ± 1.3	2.27 ± 0.33
tWZ	0.90 ± 0.12	0.82 ± 0.11	10.0 ± 1.3	1.89 ± 0.28
Total background	4676 ± 70	1140 ± 34	1322 ± 37	198 ± 14
Data	4676	1135	1321	206
$m_T = 1.2$ TeV				
$\mathcal{B}(Zt, Ht, Wb) = (0.8, 0.1, 0.1)$	0.35 ± 0.12	0.96 ± 0.13	7.01 ± 0.51	53.8 ± 1.8

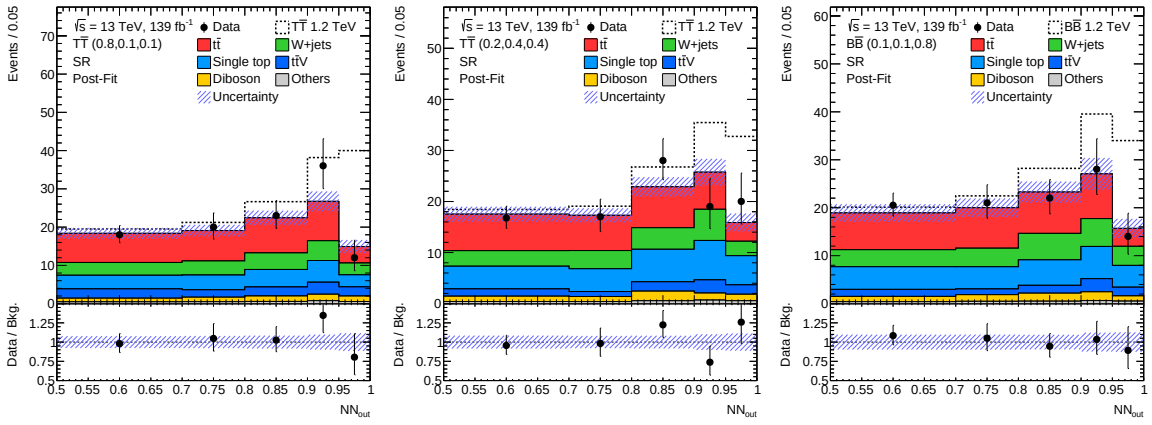

(a) **(b)** **(c)**

Figure 7.31: Data and background expectation in the signal region after the simultaneous background-only fit to data ("Post-Fit") for (a) a NN training for a VLT signal with $\mathcal{B}(Zt, Ht, Wb) = (0.8, 0.1, 0.1)$, (b) a NN training for a VLT signal with $\mathcal{B}(Zt, Ht, Wb) = (0.2, 0.4, 0.4)$, and (c) a VLB signal with $\mathcal{B}(Zb, Hb, Wt) = (0.1, 0.1, 0.8)$. Contributions from $t\bar{t}H$, tWZ, and Z+jets are combined into "Others". Expected pre-fit signal distributions with the signal branching ratio corresponding to the respective training are added on top of the background expectation, using a signal mass of 1.2 TeV. The hatched bands indicate the total post-fit uncertainty. The ratio between the data and the background expectation is shown in the bottom panels.

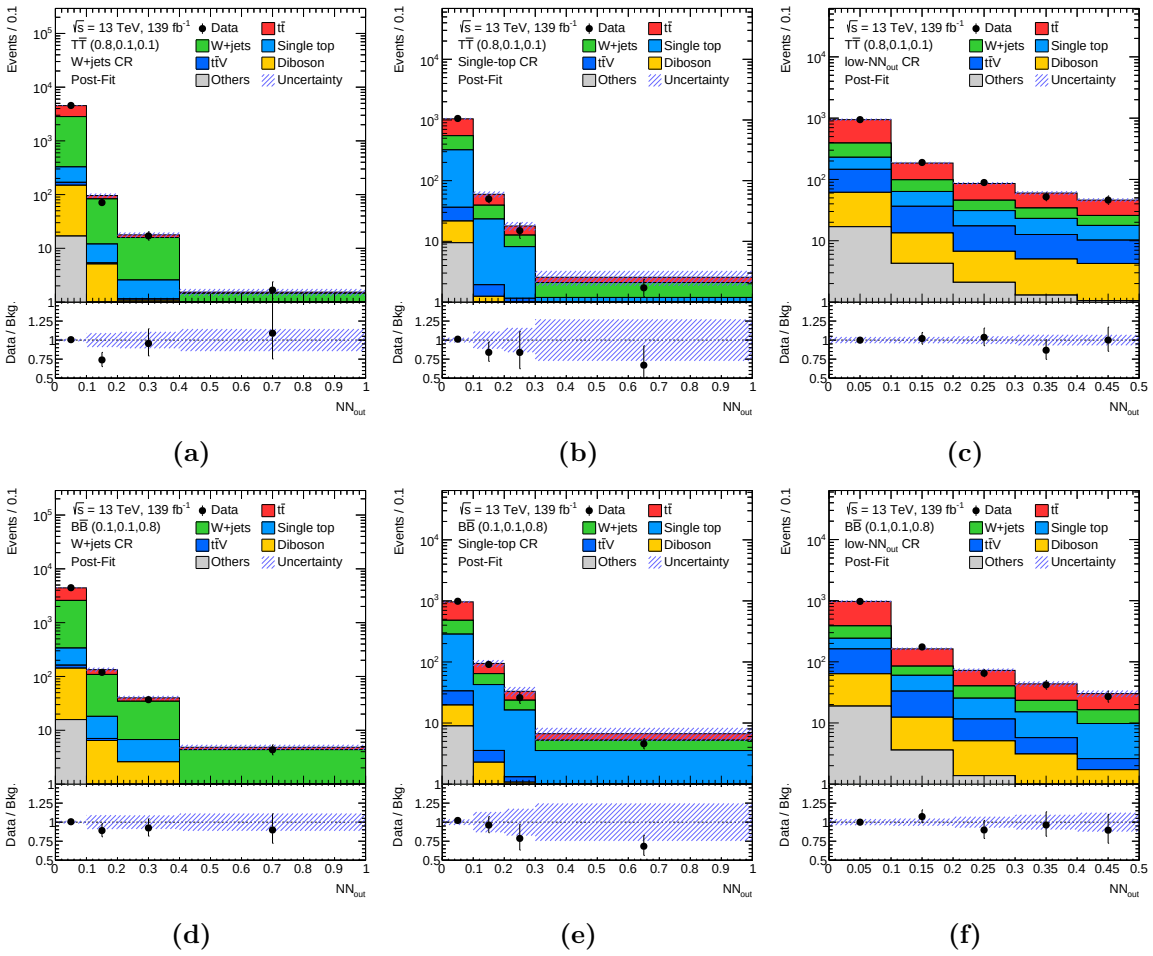

Figure 7.32: Data and background expectation in the W+jets CR (left panels), the single-top CR (middle panels), and the low-NN_{out} CR (right panels) after a background-only fit to data ("Post-Fit") for a NN considering a VLT signal with $\mathcal{B}(Zt, Ht, Wb) = (0.8, 0.1, 0.1)$ (upper panels) and a VLB signal with $\mathcal{B}(Zb, Hb, Wt) = (0.1, 0.1, 0.8)$ (lower panels), respectively. Minor background contributions from $t\bar{t}H$, tWZ, and Z+jets are combined into "Others". The hatched bands indicate the post-fit uncertainty. The lower panels show the ratio of data to the background expectation.

Apart from including the CRs as a single bin in the fit, they are used to validate the NN_{out} distributions after the likelihood fit. Figure 7.32 shows the corresponding post-fit distributions in the three CRs for two NNs. For the low-NN_{out} CR and the W+jets CR, a good agreement within uncertainties is visible across the whole NN_{out} distribution. The largest deviation between data and prediction in the W+jets CR is visible in the second bin in Figure 7.32a, which is the largest deviation in this CR for all seven NNs. For the single-top CR a downward trend in the data-prediction ratio is visible. As the single-top CR is used as a single bin in the fit, shape information is not included and, therefore, shape differences cannot be corrected. However, the visible deviations are still within the assigned uncertainties.

7.8.2 Signal-plus-background fits

As a next step, signal contributions are considered in the likelihood function, including the signal strength as an additional free parameter. In order to understand the impact of the NPs on the fitted signal strength, so-called ranking plots are produced. These are shown for two signal scenarios in Figure 7.33. The impact of a NP on the signal strength, $\Delta\mu$, is given by the shift in the signal strength between the nominal fit and another fit where the NP is fixed to $\hat{\theta} \pm x$. Here, x is defined as $\Delta\theta$, i.e. the original $\pm 1\sigma$ variation, for the pre-fit impact, while $x = \Delta\hat{\theta}$ is used for the evaluation of the post-fit impact, taking therefore constraints of the NPs into account. The impact is evaluated for all NPs, which are finally ranked according to their post-fit impact.

The systematic uncertainties with the largest impact slightly vary between the different NNs and considered signal scenarios. However, overall the modelling of the top-quark processes has the largest impact on the signal strength. In particular, the single-top DS NP is one of the highest ranked uncertainties for many scenarios. This is related to the magnitude of this uncertainty in the SR as discussed before. Also, the free-floating background normalisation factors are often within the highest ranked uncertainties. The most important experimental systematic uncertainty is related to the JER. In general, the latter is more relevant for VLB than for VLT signals. The ranking plots include the pulls and constraints of the fits under the signal-plus-background hypothesis. Comparing these with the ones from the background-only fits allows to ensure that no unexpected changes occur.

Apart from the ranking plots, another way to evaluate the relevance of certain NPs is to calculate the uncertainty on the signal strength due to a particular group of NPs. The likelihood fits are repeated multiple times, fixing a set of NPs to their best fit values. Comparing the obtained uncertainty on the signal strength, $\Delta\mu^2_{\text{not}\,i}$, where the NPs of group i are fixed, with the one from the nominal fit, $\Delta\mu^2_{\text{orig}}$, via

$$\Delta\mu_i^2 = \Delta\mu^2_{\text{orig}} - \Delta\mu^2_{\text{not}\,i}, \tag{7.23}$$

allows for the determination of the impact of a defined group of NPs. The impact of the statistical uncertainties is accordingly evaluated by fixing all systematic uncertainties and background normalisation factors to their best fit values.

The results for a VLT signal with exclusive $T \to Zt$ decays and a mass of 1.4 TeV are given in Table 7.6. For this scenario, statistical uncertainties are more relevant than systematic uncertainties. Within the systematic uncertainties, the dominant ones are related to the modelling of the $t\bar{t}$ and single top-quark processes. Further relevant sources of uncertainties are the normalisation factors, the jet calibration, and the uncertainties of the γ-factors.

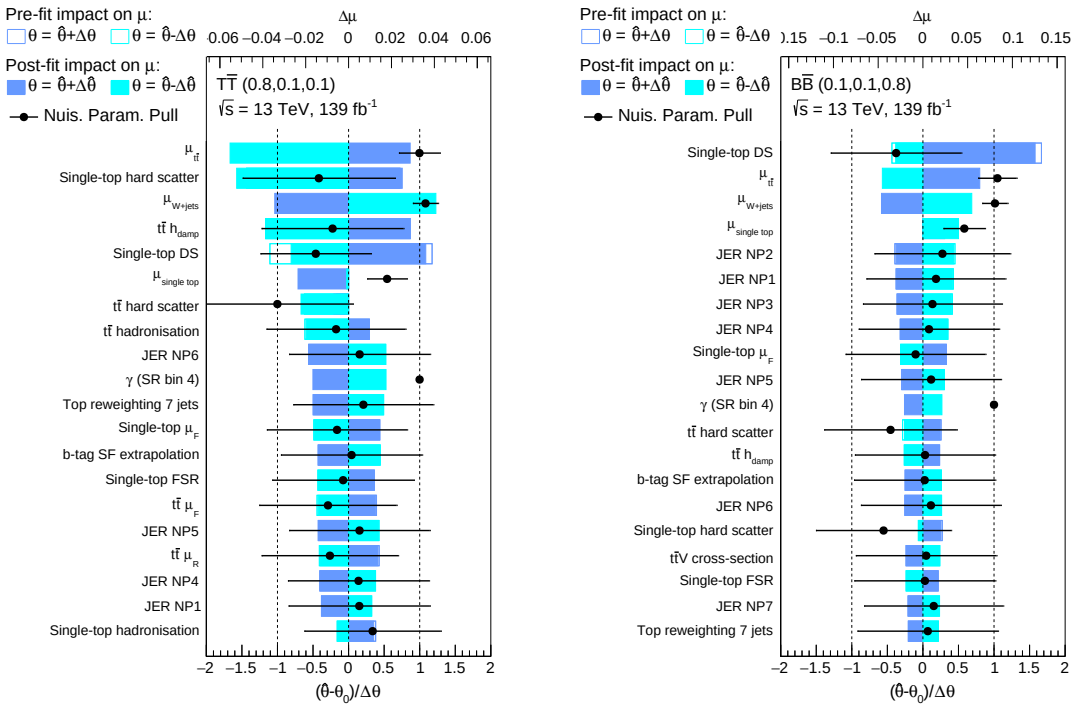

Figure 7.33: Ranking of NPs included in signal-plus-background fits of (a) a NN trained for a VLT signal with $\mathcal{B}(Zt, Ht, Wb) = (0.8, 0.1, 0.1)$ and (b) a VLB signal with $\mathcal{B}(Zb, Hb, Wt) = (0.1, 0.1, 0.8)$. The NPs are ranked according to their impact on the observed signal strength, $\Delta\mu$, which is evaluated by comparing the nominal fit result with the result of a fit where the respective NP is fixed to its uncertainty. Pre-fit impacts are indicated by empty boxes with blue borders, while post-fit impacts are shown as filled boxes. Pulls of the NPs and their post-fit uncertainties are shown as black points and error bars.

7.8.3 Exclusion limits on signal parameters

As no significant deviation from the SM expectation is found, 95 % CL upper limits on the pair-production cross-section of T and B quarks are derived as a function of the signal mass for various signal hypotheses using the statistical techniques described in Section 7.7. For each signal mass and branching ratio, the NN with the best expected limit is selected. As the NNs are trained for various branching ratios, each NN should have the best performance in a specific part of the signal branching ratio plane. This expectation is confirmed in Figure 7.34a, indicating the selected NN for various signal branching ratios using a VLT signal with a mass of 1.4 TeV.

In order to evaluate the sensitivity gain by using NNs trained for different branching ratios, the best expected limit is compared to the one obtained with the NN trained for $\mathcal{B}(Zt, Ht, Wb) = (0.8, 0.1, 0.1)$, serving as a reference. The relative differences in the expected limits are illustrated in Figure 7.34b for T quarks with a mass of 1.4 TeV. The largest differences in the expected limit are visible for large fractions of $T \to Wb$ decays, with improvements

Table 7.6: Breakdown of the contributions to the uncertainties $\Delta\mu$ on the signal strength μ for a VLT signal with exclusive $T \to Zt$ decays and $m = 1.4\,\text{TeV}$. The fitted signal strength in a signal-plus-background fit in the CRs and SR is $\mu = -0.14 \pm 0.35$. The total uncertainty is different from the sum in quadrature of the various uncertainty components due to their correlations in the fit.

Uncertainty Group	$\Delta\mu_i$
Lepton Calibration	$\pm 0.01 \cdot 10^{-1}$
Jet Calibration	$\pm 0.61 \cdot 10^{-1}$
Flavour Tagging	$\pm 0.28 \cdot 10^{-1}$
$E_{\text{T}}^{\text{miss}}$ Soft Term	$\pm 0.07 \cdot 10^{-1}$
Cross-section	$\pm 0.22 \cdot 10^{-1}$
Top Modelling	$\pm 1.35 \cdot 10^{-1}$
Other Modelling	$\pm 0.21 \cdot 10^{-1}$
γ-Factors	$\pm 0.43 \cdot 10^{-1}$
Normalisation Factors	$\pm 0.73 \cdot 10^{-1}$
Statistical	$\pm 2.97 \cdot 10^{-1}$
Full Systematics	$\pm 1.86 \cdot 10^{-1}$
Total	$\pm 3.50 \cdot 10^{-1}$

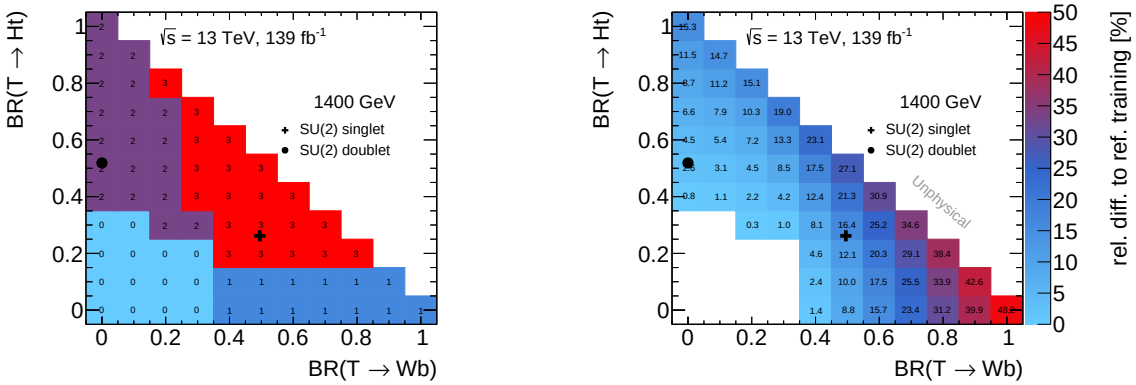

(a) **(b)**

Figure 7.34: (a) Selected NN resulting in the best expected limit for different branching ratios of the VLTs with a mass of $m = 1.4\,\text{TeV}$. The relation of the NN number to the signal branching ratio $\mathcal{B}(Zt, Ht, Wb)$ used in the training is as follows: NN0: $(0.8, 0.1, 0.1)$, NN1: $(0.4, 0.1, 0.5)$, NN2: $(0.4, 0.5, 0.1)$, NN3: $(0.2, 0.4, 0.4)$. (b) Relative difference of the best expected limit with respect to the expected limit of the NN trained for the VLT signal with $\mathcal{B}(Zt, Ht, Wb) = (0.8, 0.1, 0.1)$, serving as a reference.

up to about 40 %. For larger fractions of $T \to Ht$ decays the improvement is just of the order of 10 % as the $T \to Zt$ decays are kinematically closer to the $T \to Ht$ decays than to the $T \to Wb$ decays as in the latter no top quark is in the final state.

The obtained upper limits on the VLQ pair-production cross-section are compared to the theoretical cross-section to obtain lower limits on the signal mass. The limits are calculated for

Table 7.7: Expected (Exp.) and observed (Obs.) mass limits for the pair production of specific VLQs (T, B, X) in certain decay scenarios corresponding to SU(2) singlet or doublet representations, or to the decay into just one specific final state. In the doublet scenarios, contributions from the VLQ partner are not considered, leading to conservative limits, except for the last row where the VLQs in the doublet are assumed to be mass degenerate.

VLQ	Scenario	Exp. limit [TeV]	Obs. limit [TeV]
T	$\mathcal{B}(T \to Zt) = 100\,\%$	1.45	1.47
T	singlet	1.33	1.26
T	(T, B) or (X, T) doublet	1.41	1.41
B	singlet	1.30	1.33
B/X	$\mathcal{B}(B/X \to Wt) = 100\,\%$ or $(T, B)/(X, T)$ doublet	1.42	1.46
$T/B/X$	(T, B) or (X, T) doublet, mass degenerate	1.56	1.59

T and B quarks in the weak-isospin singlet and doublet representations, with mass dependent branching ratios, as well as for pure $T \to Zt$ and $B \to Wt$ decays. The latter is equivalent, except for charges, to the $X \to Wt$ decay and corresponds to the (T, B) doublet. As the analysis does not distinguish between particles and antiparticles, the limits for $B \to Wt$ apply to the $X \to Wt$ decays. Analogously, the limits of the (T, B) and (T, X) doublet scenarios are equivalent. For the doublet scenarios, only the contributions from one of the two VLQ types are considered, leading to conservative limits. The obtained expected and observed mass limits for the aforementioned scenarios are summarised in Table 7.7. The corresponding limits on the pair-production cross-section are shown in Figures 7.35a-7.35e.

For the (T, B) doublet scenario, limits are also calculated considering the contributions from both T and B quarks, assuming mass degeneracy. The latter is motivated by the fact that constraints from theory [34, 212] allow mass differences of at most a few GeV. The resulting upper limits on the signal cross-section are shown in Figure 7.35f. T and B quarks in this specific scenario are excluded below 1.59 TeV, see Table 7.7.

Apart from setting limits for specific models and branching ratios, lower limits on the signal mass are set as a function of the branching ratios of the T and the B quark. The resulting expected and observed limits are shown in Figure 7.36. As expected, the highest limits are found in the regions of $\mathcal{B}(T \to Zt) = 100\,\%$ and $\mathcal{B}(W \to Wt) = 100\,\%$. For the T quark, the sensitivity for mixed $ZtHt$ decay modes is slightly higher than for $ZtWb$ decays. Some deviations between the expected and observed limit are visible in the branching ratio region around the SU(2) singlet point. The respective limits are obtained from the NN trained for a branching ratio of $\mathcal{B}(Zt, Ht, Wb) = (0.2, 0.4, 0.4)$, where in the last bin, Figure 7.31b, slightly more data than predicted SM background are visible. For the B quark, the sensitivity decreases for an increasing fraction of $B \to Zb$ decays. For small fractions of $B \to Wt$ decays, the analysis does not have sensitivity for the corresponding decay modes such that

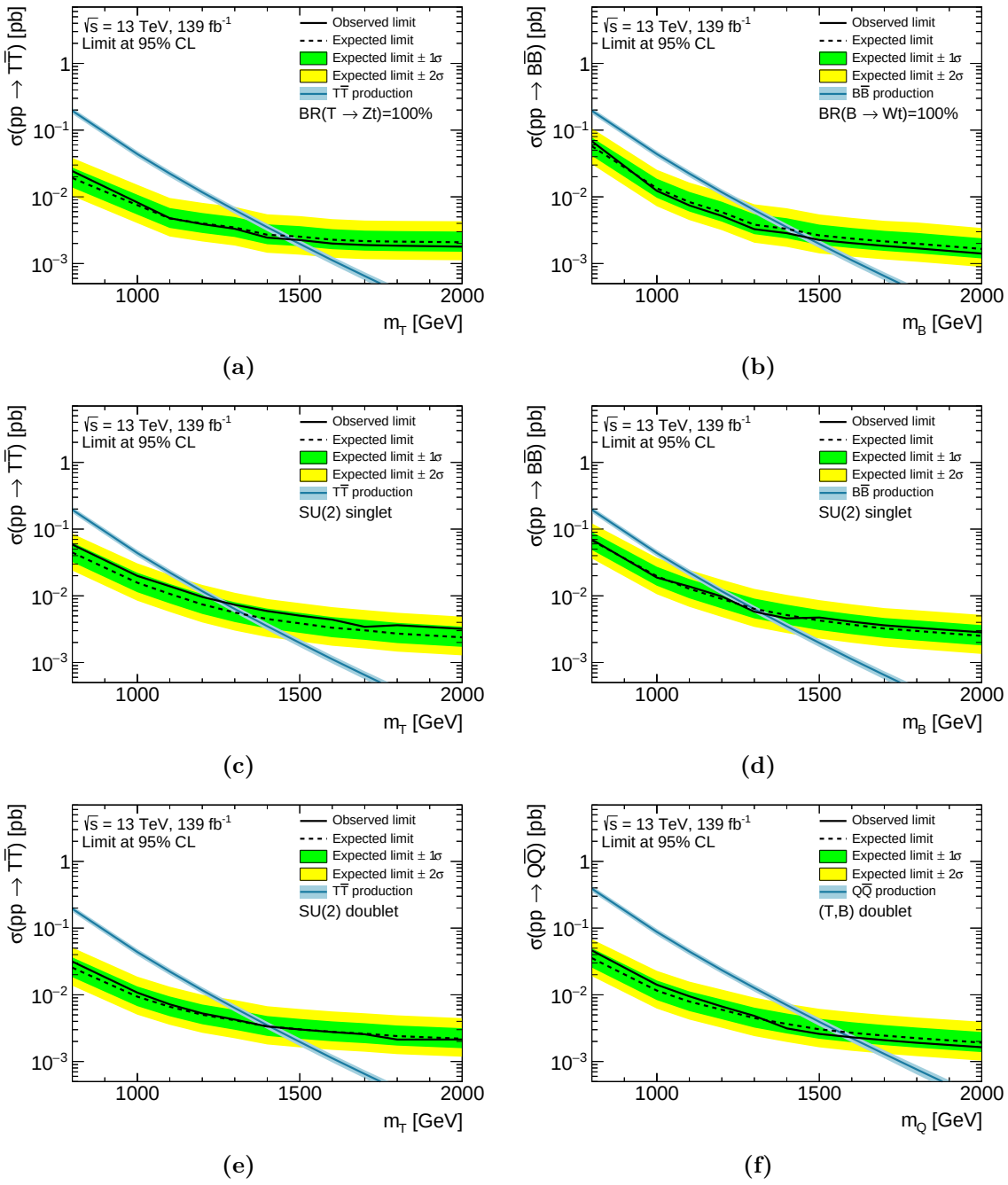

Figure 7.35: Expected and observed 95 % CL upper limits on the cross-section of pair-produced VLQs for (a) $\mathcal{B}(T \to Zt) = 100\,\%$, (b) $\mathcal{B}(B \to Wt) = 100\,\%$, (c) a T quark in the SU(2) singlet representation, (d) a B quark in the SU(2) singlet representation, and (e) a T quark in the SU(2) doublet. In these cases, contributions from either the T or B quark are considered. In (f), the limits are given for the (T, B) doublet, considering signal contributions from both the VLTs and the VLBs. The thickness of the theory curve represents the theoretical uncertainty from PDFs, scale, and the strong coupling constant α_s.

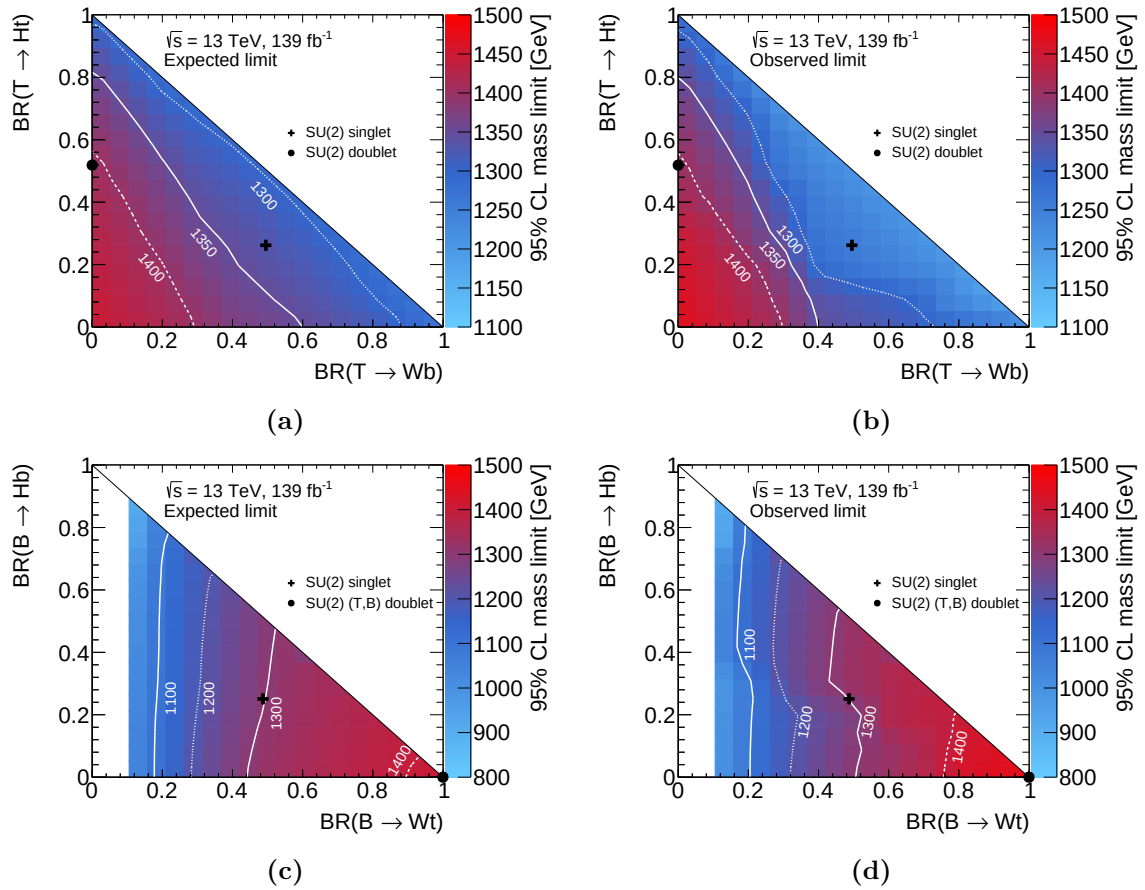

Figure 7.36: Expected (left) and observed (right) mass limits for $T\bar{T}$ (upper row) and $B\bar{B}$ (lower row) production. The mass limit is calculated using the NN with the best expected limit at each signal mass and branching ratio point. The white lines indicate mass exclusion contours. The black markers indicate the branching ratios for the SU(2) singlet and doublet scenarios with masses above 800 GeV, where they are approximately independent of the VLQ mass. The white areas indicate that no mass limits can be set for the respective branching ratios.

for branching ratio combinations with $\mathcal{B}(B \to Wt) = 0\,\%$ no lower limits on the mass can be set. Finally, the impact of the systematic uncertainties on the mass limit is evaluated for the $\mathcal{B}(T \to Zt)$ scenario, illustrated in Figure 7.37. For the higher masses, the statistical uncertainties are more important than the systematic uncertainties. However, the systematic uncertainties become more relevant for the smaller masses, indicated by the larger differences between the expected limits using both statistical and systematic uncertainties, and the expected limits based on solely statistical uncertainties. The systematic uncertainties decrease the expected limit by about 40 GeV to a value of 1.45 TeV for the discussed scenario.

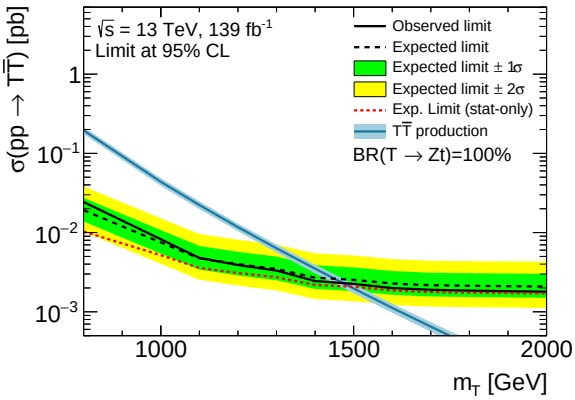

Figure 7.37: Expected and observed 95 % CL upper limits on the cross-section of $T\bar{T}$ production for $\mathcal{B}(T \to Zt) = 100\,\%$. The thickness of the theory curve represents the theoretical uncertainty from PDFs, scale, and the strong coupling constant α_s. In order to evaluate the impact of systematic uncertainties on the cross-section and mass limits, the expected stat.-only limit is presented by the red, dashed line.

7.8.4 Comparison to other VLQ searches

As already outlined in Section 2.2, searches for VLQs have been performed by both the ATLAS and the CMS collaboration, and limits on the various types of VLQs and decay modes have been set. In order to evaluate the relevance of the limits obtained in the search presented in this dissertation, they are compared to the results from existing searches published by the ATLAS collaboration. An overview about the lower limits on the signal mass, which are compared in the following, is given in Table 7.8.

First, the limits are compared to the search for VLQs in the same final state using the partial Run 2 data set [50]. For the $\mathcal{B}(T \to Zt) = 100\,\%$ scenario, the observed limit has been improved from 1.16 TeV to 1.47 TeV. Even stronger increases have been obtained for

Table 7.8: Comparison of observed mass limits for the pair production of specific VLQs for certain decay scenarios corresponding to SU(2) singlet or double representations or to the decay into one specific final state.

Analysis Data set		Thesis 139 fb^{-1}	$1\ell + E_{\mathrm{T}}^{\mathrm{miss}}$ 36 fb^{-1}	VLQ comb. 36 fb^{-1}	OSML 139 fb^{-1}
VLQ	Scenario	Obs. limit [TeV]			
T	$\mathcal{B}(T \to Zt) = 100\,\%$	1.47	1.16	1.36	1.60
T	singlet	1.26	0.87	1.31	1.27
T	(T, B) or (X, T) doublet	1.41	1.05	1.37	1.46
B	singlet	1.33	—	1.22	—
B	$\mathcal{B}(B \to Wt) = 100\,\%$ or (T, B) doublet	1.46	—	1.37	1.20

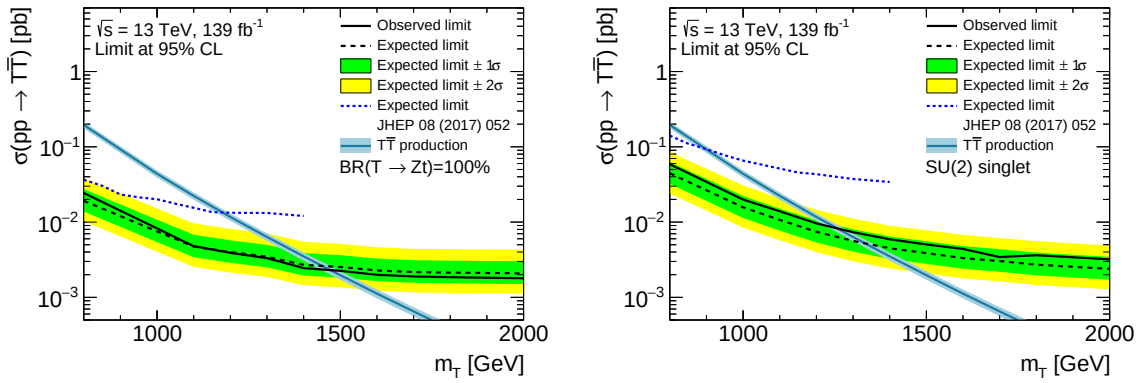

Figure 7.38: Expected and observed 95 % CL upper limits on the cross-section of $T\bar{T}$ production for (a) the $\mathcal{B}(T \to Zt) = 100\,\%$ scenario and (b) the VLT SU(2) singlet. The thickness of the theory curve represents the theoretical uncertainty from PDFs, scale, and the strong coupling constant α_s. The results of the 36 fb^{-1} search in the same final state are indicated by a blue, dashed line.

the SU(2) singlet and doublet scenarios for the T quark, where the lower limits on the signal mass are improved by 390 GeV and 360 GeV, respectively. A direct comparison of the expected cross-section limits is shown in Figure 7.38a for the $\mathcal{B}(T \to Zt) = 100\,\%$ case, and in Figure 7.38b for the SU(2) singlet scenario.

An improvement by a factor of at least two in the upper limit on the cross-section is expected due to the about four times larger data set. Furthermore, the improved analysis strategy allows to push the expected sensitivity of the search to even higher signal masses. The smallest difference between the expected limits is visible for the 800 GeV mass point in the case of the exclusive decays into Z bosons and top quarks. This can be explained by the training of the NN on higher signal masses ($1 - 1.5$ TeV) compared to a signal mass of 1 TeV used in the SR optimisation in Ref. [50], and the fact that m_{eff} is one of the most relevant variables for the NN. In addition, for the lower mass points the systematic uncertainties play a non-negligible role in the presented analysis. For a signal mass of 1.4 TeV, which is the largest one considered in the search using the partial data set, a significant improvement in the cross-section limit is visible in both figures. For the SU(2) singlet scenario, the cross-section limit improves by more than a factor of seven at 1.4 TeV, but already by more than a factor of three at 800 GeV. Here, the loose selection of the training region and the NN training for various signal decay modes allow to achieve a good sensitivity for a larger fraction of possible branching ratio combinations compared to a cut-and-count analysis based on a strict SR selection.

Considering only the partial Run 2 data set, the strongest limits on the various VLQ decay scenarios are set by the ATLAS VLQ pair-production combination [60]. This analysis performs a statistical combination of the individual searches for VLQs in order to set stronger limits on the VLQ parameters. For the exclusive $T \to Zt$ and $B \to Wt$ decays, the observed lower

limits on the signal mass are improved by about 100 GeV each in this thesis compared to the combination. For the T quark in the SU(2) singlet representation, the observed mass limit obtained in this dissertation is about 50 GeV weaker than the one from the combination, while the expected limit is about 90 GeV stronger. The different behaviour of expected and observed limits can be explained by the ratio of data and background expectation in the respective analysis region. The combination sensitivity is driven by searches for $Ht + X$ [48] and $Wb + X$ [49] in the SU(2) singlet case. An improved limit compared to the statistical combination is also obtained for the B quark in the SU(2) singlet and the T quark in an SU(2) doublet.
So far, only analyses using the partial Run 2 data set have been included in the comparison. However, a search for VLQs based on the full Run 2 data set exists, targeting VLQ decays into Z bosons and third-generation quarks [55]. This search selects multi-lepton final states and contains two separate optimisations for the 2ℓ and 3ℓ channels, which are later combined in the statistical analysis. The obtained limit on the T quark mass for the $\mathcal{B}(T \to Zt) = 100\,\%$ scenario is 1.60 TeV and, correspondingly, 130 GeV stronger than the observed limit obtained in this dissertation. Looking at the individual limits for the two channels, which are 1.43 TeV and 1.54 TeV in the 2ℓ and 3ℓ channel, respectively, the mass limit of 1.47 TeV is in between these two limits. For the T quark in the SU(2) singlet and doublet representation, the observed mass limits in the multi-lepton search are weaker for the individual channels, but the limit from the combination is again stronger than the limits obtained in the presented search. This illustrates the power of a statistical combination of two channels with a comparable sensitivity for a signal. Thus, a combination of the 1ℓ search with the multi-lepton search is expected to result in even better limits. For the B quark in the (T, B) doublet representation, the observed mass limit in this thesis is 260 GeV stronger than the limit obtained in the multi-lepton search. The smaller sensitivity of the multi-lepton search on this scenario, where the B quark decays exclusively via $B \to Wt$, is expected as this search is optimised for $B \to Zb$ decays.

7.9 Outlook

A search for vector-like top and bottom quarks is presented in this dissertation. Due to the decays of the VLQs into W, Z, or Higgs boson and a third-generation quark, a large variety of final states is possible. The presented analysis focuses on events with an isolated lepton, jets, and high missing transverse momentum in the final state, and is part of the ATLAS VLQ search programme.
The modelling of the VLQ signal events is based on Protos at LO. An alternative model for the production of VLQs with MG5_aMC@NLO is available in Ref. [213] and is used for the modelling of VLQ single production in ATLAS and CMS. A common framework for the signal generation for single and pair production, as well as between ATLAS and CMS would allow for an easier interpretation and better comparability of VLQ searches. Furthermore, alternative weights reflecting scale and PDF variations can be easily included in samples

generated with MG5_aMC@NLO. These modelling systematic uncertainties are not available in the current signal samples and are therefore not considered in the analysis. In addition, differences in the signal modelling due to the choice of the MC generator might be included as well. So far, simple VLQ models are considered in the searches and interpretations. In the future, the interpretation of the results could be extended to more complex VLQ models including also contributions from other hypothetical particles such as leptoquarks.
In the search, a kinematic reweighting is applied for the $t\bar{t}$ and single top-quark processes to account for mismodelling of the top-quark background at high transverse momenta. Such corrections are also applied in several other searches where top-quark processes are a dominant background [214–216]. It is expected that including higher-order contributions allows for a better description of the $t\bar{t}$ process at large transverse momenta of the top quarks. This expectation is confirmed by the measurement in Ref. [217] which applies parton-level reweighting on the $t\bar{t}$ events to match the NNLO QCD predictions. The reweighted distributions describe the measured data better than the NLO QCD predictions. The generation of the $t\bar{t}$ process at NNLO is available in POWHEG-BOX [218, 219] and will likely make it possible to omit the reweighting of the $t\bar{t}$ process in the future.
Furthermore, the systematic uncertainties related to the modelling of the major background processes play a non-negligible role in this analysis, and the uncertainty related to the $t\bar{t}$-tW interference effect is one of the major uncertainties in the background modelling. A first study dedicated to the handling of the interference effect in MC generators is presented in Chapter 8.
Further improvements might be possible in the reconstruction and identification of the top quark and hadronically decaying W, Z, and Higgs bosons. Instead of a simple reclustering of the small-R jets into large-R jets, dedicated reconstruction techniques, such as top tagging, might be useful in order to better identify and separate signal and background events.

8 Study of $t\bar{t}$-tW interference handling schemes

A precise simulation of the $t\bar{t}$ process is essential for SM precision measurements and searches for new physics at the LHC. One long standing issue is the handling of the overlap between $t\bar{t}$ production and single top-quark production in association with a W boson and a bottom quark (tWb). So far, samples for both processes are produced separately and the resulting overlap is removed by applying DR and DS techniques on the tW samples.
In the presented search for vector-like quarks, the obtained normalisation factors for the single top-quark background, being dominated by tW production, are of the order of 0.5. The DR scheme has been used for the nominal prediction of the tW background and a large difference between the DR and DS schemes has been found in the phase space selected by the analysis. Small normalisation factors for the single top-quark background have been also measured by other searches [220, 221]. It is common for these analyses to explore a phase space that is sensitive to the aforementioned interference effect.
New MC generator developments are available providing theoretical improvements in $t\bar{t}$ simulation and $t\bar{t}$-tW interference handling. The "$bb4\ell$" generator [222] is an NLO ME generator for $pp \to b\bar{b}\ell^+\nu\ell^-\bar{\nu}$ final states implemented in POWHEG that takes the quantum interference between Feynman diagrams with the same final state into account. Alternatively, different DR and DS models are implemented in MG5_aMC@NLO [223]. In these studies, the various predictions for $t\bar{t} + tW$ are compared to $bb4\ell$ predictions and unfolded ATLAS data. The results of these studies have been published in Ref. [224].
This chapter is structured as follows. First, the interference effect and techniques to resolve the resulting overlap are described. Afterwards, simulated samples, as well as object and analyses selections are introduced. The results of studies in various phase spaces are presented and discussed before they are summarised in a short conclusion.

8.1 Theoretical concepts

Considering tW production at NLO in QCD, the real emission of a bottom quark results in a $WbWb$ final state, which is the same as for $t\bar{t}$ production at LO with the common assumption that top quarks decay exclusively into a W boson and a bottom quark. In the following, the contributions to the $WbWb$ final state at NLO and possible methods to remove the overlap between tW and $t\bar{t}$ are discussed [178, 202, 225]. The notation follows predominantly the one

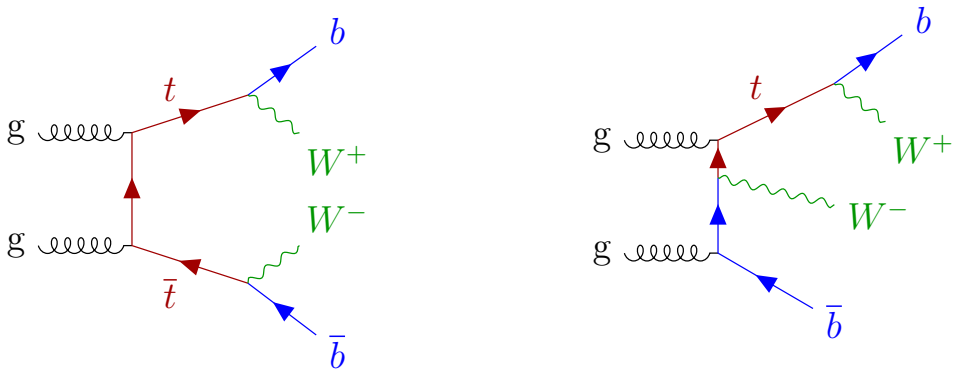

(a) A_{2t} **(b)** A_{1t}

Figure 8.1: Representative Feynman diagrams of (a) doubly and (b) singly resonant contributions to $WbWb$ production

in Ref. [225]. The squared ME amplitude for the tWb final state can be written as

$$|\mathcal{A}_{tWb}|^2 = |\mathcal{A}_{1t} + \mathcal{A}_{2t}|^2 = |\mathcal{A}_{1t}|^2 + 2\,\mathrm{Re}\,(\mathcal{A}_{1t}\mathcal{A}_{2t}^*) + |\mathcal{A}_{2t}|^2, \tag{8.1}$$

where $\mathcal{A}_{1t}$ denotes contributions from singly resonant diagrams representing tW production with real emission, while $\mathcal{A}_{2t}$ represents doubly resonant contributions describing $t\bar{t}$ production. Representative Feynman diagrams for both singly and doubly resonant contributions are shown in Figure 8.1. In principle, there are also non-resonant contributions to the $WbWb$ final state, however, they are found to be negligible [225].

The simplest method to resolve the resulting overlap is to remove the doubly resonant contributions by setting $\mathcal{A}_{2t} = 0$. In this case, not only the term $|\mathcal{A}_{2t}^2|$ is removed but also the interference term, such that only the first term of Equation 8.1 is left:

$$|\mathcal{A}_{tWb}|^2_{\mathrm{DR1}} = |A_{1t}|^2. \tag{8.2}$$

The DR scheme without interference is denoted as DR or DR1. Another version of a DR scheme, called DR2, keeps the contributions from the interference term and its ME amplitude can be written as

$$|\mathcal{A}_{tWb}|^2_{\mathrm{DR2}} = |\mathcal{A}_{1t}|^2 + 2\,\mathrm{Re}\,(\mathcal{A}_{1t}\mathcal{A}_{2t}^*)\,. \tag{8.3}$$

In contrast to DR1, the DR2 ME is not positive-definite.

Another technique to resolve the overlap are DS methods that were developed to avoid any gauge dependence. The general DS ME can be written as

$$|\mathcal{A}_{tWb}|^2_{\mathrm{DS}} = |\mathcal{A}_{1t} + A_{2t}|^2 - \mathcal{C}_{2t}, \tag{8.4}$$

Table 8.1: Schemes to remove the overlap between top-quark pair production and single top-quark production in association with a W boson and a bottom quark.

Scheme	Explanation
DR1	DR without interference
DR2	DR with interference
DS1	DS with reshuffling on initial state, standard BW
DS2	DS with reshuffling on initial state, running BW
DS3	DS with reshuffling on all final state particles, standard BW
DS4	DS with reshuffling on all final state particles, running BW

with a gauge invariant subtraction term $\mathcal{C}_{2t}$, which is defined as

$$\mathcal{C}_{2t} = f(p_{Wb}^2)|\mathcal{A}_{2t}|^2, \tag{8.5}$$

where $p_{Wb} = (p_W + p_b)$ with p_W the momentum of the W boson and p_b the momentum of the bottom quark. It depends on the prefactor $f(p_{Wb}^2)$ and the amplitude $|\mathcal{A}_{2t}|^2$. A momentum reshuffling on the external momenta is performed to obtain an on-shell top quark. There is some freedom in the choice of $f(p_{Wb}^2)$ and the reshuffling. Two different functions are implemented in MG5_aMC@NLO defined as ratios of Breit-Wigner distributions:

$$f_1(s) = \frac{(m_t\Gamma_t)^2}{(s-m_t^2)^2 + (m_t\Gamma_t)^2} \quad \text{and} \quad f_2(s) = \frac{(\sqrt{s}\,\Gamma_t)^2}{(s-m_t^2)^2 + (\sqrt{s}\,\Gamma_t)^2}, \tag{8.6}$$

where Γ_t is the width of the top quark. The function f_1 is the function that is implemented for the DS method in Powheg.

Four different implementations of the DS scheme are available. They use the two functional forms of the prefactor and two different methods for the momentum reshuffling. Table 8.1 gives a brief summary and explanation of the DR and DS schemes available in MG5_aMC@NLO that are used in the following studies.

Instead of treating $t\bar{t}$ and tW production separately, another approach is to simulate all contributions for a specific final state, i.e. $WbWb$ in the considered case, in a unified sample, which treats the quantum interference between the different diagrams properly. Apart from top-resonant contributions, also Feynman diagrams with a Z boson resonance can contribute to this process at NLO.

8.2 Simulated samples

In the following, a short description of the $t\bar{t}$, tW, and $bb4\ell$ samples used in these studies is given. All samples were produced using the five-flavour scheme and the NNPDF3.0nlo set of parton distribution functions. The top-quark mass, m_t, was set to 172.5 GeV. All events were interfaced with Pythia 8 for the parton shower and hadronisation, using the A14 set

of tuned parameters and the NNPDF2.3LO set of PDFs, and EvtGen was applied for the simulation of bottom and charm hadron decays.

The $bb4\ell$ generator [222] is part of the Powheg-Box-Res [226] framework and produces $b\bar{b}\ell^+\ell'^-\nu\bar{\nu}'$ final states that take into account quantum interference effects between $t\bar{t}$ and tW production as well as non-resonant and off-shell effects. A list of all features of the $bb4\ell$ generator can be found in Ref. [222]. The renormalisation and factorisation scales were set to $\left[\left(m_{\text{top}}^2 + p_{\text{T},t}^2\right)\left(m_{\text{top}}^2 + p_{\text{T},\bar{t}}^2\right)\right]^{\frac{1}{4}}$ based on the masses and transverse momenta of the top (anti-)quark. For diagrams containing an intermediate Z boson, the renormalisation and factorisation scales were set to $\frac{\sqrt{p_Z^2}}{2}$ with $p_Z = p_{\ell+} + p_{\nu_\ell} + p_{\ell-} + p_{\bar{\nu}_\ell}$. The h_{damp} parameter was set to the same value as the Powheg $t\bar{t}$ sample, i.e. $h_{\text{damp}} = 1.5 \cdot m_{\text{top}}$. The events were interfaced with Pythia 8.245 for the PS and hadronisation. The $bb4\ell$ sample includes the mixed-flavour states $e\mu$, $e\tau$ and $\mu\tau$, including the subsequent decays of taus to electrons or muons, but does not cover the same-flavour states ee, $\mu\mu$ and $\tau\tau$.
Top-quark pair production was modelled with Powheg+Pythia 8 using the same settings as in the search for VLQs, which are described in Section 7.1. An alternative sample of $t\bar{t}$ events was produced with MG5_aMC@NLO+Pythia 8. For the generation of the hard process MG5_aMC@NLO 2.8.1 was used with the renormalisation and factorisation scales set to the same settings as for the Powheg+Pythia 8 setup. MadSpin was used for the decays of top quarks at LO in order to preserve spin correlations. For the simulation of the PS and hadronisation, the events were interfaced with Pythia 8.244.

Single top-quark production in association with a W boson was modelled with Powheg+Pythia 8 using the same settings as described in Section 7.1. Samples exist for the DR and DS schemes with the renormalisation and factorisation scales set to the default scale, $\mu_R = \mu_F = m_{\text{top}}$.
Additional samples were produced using a dynamic scale, $\mu_R = \mu_F = H_{\text{T}}/2$, where H_{T} is defined as the sum over transverse masses of all outgoing particles in the ME. In order to evaluate the impact of the h_{damp} parameter, tW samples with the h_{damp} parameter set to $h_{\text{damp}} = 3 \cdot m_{\text{top}}$ were produced. In the case of dynamic renormalisation and factorisation scales and variation of the h_{damp} parameter, events were interfaced with Pythia 8.306.

Alternative tW samples were generated with MG5_aMC@NLO 2.8.1. The renormalisation and factorisation scales were set to the same as for the Powheg samples, i.e. $\mu_R = \mu_F = m_{\text{top}}$ or $\mu_R = \mu_F = H_{\text{T}}/2$. Samples with different implementations of the diagram removal (DR1, DR2) and diagram subtraction schemes (DS1-4) [225] were produced using the MadSTR plugin [223]. Two additional parameters (`str_include_pdf`, `str_include_flux`) can be specified in the case of the DS scheme. If set to true, they compensate for luminosity factors and the flux when doing the momentum reshuffling. The top-quark and W boson decays were handled in MadSpin to preserve spin correlations. In order to ensure positive-definite weights, the DR scheme (DR1) was applied in MadSpin for all tW samples. The events were interfaced with Pythia 8.244 for showering and hadronisation. The NLO cross-sections

Table 8.2: NLO generator cross-sections of the POWHEG+PYTHIA 8 and MG5_aMC@NLO+PYTHIA 8 tW DR samples in the dilepton final state. Cross-sections are given in pb.

Generator	μ_R, μ_F	DR1	DR2
POWHEG+PYTHIA 8	m_{top}	7.99	—
POWHEG+PYTHIA 8	$H_{\text{T}}/2$	7.58	—
MG5_aMC@NLO+PYTHIA 8	m_{top}	7.98	7.15
MG5_aMC@NLO+PYTHIA 8	$H_{\text{T}}/2$	7.57	6.94

Table 8.3: NLO generator cross-sections of the POWHEG+PYTHIA 8 and MG5_aMC@NLO+PYTHIA 8 tW DS samples with different settings of the `pdf` and `flux` parameters in the dilepton final state. Cross-sections are given in pb.

Generator	μ_R, μ_F	pdf	flux	DS1	DS2	DS3	DS4
POWHEG+PYTHIA 8	m_{top}	—	—	7.83	—	—	—
POWHEG+PYTHIA 8	$H_{\text{T}}/2$	—	—	7.48	—	—	—
MG5_aMC@NLO+PYTHIA 8	m_{top}	true	true	7.68	6.35	7.84	7.68
MG5_aMC@NLO+PYTHIA 8	m_{top}	false	true	7.77	7.59	7.79	7.65
MG5_aMC@NLO+PYTHIA 8	m_{top}	true	false	7.74	7.26	7.82	7.68
MG5_aMC@NLO+PYTHIA 8	m_{top}	false	false	7.72	7.72	7.76	7.63

for the POWHEG+PYTHIA 8 and MG5_aMC@NLO+PYTHIA 8 tW samples are summarised in Tables 8.2 and 8.3. In the following studies, all samples are normalised to their NLO cross-section prediction provided by the ME generator.

8.3 Object definition and analysis selection

RIVET v3.1.4 is used to analyse the different MC samples on particle level using stable particles with a mean lifetime of $\tau > 30\,\text{ps}$. Rivet routines are defined in different phase-space topologies to explore a broad range of observables. In the following, the used object definitions and analyses selections are explained.

Object definition

Electrons and muons are considered as leptons and required to originate from a W boson decay or a tau decay, if the tau itself originates from a W boson. They are dressed, meaning that photons that do not originate from a hadron decay and are within $\Delta R < 0.1$ around the lepton four-momentum, are added to the lepton four-momentum. Leptons are required to satisfy $p_{\text{T}} > 28\,\text{GeV}$ and $|\eta| < 2.5$. Only neutrinos that do not originate from the decay of hadrons, but including neutrinos from tau decays, are considered.
Jets are reconstructed with the anti-k_t algorithm using a radius parameter of $R = 0.4$. Jets are required to have a transverse momentum of $p_{\text{T}} > 25\,\text{GeV}$ and $|\eta| < 2.5$. Dressed leptons and neutrinos are vetoed in the jet clustering. The ghost-association technique is used in

order to identify jets that originate from b-hadrons. The missing transverse momentum is calculated from the negative vectorial sum of all visible final state particles.

Selection in $t\bar{t}$ bulk region

Since the $bb4\ell$ sample only contains events with leptons of different flavour, the presence of exactly one electron and one muon with the criteria defined above is required. The two leptons have to have opposite sign and are not allowed to both originate from a tau decay. At least two jets are required to be present in the event, with exactly two of them being b-jets. The defined event selection is a typical selection for a precision measurement such as a top-quark mass measurement.

Selection for search-like phase spaces

This selection is inspired by searches for new particles in final states with high missing transverse momentum that are sensitive to the $t\bar{t}$-tW interference effect. The lepton selection is the same as in the $t\bar{t}$ bulk selection, requiring exactly one electron and one muon. Furthermore, at least four jets have to be present in the event, exactly two of which must originate from a b-hadron. The missing transverse momentum has to fulfil the $E_{\mathrm{T}}^{\mathrm{miss}} > 200\,\mathrm{GeV}$ requirement.

Normalised differential cross-section measurement in $t\bar{t}$-tW interference phase space

To study the phase space that is sensitive to the $t\bar{t}$-tW interference more closely, a normalised differential cross-section measurement implemented in Rivet (`ATLAS_2018_I1677498` [227]) is used. The measurement is performed in a fiducial phase space where interference effects between $t\bar{t}$ production and the tWb process play an important role. Events with two leptons (ee, $\mu\mu$, $e\mu$) and two b-jets are selected in this measurement, where the object definitions, which can be found in Ref. [227], are slightly different from the ones described above. The cross-section is measured as a function of the invariant mass of a b-jet and a lepton. As there is an ambiguity in pairing the lepton and the b-jet,

$$m_{b\ell}^{\mathrm{minimax}} = \min\{\max(m_{b_1,\ell_1}, m_{b_2,\ell_2}), \max(m_{b_2,\ell_1}, m_{b_1,\ell_2})\} \tag{8.7}$$

is used, where b_i and ℓ_i, with $i \in \{1, 2\}$, are the two b-jets and leptons. The data used in this measurement correspond to the $36\,\mathrm{fb}^{-1}$ pp collision data set at $\sqrt{s} = 13\,\mathrm{TeV}$ collected in 2015 and 2016 with the ATLAS detector.

8.4 Comparisons in $t\bar{t}$ bulk region

In this and the following studies, predictions for $t\bar{t}+tW$ from various generator setups are compared to each other and to the $bb4\ell$ sample. In most cases, the POWHEG+PYTHIA 8 $t\bar{t}+tW$ (DR) prediction is chosen as the reference, as the DR scheme is the current default for the tW process in ATLAS. All samples are normalised to their NLO cross-section prediction provided by the corresponding generator. In all plots, the distributions are normalised to unity.

In a first study, the $bb4\ell$ sample is compared to the POWHEG+PYTHIA 8 predictions for $t\bar{t}+tW$ in some basic kinematic variables. For this, events have to pass the requirements for the $t\bar{t}$ bulk region. Compared to the search-like selection, this one has less restrictive cuts and allows to compare relevant variables without limiting the phase space too much.

The lepton p_{T} distribution obtained from the POWHEG+PYTHIA 8 samples is shown in Figure 8.2, in which differences between the $t\bar{t}+tW$ (DR) and $bb4\ell$ samples are visible. The latter has a softer p_{T} spectrum and a similar shape to the sample using the DS scheme.

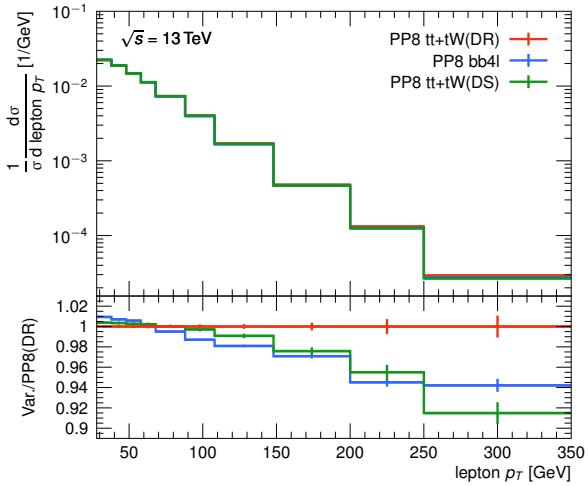

Figure 8.2: Comparison of the nominal POWHEG+PYTHIA 8 $t\bar{t}+tW$ (DR) setup (red line) to the $bb4\ell$ sample (blue line) and the POWHEG+PYTHIA 8 $t\bar{t}+tW$ (DS) setup (green line) for the lepton p_{T}. The error bars indicate the MC statistical uncertainties.

In Figure 8.3, the jet multiplicity and transverse momentum distribution of the leading b-jet are shown. The differences in the jet multiplicity between the predictions for $t\bar{t}+tW$ and $bb4\ell$ are below 5 % for small jet multiplicities. For larger jet multiplicities, the difference increases but is always below 10 %. No significant differences between the tW DR and DS schemes are visible. In the p_{T} distribution of the leading b-jet, the $bb4\ell$ sample shows a harder p_{T} spectrum at low transverse momenta than the prediction using the DR scheme for the tW sample, while the distributions exhibits a softer p_{T} spectrum in the case of the DS scheme. Comparisons for additional variables can be found in Ref. [224].

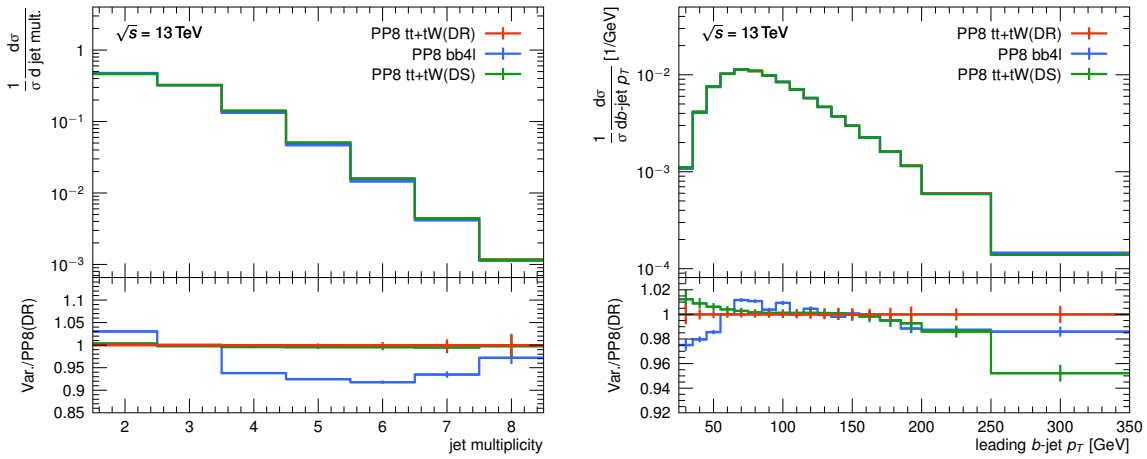

(a) **(b)**

Figure 8.3: Comparison of the nominal POWHEG+PYTHIA 8 $t\bar{t} + tW$ (DR) setup (red line) to the $bb4\ell$ sample (blue line) and the POWHEG+PYTHIA 8 $t\bar{t} + tW$ (DS) setup (green line) for the (a) jet multiplicity and (b) p_{T} spectrum of the leading b-jet. The error bars indicate the MC statistical uncertainties.

8.5 Studies in the interference region

Usually the impact of tW production is small in the $t\bar{t}$ bulk region, but becomes more relevant in phase spaces where interference effects between $t\bar{t}$ and tW play a predominant role. An example is the search-like selection defined in Section 8.3.

Instead of calculating am_{T2} as in the search for vector-like quarks, m_{T2} is considered in these studies using the two selected leptons, two b-jets, and the missing transverse momentum. The distributions for m_{T2} and $m_{b\ell}^{\mathrm{minimax}}$ are shown in Figure 8.4. The tail of both variables is sensitive to the interference effect between $t\bar{t}$ and tW resulting in large differences between the DR and DS schemes. In the bulk of the distributions, small differences of the order of 5 % between the DR and DS schemes are visible. In the tail, the DS scheme agrees well with the $bb4\ell$ prediction, but the difference to the DR scheme increases to up to 80 % in the last bins of the distributions.

To be able to make a statement about the compatibility between the different $t\bar{t} + tW$ predictions and nature, the predictions are compared to unfolded data from the measurement described in Section 8.3. In contrast to the other selections used for these studies, the measurement requires exactly two leptons (ee, $\mu\mu$, $e\mu$) without further restrictions on the lepton flavour. As the $bb4\ell$ sample does not include ee and $\mu\mu$ events, it is not compared to unfolded data. The measurement was done in the $m_{b\ell}^{\mathrm{minimax}}$ variable, in which $t\bar{t}$ production dominates up to the top-quark mass and the interference effects are large above that threshold. Figure 8.5a shows the $t\bar{t} + tW$ predictions from POWHEG+PYTHIA 8 using the DR and DS schemes. Only tiny differences between the DR and DS schemes are visible in the bulk region due to the dominance of the $t\bar{t}$ process. However, the situation is different in the tail of the

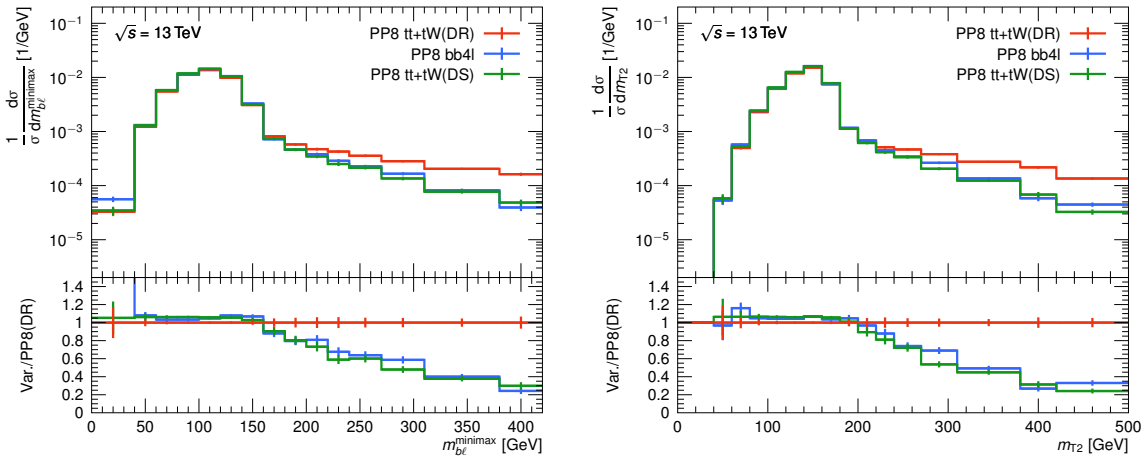

(a) **(b)**

Figure 8.4: Distributions of (a) $m_{b\ell}^{\text{minimax}}$ and (b) m_{T2} after the search-like selection requiring two leptons ($e\mu$), $E_{\text{T}}^{\text{miss}} > 200\,\text{GeV}$ and at least four jets of which exactly two must be identified as b-jets. Predictions for $t\bar{t} + tW$ obtained with POWHEG+PYTHIA 8 are compared to the $bb4\ell$ sample.

$m_{b\ell}^{\text{minimax}}$ distribution. While the DR scheme overestimates the data above 240 GeV, the DS scheme underestimates the data in the range dominated by the interference effect. When comparing the predictions using a fixed scale for the tW sample to predictions using a dynamic scale, the latter predict always less events in the tail of the distribution. While the agreement for the DR scheme improves with a dynamic scale, the agreement for the DS scheme gets slightly worse. However, the impact of the scale choice on the DS scheme is smaller than on the DR scheme.

The h_{damp} parameter regulates the first real emission in POWHEG and is used as a systematic uncertainty for the $t\bar{t}$ process. Its impact on the $m_{b\ell}^{\text{minimax}}$ variable is shown in Figure 8.5b. While the distributions for $t\bar{t} + tW$ (DR) only slightly differ when using a fixed scale, which is the default, the impact of the h_{damp} parameter becomes larger when using a dynamic scale. This behaviour can be deduced from the definition of the dynamic scale that is based on the kinematics of all final state particles which leads to a higher sensitivity of the first real emission.

As mentioned in the description of the tW samples, various implementations of the DR and DS schemes are available in MG5_aMC@NLO. The predictions for the DR1 and DR2 schemes are shown in Figure 8.5c. In addition, the plot includes the predictions for tW samples produced with dynamic renormalisation and factorisation scales. For the DR1 scheme, the sample with a dynamic scale is closer to the reference data than the sample with a fixed scale. Both predictions using the DR2 scheme strongly underestimate the data in the interference region.

The predictions for $t\bar{t}+tW$ using MG5_aMC@NLO+PYTHIA 8 with different implementations

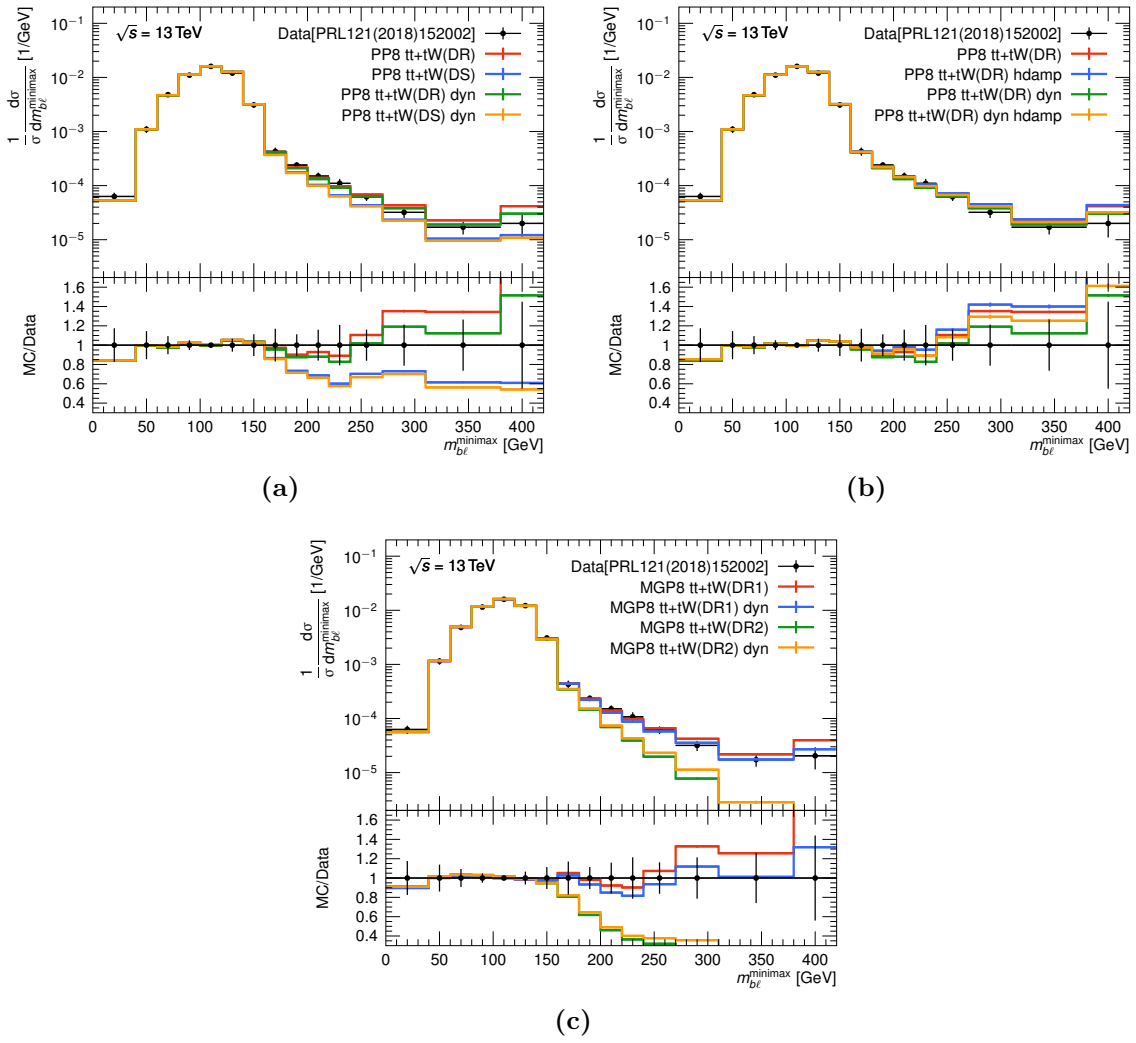

Figure 8.5: Distributions of the $m_{b\ell}^{\text{minimax}}$ variable. Predictions for $t\bar{t} + tW$ from (a) POWHEG+PYTHIA 8 and (c) MG5_aMC@NLO+PYTHIA 8 using different scale choices and different methods for the interference handling are compared to unfolded reference data [227]. The impact of changing the POWHEG h_{damp} parameter setting is shown in (b). The label "dyn" in the legend denotes the usage of dynamic scales. The last bin includes the overflow bin.

of the DS scheme are shown in Figure 8.6. For each DS scheme, all combinations of the `pdf` and `flux` parameter settings are compared. The choice of `pdf` and `flux` parameters has only some impact on the predictions for DS1 and DS2, while the impact on the predictions for DS3 and DS4, where the reshuffling is performed on all final-state particles, is negligible. The predictions where both `pdf` and `flux` parameters are set to false agree best with data. The largest impact of the two parameters is visible for the DS2 scheme. In case the `pdf` parameter is set to true, large deviations of the prediction to the unfolded data are visible.

The DR1 scheme is compared to all variants of the DS scheme, with the `pdf` and `flux`

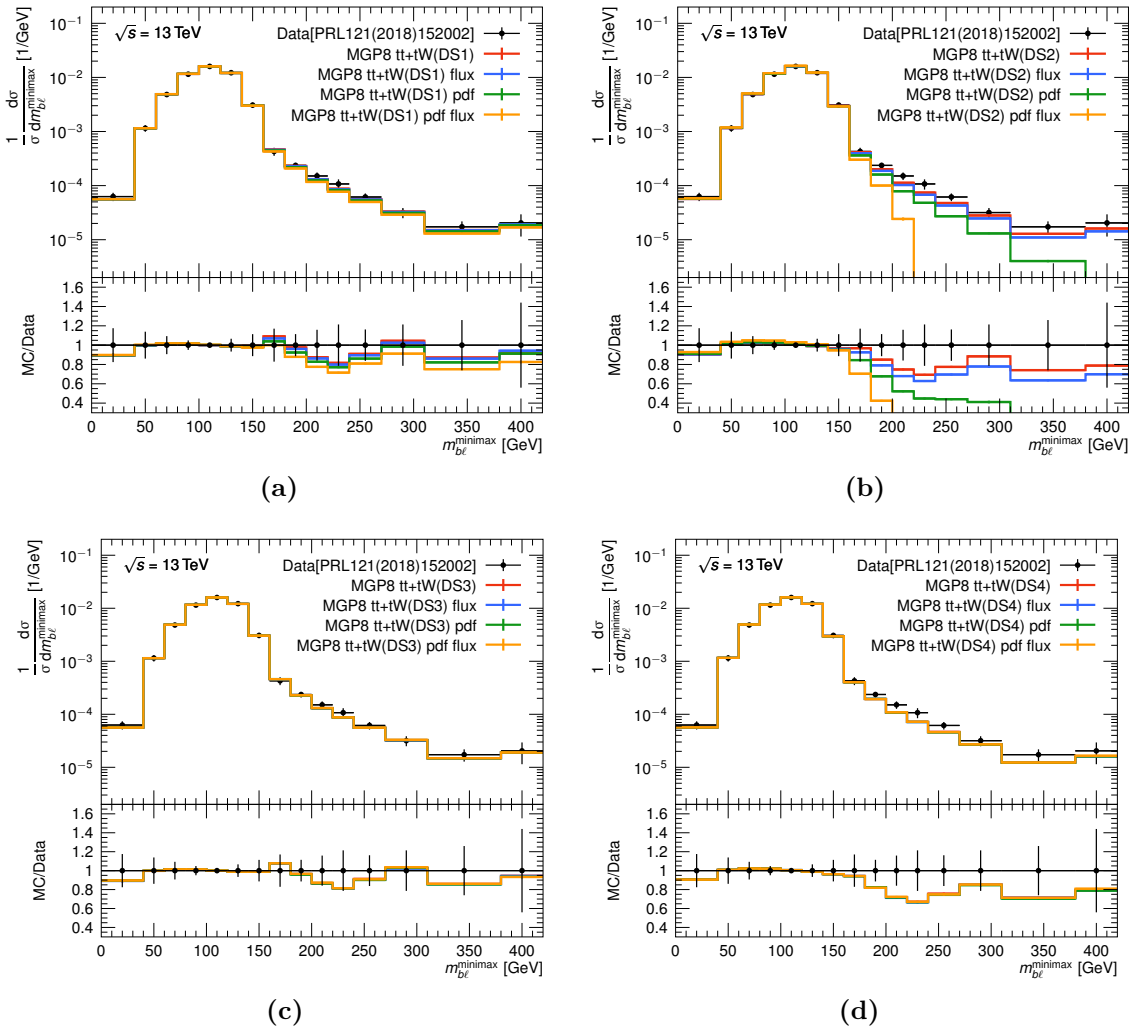

Figure 8.6: Predictions of MG5_aMC@NLO+Pythia 8 $t\bar{t} + tW$ samples with different settings for the DS scheme are compared to unfolded reference data from Ref. [227]. The `pdf` and `flux` label in the legend indicates that the corresponding parameter is set to true in the generation of the tW sample. The last bin includes the overflow bin.

parameters set to false, in Figure 8.7. The predictions using DS1 and DS3 describe the data better than DS2 and DS4.

Finally, the $t\bar{t} + tW$ predictions are compared between the two chosen MC generators. Figure 8.8a compares the Powheg+Pythia 8 and MG5_aMC@NLO+Pythia 8 $t\bar{t} + tW$ DR and DS predictions to the unfolded data. The two predictions for the DR scheme using the fixed scales agree well between the two generators, while a 30 % difference appears for the DS predictions between Powheg and MG5_aMC@NLO in the tail of the distribution. The MG5_aMC@NLO+Pythia 8 prediction, using DS1 with the `pdf` and `flux` parameters set to false, is closer to data than the one obtained from Powheg+Pythia 8. The difference would be slightly smaller when using the MG predictions with `pdf` and `flux` parameters set to true.

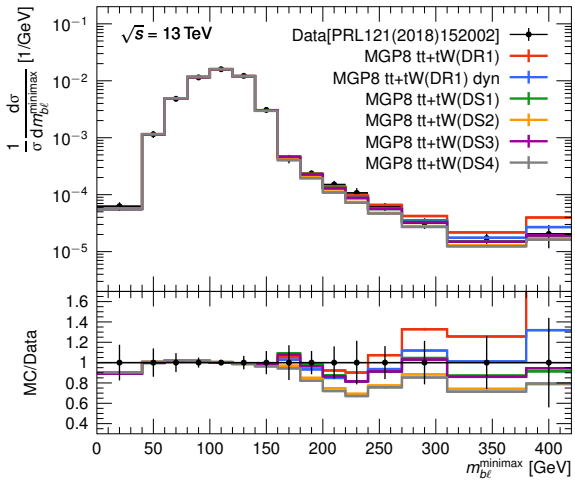

Figure 8.7: Predictions from MG5_aMC@NLO+Pythia 8 samples with different settings for the DR and DS schemes and scale choices are compared to unfolded data from Ref. [227] in the $m_{b\ell}^{\text{minimax}}$ variable. The label "dyn" in the legend denotes the usage of dynamic scales. The `pdf` and `flux` parameters were set to false in the generation of the tW (DS) samples. The last bin includes the contributions from the overflow bin.

The same comparison is performed in the more restrictive search-like phase space. The resulting $m_{b\ell}^{\text{minimax}}$ and m_{T2} distributions are shown in Figures 8.8b and 8.8c, respectively, including the predictions of the $bb4\ell$ sample. Again, the DR samples agree well with each other. In contrast to the measurement phase space, the predictions for the DS setups are closer to each other. The prediction using the DR scheme and the dynamic scales is always between the $t\bar{t} + tW$ predictions using the DR or DS scheme and fixed scales. Additional distributions can be found in Appendix C.

In order to quantify the agreement between the various $t\bar{t} + tW$ predictions and the unfolded data from Ref. [227], χ^2 calculations using the full covariance matrix are performed. The results are summarised in Table 8.4 for all studied $t\bar{t} + tW$ setups. The numbers support the previous findings. While the most scenarios provide a relatively good description of the data within the uncertainties, the DR2 scheme and the DS2 scheme with the `pdf` parameter set to true can be excluded.

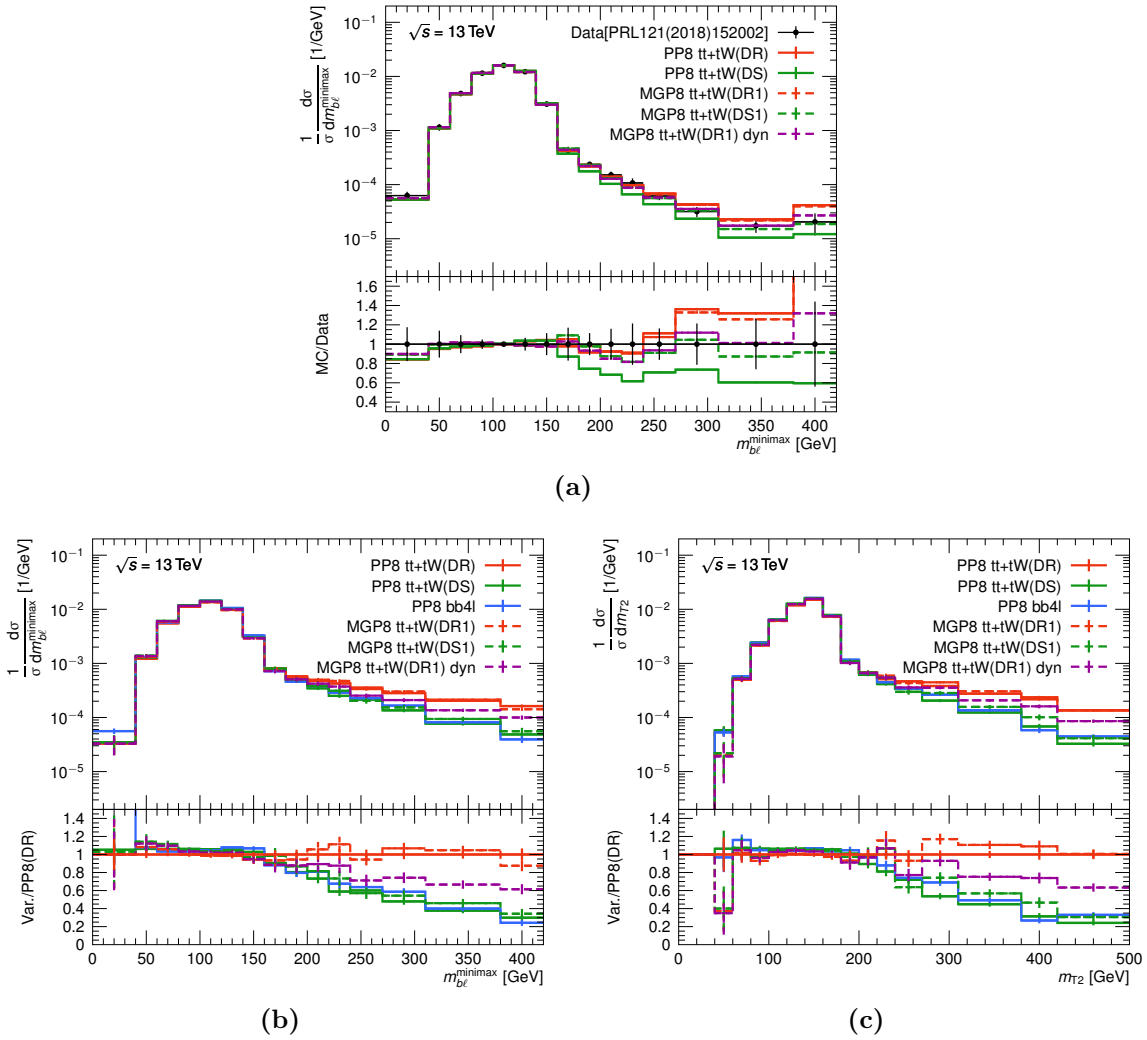

(a) **(b)** **(c)**

Figure 8.8: A comparison of predictions for $t\bar{t} + tW$ from the POWHEG+PYTHIA 8 and MG5_aMC@NLO+PYTHIA 8 samples to unfolded data from Ref. [227] in the $m_{b\ell}^{\text{minimax}}$ distribution is shown in (a). The last bin includes the overflow bin in this distribution. Comparison of predictions for $t\bar{t} + tW$ from the POWHEG+PYTHIA 8 and MG5_aMC@NLO+PYTHIA 8 samples and POWHEG+PYTHIA 8 $bb4\ell$ in the (b) $m_{b\ell}^{\text{minimax}}$ and (c) m_{T2} distributions after applying the defined search-like selection. The label "dyn" in the legend denotes the usage of dynamic scales.

Table 8.4: Comparison of the unfolded data from Ref. [227] to predictions for $t\bar{t} + tW$ from POWHEG+PYTHIA 8 and MG5_aMC@NLO+PYTHIA 8. The χ^2 values are calculated using the full covariance matrix.

Model	μ_R, μ_F	**pdf**	**flux**	h_{damp}	χ^2/ndf	**p-value**
PP8 $t\bar{t} + tW$ (DR)	m_{top}	—	—	$1.5\, m_{\text{top}}$	11.1/14	0.68
PP8 $t\bar{t} + tW$ (DR)	m_{top}	—	—	$3\, m_{\text{top}}$	13.0/14	0.53
PP8 $t\bar{t} + tW$ (DR)	$H_{\text{T}}/2$	—	—	$1.5\, m_{\text{top}}$	4.9/14	0.99
PP8 $t\bar{t} + tW$ (DR)	$H_{\text{T}}/2$	—	—	$3\, m_{\text{top}}$	7.09/14	0.93
PP8 $t\bar{t} + tW$ (DS)	m_{top}	—	—	$1.5\, m_{\text{top}}$	11.2/14	0.67
PP8 $t\bar{t} + tW$ (DS)	$H_{\text{T}}/2$	—	—	$1.5\, m_{\text{top}}$	13.3/14	0.50
MGP8 $t\bar{t} + tW$ (DR1)	m_{top}	—	—	—	10.7/14	0.71
MGP8 $t\bar{t} + tW$ (DR1)	$H_{\text{T}}/2$	—	—	—	5.1/14	0.98
MGP8 $t\bar{t} + tW$ (DR2)	m_{top}	—	—	—	47.3/14	$1.7 \cdot 10^{-5}$
MGP8 $t\bar{t} + tW$ (DR2)	$H_{\text{T}}/2$	—	—	—	35.6/14	$1.2 \cdot 10^{-3}$
MGP8 $t\bar{t} + tW$ (DS1)	m_{top}	true	true	—	6.0/14	0.97
MGP8 $t\bar{t} + tW$ (DS1)	m_{top}	false	true	—	4.7/14	0.99
MGP8 $t\bar{t} + tW$ (DS1)	m_{top}	true	false	—	5.0/14	0.99
MGP8 $t\bar{t} + tW$ (DS1)	m_{top}	false	false	—	5.1/14	0.98
MGP8 $t\bar{t} + tW$ (DS2)	m_{top}	true	true	—	460.7/14	0.0
MGP8 $t\bar{t} + tW$ (DS2)	m_{top}	false	true	—	10.2/14	0.75
MGP8 $t\bar{t} + tW$ (DS2)	m_{top}	true	false	—	30.7/14	0.006
MGP8 $t\bar{t} + tW$ (DS2)	m_{top}	false	false	—	6.6/14	0.95
MGP8 $t\bar{t} + tW$ (DS3)	m_{top}	true	true	—	4.6/14	0.99
MGP8 $t\bar{t} + tW$ (DS3)	m_{top}	false	true	—	4.6/14	0.99
MGP8 $t\bar{t} + tW$ (DS3)	m_{top}	true	false	—	4.8/14	0.99
MGP8 $t\bar{t} + tW$ (DS3)	m_{top}	false	false	—	4.9/14	0.99
MGP8 $t\bar{t} + tW$ (DS4)	m_{top}	true	true	—	7.4/14	0.92
MGP8 $t\bar{t} + tW$ (DS4)	m_{top}	false	true	—	8.1/14	0.88
MGP8 $t\bar{t} + tW$ (DS4)	m_{top}	true	false	—	8.0/14	0.89
MGP8 $t\bar{t} + tW$ (DS4)	m_{top}	false	false	—	7.5/14	0.91

8.6 Conclusion

The presented study investigates predictions for the $pp \to b\bar{b}\ell^+\nu\ell^-\bar{\nu}$ final state with a focus on the interference between the $t\bar{t}$ and tW processes at NLO. The various predictions for $t\bar{t}+tW$ are compared to the $bb4\ell$ sample. In variables like lepton p_{T} or $m_{b\ell}^{\mathrm{minimax}}$, the $bb4\ell$ distributions have a more similar shape to the prediction using the DS scheme than the one using the DR scheme.

Comparing the different predictions for $t\bar{t}+tW$ using MG5_aMC@NLO, various conclusions on the existing interference handling techniques can be drawn. The DR2 scheme and the DS2 scheme with the `pdf` parameter set to true show large deviations from data and can be therefore excluded. For DR1, the dynamic scale choice slightly improves the modelling in the interference region. The two parameters for the DS scheme, `pdf` and `flux`, are only relevant for DS1 and DS2. Setting the parameters to true gives a worse agreement with the observed data. DS1 and DS3 without `pdf` and `flux` parameters agree well with the data within the uncertainties, while DS2 and DS4 are at the border of the experimental uncertainties. Comparing the predictions between POWHEG and MG5_aMC@NLO, the distributions for the DR scheme agree well, while differences in the tail of the $m_{b\ell}^{\mathrm{minimax}}$ are visible for the DS scheme.
These results allow to draw first conclusions about the handling of the interference effect in MC samples. The $bb4\ell$ sample is not available for the hadronic final states. Hence, separate samples for $t\bar{t}$ and tW will still be used in the near future. So far, the tW sample using the DR scheme and fixed scales has been used as the default sample. The presented studies suggest that replacing the fixed scales by dynamic scales might be beneficial. At the same time, the h_{damp} variation for the tW process should be used as an additional systematic uncertainty in order to be consistent with the $t\bar{t}$ process for which a systematic uncertainty is already assigned to the h_{damp} variation. Before a new prescription for the interference uncertainty can be recommended, which has been calculated by comparing the POWHEG+PYTHIA 8 predictions using the DR and DS schemes with fixed scales so far, it is necessary to understand the observed differences for the DS scheme among the different generators. Therefore, further studies, which should include the effect of scale variations as well, are required.

Conclusion

The limitations and open questions of the Standard Model point to the need for physics beyond. Several new theories that try to solve the hierarchy problem, including Little Higgs and Composite Higgs models, feature vector-like quarks around the TeV scale, which would make them detectable in the ATLAS and CMS experiments at the Large Hadron Collider.

In this context, a search for pair-produced vector-like partners of the top and bottom quarks, decaying into a W, Z, or Higgs boson and a third-generation quark, is presented. Due to the different decay modes, a large variety of final states is possible. The presented analysis focuses on events with an isolated lepton, jets, and high missing transverse momentum in the final state, and is part of the ATLAS vector-like quark search programme analysing the full Run 2 data set with an integrated luminosity of $139\,\text{fb}^{-1}$ collected with the ATLAS detector from 2015 to 2018. The analysis considers all possible decays of the vector-like quarks, but it has the highest sensitivity on the $T \to Zt$ and $B \to Wt$ decay modes.

The analysis strategy is based on the separation of the vector-like quark signal from the Standard Model background processes using neural networks, which are trained for various signal hypotheses. In order to account for mismodelling of top-quark processes at large top-quark transverse momenta, a kinematic reweighting procedure depending on the effective mass of the event and the jet multiplicity is applied on events containing singly or pair-produced top quarks. Apart from the selection for the neural network training, additional control regions are defined in order to constrain the normalisation of the major background processes, namely $t\bar{t}$, W+jets, and single top-quark production. Simultaneous profile likelihood fits in the signal and control regions are performed, and no significant deviation from the Standard Model expectation is observed. Upper limits on the signal production cross-section and lower limits on the signal mass are set at the 95 % confidence level. The lower limits on the mass of the T and B quarks in the weak-isospin singlet model are 1.26 TeV and 1.33 TeV, respectively, and 1.41 TeV for the T quark in the doublet representation. Stronger limits are set for the pure $T \to Zt$ and $B \to Wt$ decays with 1.47 TeV and 1.46 TeV, where the latter corresponds to the (T, B) doublet case. For the three discussed scenarios of the T quark, the obtained mass limits are extended by more than 300 GeV compared to an earlier analysis in the same final state using a subset of the Run 2 data set. Limits on the T and B quark masses are also set for all combinations of possible branching ratios. Finally, the strongest limits are at 1.59 TeV for the (T, B) weak-isospin doublet where contributions from both vector-like quarks, which are assumed to be mass degenerate, are considered.

The modelling of top-quark pair production and single top-quark production in association with a W boson, and the handling of the interference effect between these two processes play a relevant role in the search for vector-like quarks, but also in many other analyses with top quarks in the final state. A dedicated study investigating the handling of this interference effect in the Monte Carlo event generation is presented. So far, separate samples for $t\bar{t}$ and tW production are produced, where diagram removal and diagram subtraction techniques are applied on the tW sample in order to remove the overlap. Some of the existing schemes are discarded by a comparison to unfolded reference data, and the prediction with the diagram removal scheme using dynamic scales is found to be in better agreement with data than the prediction with fixed scales. A recent approach is to simulate the complete $WbWb$ in a single sample taking quantum interference effects as well as off-shell effects into account. At present, this is only possible in the case of leptonic W decays. Predictions from the so-called $bb4\ell$ generator are compared to various predictions for $t\bar{t} + tW$ in the presented studies.
In view of the upcoming LHC Run 3, an increased centre-of-mass energy of $\sqrt{s} = 13.6\,\text{TeV}$ leads to a higher signal cross-section and, together with the enhanced expected integrated luminosity of about $300\,\text{fb}^{-1}$, enables great opportunities for upcoming searches for vector-like quarks. These can benefit from new developments in the most recent versions of the Monte Carlo event generators, which are validated for the usage in ATLAS with the help of the extended validation framework.

A ATLAS MC validation - PAVER webpage

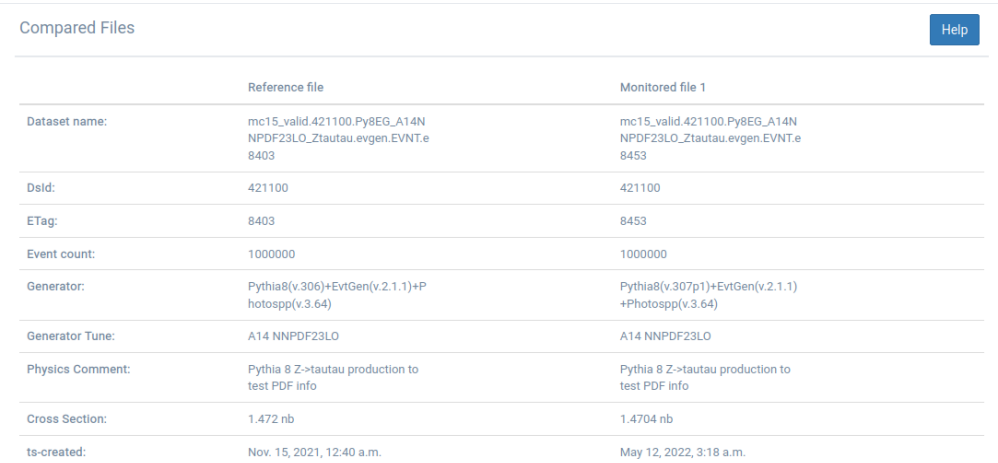

Figure A.1: Example for the sample information given on the validation results webpage. The help button opens a window with useful information about the validation and the results page.

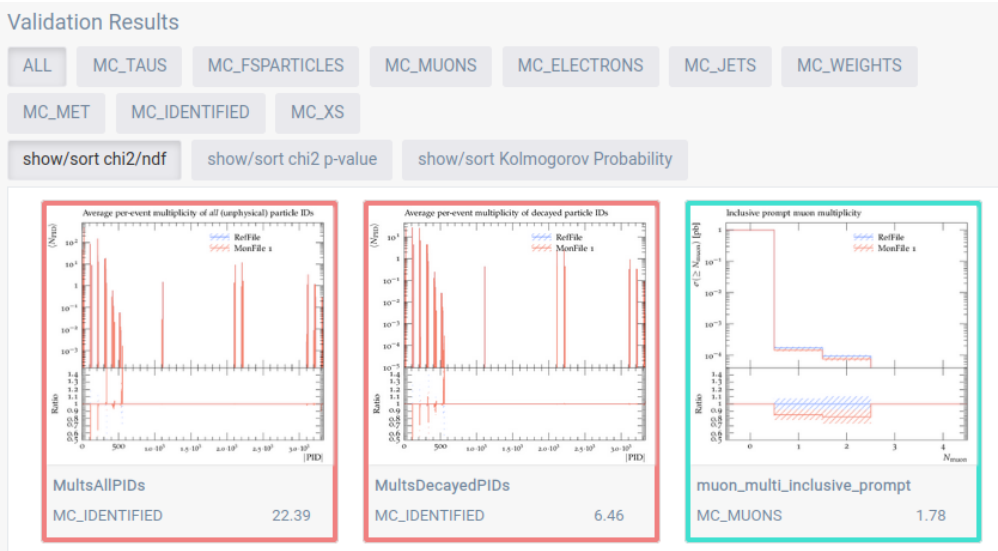

Figure A.2: Example for validation plots on the webpage. A specific analysis can be selected by the user in order to reduce the number of displayed figures. Furthermore, the test statistic used for the sorting of the validation plots can be chosen. The number in the coloured frame gives the result of the selected test statistic.

B Search for vector-like quarks

B.1 Additional signal and background shape distributions

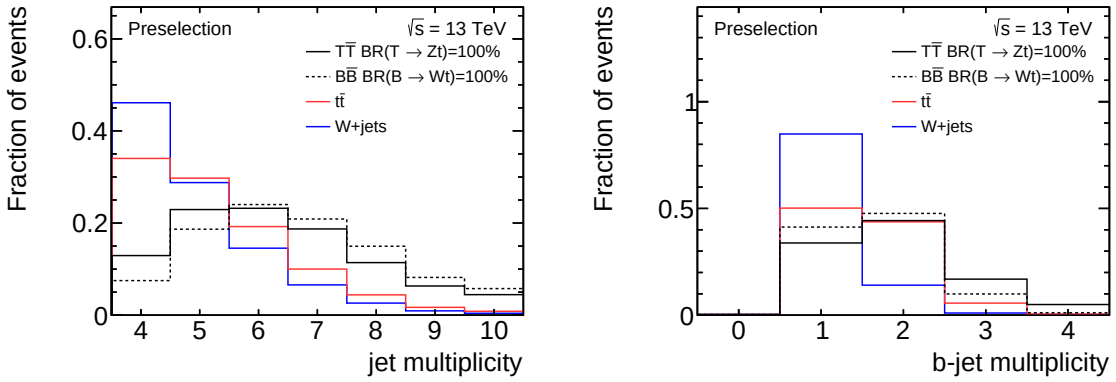

(a) (b)

Figure B.1: Shape distributions of (a) the jet multiplicity and (b) the b-jet multiplicity after the preselection for $t\bar{t}$, W+jets, the VLT signal with exclusive $T \to Zt$ decays, and the VLB signal with exclusive $B \to Wt$ decays where the signal mass is considered to be 1.2 TeV. The last bin in each distribution contains the overflow.

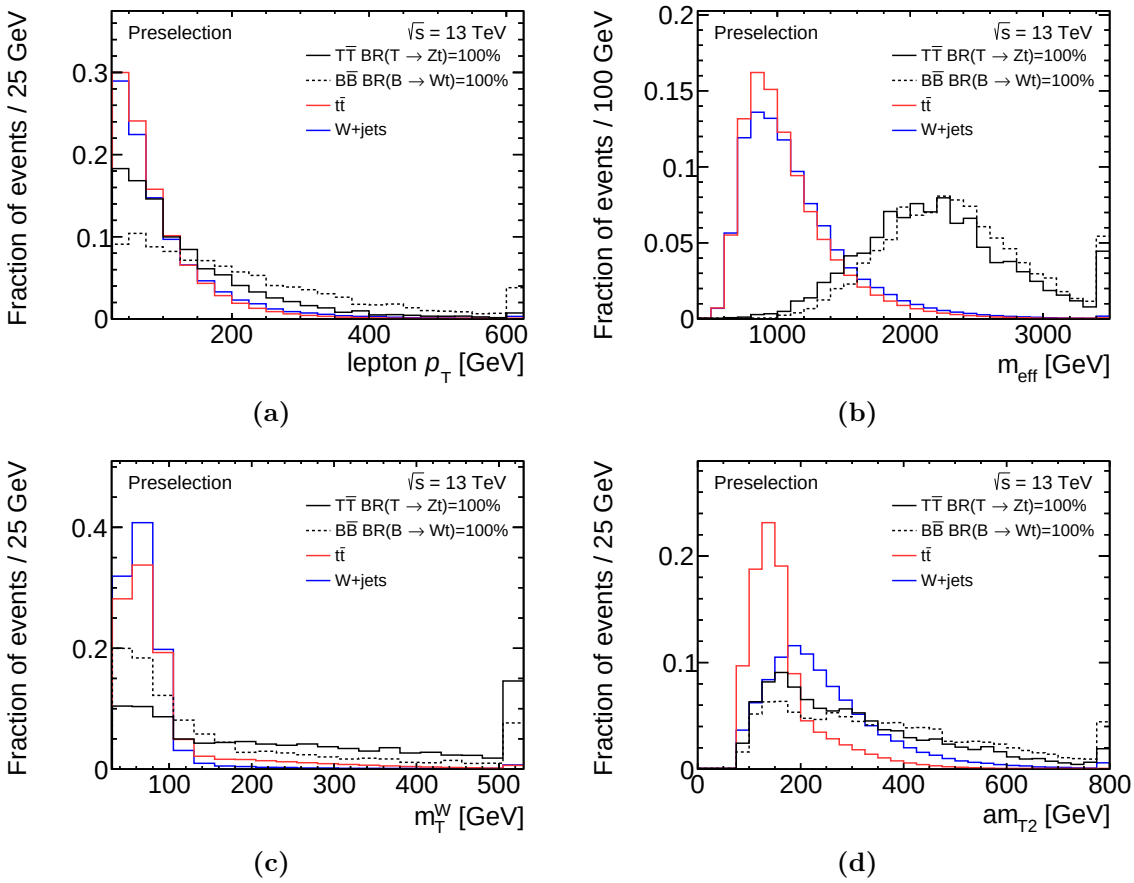

Figure B.2: Shape distributions of (a) the lepton p_{T}, (b) m_{eff}, (c) m_{T}^{W}, and (d) am_{T2} after the preselection for $t\bar{t}$, W+jets, the VLT signal with exclusive $T \to Zt$ decays, and the VLB signal with exclusive $B \to Wt$ decays where the signal mass is considered to be 1.2 TeV. The last bin in each distribution contains the overflow.

B.2 NN input variables in the training region

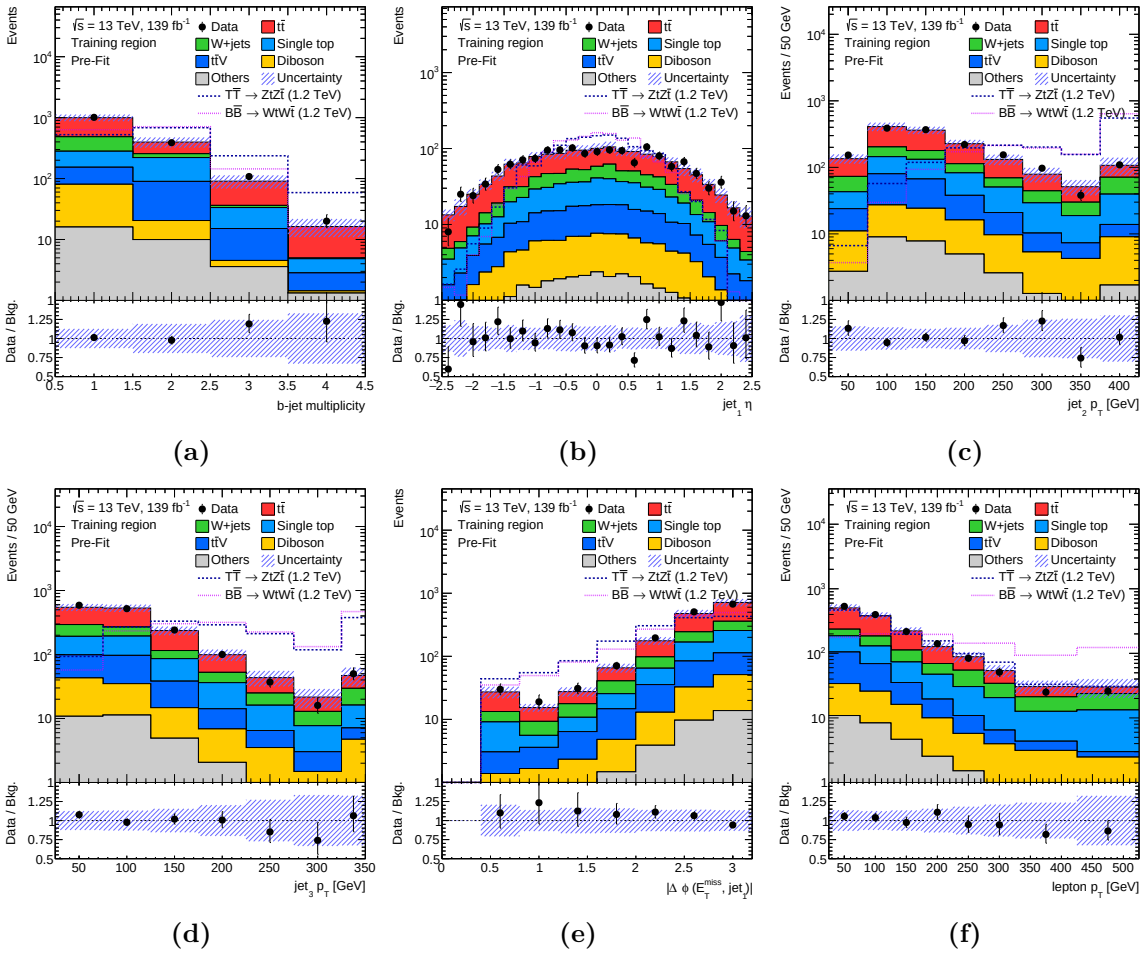

Figure B.3: Distributions of NN input variables in the training region for (a) the b-jet multiplicity, (b) $\eta(\text{jet}_1)$, (c) $p_{\text{T}}(\text{jet}_2)$, (d) $p_{\text{T}}(\text{jet}_3)$, (e) $|\Delta\phi(\text{jet}_1, E_{\text{T}}^{\text{miss}})|$, and (f) $p_{\text{T}}(\ell)$. The hatched bands indicate the total uncertainty including statistical and systematic uncertainties. The ratios of the data and the expected background events are shown in the bottom panels. The last bin in each distribution contains the overflow. The benchmark signal processes, normalised to the total background expectation, are overlaid as dashed lines.

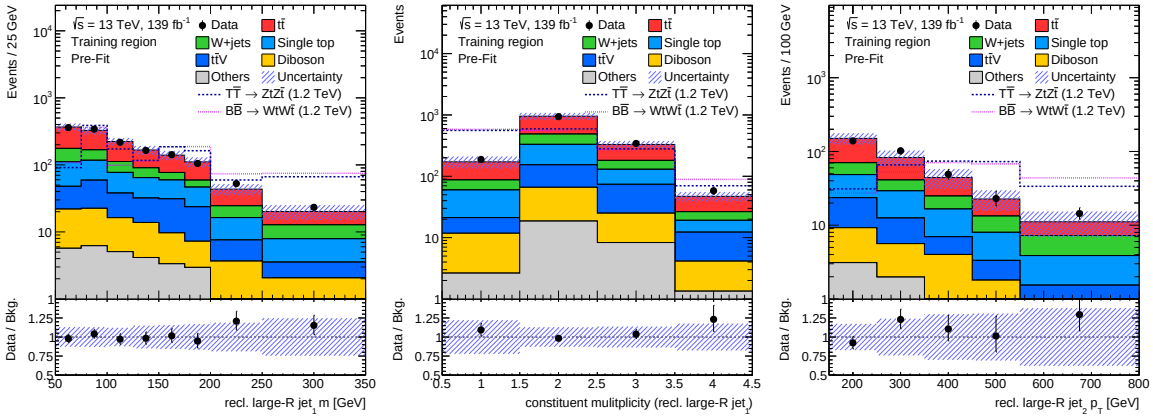

(a) **(b)** **(c)**

Figure B.4: Distributions of NN input variables in the training region for (a) m(large-R jet$_1$), (b) N_{const}(large-R jet$_1$), and (c) p_{T}(large-R jet$_2$). The hatched bands indicate the total uncertainty including statistical and systematic uncertainties. The ratios of the data and the expected background events are shown in the bottom panels. The last bin in each distribution contains the overflow. The benchmark signal processes, normalised to the total background expectation, are overlaid as dashed lines.

B.3 Additional distributions in the single-top CR and W+jets CR

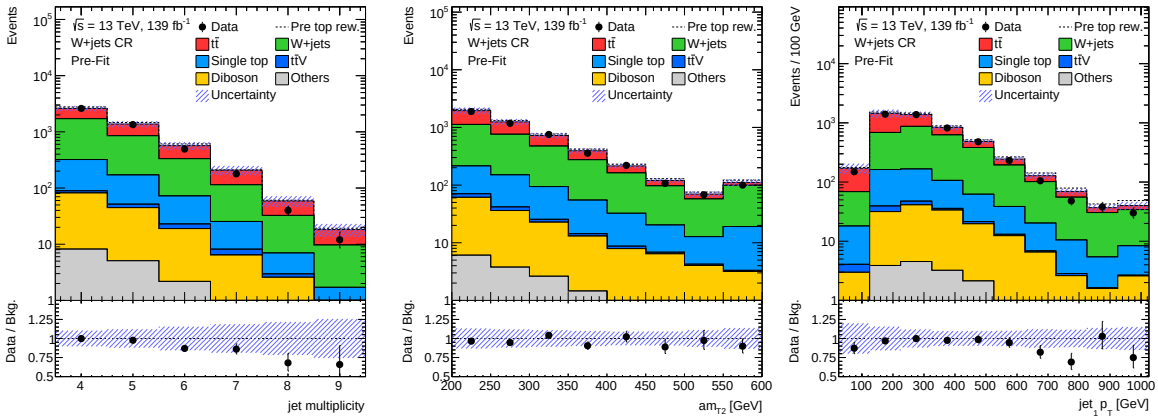

(a) (b) (c)

Figure B.5: Distributions of (a) the jet multiplicity, (b) am_{T2}, and (c) $p_{\mathrm{T}}(\mathrm{jet}_1)$ in the W+jets CR after applying the top reweighting factors and before applying the fit to the CRs and SR ("Pre-Fit"). The contributions from $t\bar{t}H$, tWZ, and Z+jets are summarised as "Others". The hatched bands indicate the total uncertainty. The total background prediction before applying the top reweighting is shown as a dashed line. The lower panels show the ratio of the data to the SM prediction. The last bin contains the overflow.

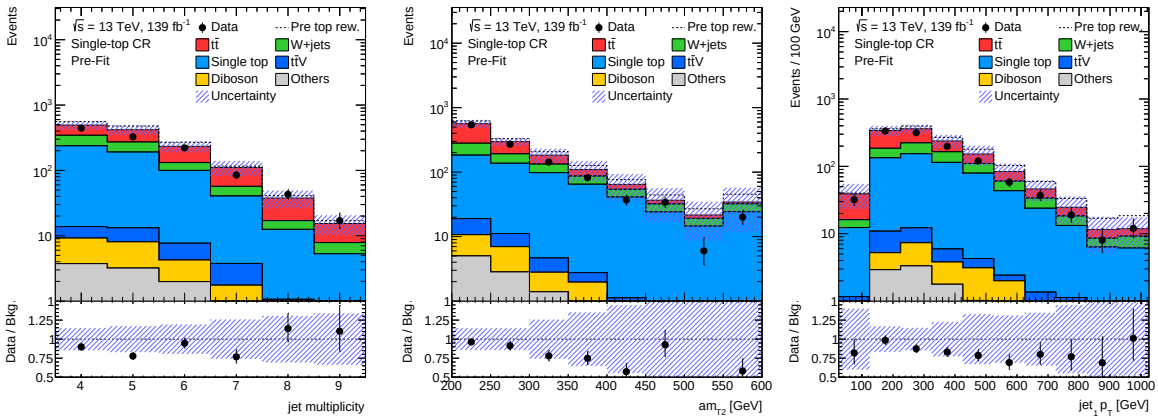

(a) (b) (c)

Figure B.6: Distributions of (a) the jet multiplicity, (b) am_{T2}, and (c) $p_{\mathrm{T}}(\mathrm{jet}_1)$ in the single-top CR after applying the top reweighting factors and before applying the fit to the CRs and SR ("Pre-Fit"). The contributions from $t\bar{t}H$, tWZ, and Z+jets are summarised as "Others". The hatched bands indicate the total uncertainty. The total background prediction before applying the top reweighting is shown as a dashed line. The lower panels show the ratio of the data to the SM prediction. The last bin contains the overflow.

B.4 Background-only fits

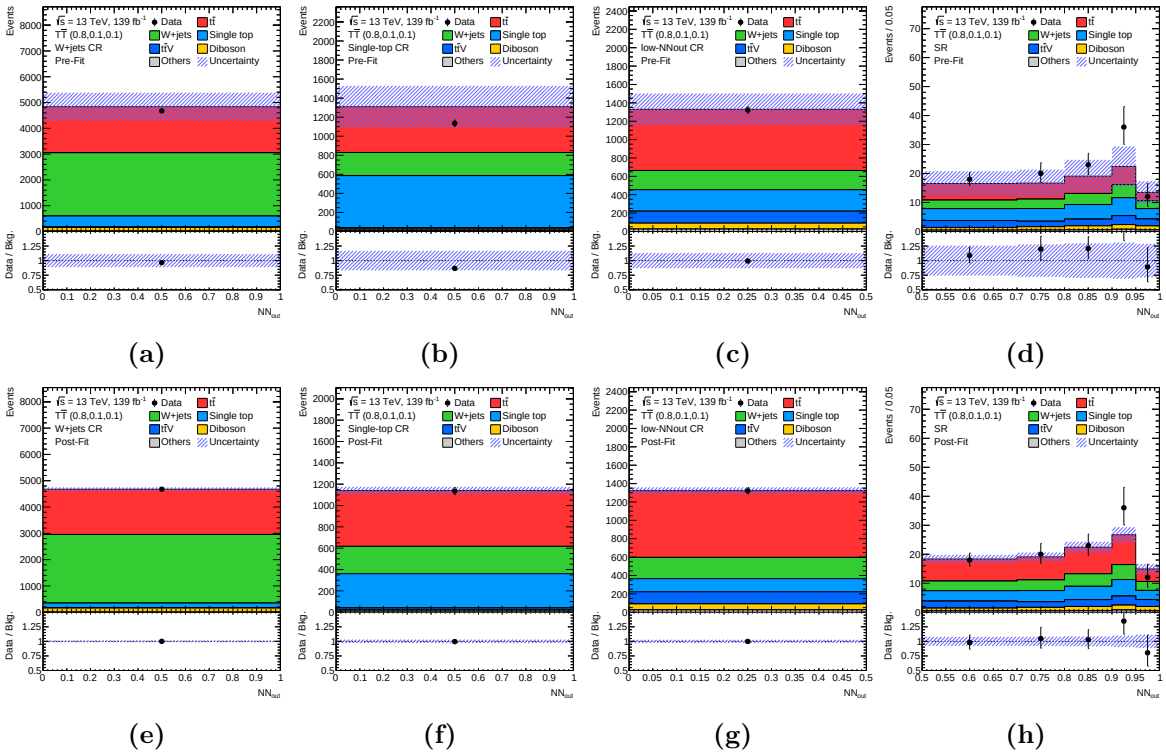

Figure B.7: Data and background expectation in the W+jets CR, single-top CR, low-NN_{out} CR, and the SR using the NN trained for a VLT signal with $\mathcal{B}(Zt, Ht, Wb) = (0.8, 0.1, 0.1)$. The upper row, (a)-(d), shows the input distributions for the likelihood fit, and the lower row, (e)-(h), shows the corresponding post-fit distributions. Contributions from $t\bar{t}H$, tWZ, and Z+jets are combined into "Others". The hashed band includes statistical and systematic uncertainties. The ratios between the data and the background expectation are shown in the bottom panels.

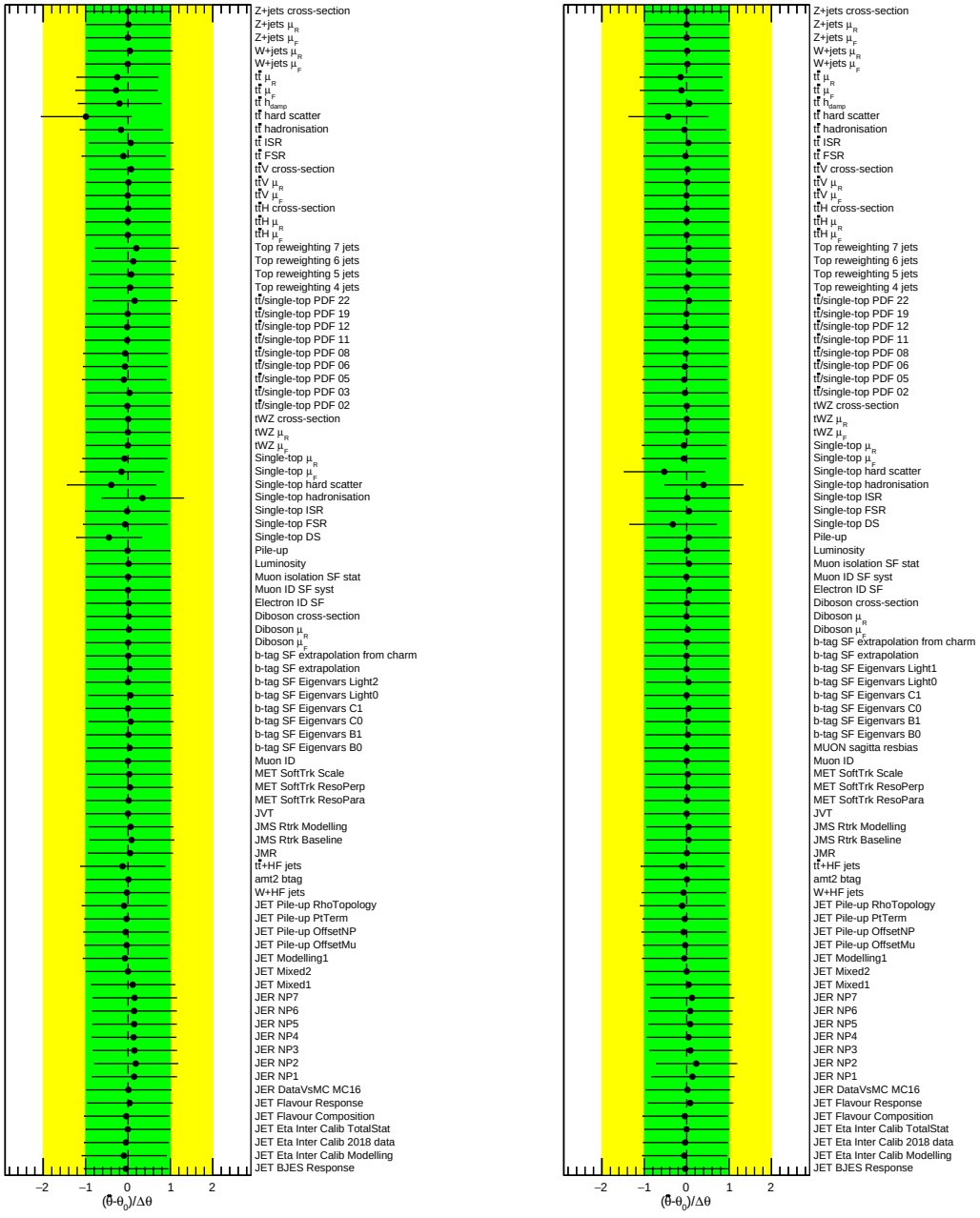

(a) **(b)**

Figure B.8: Pulls and constraints of NPs related to the modelling of the background processes. In (a) the NN trained for the the VLT signal with $\mathcal{B}(Zt, Ht, Wb) = (0.8, 0.1, 0.1)$ is used in the background-only fit, while the NN trained for the VLB signal with $\mathcal{B}(Zb, Hb, Wt) = (0.1, 0.1, 0.8)$ is considered in (b).

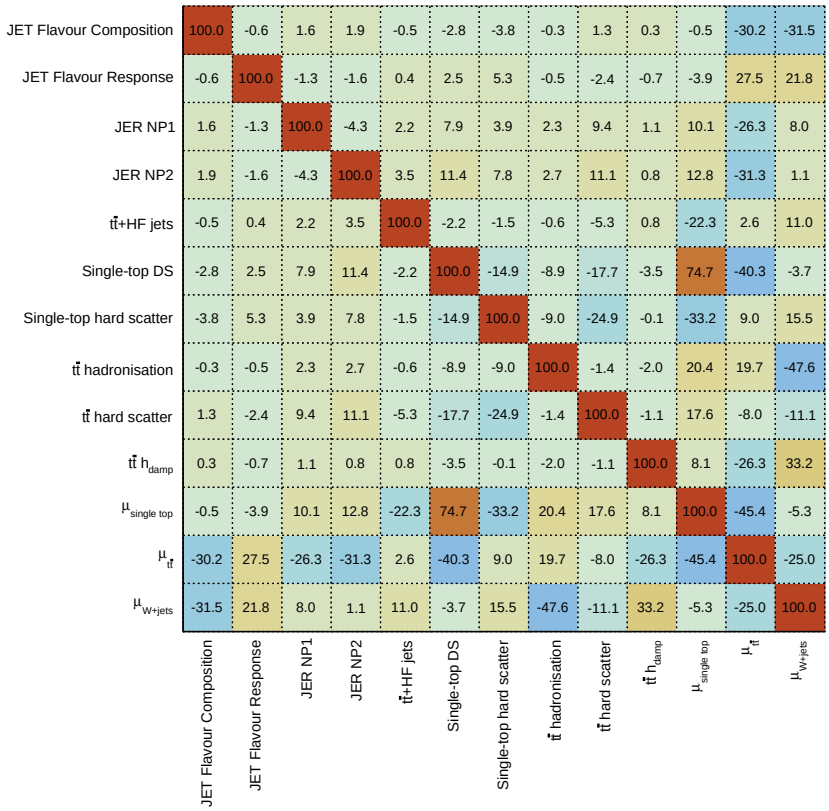

Figure B.9: Correlations between NPs and normalisation factors in a background-only fit in CRs and SR using the NN trained for the VLB signal with $\mathcal{B}(Zb, Hb, Wt) = (0.1, 0.1, 0.8)$. Only parameters having a correlation of at least 20 % with at least one other parameter are displayed in the matrix.

Table B.1: Observed and expected event yields including their total uncertainty (stat.+syst.) in the control and signal regions considering an NN training for a VLB signal with a branching ratio of $\mathcal{B}(Zb, Hb, Wt) = (0.1, 0.1, 0.8)$ after the background-only fit. For comparison, the expected event yields for a VLB signal with a mass of 1.2 TeV and a branching ratio of $\mathcal{B}(Zb, Hb, Wt) = (0.1, 0.1, 0.8)$ are given.

	W+jets CR	Single-top CR	low-NN_{out} CR	SR
$t\bar{t}$	1880 ± 420	530 ± 110	740 ± 120	78 ± 27
W+jets	2420 ± 370	236 ± 47	204 ± 44	43 ± 11
Single top	200 ± 210	329 ± 116	143 ± 79	50 ± 30
$t\bar{t}V$	20.2 ± 3.2	15.8 ± 2.6	138 ± 22	16.1 ± 2.9
Diboson	139 ± 17	14.0 ± 2.2	63.4 ± 8.2	13.4 ± 2.2
Z+jets	13.7 ± 3.5	3.93 ± 0.73	4.63 ± 0.74	1.30 ± 0.19
$t\bar{t}H$	2.54 ± 0.33	5.59 ± 0.69	11.2 ± 1.4	1.90 ± 0.31
tWZ	0.90 ± 0.12	0.82 ± 0.11	10.3 ± 1.4	1.51 ± 0.24
Total background	4676 ± 74	1139 ± 34	1319 ± 36	205 ± 18
Data	4676	1135	1317	210
$m_B = 1.2\,\text{TeV}$				
$\mathcal{B}(Zb, Hb, Wt) = (0.1, 0.1, 0.8)$	0.67 ± 0.09	1.49 ± 0.11	6.51 ± 0.31	50.52 ± 0.86

B.5 Post-fit neural network output distributions in the signal regions

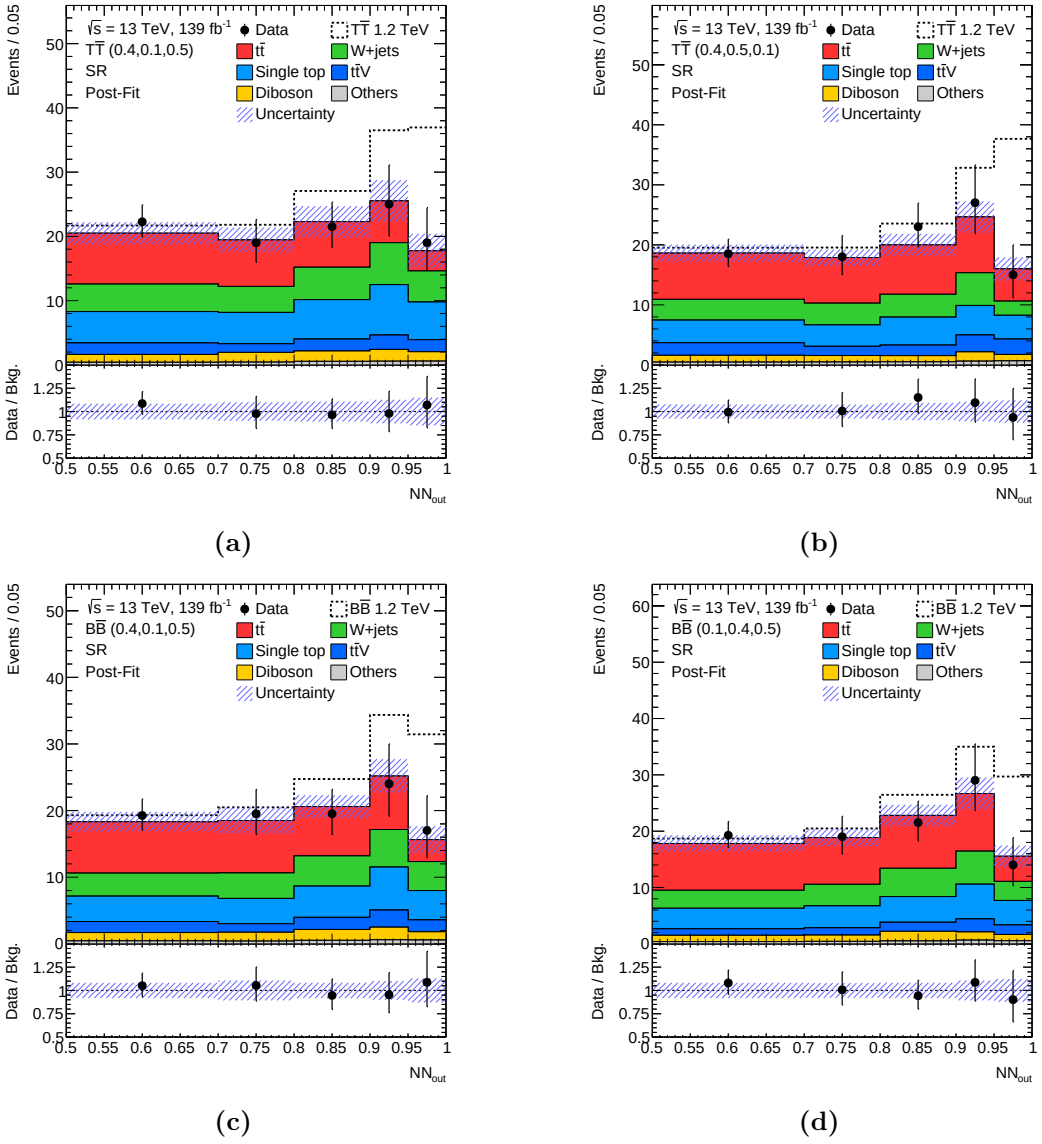

Figure B.10: Data and background expectation in the signal region after the simultaneous background-only fit to data ('Post-Fit') for (a) a NN training for a VLT signal with $\mathcal{B}(Zt, Ht, Wb) = (0.4, 0.1, 0.5)$, (b) a NN training for a VLT signal with $\mathcal{B}(Zt, Ht, Wb) = (0.4, 0.5, 0.1)$, (b) a VLB signal with $\mathcal{B}(Zb, Hb, Wt) = (0.4, 0.1, 0.5)$, and a VLB signal with $\mathcal{B}(Zb, Hb, Wt) = (0.1, 0.4, 0.5)$. Contributions from $t\bar{t}H$, tWZ, and Z+jets are combined into "Others". Expected pre-fit signal distributions with the signal branching ratio corresponding to the respective training are added on top of the background expectation, using a signal mass of 1.2 TeV. The hatched bands indicate the total post-fit uncertainty. The ratios between the data and the background expectation are shown in the bottom panels.

C Interference study

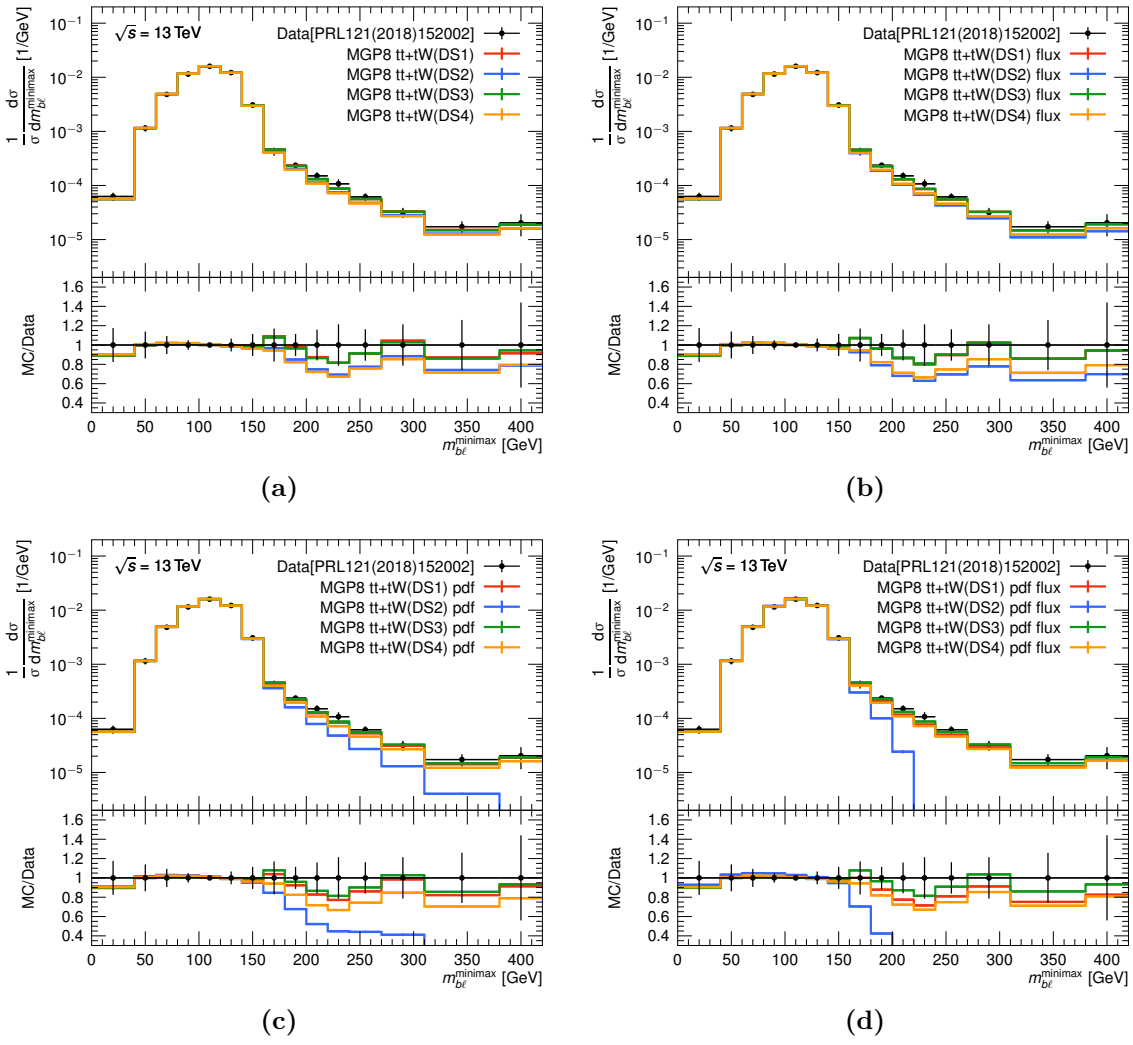

Figure C.1: Distributions of the $m_{b\ell}^{\text{minimax}}$ variable. Predictions for $t\bar{t} + tW$ from various MG5_aMC@NLO+Pythia 8 samples using different DR and DS schemes are compared to unfolded data from Ref. [227]. The `pdf` and `flux` label in the legend indicates that the corresponding parameter is set to true in the generation of the tW sample. The last bin of the distribution includes contributions from the overflow bin.

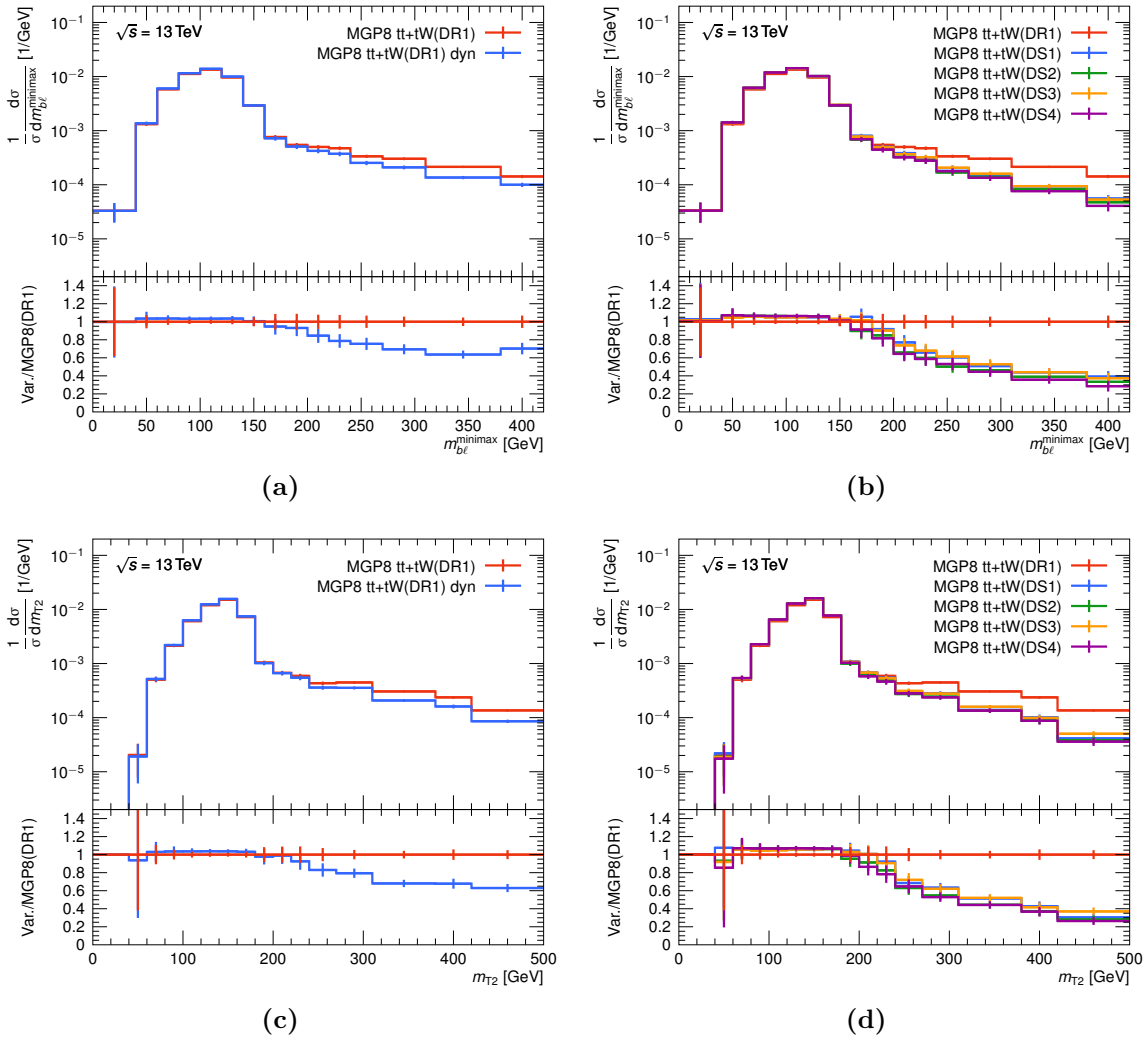

Figure C.2: Distributions of (a), (b) $m_{b\ell}^{\text{minimax}}$ and (c), (d) m_{T2} after the search-like selection requiring two leptons ($e\mu$), $E_{\text{T}}^{\text{miss}} > 200\,\text{GeV}$ and at least four jets of which two must be b-jets. Predictions for $t\bar{t} + tW$ of different MG5_aMC@NLO+Pythia 8 samples with various implementations of the DR and DS schemes, and different scale choices are compared. The label "dyn" in the legend denotes the usage of dynamic scales.

Bibliography

[1] D. Griffiths, *Introduction to elementary particles*, Weinheim, Germany: Wiley-VCH, 2008.

[2] M. E. Peskin and D. V. Schroeder, *An Introduction to quantum field theory*, Reading, USA: Addison-Wesley, 1995.

[3] ATLAS Collaboration, *Observation of a new particle in the search for the Standard Model Higgs boson with the ATLAS detector at the LHC*, Phys. Lett. B **716** (2012) 1, arXiv: 1207.7214 [hep-ex].

[4] CMS Collaboration, *Observation of a new boson at a mass of 125 GeV with the CMS experiment at the LHC*, Phys. Lett. B **716** (2012) 30, arXiv: 1207.7235 [hep-ex].

[5] P. A. Zyla et al., *Review of Particle Physics*, PTEP **2020** (2020) 083C01.

[6] S. Weinberg, *A Model of Leptons*, Phys. Rev. Lett. **19** (1967) 1264.

[7] S. L. Glashow, *Partial Symmetries of Weak Interactions*, Nucl. Phys. **22** (1961) 579.

[8] M. Kobayashi and T. Maskawa, *CP Violation in the Renormalizable Theory of Weak Interaction*, Prog. Theor. Phys. **49** (1973) 652.

[9] N. Cabibbo, *Unitary Symmetry and Leptonic Decays*, Phys. Rev. Lett. **10** (1963) 531.

[10] T. Nakano and K. Nishijima, *Charge Independence for V-particles*, Prog. Theor. Phys. **10** (1953) 581.

[11] M. Gell-Mann, *The interpretation of the new particles as displaced charge multiplets*, Nuovo Cim. **4** (1956) 848.

[12] P. W. Higgs, *Broken Symmetries and the Masses of Gauge Bosons*, Phys. Rev. Lett. **13** (1964) 508, ed. by J. C. Taylor.

[13] F. Englert and R. Brout, *Broken Symmetry and the Mass of Gauge Vector Mesons*, Phys. Rev. Lett. **13** (1964) 321, ed. by J. C. Taylor.

[14] J. Goldstone, A. Salam, and S. Weinberg, *Broken Symmetries*, Phys. Rev. **127** (1962) 965.

[15] D. J. Gross and F. Wilczek, *Ultraviolet Behavior of Nonabelian Gauge Theories*, Phys. Rev. Lett. **30** (1973) 1343, ed. by J. C. Taylor.

[16] H. D. Politzer, *Reliable Perturbative Results for Strong Interactions?*, Phys. Rev. Lett. **30** (1973) 1346, ed. by J. C. Taylor.

[17] K. G. Wilson, *Confinement of Quarks*, Phys. Rev. D **10** (1974) 2445, ed. by J. C. Taylor.

[18] UA1 Collaboration, *Experimental Observation of Isolated Large Transverse Energy Electrons with Associated Missing Energy at* $\sqrt{s} = 540$ *GeV*, Phys. Lett. B **122** (1983) 103.

[19] UA1 Collaboration, *Experimental Observation of Lepton Pairs of Invariant Mass Around 95-GeV/c**2 at the CERN SPS Collider*, Phys. Lett. B **126** (1983) 398.

[20] CDF Collaboration, *Observation of top quark production in* $\bar{p}p$ *collisions*, Phys. Rev. Lett. **74** (1995) 2626, arXiv: hep-ex/9503002.

[21] D0 Collaboration, *Observation of the top quark*, Phys. Rev. Lett. **74** (1995) 2632, arXiv: hep-ex/9503003.

[22] R. J. Crewther, P. Di Vecchia, G. Veneziano, and E. Witten, *Chiral Estimate of the Electric Dipole Moment of the Neutron in Quantum Chromodynamics*, Phys. Lett. B **88** (1979) 123, [Erratum: Phys.Lett.B 91, 487 (1980)].

[23] C. Abel et al., *Measurement of the Permanent Electric Dipole Moment of the Neutron*, Phys. Rev. Lett. **124** (2020) 081803, arXiv: 2001.11966 [hep-ex].

[24] ATLAS Collaboration, *Measurement of the Higgs boson mass in the* $H \to ZZ^* \to 4\ell$ *and* $H \to \gamma\gamma$ *channels with* $\sqrt{s} = 13$ *TeV pp collisions using the ATLAS detector*, Phys. Lett. B **784** (2018) 345, arXiv: 1806.00242 [hep-ex].

[25] J. Haller et al., *Update of the global electroweak fit and constraints on two-Higgs-doublet models*, Eur. Phys. J. C **78** (2018) 675, arXiv: 1803.01853 [hep-ph].

[26] ATLAS Collaboration, *Standard Model Summary Plots February 2022*, ATL-PHYS-PUB-2022-009, 2022, URL: http://cds.cern.ch/record/2804061.

[27] Super-Kamiokande Collaboration, *Evidence for oscillation of atmospheric neutrinos*, Phys. Rev. Lett. **81** (1998) 1562, arXiv: hep-ex/9807003.

[28] P. F. De Salas, S. Gariazzo, O. Mena, C. A. Ternes, and M. Tórtola, *Neutrino Mass Ordering from Oscillations and Beyond: 2018 Status and Future Prospects*, Front. Astron. Space Sci. **5** (2018) 36, arXiv: 1806.11051 [hep-ph].

[29] Planck Collaboration, *Planck 2018 results. VI. Cosmological parameters*, Astron. Astrophys. **641** (2020) A6, [Erratum: Astron.Astrophys. 652, C4 (2021)], arXiv: 1807.06209 [astro-ph.CO].

[30] L. Canetti, M. Drewes, and M. Shaposhnikov, *Matter and Antimatter in the Universe*, New J. Phys. **14** (2012) 095012, arXiv: 1204.4186 [hep-ph].

[31] K. G. Begeman, A. H. Broeils, and R. H. Sanders,
Extended rotation curves of spiral galaxies: Dark haloes and modified dynamics,
Mon. Not. Roy. Astron. Soc. **249** (1991) 523.

[32] L. Susskind,
Dynamics of Spontaneous Symmetry Breaking in the Weinberg-Salam Theory,
Phys. Rev. D **20** (1979) 2619.

[33] A. Djouadi and A. Lenz, *Sealing the fate of a fourth generation of fermions*,
Phys. Lett. **B715** (2012) 310, arXiv: 1204.1252v2 [hep-ph].

[34] J. A. Aguilar-Saavedra, R. Benbrik, S. Heinemeyer, and M. Pérez-Victoria,
Handbook of vectorlike quarks: Mixing and single production,
Phys. Rev. D **88** (2013) 094010, arXiv: 1306.0572 [hep-ph].

[35] M. Schmaltz and D. Tucker-Smith, *Little Higgs Theories*,
Ann. Rev. Nucl. Part. Sci. **55** (2005) 229, arXiv: hep-ph/0502182.

[36] N. Arkani-Hamed, A. G. Cohen, E. Katz, and A. E. Nelson, *The Littlest Higgs*,
JHEP **07** (2002) 034, arXiv: hep-ph/0206021.

[37] K. Agashe, R. Contino, and A. Pomarol, *The minimal composite Higgs model*,
Nucl. Phys. B **719** (2005) 165, arXiv: hep-ph/0412089.

[38] D. B. Kaplan, H. Georgi, and S. Dimopoulos, *Composite Higgs scalars*,
Phys. Lett. B **136** (1984) 187.

[39] S. P. Martin, *A Supersymmetry primer*,
Adv. Ser. Direct. High Energy Phys. **18** (1998) 1, ed. by G. L. Kane,
arXiv: hep-ph/9709356.

[40] J. L. Hewett and T. G. Rizzo,
Low-Energy Phenomenology of Superstring Inspired E(6) Models,
Phys. Rept. **183** (1989) 193.

[41] I. Antoniadis, *A Possible new dimension at a few TeV*, Phys. Lett. B **246** (1990) 377.

[42] L. Randall and R. Sundrum, *A Large mass hierarchy from a small extra dimension*,
Phys. Rev. Lett. **83** (1999) 3370, arXiv: hep-ph/9905221.

[43] Y. Okada and L. Panizzi, *LHC Signatures of Vector-Like Quarks*,
Adv. High Energy Phys. **2013** (2013) 364936, arXiv: 1207.5607 [hep-ph].

[44] M. Czakon and A. Mitov,
Top++: A program for the calculation of the top-pair cross-section at hadron colliders,
Comput. Phys. Commun. **185** (2014) 2930, arXiv: 1112.5675 [hep-ph].

[45] S. L. Glashow, J. Iliopoulos, and L. Maiani,
Weak Interactions with Lepton-Hadron Symmetry, Phys. Rev. D **2** (1970) 1285.

[46] J. A. Aguilar-Saavedra, *Identifying top partners at LHC*, JHEP **11** (2009) 030, arXiv: 0907.3155 [hep-ph].

[47] ATLAS Collaboration,
Search for production of vector-like quark pairs and of four top quarks in the lepton-plus-jets final state in pp collisions at $\sqrt{s} = 8$ TeV with the ATLAS detector, JHEP **08** (2015) 105, arXiv: 1505.04306 [hep-ex].

[48] ATLAS Collaboration, *Search for pair production of up-type vector-like quarks and for four-top-quark events in final states with multiple b-jets with the ATLAS detector*, JHEP **07** (2018) 089, arXiv: 1803.09678 [hep-ex].

[49] ATLAS Collaboration, *Search for pair production of heavy vector-like quarks decaying to high-p_T W bosons and b quarks in the lepton-plus-jets final state in pp collisions at $\sqrt{s} = 13$ TeV with the ATLAS detector*, JHEP **10** (2017) 141, arXiv: 1707.03347 [hep-ex].

[50] ATLAS Collaboration,
Search for pair production of vector-like top quarks in events with one lepton, jets, and missing transverse momentum in $\sqrt{s} = 13$ TeV pp collisions with the ATLAS detector, JHEP **08** (2017) 052, arXiv: 1705.10751 [hep-ex].

[51] ATLAS Collaboration, *Search for new phenomena in events with same-charge leptons and b-jets in pp collisions at $\sqrt{s} = 13$ TeV with the ATLAS detector*, JHEP **12** (2018) 039, arXiv: 1807.11883 [hep-ex].

[52] ATLAS Collaboration, *Search for pair- and single-production of vector-like quarks in final states with at least one Z boson decaying into a pair of electrons or muons in pp collision data collected with the ATLAS detector*, Phys. Rev. D **98** (2018) 112010, arXiv: 1806.10555 [hep-ex].

[53] ATLAS Collaboration, *Search for pair production of heavy vector-like quarks decaying into hadronic final states in pp collisions at $\sqrt{s} = 13$ TeV with the ATLAS detector*, Phys. Rev. D **98** (2018) 092005, arXiv: 1808.01771 [hep-ex].

[54] ATLAS Collaboration, *Search for pair production of heavy vector-like quarks decaying into high-p_T W bosons and top quarks in the lepton-plus-jets final state in pp collisions at $\sqrt{s} = 13$ TeV with the ATLAS detector*, JHEP **08** (2018) 048, arXiv: 1806.01762 [hep-ex].

[55] ATLAS Collaboration, *Search for pair-production of vector-like quarks in pp collision events at $\sqrt{s} = 13$ TeV with at least one leptonically-decaying Z boson and a third-generation quark with ATLAS detector*, ATLAS-CONF-2021-024, 2021, URL: https://cds.cern.ch/record/2773300.

[56] CMS Collaboration, *A search for bottom-type, vector-like quark pair production in a fully hadronic final state in proton–proton collisions at* $\sqrt{s} = 13$ *TeV*, Phys. Rev. D **102** (2020) 112004, arXiv: 2008.09835 [hep-ex].

[57] CMS Collaboration, *Search for vector-like* T *and* B *quark pairs in final states with leptons at* $\sqrt{s} = 13$ *TeV*, JHEP **08** (2018) 177, arXiv: 1805.04758 [hep-ex].

[58] CMS Collaboration, *Search for vector-like quarks in events with two oppositely charged leptons and jets in proton–proton collisions at* $\sqrt{s} = 13$ *TeV*, Eur. Phys. J. C **79** (2019) 364, arXiv: 1812.09768 [hep-ex].

[59] CMS Collaboration, *Search for pair production of vector-like quarks in the* $bW\bar{b}W$ *channel from proton–proton collisions at* $\sqrt{s} = 13$ *TeV*, Phys. Lett. B **779** (2018) 82, arXiv: 1710.01539 [hep-ex].

[60] ATLAS Collaboration, *Combination of the searches for pair-produced vector-like partners of the third-generation quarks at* $\sqrt{s} = 13$ *TeV with the ATLAS detector*, Phys. Rev. Lett. **121** (2018) 211801, arXiv: 1808.02343 [hep-ex].

[61] ATLAS Collaboration, *Search for large missing transverse momentum in association with one top-quark in proton–proton collisions at* $\sqrt{s} = 13$ *TeV with the ATLAS detector*, JHEP **05** (2019) 041, arXiv: 1812.09743 [hep-ex].

[62] ATLAS Collaboration, *Search for single production of vector-like quarks decaying into* Wb *in pp collisions at* $\sqrt{s} = 13$ *TeV with the ATLAS detector*, JHEP **05** (2019) 164, arXiv: 1812.07343 [hep-ex].

[63] CMS Collaboration, *Search for electroweak production of a vector-like* T *quark using fully hadronic final states*, JHEP **01** (2020) 036, arXiv: 1909.04721 [hep-ex].

[64] CMS Collaboration, *Search for single production of vector-like quarks decaying to a top quark and a* W *boson in proton–proton collisions at* $\sqrt{s} = 13$ *TeV*, Eur. Phys. J. C **79** (2019) 90, arXiv: 1809.08597 [hep-ex].

[65] CMS Collaboration, *Search for single production of vector-like quarks decaying to a* Z *boson and a top or a bottom quark in proton–proton collisions at* $\sqrt{s} = 13$ *TeV*, JHEP **05** (2017) 029, arXiv: 1701.07409 [hep-ex].

[66] A. Buckley, J. M. Butterworth, L. Corpe, D. Huang, and P. Sun, *New sensitivity of current LHC measurements to vector-like quarks*, SciPost Phys. **9** (2020) 069, arXiv: 2006.07172 [hep-ph].

[67] J. C. Collins, D. E. Soper, and G. F. Sterman, *Factorization of Hard Processes in QCD*, Adv. Ser. Direct. High Energy Phys. **5** (1989) 1, arXiv: hep-ph/0409313.

[68] A. Buckley et al., *General-purpose event generators for LHC physics*, Phys. Rept. **504** (2011) 145, arXiv: 1101.2599 [hep-ph].

[69] J. Kuechler, *Search for Partners of the Top Quark with the ATLAS Experiment*, 2018, URL: https://cds.cern.ch/record/2638106.

[70] H.-L. Lai et al., *New parton distributions for collider physics*, Phys. Rev. D **82** (2010) 074024, arXiv: 1007.2241 [hep-ph].

[71] R. D. Ball et al., *Parton distributions for the LHC run II*, JHEP **04** (2015) 040, arXiv: 1410.8849 [hep-ph].

[72] G. Altarelli and G. Parisi, *Asymptotic Freedom in Parton Language*, Nucl. Phys. B **126** (1977) 298.

[73] V. N. Gribov and L. N. Lipatov, *Deep inelastic e p scattering in perturbation theory*, Sov. J. Nucl. Phys. **15** (1972) 438.

[74] Y. L. Dokshitzer, *Calculation of the Structure Functions for Deep Inelastic Scattering and e+ e- Annihilation by Perturbation Theory in Quantum Chromodynamics.*, Sov. Phys. JETP **46** (1977) 641.

[75] A. Buckley et al., *LHAPDF6: parton density access in the LHC precision era*, Eur. Phys. J. C **75** (2015) 132, arXiv: 1412.7420 [hep-ph].

[76] P. Skands, "Introduction to QCD", *Theoretical Advanced Study Institute in Elementary Particle Physics: Searching for New Physics at Small and Large Scales*, 2013 341, arXiv: 1207.2389 [hep-ph].

[77] T. D. Lee and M. Nauenberg, *Degenerate Systems and Mass Singularities*, Phys. Rev. **133** (1964) B1549, ed. by G. Feinberg.

[78] T. Kinoshita, *Mass singularities of Feynman amplitudes*, J. Math. Phys. **3** (1962) 650.

[79] S. Höche, "Introduction to parton-shower event generators", *Theoretical Advanced Study Institute in Elementary Particle Physics: Journeys Through the Precision Frontier: Amplitudes for Colliders*, 2015 235, arXiv: 1411.4085 [hep-ph].

[80] S. Frixione, P. Nason, and C. Oleari, *Matching NLO QCD computations with parton shower simulations: the POWHEG method*, JHEP **11** (2007) 070, arXiv: 0709.2092 [hep-ph].

[81] S. Frixione and B. R. Webber, *Matching NLO QCD computations and parton shower simulations*, JHEP **06** (2002) 029, arXiv: hep-ph/0204244.

[82] S. Catani, F. Krauss, B. R. Webber, and R. Kuhn, *QCD Matrix Elements + Parton Showers*, JHEP **11** (2001) 063, arXiv: hep-ph/0109231.

[83] L. Lönnblad,
Correcting the Colour-Dipole Cascade Model with Fixed Order Matrix Elements,
JHEP **05** (2002) 046, arXiv: hep-ph/0112284.

[84] M. L. Mangano, M. Moretti, F. Piccinini, and M. Treccani, *Matching matrix elements and shower evolution for top-quark production in hadronic collisions*,
JHEP **01** (2007) 013, arXiv: hep-ph/0611129.

[85] R. Frederix and S. Frixione, *Merging meets matching in MC@NLO*,
JHEP **12** (2012) 061, arXiv: 1209.6215 [hep-ph].

[86] K. Hamilton, P. Nason, and G. Zanderighi, *MINLO: multi-scale improved NLO*,
JHEP **10** (2012) 155, arXiv: 1206.3572 [hep-ph].

[87] S. Höche, F. Krauss, S. Schumann, and F. Siegert,
QCD matrix elements and truncated showers, JHEP **05** (2009) 053,
arXiv: 0903.1219 [hep-ph].

[88] B. R. Webber, *A QCD Model for Jet Fragmentation Including Soft Gluon Interference*,
Nucl. Phys. B **238** (1984) 492.

[89] T. Sjöstrand, *Jet fragmentation of multiparton configurations in a string framework*,
Nucl. Phys. B **248** (1984) 469.

[90] B. Andersson, G. Gustafson, G. Ingelman, and T. Sjöstrand,
Parton fragmentation and string dynamics, Phys. Rept. **97** (1983) 31.

[91] D. Amati and G. Veneziano, *Preconfinement as a Property of Perturbative QCD*,
Phys. Lett. B **83** (1979) 87.

[92] ATLAS Collaboration,
Measurement of charged-particle distributions sensitive to the underlying event in $\sqrt{s} = 13$ TeV proton–proton collisions with the ATLAS detector at the LHC,
JHEP **03** (2017) 157, arXiv: 1701.05390 [hep-ex].

[93] T. Sjöstrand, S. Mrenna, and P. Skands, *A brief introduction to PYTHIA 8.1*,
Comput. Phys. Commun. **178** (2008) 852, arXiv: 0710.3820 [hep-ph].

[94] T. Sjöstrand et al., *An introduction to PYTHIA 8.2*,
Comput. Phys. Commun. **191** (2015) 159, arXiv: 1410.3012 [hep-ph].

[95] J. Bellm et al., *Herwig 7.0/Herwig++ 3.0 release note*, Eur. Phys. J. C **76** (2016) 196,
arXiv: 1512.01178 [hep-ph].

[96] J. Bellm et al., *Herwig 7.1 Release Note*, (2017), arXiv: 1705.06919 [hep-ph].

[97] E. Bothmann et al., *Event generation with Sherpa 2.2*, SciPost Phys. **7** (2019) 034,
arXiv: 1905.09127 [hep-ph].

[98] S. Schumann and F. Krauss,
A parton shower algorithm based on Catani–Seymour dipole factorisation,
JHEP **03** (2008) 038, arXiv: 0709.1027 [hep-ph].

[99] S. Höche, F. Krauss, M. Schönherr, and F. Siegert,
A critical appraisal of NLO+PS matching methods, JHEP **09** (2012) 049,
arXiv: 1111.1220 [hep-ph].

[100] S. Höche, F. Krauss, M. Schönherr, and F. Siegert,
QCD matrix elements + parton showers. The NLO case, JHEP **04** (2013) 027,
arXiv: 1207.5030 [hep-ph].

[101] P. Nason,
A new method for combining NLO QCD with shower Monte Carlo algorithms,
JHEP **11** (2004) 040, arXiv: hep-ph/0409146.

[102] S. Alioli, P. Nason, C. Oleari, and E. Re, *A general framework for implementing NLO calculations in shower Monte Carlo programs: the POWHEG BOX*,
JHEP **06** (2010) 043, arXiv: 1002.2581 [hep-ph].

[103] S. Frixione, G. Ridolfi, and P. Nason,
A positive-weight next-to-leading-order Monte Carlo for heavy flavour hadroproduction,
JHEP **09** (2007) 126, arXiv: 0707.3088 [hep-ph].

[104] J. Alwall et al., *The automated computation of tree-level and next-to-leading order differential cross sections, and their matching to parton shower simulations*,
JHEP **07** (2014) 079, arXiv: 1405.0301 [hep-ph].

[105] J. A. Aguilar-Saavedra, *PROTOS, a PROgram for TOp Simulations*,
URL: http://jaguilar.web.cern.ch/jaguilar/protos/.

[106] D. J. Lange, *The EvtGen particle decay simulation package*,
Nucl. Instrum. Meth. A **462** (2001) 152.

[107] N. Davidson, G. Nanava, T. Przedzinski, E. Richter-Was, and Z. Was,
Universal Interface of TAUOLA Technical and Physics Documentation,
Comput. Phys. Commun. **183** (2012) 821, arXiv: 1002.0543 [hep-ph].

[108] P. Golonka and Z. Was,
PHOTOS Monte Carlo: a precision tool for QED corrections in Z and W decays,
Eur. Phys. J. C **45** (2006) 97, arXiv: hep-ph/0506026.

[109] N. Davidson, T. Przedzinski, and Z. Was,
PHOTOS Interface in C++: Technical and physics documentation,
Comput. Phys. Commun. **199** (2016) 86, arXiv: 1011.0937 [hep-ph].

[110] P. Artoisenet, R. Frederix, O. Mattelaer, and R. Rietkerk,
Automatic spin-entangled decays of heavy resonances in Monte Carlo simulations,
JHEP **03** (2013) 015, arXiv: 1212.3460 [hep-ph].

[111] S. Frixione, E. Laenen, P. Motylinski, and B. R. Webber, *Angular correlations of lepton pairs from vector boson and top quark decays in Monte Carlo simulations*, JHEP **04** (2007) 081, arXiv: hep-ph/0702198.

[112] ATLAS Collaboration, *The ATLAS Simulation Infrastructure*, Eur. Phys. J. C **70** (2010) 823, arXiv: 1005.4568 [physics.ins-det].

[113] GEANT4 Collaboration, S. Agostinelli, et al., *GEANT4 – a simulation toolkit*, Nucl. Instrum. Meth. A **506** (2003) 250.

[114] ATLAS Collaboration, *The simulation principle and performance of the ATLAS fast calorimeter simulation FastCaloSim*, ATL-PHYS-PUB-2010-013, 2010, URL: https://cds.cern.ch/record/1300517.

[115] *Generator Service Project (GENSER)*, URL: https://ep-dep-sft.web.cern.ch/project/generator-service-project-genser.

[116] C. Ay et al., *Monte Carlo generators in ATLAS software*, J. Phys. Conf. Ser. **219** (2010) 032001, ed. by J. Gruntorad and M. Lokajicek.

[117] M. Dobbs and J. B. Hansen, *The HepMC C++ Monte Carlo event record for High Energy Physics*, Comput. Phys. Commun. **134** (2001) 41.

[118] R. Brun and F. Rademakers, *ROOT – An object oriented data analysis framework*, Nucl. Instrum. Meth. A **389** (1997) 81, ISSN: 0168-9002.

[119] J. Alwall et al., *A Standard format for Les Houches event files*, Comput. Phys. Commun. **176** (2007) 300, arXiv: hep-ph/0609017 [hep-ph].

[120] *LHC computing Grid. Technical design report*, (2005), ed. by I. Bird et al.

[121] ATLAS Collaboration, *Validation of Monte Carlo event generators in the ATLAS Collaboration for LHC Run 2*, ATL-PHYS-PUB-2016-001, 2016, URL: https://cds.cern.ch/record/2119984.

[122] T. C. Donszelmann, W. Lampl, and G. A. Stewart, *ART ATLAS Release Tester using the Grid*, EPJ Web Conf. **245** (2020) 05015, ed. by C. Doglioni et al.

[123] A. Buckley et al., *Rivet user manual*, Comput. Phys. Commun. **184** (2013) 2803, arXiv: 1003.0694 [hep-ph].

[124] ATLAS Collaboration, *Modelling and computational improvements to the simulation of single vector-boson plus jet processes for the ATLAS experiment*, (2021), arXiv: 2112.09588 [hep-ex].

[125] C. Ay, S. Johnert, J. Katzy, and Z.-H. Qin, *HepMCAnalyser: A tool for Monte Carlo generator validation*, J. Phys. Conf. Ser. **219** (2010) 032029, ed. by J. Gruntorad and M. Lokajicek.

[126] C. Bierlich et al.,
Robust Independent Validation of Experiment and Theory: Rivet version 3,
SciPost Phys. **8** (2020) 026, arXiv: 1912.05451 [hep-ph].

[127] S. Albrand, J. Fulachier, and F. Lambert, *The ATLAS metadata interface*,
J. Phys. Conf. Ser. **219** (2010) 042030, ed. by J. Gruntorad and M. Lokajicek.

[128] A. Buckley et al., *The HepMC3 event record library for Monte Carlo event generators*,
Comput. Phys. Commun. **260** (2021) 107310, arXiv: 1912.08005 [hep-ph].

[129] S. Porteboeuf, T. Pierog, and K. Werner, "Producing Hard Processes Regarding the Complete Event: The EPOS Event Generator",
45th Rencontres de Moriond on QCD and High Energy Interactions,
Gioi Publishers, 2010 135, arXiv: 1006.2967 [hep-ph].

[130] O. Mattelaer and K. Ostrolenk, *Speeding up MadGraph5_aMC@NLO*,
Eur. Phys. J. C **81** (2021) 435, arXiv: 2102.00773 [hep-ph].

[131] ATLAS Collaboration, *Measurement of jet activity produced in top-quark events with an electron, a muon and two b-tagged jets in the final state in pp collisions at $\sqrt{s} = 13$ TeV with the ATLAS detector*, Eur. Phys. J. C **77** (2017) 220,
arXiv: 1610.09978 [hep-ex].

[132] L. Evans and P. Bryant, *LHC Machine*, JINST **3** (2008) S08001.

[133] ALICE Collaboration, *The ALICE Experiment at the CERN LHC*,
JINST **3** (2008) S08002.

[134] ATLAS Collaboration, *The ATLAS Experiment at the CERN Large Hadron Collider*,
JINST **3** (2008) S08003.

[135] CMS Collaboration, *The CMS Experiment at the CERN LHC*,
JINST **3** (2008) S08004.

[136] LHCb Collaboration, *The LHCb Detector at the LHC*, JINST **3** (2008) S08005.

[137] C. Lefèvre, "The CERN accelerator complex. Complexe des accélérateurs du CERN",
2008, URL: https://cds.cern.ch/record/1260465.

[138] ATLAS Collaboration, *Delivered Luminosity versus time for 2011-2018 (pp data only)*,
2018, URL: https://twiki.cern.ch/twiki/bin/view/AtlasPublic/LuminosityPublicResultsRun2.

[139] ATLAS Collaboration, *Number of Interactions per Crossing*, 2018, URL: https://twiki.cern.ch/twiki/bin/view/AtlasPublic/LuminosityPublicResultsRun2.

[140] B. Salvachua, "Overview of Proton-Proton Physics during Run 2",
9th LHC Operations Evian Workshop, 2019 7.

[141] J. Pequenao, *Computer generated image of the whole ATLAS detector*, 2008,
URL: https://cds.cern.ch/record/1095924.

[142] ATLAS Collaboration, *ATLAS Inner Detector: Technical Design Report, Volume 1*, ATLAS-TDR-4; CERN-LHCC-97-016, 1997, URL: https://cds.cern.ch/record/331063.

[143] ATLAS Collaboration, *ATLAS Inner Detector: Technical Design Report, Volume 2*, ATLAS-TDR-5, CERN-LHCC-97-017, 1997, URL: https://cds.cern.ch/record/331064.

[144] ATLAS Collaboration, *Performance of the ATLAS track reconstruction algorithms in dense environments in LHC Run 2*, Eur. Phys. J. C **77** (2017) 673, arXiv: 1704.07983 [hep-ex].

[145] B. Abbott et al., *Production and integration of the ATLAS Insertable B-Layer*, JINST **13** (2018) T05008, arXiv: 1803.00844 [physics.ins-det].

[146] ATLAS Collaboration, *ATLAS Calorimeter Performance: Technical Design Report*, ATLAS-TDR-1; CERN-LHCC-96-040, 1996, URL: https://cds.cern.ch/record/331059.

[147] J. Pequenao, "Computer Generated image of the ATLAS calorimeter", 2008, URL: http://cds.cern.ch/record/1095927.

[148] ATLAS Collaboration, *ATLAS Muon Spectrometer: Technical Design Report*, ATLAS-TDR-10; CERN-LHCC-97-022, CERN, 1997, URL: https://cds.cern.ch/record/331068.

[149] J. Pequenao, "Computer generated image of the ATLAS Muons subsystem", 2008, URL: http://cds.cern.ch/record/1095929.

[150] ATLAS Collaboration, *Performance of the ATLAS trigger system in 2015*, Eur. Phys. J. C **77** (2017) 317, arXiv: 1611.09661 [hep-ex].

[151] ATLAS Collaboration, *Operation of the ATLAS trigger system in Run 2*, JINST **15** (2020) P10004, arXiv: 2007.12539 [hep-ex].

[152] ATLAS Collaboration, *Performance of the missing transverse momentum triggers for the ATLAS detector during Run-2 data taking*, JHEP **08** (2020) 080, arXiv: 2005.09554 [hep-ex].

[153] ATLAS Collaboration, *Luminosity determination in pp collisions at $\sqrt{s} = 8$ TeV using the ATLAS detector at the LHC*, Eur. Phys. J. C **76** (2016) 653, arXiv: 1608.03953 [hep-ex].

[154] ATLAS Collaboration, *Luminosity determination in pp collisions at $\sqrt{s} = 13$ TeV using the ATLAS detector at the LHC*, ATLAS-CONF-2019-021, 2019, URL: https://cds.cern.ch/record/2677054.

[155] S. van der Meer, *Calibration of the effective beam height in the ISR*, tech. rep., CERN, 1968, URL: https://cds.cern.ch/record/296752.

[156] R. Fruhwirth, *Application of Kalman filtering to track and vertex fitting*, Nucl. Instrum. Meth. A **262** (1987) 444.

[157] ATLAS Collaboration, *Reconstruction of primary vertices at the ATLAS experiment in Run 1 proton–proton collisions at the LHC*, Eur. Phys. J. C **77** (2017) 332, arXiv: 1611.10235 [hep-ex].

[158] ATLAS Collaboration, *Electron and photon performance measurements with the ATLAS detector using the 2015–2017 LHC proton–proton collision data*, JINST **14** (2019) P12006, arXiv: 1908.00005 [hep-ex].

[159] ATLAS Collaboration, *Topological cell clustering in the ATLAS calorimeters and its performance in LHC Run 1*, Eur. Phys. J. C **77** (2017) 490, arXiv: 1603.02934 [hep-ex].

[160] ATLAS Collaboration, *Electron and photon energy calibration with the ATLAS detector using 2015–2016 LHC proton–proton collision data*, JINST **14** (2019) P03017, arXiv: 1812.03848 [hep-ex].

[161] ATLAS Collaboration, *Electron reconstruction and identification in the ATLAS experiment using the 2015 and 2016 LHC proton–proton collision data at $\sqrt{s} = 13$ TeV*, Eur. Phys. J. C **79** (2019) 639, arXiv: 1902.04655 [hep-ex].

[162] ATLAS Collaboration, *Muon reconstruction performance of the ATLAS detector in proton–proton collision data at $\sqrt{s} = 13$ TeV*, Eur. Phys. J. C **76** (2016) 292, arXiv: 1603.05598 [hep-ex].

[163] ATLAS Collaboration, *Muon reconstruction and identification efficiency in ATLAS using the full Run 2 pp collision data set at $\sqrt{s} = 13$ TeV*, Eur. Phys. J. C **81** (2021) 578, arXiv: 2012.00578 [hep-ex].

[164] ATLAS Collaboration, *Jet reconstruction and performance using particle flow with the ATLAS Detector*, Eur. Phys. J. C **77** (2017) 466, arXiv: 1703.10485 [hep-ex].

[165] M. Cacciari, G. P. Salam, and G. Soyez, *The anti-k_t jet clustering algorithm*, JHEP **04** (2008) 063, arXiv: 0802.1189 [hep-ph].

[166] M. Cacciari, G. P. Salam, and G. Soyez, *FastJet user manual*, Eur. Phys. J. C **72** (2012) 1896, arXiv: 1111.6097 [hep-ph].

[167] ATLAS Collaboration, *Jet energy scale and resolution measured in proton–proton collisions at $\sqrt{s} = 13$ TeV with the ATLAS detector*, Eur. Phys. J. C **81** (2020) 689, arXiv: 2007.02645 [hep-ex].

[168] M. Cacciari, G. P. Salam, and G. Soyez, *The Catchment Area of Jets*, JHEP **04** (2008) 005, arXiv: 0802.1188 [hep-ph].

[169] ATLAS Collaboration,
Tagging and suppression of pileup jets with the ATLAS detector,
ATLAS-CONF-2014-018, 2014, URL: https://cds.cern.ch/record/1700870.

[170] ATLAS Collaboration, *ATLAS b-jet identification performance and efficiency measurement with $t\bar{t}$ events in pp collisions at $\sqrt{s} = 13$ TeV*,
Eur. Phys. J. C **79** (2019) 970, arXiv: 1907.05120 [hep-ex].

[171] ATLAS Collaboration, *Optimisation and performance studies of the ATLAS b-tagging algorithms for the 2017-18 LHC run*, ATL-PHYS-PUB-2017-013, 2017,
URL: https://cds.cern.ch/record/2273281.

[172] ATLAS Collaboration, *b-tagging in dense environments*, ATL-PHYS-PUB-2014-014, 2014, URL: https://cds.cern.ch/record/1750682.

[173] ATLAS Collaboration, *Performance of missing transverse momentum reconstruction with the ATLAS detector using proton–proton collisions at $\sqrt{s} = 13$ TeV*,
Eur. Phys. J. C **78** (2018) 903, arXiv: 1802.08168 [hep-ex].

[174] ATLAS Collaboration,
E_T^{miss} performance in the ATLAS detector using 2015–2016 LHC pp collisions,
ATLAS-CONF-2018-023, 2018, URL: https://cds.cern.ch/record/2625233.

[175] J. Roggel, *Search for vector-like top quarks and third-generation leptoquarks at $\sqrt{s} = 13$ TeV with the ATLAS experiment*,
Master thesis: Bergische Universität Wuppertal, 2018.

[176] ATLAS Collaboration,
ATLAS data quality operations and performance for 2015–2018 data-taking,
JINST **15** (2020) P04003, arXiv: 1911.04632 [physics.ins-det].

[177] ATLAS Collaboration, *Studies on top-quark Monte Carlo modelling for Top2016*,
ATL-PHYS-PUB-2016-020, 2016, URL: https://cds.cern.ch/record/2216168.

[178] S. Frixione, E. Laenen, P. Motylinski, C. White, and B. R. Webber,
Single-top hadroproduction in association with a W boson, JHEP **07** (2008) 029,
arXiv: 0805.3067 [hep-ph].

[179] M. Aliev et al., *HATHOR – HAdronic Top and Heavy quarks crOss section calculatoR*,
Comput. Phys. Commun. **182** (2011) 1034, arXiv: 1007.1327 [hep-ph].

[180] P. Kant et al., *HatHor for single top-quark production: Updated predictions and uncertainty estimates for single top-quark production in hadronic collisions*,
Comput. Phys. Commun. **191** (2015) 74, arXiv: 1406.4403 [hep-ph].

[181] N. Kidonakis, *Two-loop soft anomalous dimensions for single top quark associated production with a W^- or H^-*, Phys. Rev. D **82** (2010) 054018,
arXiv: 1005.4451 [hep-ph].

[182] N. Kidonakis, "Top Quark Production", *Proceedings, Helmholtz International Summer School on Physics of Heavy Quarks and Hadrons (HQ 2013)* (JINR, Dubna, Russia, July 15–28, 2013) 139, arXiv: 1311.0283 [hep-ph].

[183] T. Gleisberg and S. Höche, *Comix, a new matrix element generator*, JHEP **12** (2008) 039, arXiv: 0808.3674 [hep-ph].

[184] F. Buccioni et al., *OpenLoops 2*, Eur. Phys. J. C **79** (2019) 866, arXiv: 1907.13071 [hep-ph].

[185] F. Cascioli, P. Maierhöfer, and S. Pozzorini, *Scattering Amplitudes with Open Loops*, Phys. Rev. Lett. **108** (2012) 111601, arXiv: 1111.5206 [hep-ph].

[186] A. Denner, S. Dittmaier, and L. Hofer, *Collier: A fortran-based complex one-loop library in extended regularizations*, Comput. Phys. Commun. **212** (2017) 220, arXiv: 1604.06792 [hep-ph].

[187] C. Anastasiou, L. Dixon, K. Melnikov, and F. Petriello, *High-precision QCD at hadron colliders: Electroweak gauge boson rapidity distributions at next-to-next-to leading order*, Phys. Rev. D **69** (2004) 094008, arXiv: hep-ph/0312266.

[188] ATLAS Collaboration, *ATLAS Pythia 8 tunes to 7 TeV data*, ATL-PHYS-PUB-2014-021, 2014, URL: https://cds.cern.ch/record/1966419.

[189] R. D. Ball et al., *Parton distributions with LHC data*, Nucl. Phys. B **867** (2013) 244, arXiv: 1207.1303 [hep-ph].

[190] ATLAS Collaboration, *The Pythia 8 A3 tune description of ATLAS minimum bias and inelastic measurements incorporating the Donnachie–Landshoff diffractive model*, ATL-PHYS-PUB-2016-017, 2016, URL: https://cds.cern.ch/record/2206965.

[191] C. G. Lester and D. J. Summers, *Measuring masses of semiinvisibly decaying particles pair produced at hadron colliders*, Phys. Lett. B **463** (1999) 99, arXiv: hep-ph/9906349.

[192] H.-C. Cheng and Z. Han, *Minimal Kinematic Constraints and m(T2)*, JHEP **12** (2008) 063, arXiv: 0810.5178 [hep-ph].

[193] ATLAS Collaboration, *Search for top squark pair production in final states with one isolated lepton, jets, and missing transverse momentum in $\sqrt{s} = 8$ TeV pp collisions with the ATLAS detector*, JHEP **11** (2014) 118, arXiv: 1407.0583 [hep-ex].

[194] P. Konar, K. Kong, K. T. Matchev, and M. Park, *Dark Matter Particle Spectroscopy at the LHC: Generalizing M(T2) to Asymmetric Event Topologies*, JHEP **04** (2010) 086, arXiv: 0911.4126 [hep-ph].

[195] C. G. Lester and B. Nachman, *Bisection-based asymmetric M_{T2} computation: a higher precision calculator than existing symmetric methods*, JHEP **03** (2015) 100, arXiv: 1411.4312 [hep-ph].

[196] ATLAS Collaboration,
Measurements of top-quark pair differential and double-differential cross-sections in the ℓ+jets channel with pp collisions at $\sqrt{s} = 13$ TeV using the ATLAS detector,
Eur. Phys. J. C **79** (2019) 1028, arXiv: 1908.07305 [hep-ex],
Erratum: Eur. Phys. J. C **80** (2020) 1092.

[197] ATLAS Collaboration,
Measurement of the $t\bar{t}$ production cross-section and lepton differential distributions in $e\mu$ dilepton events from pp collisions at $\sqrt{s} = 13$ TeV with the ATLAS detector,
Eur. Phys. J. C **80** (2020) 528, arXiv: 1910.08819 [hep-ex].

[198] M. Feindt, *A Neural Bayesian Estimator for Conditional Probability Densities*, (2004), arXiv: physics/0402093 [physics.data-an].

[199] M. Feindt and U. Kerzel, *The NeuroBayes neural network package*,
Nucl. Instrum. Meth. A **559** (2006) 190, ed. by J. Blumlein et al.

[200] CMS Collaboration, *Measurement of the Polarization of W Bosons with Large Transverse Momenta in W+Jets Events at the LHC*,
Phys. Rev. Lett. **107** (2011) 021802, arXiv: 1104.3829 [hep-ex].

[201] J. Butterworth et al., *PDF4LHC recommendations for LHC Run II*,
J. Phys. G **43** (2016) 023001, arXiv: 1510.03865 [hep-ph].

[202] E. Re, *Single-top Wt-channel production matched with parton showers using the POWHEG method*, Eur. Phys. J. C **71** (2011) 1547, arXiv: 1009.2450 [hep-ph].

[203] ATLAS Collaboration,
Search for the standard model Higgs boson produced in association with top quarks and decaying into a $b\bar{b}$ pair in pp collisions at $\sqrt{s} = 13$ TeV with the ATLAS detector,
Phys. Rev. D **97** (2018) 072016, arXiv: 1712.08895 [hep-ex].

[204] ATLAS Collaboration, *Measurements of WH and ZH production in the $H \to b\bar{b}$ decay channel in pp collisions at 13 TeV with the ATLAS detector*,
Eur. Phys. J. C **81** (2021) 178, arXiv: 2007.02873 [hep-ex].

[205] D. de Florian et al.,
Handbook of LHC Higgs Cross Sections: 4. Deciphering the Nature of the Higgs Sector, (2016), arXiv: 1610.07922 [hep-ph].

[206] ATLAS Collaboration, *Multi-boson simulation for 13 TeV ATLAS analyses*,
ATL-PHYS-PUB-2016-002, 2016, URL: https://cds.cern.ch/record/2119986.

[207] ATLAS Collaboration, *Measurement of $W^{\pm}$ and Z-boson production cross sections in pp collisions at $\sqrt{s} = 13$ TeV with the ATLAS detector*, Phys. Lett. B **759** (2016) 601, arXiv: 1603.09222 [hep-ex].

[208] ATLAS Collaboration, *In situ calibration of large-radius jet energy and mass in 13 TeV proton–proton collisions with the ATLAS detector*, Eur. Phys. J. C **79** (2019) 135, arXiv: 1807.09477 [hep-ex].

[209] G. Cowan, K. Cranmer, E. Gross, and O. Vitells, *Asymptotic formulae for likelihood-based tests of new physics*, Eur. Phys. J. C **71** (2011) 1554, [Erratum: Eur.Phys.J.C 73, 2501 (2013)], arXiv: 1007.1727 [physics.data-an].

[210] J. Neyman and E. S. Pearson, *On the Problem of the Most Efficient Tests of Statistical Hypotheses*, Phil. Trans. Roy. Soc. Lond. A **231** (1933) 289.

[211] A. L. Read, *Presentation of search results: The CL(s) technique*, J. Phys. **G28** (2002) 2693.

[212] J. A. Aguilar-Saavedra, *Mixing with vector-like quarks: constraints and expectations*, EPJ Web Conf. **60** (2013) 16012, arXiv: 1306.4432 [hep-ph].

[213] M. Buchkremer, G. Cacciapaglia, A. Deandrea, and L. Panizzi, *Model Independent Framework for Searches of Top Partners*, Nucl. Phys. B **876** (2013) 376, arXiv: 1305.4172 [hep-ph].

[214] ATLAS Collaboration, *Search for single production of vector-like T quarks decaying to Ht or Zt in pp collisions at $\sqrt{s} = 13$ TeV with the ATLAS detector*, ATLAS-CONF-2021-040, 2021, URL: https://cds.cern.ch/record/2779174.

[215] ATLAS Collaboration, *Search for pair-produced scalar and vector leptoquarks decaying into third-generation quarks and first- or second-generation leptons in pp collisions with the ATLAS detector*, ATLAS-CONF-2022-009, 2022, URL: https://cds.cern.ch/record/2805213.

[216] ATLAS Collaboration, *Search for pair production of third-generation scalar leptoquarks decaying into a top quark and a τ-lepton in pp collisions at $\sqrt{s} = 13$ TeV with the ATLAS detector*, JHEP **06** (2021) 179, arXiv: 2101.11582 [hep-ex].

[217] ATLAS Collaboration, *Measurements of differential cross-sections in top-quark pair events with a high transverse momentum top quark and limits on beyond the Standard Model contributions to top-quark pair production with the ATLAS detector at $\sqrt{s} = 13$ TeV*, (2022), arXiv: 2202.12134 [hep-ex].

[218] J. Mazzitelli et al., *Top-pair production at the LHC with MiNNLO$_{PS}$*, (2021), arXiv: 2112.12135 [hep-ph].

[219] J. Mazzitelli et al., *Next-to-Next-to-Leading Order Event Generation for Top-Quark Pair Production*, Phys. Rev. Lett. **127** (2021) 062001, arXiv: 2012.14267 [hep-ph].

[220] ATLAS Collaboration, *Search for new phenomena with top quark pairs in final states with one lepton, jets, and missing transverse momentum in pp collisions at $\sqrt{s} = 13$ TeV with the ATLAS detector*, JHEP **04** (2020) 174, arXiv: 2012.03799 [hep-ex].

[221] ATLAS Collaboration, *Search for new phenomena in pp collisions in final states with tau leptons, b-jets, and missing transverse momentum with the ATLAS detector*, Phys. Rev. D **104** (2021) 112005, arXiv: 2108.07665 [hep-ex].

[222] T. Ježo, J. M. Lindert, P. Nason, C. Oleari, and S. Pozzorini, *An NLO+PS generator for $t\bar{t}$ and Wt production and decay including non-resonant and interference effects*, Eur. Phys. J. C **76** (2016) 691, arXiv: 1607.04538 [hep-ph].

[223] S. Frixione et al., *Automated simulations beyond the Standard Model: supersymmetry*, JHEP **12** (2019) 008, arXiv: 1907.04898 [hep-ph].

[224] ATLAS Collaboration, *Studies of $t\bar{t}/tW$ interference effects in $b\bar{b}\ell^+\ell^{-\prime}\nu\bar{\nu}'$ final states with Powheg and MadGraph5_aMC@NLO setups*, ATL-PHYS-PUB-2021-042, 2021, URL: https://cds.cern.ch/record/2792254.

[225] F. Demartin, B. Maier, F. Maltoni, K. Mawatari, and M. Zaro, *tWH associated production at the LHC*, Eur. Phys. J. C **77** (2017) 34, arXiv: 1607.05862 [hep-ph].

[226] T. Ježo, J. M. Lindert, N. Moretti, and S. Pozzorini, *New NLOPS predictions for $t\bar{t}$ + b-jet production at the LHC*, Eur. Phys. J. C **78** (2018) 502, arXiv: 1802.00426 [hep-ph].

[227] ATLAS Collaboration, *Probing the Quantum Interference between Singly and Doubly Resonant Top-Quark Production in pp Collisions at $\sqrt{s} = 13$ TeV with the ATLAS Detector*, Phys. Rev. Lett. **121** (2018) 152002, arXiv: 1806.04667 [hep-ex].

Acknowledgements

This dissertation would not have been possible without the support from a number of people. First of all, I would like to thank my supervisor PD Dr. Frank Ellinghaus for all the support and guidance during my last years at Wuppertal university. I am also grateful to Prof. Dr. Wolfgang Wagner for agreeing to be a referee for this dissertation and all the constructive comments over the last years.
Furthermore, I would like to thank all members of the Wuppertal particle physics group. I am thankful to Dr. Dominic Hirschbühl for all the support and discussions concerning Monte Carlo event generators. Thanks goes to the cluster team for their general technical support and the always good performance of the cluster.
A special thanks goes to Volker. Working with him was always a pleasure.
Furthermore, I would like to thank the Wuppertal PhD students, namely Frederic, Johanna, Joshua, Maren, Marvin, Oliver, Shayma, and Volker. You made the time at work enjoyable and the collaboration was always helpful.
Finally, I am deeply grateful to my parents and my sister. I would have not been able to complete this dissertation without your support and encouragement.